Pulsar Astrometry by VLBI

Mamoru Sekido

Communications Research Laboratory

Supervisor: Prof. Yuri Petrovich Ilyasov

Pushchino Radio Astronomy Observatory of

the Lebedev Physical Institute, Russia

Acknowledgements

I am grateful to Prof. Tetsuo Sasao of National Astronomical Observatory of Japan for his kind consultation, encouragement, and efforts to introduce this paper to the PhD justification stage of the Graduate University for Advanced Studies. This research work was made on the basis of collaboration between the Communications Research Laboratory in Japan and the Pushchino Radio Astronomy Observatory (PRAO) of the Astro Space Center of the P.N. Lebedev Physical Institute of Russia. This inter-government collaboration agreement was made by Prof. Yuri Petrovich Ilyasov of the PRAO and Michito Imae of the CRL. I am also grateful to Prof. Yuri Petrovich Ilyasov and Michito Imae for supporting this study. Prof. Yuri P. Ilyasov has been strongly supporting the pulsar VLBI experiments and research work from the Russian side. His great enthusiasm for pulsar research has overcome many problems facing us and always encouraged the author. Michito Imae opened the door to collaboration between Russia and Japan on pulsar research and he helped the VLBI experiments and this study both directly and indirectly. Especially, he supported this research work from the budgetary and environmental points of view. I also thankful to S. Hama, and H. Kiuchi for their cooperation on designing and development of the K4 correlator. In particular, S. Hama led my interest in pulsar VLBI data processing. I also thankful T. Masubuchi of Cosmo Research Corp. for the actual hardware production and much help in the development of the K4 correlator.

I appreciate to Dr. Alexander E. Rodin of the PRAO for his contribution to development of pulse arrival time and frequency calculation software for the K4 correlator's gating function, his help in data processing, and useful discussions with him. I appreciate to Mr. Vasilli V. Oreshko of the PRAO and, and Yuko Hanado of CRL for supporting this work. They gave me much technical aid, useful advise, and encouragement.

I also thank all the people who took part in this observational research work: Dr. J. Nakajima, E. Kawai, N. Kurihara, Y. Takahashi, Dr. T. Kondo. Y. Koyama, H. Kiuchi, H. Okubo, Dr. H. Osaki, Dr. M. Hosokawa, Dr. R. Ichikawa of CRL. Especially, Dr. J. Nakajima, Mr. E. Kawai, Mr. N. Kurihara, Mr. H. Okubo, and Dr. H. Osaki supported the observations with the 34-m antenna. Y. Koyama helped the author to use the VLBI data-analysis software *CALC/SOLVE* in this study. Also I wish to again thank Dr. H. Osaki for checking my thesis several times and thanks Ms. Arimura for supporting.

I am thankful to Prof. Boris Alekseevich Poperechenko, Viktor Alekseevich Agafonov, Fateev Aleksey Nikitich, Mikhail Dolgov, and Igor Germanovich Lukin of the Special Research Bureau of Moscow Power Engineering Institute for supporting the operation of the Kalyazin 64-m antenna and their warm hospitality. I am also thankful to Artur Viktorovich Serov, Dr. Arkadii Efimovich Avramenko, Dr. Oreg Valer'evich Doroshenko, Vlagimir Potapov, Anatolii Aleksandrovich Nikolenko, Prof. Rustam Davudovich Dagkesamansky, and the staff of the PRAO of the Lebedev Physical Institute; they also supported the observations with their warm friendship and hospitality. I am also thankful to Dr. Komar of the Russian Science and Technology Agency for supporting this inter-government collaboration from Russian government side.

The author also thanks Dr. Stefan Schaer at Bern University for kindly providing the GIM data and related subroutines and Dr. Stefan Schlueter at the DLR for kindly providing the

satellite DCB data. I thank Yoshiki Igarashi and Hisamitsu Minakoshi of CRL for providing the TECMETER data. Part of this research has made use of international geodetic VLBI experiment data NEOS-A735, NEOS-A736, NEOS-A737, NEOS-A738, CORE-1001, and CORE-3001 provided by International VLBI Service for Geodesy and Astrometry. Pulsar's pulse profile data was used from the data base of published pulse profiles maintained by the European Pulsar Network, available at: http://www.mpifr-bonn.mpg.de/pulsar/data/. Finally, I am thankful to my wife Hiroko and sons Ryota and Tatsuya for supporting me and giving me a lot of fun.

This research work was performed under the budgetary support of the International Collaboration Fund of Science and Technology Agency of Japan and the Russian Fund of Basic Research, Grant No. 97-02-16446.

Contents

List of Tables

List of Figures

Chapter 1

General Introduction

1.1 Overview of Pulsar

Pulsar was discovered by J. Bell and A. Hewish in 1968, and later it was recognised as a rotating neutron star with a high magnetic field. More than 1000 pulsars have been discovered since then [*Taylor et al.*, 1993], and their pulse periods are in the range of 1.6 ms to several seconds. A pulsar (neutron star) is thought to be born after a super-nova explosion caused by the gravitational collapse of star with 8 - 30 solar masses [*Shibazaki,* 1993]. Although only several pulsars are identified the relation with super-nova remnant as their progenitor. The reason of the poor identification between pulsars and super-nova remnants will be that they were escaped from their birth place with the high velocity. In general, pulsars have high birth velocity [*Lyne and Lolimer,* 1994].

Pulsar is investigated not only because of its own astrophysical property but also its unique emission property; that is quite small point radio source. The radius of a neutron star is thought about 10 km and the radius of its light cylinder is about 10^9 cm. When this object is seen from 1 kilo-parsec away, the angular diameter is about 10^{-7} arc seconds. A signal emitted from such a very small angular source has a very pure spatial frequency. It means that two signals, which are distantly separated after propagation, have a coherence to interfere with each other. Microwave or lower frequency electromagnetic wave is scattered by ionized medium (Interstellar scattering). The interstellar scattering modulate a phase of the radio-wave signal, so a diffraction pattern is formed at the observer plane. The time variation of this diffraction pattern is observed as interstellar scintillation (ISS). However, a quasar does not shows ISS feature because it has a larger angular size. This phenomenon can be understood more easily by the analogy that stars twinkle but planets do not. The interstellar scattering also broaden the apparent angular size of a source and distorts the frequency spectrum (as it is demonstrated in the Chapter 5). This angular broadening has to be taken into account in astrometric observation, especially at lower frequency.

One major property of a pulsar is the high stability of its pulse period. Consequently pulsars are investigated as clocks for keeping long term stability of time [*Taylor,* 1991; *Guinot and Petit,* 1991]. The stability of pulse arrival time is expected to exceed the that of atomic time standards over long time interval, since it is not affected by the gravity of celestial bodies in the solar system. The high rotation stability is kept by the huge inertia (10^{38} $kg \cdot m^2$) and huge rotational kinetic energy of a high density neutron star. The rotation energy of a pulsar (10^{38} – 10^{45} J) is much larger than that of the Earth (10^{29} J) and the Sun (10^{35} J). By using the high stability of the pulse time of arrival (TOA), positions of millisecond pulsars can be measured very accurately in relation to the revolutionary orbit of the Earth around the Sun. Thus millisecond pulsar coordinates can be determined accurately in the reference frame of planetary ephemeris (dynamical reference frame: DRF) used for pulse TOA analysis.

1.2 History of Interferometric Observation of Pulsars

A pulsar is known as a stellar object with relatively high velocity [e.g., *Lyne and Lorimer,* 1994]. Pulsars have been mainly observed by using a single dish antenna for pulse TOA [e.g., *Kaspi et al.,* 1994] and scintillation [e.g., *Scheuer,* 1968; *Rickett,* 1969] observations. And the properties of pulsar have also mainly been derived from single dish observations. The main difficulty with such observation is the weak flux density of the pulsars. The proper motion of a pulsar can be derived from scintillation observation (scintillation time scale τ_s and scattering disk size θ_{scat}) by assuming a phase screen placed in the intermediate space between the pulsar and the observer (see Chapter 5). Although, Pulsar coordinates, proper motion, and parallax can be measured by pulsar timing observation [e.g., *Kaspi et al,* 1994; Camilo et al.; 1994], the accurate coordinates and proper motions are obtained only when pulse signals are as stable as atomic standards and they are observed for a long time span. Distances to most pulsars are evaluated with dispersion measure (DM) obtained by pulsar-timing observation, however, the distance depends on interstellar free-electron distribution model. Proper motions derived from scintillation observation are also affected by the assumed phase-screen model.

Interferometric pulsar observation enables model independent measurement of pulsar coordinates, proper motion and distance. If a pulsar's birth place is identified from astrometric measurements, comparison between derived kinetic age (τ_k) and characteristic age (τ_c), which is derived from the spin-down rate of the pulsar, will reveal neutron star's magnetic field decay characteristic [e.g., *Harrison et al.,* 1993]. The characteristic age of a pulsar is expressed by

$$\tau_c = \frac{P}{\dot{P}_{int}(n-1)}, \tag{1.1}$$

where n is the braking index and $\dot{P}_{int}$ is the intrinsic pulse period decay rate. Nice and Taylor (1995) pointed out that $\dot{P}_{int}$ needs correction since it is affected by its proper motion.

Model independent distance determination by trigonometric parallax measurement is also important for evaluation of pulsar velocity, pulsar population, and free electron density distribution in the Galaxy. Pulse arrival time to an observer is delayed by free-electrons in the cold plasma between the observer and the pulsar. As it is discussed in Chapter 4, the microwave propagation delay in the cold plasma is proportional to DM/f^2, where DM is column density of free electrons (called 'dispersion measure') and f is radio frequency. Thus, a combination of DM, which was derived from pulse TOA measurements at different radio frequencies, and distance to the pulsar gives free-electron density in the interstellar medium. Taylor and Codes (1993) compiled pulsars distances (by interferometers and HI absorption measurements) and DMs measured by pulsar timing, and they constructed a free-electron-density-distribution model in the Galaxy. Consequently most of the pulsar's distances evaluated by DM were revised and the mean birth velocity of pulsar was found to be more than two times faster than previously thought [*Lyne and Lorimer,* 1994].

Comparisons of pulsar coordinates between Very Long Baseline Interferometry (VLBI) and pulsar timing enable fundamental reference frame tie between the International Reference Frame (ICRF) and dynamical reference frame (planetary ephemeris). More detail on the frame tie is given in the next Section.

For these purposes described above, interferometric observations of pulsars have been performed, although they were not easy because of the small flux density and steep spectrum characteristic of pulsars. A brief history of interferometric pulsar observations published is given as follows:

1975 Anderson, Lyne, and Peckham (1975) measured proper motions of six pulsars by using the Jodrell Bank (76-m) – Defford (25-m) radio-link interferometer (127-km baseline). Obser-

vation frequency was 408 MHz with a 4MHz band width. The proper motion measurement accuracy was 4-36 mas/year.

1976 Backer and Sramek (1976; 1981) measured proper motions of five pulsars by using the NRAO 35-km interferometer. Observation frequency was 2.7 GHz with a bandwidth 30 MHz. The observation accuracy was 10-200 mas/year.

1979 Salter, Lyne and Anderson (1979) measured parallax of nine pulsars at an accuracy of 1-8 mas by using the Jodrell Bank-Defford radio-link interferometer. Observation frequency was 408 MHz.

1982 Lyne, Anderson, and Salter (1982) measured proper motions of 26 pulsars by using MkIA-Defford radio-link interferometer (127-km baseline). Observation frequency was 408 MHz and the accuracy of proper motion was 1-28 mas/year.

1983 Manchester R. N., et al. (1983) measured the coordinates of binary pulsar PSR B0820+02 by the Very Large Array (VLA) and compared them with timing results. The observation frequencies were 1465 MHz and 4885 MHz. The accuracy of interferometric measurement was 500 mas.

1984 Fomalont et al. (1984) measured coordinates of 59 pulsars by the VLA and compared them with timing results. Observation radio frequencies were 1385 MHz and 1665 MHz. The accuracy of the interferometric observation was around 0.2 arc sec.

1985 Backer et al. (1985) measured the coordinates of millisecond pulsar PSR B1937+21 and binary pulsar PSR B1913+16 by the VLA and compared with pulsar timing results. Observation frequencies were 1415 MHz and 1635 MHz with a bandwidth 50 MHz. The coordinate accuracy of the interferometric measurements was 30-190 mas.

1985 Bartel et al., (1985a) observed pulsars PSR B0329+54 and PSR 1133+16 with VLBI (Green Bank:43-m, Owens Valley:40-m, Effelsberg:100-m) with the Mark-III VLBI system. Observation radio frequency was in S-band (2 MHz $\times$ 6 channels) and X-band (2 MHz $\times$ 8 channels). The accuracy of the coordinate measurements was 5-200 mas.

1985 Bartel et al., (1985b) investigated pulse profile of PSR B0329+54 by using the pulsar-gating function of the Mark-III correlator. The observed data of Bartel et al. (1995a) was used in this study.

1986 Gwinn et al. (1986) measured parallax and proper motion of pulsar PSR B0823+26 and PSR B0950+08 by VLBI (Arecibo:305-m, Green Bank:43-m, Owens Valley:40-m) with the phase reference method. Observation radio frequency was 1.6 GHz. The accuracy was 2-4 mas/year for proper motion and 0.6-0.8 mas for parallax.

1989 Bailes et al. (1989) measured proper motion of the Vela pulsar (PSR B0833-45) by using the Parks-Tidbinbilla radio-link interferometer (275-km). Observation radio frequency was 1.6 GHz and the accuracy of the measurement was 2-4 mas/year.

1992 Fomalont et al. measured positions of 40 pulsars and proper motions of 21 pulsars by the VLA. Observation radio frequency was 1.4 GHz. The accuracy of the measurement was 50-200 mas for coordinates and about 10 mas/year for proper motion.

1993 Harrison, Lyne, and Anderson (1993) measured proper motions of 44 pulsars by using the Multi-Element Radio Linked Interferometer Network (MERLIN) at 408 MHz. The measurement accuracy was 1-35 mas/year.

1994 Petit G (1994) observed millisecond pulsar PSR B1937+21 by VLBI (Effelsberg:100m, Jodrell Bank:76-m, Nançay:90-m) with the phase reference method. Observation radio frequency was 1.6 GHz. The coordinates accuracy was about 4 mas.

1996 Campbell et al. (1996, 2000) measured parallax and proper motion of pulsar PSR B2021+51 at 2.218 GHz with the Mark-IIIA VLBI system (14 x 2MHz). They used a global VLBI network (Medicina, Westford, Algonquin, Green Bank, Richmond, Fairbanks, Hancock, North Liberty, Pie Town, Kitt Peak, Brewster, and Owens Valley) with the phase-reference technique. The accuracy of proper motion was 0.2 mas/year and parallax was 0.37 mas.

1996 Dewey at al. (1991) measured coordinates of millisecond pulsar PSR B1937+21 by VLBI (Arecibo:305-m, DSN 70-m antennas at Goldstone and Madrid). Observation radio frequency was 1.67 GHz. The coordinates accuracy was 4 mas in right ascension and 16 mas in declination.

1996 Bartel et al. measured the position of PSR B1937+21 by VLBI (Green Bank 43-m, VLA:27 $\times$ 25-m, Owens Valley:40-m) with phase-reference technique and compared them with pulsar timing results for reference frame tie. The interferometric measurement accuracy was 5.5 mas in right ascension and 3 mas in declination.

1997 Gwinn et al. (1997, 1998, 2000a) observed the Vela pulsar with a global VLBI network (Tidbinbilla:70-m, Parks:64-m, Hobart:25-m, Hartebeesthoek:25-m, and seven antennas of the VLBA) in S-band by using the Mark -III VLBI system (14 x 2 MHz). They inferred that the size of the emission region of the Vela pulsar as about 500 km based on considerations on optics of interstellar scattering. They also inferred that the broadening size of the radio source produced by Vela supernova remnant as 3.3 x 2 mas in S-band. Gwinn et al. (2000b, 2000c) also observed Vela pulsar with the VLBI Space Observatory Programme (VSOP).

1997 Fomalont et al. (1997) measured positions of 18 pulsars by VLA and improved the proper motion measurement by combination with former published results (Fomalont et al., 1992) . The accuracy of proper motion was 3-47 mas/year.

1998 Galama et al.,(1999) observed pulsars PSR B2020+51, PSR B1508+55, and PSR B0450+55 by using a eight-station network (Effelsberg, Westerbork, and Onsala in Europe; and VLBA-SC, VLBA-NL, VLBA-HN, VLA, and NRAO-140 in the USA) with 7 x 4 MHz bandwidth. They used phase-referenced technique and proper motions of PSR B2020+51 and PSR B1508+55 were measured.

1998 Nunes and Bartel (1998) measured coordinates of pulsar PSR B1257+12 by phase-reference technique at 1.667 GHz with VLBI (Effelsberg:100-m, Goldstone:70-m, Madrid:70-m, and the VLA). Weighted rms of the post-fit residual in their analysis was 0.1 ns, and the accuracy of the coordinates was 3-7 mas.

1999 Sekido et al., (1999a, 199b) measured coordinate and proper motion of pulsar PSR 0329+54 with VLBI (Kashima:34-m - Kalyazin:64-m, 7000 km baseline). Observation frequency was 1.4 GHz with 2 MHz $\times$ 16 channels via the K4 VLBI system. The coordinates accuracy of each epoch was 12-27 mas. Proper motion and position were estimated from combination of our results and Bartel's measurements (1985a), then a accuracy of the final result was 10 mas for position and 0.6 mas/year for proper motion.

1999 Fomalont et al. (1999) measured proper motion and parallax of pulsar B0919+06 and B1857-26 with VLA by using an in-beam calibrator source. Eight channels of observation

frequency band with 8 MHz bandwidth were selected within a range of 1.4 - 1.6 GHz. Coordinates of the pulsar were measured at an accuracy of 0.1-0.4 mas and accuracy of proper motion was 0.3-0.9 mas/year, and that of parallax was 0.14-0.6 mas.

2000 Chatterjee and Codes J. (2000) observed PSR B0919+16, PSR B1133+16, PSR B0823+26, and PSR B1642-03 with VLBA at 1.4 GHz. They used phase-referenced mapping and tried to calibrate ionospheric delay by using a GPS-based ionospheric map. The accuracy of the proper motion was 0.2-0.3 mas/year for PSR B0919+06 and 5-10 mas/year for the other pulsars.

2000 Legge (2000) conducted pulsar astrometry observation with the Australian and South African Long baseline Array (LBA) from 1993 to 1999 in 2 and 8 GHz. He measured proper motion and parallax of the Vela pulsar by phase-referenced mapping at accuracy of 0.1-0.2 mas/year and 0.33 mas, respectively.

2000 M^{c}Key et al. (2000) have been measuring proper motion of young pulsars by using the MERLIN array at 1.4 GHz. They used an in-beam calibrator for phase reference.

2000 Brisken et al. (2000) observed PSR B0950+08 by using VLBA in the 1410 - 1730 MHz frequency band. The recoding bandwidth was 8 x 8 MHz and the widely separated observation frequencies were used to correct the systematic position shift caused by ionospheric delay. They measured proper motion and parallax at accuracy of 0.4-0.5 mas/year and 0.3 mas by using phase-referenced mapping.

2000 Gwinn et al. (2000b, 2000c) and Minter (2000) observed pulsars with the space VLBI programme (VSOP).

Over the last few years, pulsar investigations with interferometry have been increasing. One reason of this might be the improvement of VLBI observation facilities (the VLBA became fully available in the middle of the 1990's and space-VLBI observation started in 1997) and the improvement of observation techniques (e.g., phase referenced mapping) and software (e.g., AIPS++).

1.3 Problem of Phase-Delay Measurements and Group-Delay Measurements

The techniques used in interferometric astrometry are divided into group-delay measurements [e.g., *Bartel et al.,* 1985a; *Sekido et al,* 1999a, 1999b] and phase-delay measurements [e.g., *Salter et al.,* 1979; *Gwinn et al.,* 1986; *Bartel et al.,* 1996; *Fomalont et al., 1999*]. The former is analyzed in two kinds of technique: absolute astrometry with group-delay and differential group-delay measurement. Phase-delay measurements are basically analyzed by differential method because absolute phase-delay measurement is almost impossible due to ambiguity. And this measurement data is analyzed by two techniques: least square analysis by phase delay modeling and phase-referenced mapping. Phase-delay measurement has higher coordinates resolution than group-delay measurement, and is inevitable for parallax measurement. The difficulty of this method is phase connection between scans by resolving phase ambiguity. And this method can also potentially cause incorrect choice of ambiguity and consequently incorrect astrometric results. Usually, nearby compact reference sources are used to calibrate the propagation delay effect including that of troposphere and ionosphere. However, the phase connection is still difficult at low radio frequency mainly due to large ionospheric delay .

Further difficulty of phase connection is caused by the weak flux density of a pulsar and the necessity of fast beam switching between the reference sources and the pulsar. Since phase

error is approximately 1/SNR, shorter integration time for fast beam switching results in lower SNR and larger phase noise. Although large diameter antenna is necessary for higher SNR, it is not suitable for fast beam switching due to large inertia of the antenna. A best solution to overcome the difficulties of phase connection and propagation delay calibration is to use an in-beam calibrator, which is so close to the pulsar that it can be observed simultaneously with the target pulsar. Salter et al. (1979), Lyne et al. (1982), and Harrison et al. (1993) used this technique with MERLIN interferometer at 408 MHz. As frequency is lower, this technique is more advantage because of wider beam width. Fomalont et al. (1999) and Brisken et al. (2000) have successfully performed sub-milli-arc-second pulsar astrometry by using an in-beam calibrator with the VLBA at L-band. However, searching for in-beam calibrator is also hard work. Such in-beam calibrators are not always the ICRF sources nor are their coordinates accurately known.

Because of the difficulties mentioned above, phase delay measurements have possibility of miss-adjustment of the phase ambiguity and miss-leading to wrong solution, in general. The most surprising example is that the proper motion and parallax of PSR B0950+08 measured by Gwinn et al. (1986) is suspected to be inaccurate due to inappropriate choice of lobes [*Brisken et al.,* 2000]. If measurements by Brisken et al. is correct, PSR B0950+08's proper motions measured by Lyne et al. (1984) and Gwinn et al. (1986) are concluded to be incorrect. And both Lyne et al. and Gwinn et al. used phase measurements.

On the other hand, observation of group delay is a relatively conservative approach for pulsar astrometry, since the spatial resolution of source position is less than phase method but no necessity to take care of phase connection between scans. Thus rather long integration time can be taken in each scan for enough SNR and slower beam switching is suitable for large diameter antenna.

Additionally absolute astrometry by using group delay is basically the same procedure to determine source position to maintain the ICRF. Phase delay measurement is no good for absolute coordinates determination, since total delay is unknown due to phase ambiguity. Absolute astrometry by using group delay is superior to phase delay method on determination of absolute coordinates in the reference frame. And proper motions of pulsars can be determined without ambiguity through repetition of the absolute astrometry measurements with several years intervals. Because of these reasons, we chose absolute astrometry for our Japan-Russia pulsar VLBI observation project.

1.4 Purposes

1.4.1 Reference Frame Tie

The reference frame is the foundation of astronomy and its accuracy has been improved by new astronomical instruments and improved technology. The FK5 system has been used for reference frame of optical astronomy and now the Hipparcos catalog, which is constructed from observations of astrometry satellite HIPPARCOS, has taken its place. At the 23rd General Assembly in August 1997, the International Astronomical Union (IAU) decided that from 1 January 1998, the IAU Celestial Reference System would become the International Celestial Reference System (ICRS) in stead of the FK5. The ICRS is realized by estimation of equatorial coordinates of a set of extragalactic radio sources, which makes up the International Celestial Reference Frame (ICRF). Planetary ephemeris (dynamical reference frame: DRF) was developed and improved mainly by the Jet NASA Jet Propulsion Laboratory (JPL) [*Williams and Standish,* 1989] and the The Massachusetts Institute for Technology (MIT). Each of them has internally sub-milli arc second accuracy, but accuracy of the frame tie between the DRF and the ICRF is not so high. Linking between extragalactic reference frame and Hipparcos catalog is also in

progress [*Lindegren and Kovalevsky*, 1995; *Lestrade et al.,* 1999]. Folkner et al. (1994) performed joint analysis of global VLBI data, which obtained by NASA's Deep Space Network in the period 1978 - 1992, and lunar laser ranging (LLR) data, which acquired by LLR tracking station since 1969 till to 1992. From this joint analysis, rotation matrices between planetary ephemerides (DE200, DE210) and ICRF92 were derived. The accuracy of Folkner's frame tie was in about 3 mas.

Better determination of frame tie will benefit to the navigation of interplanetary spacecraft and it will enable study of dynamics of solar system in inertial system more accurately. The ICRF is fixed to extragalactic radio sources and it can be assumed as non-rotation quasi-inertial reference frame. The equinox is defined by intersection of the mean equator with the mean elliptic of the reference epoch (J2000). The direction of equinox changes with time, but it cannot be observed by VLBI accurately, since VLBI is not sensitive to the direction of the Sun. Thus the frame tie and monitoring of its change enables monitoring of motion of equatorial plane, and consequently contribute more accurate estimation of mass of planets.

Frame tie needs radio source, whose coordinates can be measured accurately in both the ICRF and the DRF. Radio pulsar is one of a few radio sources whose position can be measured accurately in both reference frames. Pulsar coordinates derived from pulsar-timing observation are based on the planetary ephemeris, which is used in the pulsar-timing analysis. And radio pulsar's coordinates in the ICRF can be measured by VLBI. Then comparison of pulsar coordinates measured by these two techniques enables a reference frame tie between the ICRF and the DRF. Petit (1994), Dewey et al. (1996), and Bartel et al. (1996) performed astrometric VLBI observation of PSR B1937+21, and they compared the coordinates of the pulsar with that in DE200 measured by pulsar timing observation. Still only one pulsar is used for the frame comparison so far, thus more pulsar's coordinates in need to be measured VLBI accurately.

1.4.2 Accurate Proper Motion and Pulsar Coordinates Measurements

It is known that pulsar have large space velocity in general, then proper motions of pulsars can be measured by a few years of VLBI observations. Proper motion data of pulsars are used for variety of pulsar investigations. Pulsar as rotating neutron star is though to be born as result of super-nova explosion, however, the relation of super-nova-remnant and pulsars are confirmed only for a ten pulsars or so. Precise proper motion and coordinates of pulsar are important for the identification of progenitor of the pulsar.

Also, proper motion is used for estimation of kinetic age of the pulsar. By comparing the kinetic age and a characteristic age, which is defined by using rotation period and period derivative, gives us decay rate of magnetic field of the neutron star [e.g., *Harrison et al.,* 1993].

Precise proper motion and coordinates are important for frame time by using pulsars. Since the epochs of coordinates measurements by VLBI and pulsar-timing are normally different each other. Estimating a rotation matrix between reference frames is done at a an appropriate reference epoch, hence, the coordinates of pulsars need to be propagated to the those at the reference epoch by using proper motion. Errors of pulsar coordinates are are magnified by product of proper motion error and the epoch difference. Then accurate proper motion is useful to connect measurements results at different epochs.

It is possible to measure a proper motion of pulsar through pulse timing analysis, but interferometric measurement is more direct and more reliable.

Accurate absolute coordinates and proper motion of pulsars are also very important for identification or associating pulsars with object at optical or other wavelengths.

1.5 Pulsar VLBI Astrometry under the Japan-Russia collaboration

The Communications Research Laboratory and the Pushchino Radio Astronomy Observatory of the Astro Space Center of the Lebedev Physical Institute in Russia have been collaborating on pulsar observation by pulsar timing and VLBI. The collaboration had started on the basis of an inter-government agreement for cooperation on "Pulsar Time Scales: Precise measurement of millisecond pulsar timing signals". The collaboration program was co-signed by Dr. Yu. P. Ilyasov of the Pushchino Radio Astronomy Observatory and M. Imae of the Communications Research Laboratory in 1994. The Kalyazin 64 m diameter radio telescope in Russia and the Kashima 34 m diameter radio telescope in Japan were used for intercontinental VLBI observation. Observation wavelength 21 cm or 14 cm were used. The main purposes of this project were absolute coordinates and proper motion determination of pulsars on the ICRF by using group delay. Long baseline was required to achieve higher angular resolution by using low delay resolution of group delay and long wavelength. Constant VLBI observation with large diameter antennas were necessary for high SNR in astrometry measurement by VLBI. The Kashima-Kalyazin baseline was one of the best combination of world largest antennas for such purposes, and the collaboration relation between Japanese and Russian team have been quite reliable and friendly each other through the whole collaboration duration.

In spite of the importance of interferometric absolute coordinates measurements of pulsars as mentioned in former Section, such observation had not been performed so frequently. The reasons are mainly two folds: (1) absolute coordinates are difficult to measure with phase delay, (2) long baselines are necessary for high resolution in absolute astrometry with group delay, however it is difficult to use large diameter antennas for long time interval. Thus our 34-m and 64-m antenna pair of the 7000 km baseline is quite unique interferometer devoted for pulsar observation during long period. It is just one baseline interferometer, but this East-West baseline can determine both right ascension and declination precisely especially when the pulsar is at high declination. The Chapter 2 shows overview of the VLBI facilities used in this project. Data reduction and analysis procedures are described in the Chapter 3. Amplitude time variation of pulsar signal after SNR improvement by pulsar-gating function in correlation processing is also shown in this Chapter.

The most significant error source in absolute astrometry of pulsars by VLBI observation is ionospheric propagation delay. Because microwave propagation delay through ionized medium increases in proportion to the square of wavelength. To reduce the error caused from this uncertainty, ionospheric total electron content (TEC) measurement by using GPS data was investigated (Chapter 4).

Radio signal emitted from quite compact radio source is affected by interstellar scattering. The interstellar scattering causes variety of phenomena on radio signal originated from quite compact radio source. The interstellar scintillation and angular broadening of radio source image are typical phenomena of them. Radio emission region of pulsar is quite small in general, thus VLBI observation data of pulsar is distinguished from quasar's data by these phenomena. Since angular broadening smears the position of pulsar at lower radio frequency, this effect may be taken into account for error of astrometry if it is significant. The interstellar scintillation observed in our pulsar VLBI observation is reviewed in Chapter 5. And scattering disk sizes of each pulsars were estimated from our data by assuming thin screen model of the interstellar medium.

Astrometry analysis and results of our pulsar VLBI observations are described in Chapter 6. Ionospheric delay correction by using GPS-based TEC measurement (Chapter 4) was applied in absolute astrometry analysis. Error analysis including station coordinates uncertainty and effect of interstellar scattering are described in this Chapter.

Pulsar is faint radio source in general, thus special digital processing technique pulsar-gating is useful in correlation processing to improve the signal-to-noise ratio (SNR). We had developed a K4 type VLBI correlation processor with the pulsar-gating function and it was applied for data processing of Japan-Russia VLBI observation. The pulsar-gating was essential for detection of pulsar signal. The architecture of the K4 correlator and pulsar-gating function is described in Chapter 7. And Chapter 8 summarize the results, problems, and future prospects.

Chapter 2

Pulsar VLBI Observations by Using the Kashima-Kalyazin Baseline

2.1 Introduction

The Very-Long-Baseline-Interferometry (VLBI) observation of Pulsar with the Kashima 34-m-diameter antenna and Kalyazin 64-m-diameter antenna was started under an inter-government agreement on science and technology between Russia and Japan named, "Pulsar Time Scales. Precise measurement of millisecond pulsar timing signals". Author conducted regular pulsar VLBI observation with a 7000 km baseline for the purpose of pulsar astrometry. Precise measurements of pulsar coordinates and proper motions are the main aim of this project. Such measurements are important as fundamental data for pulsar study. Also frame tie between the International Celestial Reference Frame and Dynamical Reference Frame will be possible by comparison between pulsar coordinates determined by VLBI and pulsar timing observation. Additionally, information on the electron density distribution in interstellar medium was expected to be obtained as by-products of the VLBI observations.

2.2 VLBI Facilities

2.2.1 Stations

The Kalyazin 64-m-diameter radio telescope (TNA-1500 of the Special Research Bureau of the Moscow Power Engineering Institute (SRBMPEI): Figure 2.2 left; hear-after RT-64) is an Az-El-mount-type parabolic antenna with a cassegrain focus system. It has a Multi frequency feed system of receiver and it provides simultaneous multi-frequency and double polarization observation at 600 MHz, 1.4 GHz, 2.2 GHz and 8.3 GHz. Figure 2.1 shows block diagram (left) and photograph (right) of 1.4 GHz receiver system and cryogenics of the RT-64. Its receiver parameters and antenna efficiency are listed in Table 2.1.

This antenna was constructed for deep space tracking by the SRBMPEI. However, it was not used until our first pulsar VLBI experiment in 1995 because of economical problems and the political upheaval of the former Soviet Union. The RT-64 has two sets of driving motor: one for fast slewing (max speed: 1 deg/sec), and the other for slow slewing (max speed: 20 arc minutes/sec). Since the antenna is a huge construction, it cannot move quickly, so users have to carefully prepare the observation schedule. The antenna parameters used for scheduling are listed in Table 2.2. The column of "Const" means the time for the transition of the state of driving from slewing to tracking. The huge inertia of the antenna needs to be taken into account for successful observation and safe operation. For extra safety, we actually used longer times than the "20 sec" in the table.

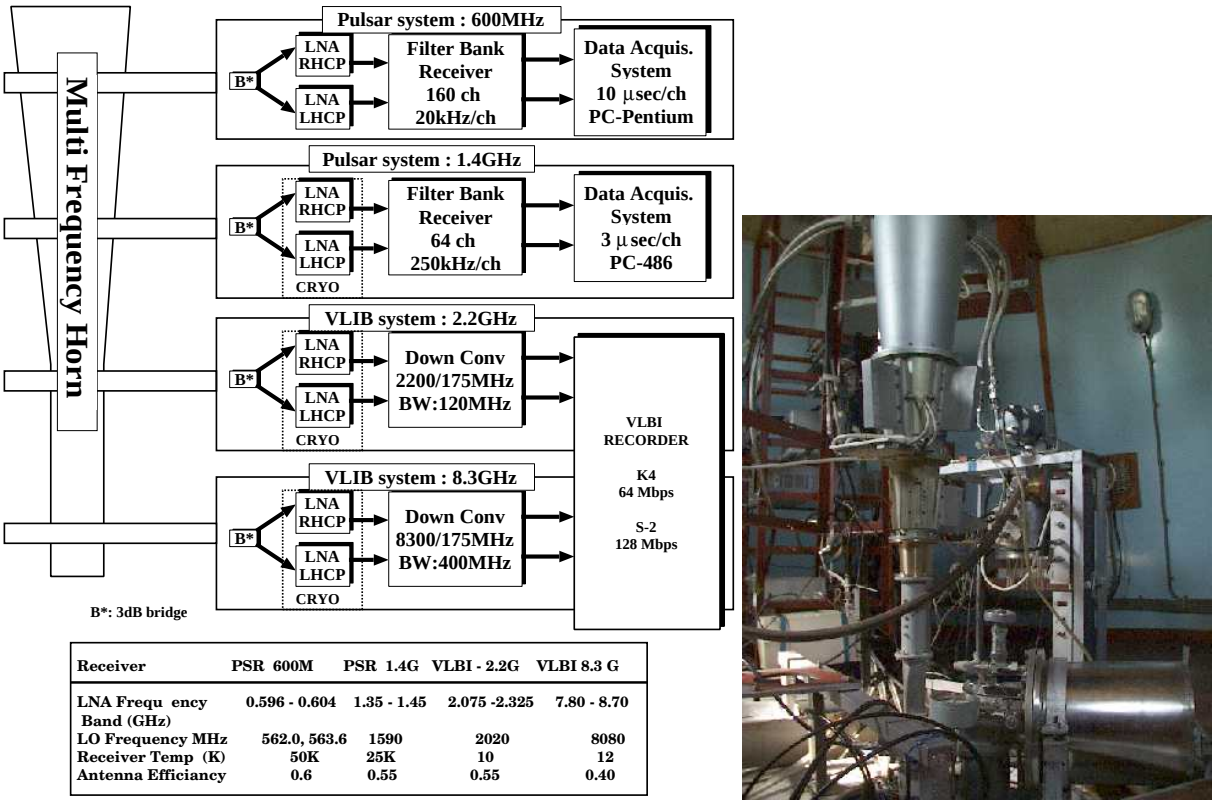

Receiver	PSR 600M	PSR 1.4G	VLBI - 2.2G	VLBI 8.3 G
LNA Frequ ency Band (GHz)	0.596 - 0.604	1.35 - 1.45	2.075 -2.325	7.80 - 8.70
LO Frequency MHz	562.0, 563.6	1590	2020	8080
Receiver Temp (K)	50K	25K	10	12
Antenna Efficiancy	0.6	0.55	0.55	0.40

Figure 2.1: Multi-frequency receivers of Kalyazin Radio Telescope RT-64: block diagram (left) and 1.4-GHz receiver and cryogenic system (right)

Another limitation on the scheduling of the RT-64 is the limited number of tracking points. The operation system of the RT-64 antenna uses a 256-point register for Az-El tracking. An operator thus needs to input 256 points of Az-El data after every 256-point for tracking. When five points are used for tracking one source, about 20 minutes are necessary for every 50 scans for downloading tracking data to the register. We used a 30-minutes time interval every 2.5 to 3 hours for that downloading and also for cooling to avoid over-heating the fast-mode solenoid brakes.

The Kashima 34-m-diameter radio telescope [*Koyama et al.,* 1990; *Imae et al.,* 1995](CRL; Figure 2.2, right) is also an Az-El-mount-type parabola antenna with a cassegrain type receiver feed system. It was constructed in 1988 for VLBI observation as a part of the western Pacific radio interferometer. Multi frequency receivers are interchanged by trolley a system. It can receive frequencies of 1.4, 1.6-1.7, 2.1-2.3, 4.6-5.1, 7.8-8.6, and 21.8-23.8 GHz at present (April 2001). Additional 43-GHz receiver system is under construction in collaboration with CRL, Kagoshima University, and the National Astronomical Observatory of Japan. Receiver noise temperature and antenna efficiency of S and L bands are listed in Table 2.1.

Phase calibration (P-cal) signal generators were installed for both L-band and S-band receivers at both stations. The P-cal signal is injected just after the low noise amplifier of the receiver at both Kashima and Kalyazin stations. A group of comb-tone signals with 10 MHz frequency interval are generated in phase from the P-cal signal generator. This signal is used for compensating the group delay variation, which is caused from intermediate-frequency (IF) signal transmission cable delay variation and variations of local oscillator phases of the video converters.

Antenna parameters used for for scheduling are listed in Table 2.2.

The Kalyazin–Kashima interferometer has a baseline of 7000 km (Figure 2.2 center) in the

Table 2.1: Antenna Parameters of Kashima 34-m-diameter and Kalyazin 64-m-diameter stations

Parameters	Kalyazin	Kashima
Diameter	64 m	34 m
Coordinates (ITRF)	X = 2731190.445 ± 0.01 Y = 2126198.279 ± 0.1 Z = 5339535.645 ± 0.02	X = -3997649.233 ± 0.003 Y = 3276690.768 ± 0.003 Z = 3724278.216 ± 0.003
Epoch (year)	1995.0	1997.0
Site velocity(1)	Vx = -0.0158 Vy = 0.0171 Vz = 0.0071	Vx = -0.0021 Vy = 0.0036 Vz = -0.0135
T_{rec}(L-band)	25 K	20 K
T_{rec}(S-band)	10 K	20 K
η(L-band)	55%	55%
η(S-band)	55%	60%
Frequency Band (GHz)	1.4, 2.2, 8.3	1.4, 1.6, 2.2 5.0, 8.3, 22.2
Hydrogen maser	Kvarz CH1-80	Anritsu RH401A

(1) Site velocity of Wettzell was used for Kalyazin since they were assumed to be on the same plate.

Table 2.2: Antenna parameters of Kashima 34-m and Kalyazin 64-m for observation scheduling

Station		Rate (deg/min)	Const (sec)	Limit1	Limit2
Kalyazin (64 m)	Az	18.0	20.0	65.0	655.0
	El	18.0	20.0	4.0	88.0
Kashima (34 m)	Az	45.0	0.0	90.0	630.0
	El	40.0	0.0	10.0	88.0

east-west direction, and its minimum fringe spacing is 6 mas at 1.4 GHz and about 4 mas at 2.1 GHz.

The station coordinates of the Kashima 34-m-diameter antenna are determined very accurately by international and domestic geodetic VLBI experiments. However, the coordinates of the Kalyazin station have not been measured by VLBI; instead, the station position was determined by a combination of GPS observation and ground measurements in 1995. Thus, the coordinates of the Kalyazin station are expressed in the WGS84 coordinate system. According to the International Earth Rotation Service (IERS), WGS84 coordinates measured by GPS are identical to the International Terrestrial Reference Frame (ITRF) within 10 cm [*ITRF*, 2001]. Station coordinates and antenna parameters are listed in Table 2.1. The site velocity of Wettzell station was used to calculate the station coordinates of Kalyazin at other epoch from 1995, since the sites of Kalyazin and Wettzell are assumed to be on the same crustal plate according to the NUVEL-1A model [*Argus and Gordon*, 1994]. Both stations use hydrogen maser frequency standards as references for clock and frequency. Time synchronization between station clocks and UTC was done by using GPS receivers at both stations.

Figure 2.2: Kalyazin 64-m-diameter antenna (left) of the Special Research Bureau of Moscow Power Engineering Institute of Russia. Kashima 34-m-diameter antenna (right) belongs to the Communications Research laboratory of Japan. These two antennas makes up an east-west direction, 7000-km-baseline interferometer.

2.2.2 Data Acquisition System

The K4 VLBI data acquisition system (K4-DAS Type-1) [Kiuchi et al. 1997] was installed at Kashima 34-m antenna and the Kalyazin 64-m antenna. The K4 data acquisition system (K4-DAS) consists of a local oscillator (Nihon Tsushinki 7632A), a video converter (Nihon Tsushinki 7631A), a data input interface (Sony DFC-1100) and a data recorder (Sony DIR-1000L). By combination of the K4 local oscillator and the video converter, any 16 of 2-MHz channels in the intermediate frequency (100 - 500 MHz) can be selected by 10-kHz step. Every local oscillator is locked to a 5-MHz or 10-MHz reference signal supplied from a hydrogen maser local frequency standard. The K4 input interface DFC-1100 samples 16 channels of signals at a 4-MHz sampling rate by 1 bit quantisation. The sampling frequency is also locked with the reference signal from the hydrogen maser. The DFC-1100 outputs the sampled data stream with a time stamp to the DIR-1000L data recorder. Although this data acquisition system itself has the capability to record at a 64-Mbps rate, the sixteenth channel was terminated with a 50 ohms impedance load and not used. The reason for doing so is given as follows. Interference from mobile communication is getting severer day by day, especially in the 1.4 GHz band. It sometimes overloads the observation system. Consequently, it sometimes makes all the channels' sampled data bit fix to '1' for a while. Since the K4 VLBI system (type-1) uses a sync pattern 'FFFF' as a header of time stamp in the data, the overloaded '1' bit caused by interference confuses the sync pattern and disrupts tape synchronization in correlation processing. To avoid this trouble, we use the 16th channel termination described above. The K4 data acquisition system installed at the Kalyazin station is displayed in Figure 2.3.

2.2.3 Sensitivity of the Kashima-Kalyazin Interferometer

Correlation amplitude of observed signal by a interferometer is given as

$$\rho = \sqrt{\frac{T_{\mathrm{a},1}T_{\mathrm{a},2}}{(T_{\mathrm{sys},1}+T_{\mathrm{a},1})(T_{\mathrm{sys},2}+T_{\mathrm{a},2})}}$$

Figure 2.3: The K4 data acquisition system (Type-1) used for Japan-Russia pulsar VLBI observation. The K4 video converter, K4 local oscillator, and data input interface (DFC-1100) are seen on the left side of the desk. The K4 recorder (DIR-1000L) and the control computer are in the middle of the desk. The S2 type VLBI recording terminal (S2-RT) is seen on the right-most side of the picture.

$$= \frac{\pi}{8k_{\rm B}} D_1 D_2 S \sqrt{\frac{\eta_1 \eta_2}{(T_{\rm sys,1} + T_{\rm a,1})(T_{\rm sys,2} + T_{\rm a,2})}}, \tag{2.1}$$

where T_a and T_{sys} are antenna and system temperatures; D_i, and η_i (i=1,2) are the diameter of the antenna and antenna efficiency; S is flux density of the radio source. Then, by using the antenna parameters $T_{sys,1}$ of 45 K, $T_{sys,2}$ of 50 K, η_1 of 0.5, and η_2 of 0.55 (Table 2.1), correlation amplitude (proportional to the flux density S) is given as

$$\rho = 6.8 \times 10^{-3} (\frac{S}{1Jy}). \tag{2.2}$$

As discussed by Rogers [*Rogers,* 1970] and Moran [*Moran,* 1973], correlation of the radio source signal S and uncorrelated noise N averaged over bandwidth B and integration time T are expressed as

$$\begin{aligned} S &= \sqrt{T_{a,1} T_{a,2}} \qquad \text{and} \\ N &= \sqrt{\frac{(T_{a,1} + T_{sys,1})(T_{a,2} + T_{sys,2})}{2BT}}. \end{aligned} \tag{2.3}$$

The signal-to-noise ratio (SNR) is thus

$$\begin{aligned} SNR = \rho\sqrt{2BT} &= 6.8 \times 10^{-3} S \sqrt{2BT} \\ &= 6.8 \times 10^{-3} S \sqrt{2BTN_{\rm div}}, \end{aligned} \tag{2.4}$$

where $S_r = 2B$ is Niquist sampling rate of bandwidth B, and equation (2.2) is used. $N_{\rm div}$ denotes number of divisions of the pulse period, and it is used as gate width. The last equation of (2.4) is taking into account the SNR improvement factor for processing of pulsar data: (1)

effective flux density of pulsar increases in proportion to $N_{\rm div}$ and (2) integration time decreases by factor $1/N_{\rm div}$ (see Chapter 7), thus totally SNR increases in propotional to $\sqrt{N_{\rm div}}$. $N_{\rm div}$ is unity for non-pulsar data processing. As an example of an actual case, where integration time T is 300 sec. and S_r is 4×10^6,

$$SNR = 230\ (\frac{S}{1Jy})\sqrt{(\frac{T}{300sec})(\frac{S_r}{4 \times 10^6 Hz})}. \tag{2.5}$$

Since SNR of 7 is the detection limit of VLBI, the minimum fringe detection limit $S_{\rm min}$ is

$$S_{\rm min} = 30\ mJy\sqrt{(\frac{300sec}{T})(\frac{4 \times 10^6 Hz}{S_r})} \tag{2.6}$$

$$= 6.7\ mJy\sqrt{(\frac{300sec}{T})(\frac{4 \times 10^6 Hz}{S_r})(\frac{20}{N_{\rm div}})}. \tag{2.7}$$

Here, the gate width is assumed to be larger than the effective pulse width. Narrowing the gate width increases the effective flux density and reduces integration time. (More detail about pulsar-gating function is discussed in Section 7.6.3). When $N_{\rm div} = 20$ is supposed, the minimum detectable pulsar's flux density is 6.7 mJy. According to the catalog of Taylor et al. (1993), 40 pulsars satisfy the condition ($S > 7$ mJy and $\delta > -20$). These pulsars should be detectable with our Kashima-Kalyazin interferometer.

2.3 VLBI Observations

2.3.1 Observation Strategy

VLBI attains the highest angular resolution by separating the antenna pairs by a distance of up to the Earth's diameter distance or more. Two kinds of observables (delay and delay rate) are obtained by VLBI observation, and two sorts of observation strategies are applied for estimating source coordinates. One is differential VLBI, which measures the angular distances between the target source and nearby reference sources by using mostly phase delay as observable. And the other is absolute astrometry by using group delay. The advantages of phase-referenced differential VLBI are that its has an angular resolution one order higher than group-delay measurements and that most parts of the ionospheric and atmospheric propagation delay errors are cancelled by using reference sources. On the contrary, the disadvantage is the difficulty of phase connection between scans of reference sources and between scans of target source. Because phase delay changes by large number of rotation between a scan to the next scan during a few minutes of interval. For successful phase connection between scans without phase ambiguity, accurate delay model is inevitable but it is impossible to predict the complete behaviour of propagation medium (ionosphere and troposphere).

The error of phase is approximately $\rm SNR^{-1}$; thus, a high signal-to-noise ratio (SNR) is necessary to deal with phase as an observable. However, high SNR is often difficult for a weak target source such as pulsars. Additionally, the integration time for one scan is limited due to switching observation between reference source and target source. Also, the structure of the reference source and its change with time may cause a systematic change of obtained target source position. Furthermore, the reference source needs to be a distant sources or its proper motion has to be determined in advance; otherwise, the proper motion of the reference source will bias the proper motion of target source. Dispersive delay of the un-modeled ionosphere may still be a large error source below 3 GHz even in differential VLBI [*Fomalont et al.,* 1999; *Chatterjee and Codes,* 2000]. For these difficulty of phase delay measurements, the phase referenced pulsar observation is attractive but still risky.

Table 2.3: Observed pulsars

Dates	Observed Pulsar	Band	Comments
14 March 1995	$B1919+21$, $B1933+16$, $B0329+54$, $B1133+16$, $B1937+21$, $B2016+28$, $B0355+54$, $B2021+51$	L	Successful
10 April 1995	$B0031-07$, $B0450+55$, $B0809+74$, $B0823+26$, $B0834+06$, $B0950+08$, $B1237+25$, $B1642-03$, $B1804-08$, $B1831-04$, $B1822-09$, $B1845-01$, $B1929+10$, $B2020+28$, $B2111+46$, $B2154+40$, $B2310+42$, $B2319+60$	L	Part of data could not be processed because of strong interference
12 May 1996	$B0329+54$, $B0950+08$	L	Successful
23 May 1997	$B2111+46$, $B0329+54$	L	B2111+46 was not detected
25 May 1998	$B0329+54$, $B0950+08$, $B1237+25$	S	Successful

The second technique is absolute astrometry with group delay. Its advantage is that observation duration is not limited to such a short time as the phase-reference method. This is especially important when observing a weak source such as pulsars. Its second advantage is that the target source coordinates are obtained in the International Celestial Reference Frame (ICRF). The pulsar coordinates in the ICRF is important for the purpose of frame tie between the ICRF and a dynamical reference frame. In the absolute astrometry, source coordinates are estimated in reference to the Earth's orientation. The Earth orientation parameter (EOP) and correction of celestial pole offset (CPO) (see Section 7.3 or [*McCarthy,* 1996]) are provided by the International Earth Rotation Service (IERS) at sub milli-arc-second accuracy. Absolute astrometry by using group delay might have a lower angular resolution than the differential phase method, but it gives the steady coordinates of the target source in the ICRF and it can steadily produces a result. Thus, we took this rather conservative strategy. Since much time and resources have been spent on this international collaboration, steady outputs were required.

2.3.2 Observations Overview

An observation frequency of 1.4 GHz (L-band) was used from 1995 to March 1998, and 2.2 GHz (S-band) was used from May 1998 to May 1999. The minimum fringe spacings on the Kashima-Kalyazin baseline were 6 milli-arc-seconds (mas) for the L-band and 4 mas for the S-band. All observations were performed with right-hand-circular-polarization (RHCP).

Observed pulsars are listed in Table 2.3 and characteristic parameters of those pulsars are listed in Table 2.4. Projected baseline distances in the u and v directions are directly related with angular resolution. In spite of the disadvantage of single baseline interferometer, our east-west direction and 7000 km long baseline could measure both right ascension (α) and declination (δ) coordinates of high declination sources, precisely. An example of the uv track and the synthesized beam formed on pulsar B0329+54 in May 1996 observation are given in Figure 2.4.

March 1995 VLBI Experiment Pulsar B0329+54 was chosen as the first target of our observation, since it is the strongest pulsar at high declination. The first Japan-Russia pulsar VLBI observation was performed from 23:00 (UT) of March 15th to 23:00 of March 17th, 1995 with L-band right-hand-circular-polarization (RHCP). In spite of that it was the first VLBI experiment using the Kalyazin 64-m antenna, interferometer fringe was detected from the beginning. And this experiment was successfully finished owing to careful preparation from both sides. The duration of observation was 900 seconds for each pulsar and 300 seconds for each

Table 2.4: Parameters of observed pulsars (referred from the Taylor catalog [*Taylor et al.*, 1993]). Pulsar period and dispersion measure values are rounded to 0.1 for simplicity.

Bname	Jname	Flux (1.4 GHz) mJy	DM cm^{-3} pc	P msec	μ_α^a mas/yr	μ_δ^a mas/yr	Distance[b] kpc
B0031-07	J0034-0721	11	10.9	943.0	-	-	0.68
B0450+55	J0454+5543	13	14.6	340.7	52(6)	-17(2)	0.79
B0329+54	J0332+5434	203	26.8	714.5	17(1)	-13(1)	1.43 (1 - 2.8)
B0355+54	J0358+5413	23	57.1	156.4	5(4)	6(3)	2.07 (0.7 - 3.1)
B0809+74	J0814+7429	10	5.8	1292.2	15(7)	-49(6)	0.31
B0823+26	J0826+2637	10	19.5	530.7	61(3)	-90(2)	0.38 (0.3 - 0.45)
B0834+06	J0837+0610	4	12.9	1273.8	2(5)	51(3)	0.72
B0950+08	J0953+0755	84	3.0	253.1	15(8)	31(5)	0.12 (0.11 - 0.14)
B1133+16	J1136+1511	32	4.8	1187.9	-102(5)	357(3)	0.27
B1237+25	J1239+2453	10	9.3	1382.5	-106(4)	42(3)	0.56
B1642-03	J1645-0317	21	35.7	387.7	41(17)	-25(11)	2.9
B1804-08	J1807-0847	16	112.8	163.7	8(15)	4(20)	3.61 (0.8 -)
B1822-09	J1825-0935	11	19.5	769.0	10(19)	-23(-19)	1.01 (- 2.4)
B1831-04	J1834-0426	15	78.8	290.1	-	-	2.29
B1845-01	J1848-0123	10	159.1	659.4	-	-	3.8 (3.8 - 5.2)
B1919+21	J1921+2153	6	12.4	1337.3	11(14)	2(15)	0.66 (- 4)
B1929+10	J1932+1059	41	3.2	226.5	99(6)	39(4)	0.17 (- 2.1)
B1933+16	J1935+1616	42	158.5	358.7	2(3)	-25(5)	7.94 (3.5 -)
B1937+21	J1939+2134	16	71.0	1.6	-0.13(0.008)	-0.464(0.009)	3.6 (3.6 - 15.7)
B2016+28	J2018+2839	30	14.2	558.0	2(3)	1(2)	1.1 (1.1 -)
B2020+28	J2022+2854	38	24.6	343.4	-9(3)	-13(2)	1.3 (1 -)
B2021+51	J2022+5154	27	22.6	529.2	6(4)	17(4)	1.22
B2111+46	J2111+4644	19	141.5	1014.7	-	-	5 (3.5 - 7.2)
B2154+40	J2157+4017	17	70.6	1525.3	18(1)	-3(1)	5.53
B2310+42	J2313+4253	15	17.3	349.4	-41(3)	21(29)	0.96
B2319+60	J2319+6024	12	94.8	2256.5	-	-	3.22 (2 -)

a: Notation (μ_α, μ_δ) is proper motion and digits inside the bracket indicates error.
b: Digits inside bracket indicate possible range of distance derived from HI absorption observation.

reference sources. Details of the observation time for each sources and reference sources are described in the Section 6.2 of Chapter 6.

April 1995 VLBI Experiment The second pulsar VLBI observation was conducted from 22:30 (UT) of April 10 to 0:22 of April 12, 1995 with L-band RHCP. Because of radio interference from mobile communication, some parts of the data could not be correlated. This is because the time code of the data was affected by the interference. (see also Section 2.2.2 and Section 6.2.2). The Purpose of this observation was to survey the pulsar detectability with the Kashima-Kalyazin baseline. Four radio sources were detected (as described in Section 6.2.2).

May 1996 VLBI Experiment This experiment was conducted for astrometry observation of PSRs B0329+54 and B0950+09. PSR B0329+54 was observed over a long time from its rise up till to its sinking except for some intervals for Kalyazin antenna. Observation was performed from 17:00 (UT) of May 12 to 14:50 of May 13, 1996 with L-band RHCP. Observation duration for one scan was 5 min. for pulsars and 4 min. for each reference sources.

May 1997 VLBI Experiment This experiment was conducted for astrometry observation of PSRs B2111+46 and B0329+54; however, fringes of B2111+46 were not detected even after using the pulsar-gating function of the K4 correlator. Observation was performed from 12:00

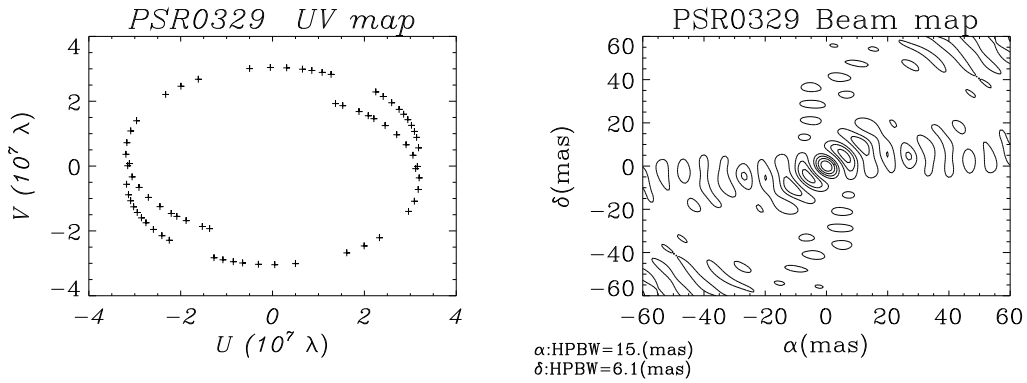

Figure 2.4: UV plot of Kashima-Kalyazin baseline on PSR B0329+54 in May 1996 VLBI observation is given in left panel; and synthesised beam contour map computed with uniform waiting is given in right panel. PSR B0329+54 and reference sources were observed for 17 hours in this observation. Even with a single baseline, UV coverage is good for high declination source, and full width of half maximum (FWHM) of the synthesised beam is almost equal to the minimum fringe spacing of the baseline.

(UT) of May 22 to 7:20 of May 23, 1997 with L-band RHCP.

May 1998 VLBI Experiment This experiment was almost a repetition of the May 1996 experiment, except that observation frequency was changed from L-band (1.4G Hz) to S-band (2.3 GHz), because the L-band receiver at the Kashima station suffered from strong interference due to microwave mobile communication. The accuracy of the position measurement was improved by changing from L-band to S-band, because of less ionospheric delay and higher angular resolution. However, the signal-to-noise ratio (SNR) and fringe detection probability decreased because the flux of the pulsar decreased rapidly at higher frequency with spectrum index from -2 to -3. Observation was performed from 16:35 (UT) of May 24 to 15:00 of May 25, 1998 with S-band RHCP; observation duration for one scan was 5 min. for the pulsar and 4 min. for each reference source.

2.4 Summary

The VLBI observation facilities at KALYAZIN 64-m-diameter antenna and Kashima 34-m-diameter antenna were introduced. Station coordinates, antenna parameters for scheduling of VLBI observation, and conditions to use the antennas were described. The sensitivity of this interferometer was evaluated as about 30 mJy and it is expected to be improved to 7 mJy by using pulsar-gating function of the K4 correlator. Totally 26 pulsars were observed in 6 times of VLBI observations.

Chapter 3

VLBI Data Processing and Analysis

3.1 Introduction

Correlation processing is the heart of Very Long Baseline Interferometry. Observed data is cross correlated by a special hardware named correlator and then the pairs of distant antennas forms an interferometer. Observed data on Kashima-Kalyazin baseline were sent to the Kashima Space Research center for data reduction. We processed the data with the KSP correlator at first without pulsar-gating function, and the early result obtained without the pulsar-gating for B0329+54 has been already published [*Sekido et al.,* 1999a; *Sekido et al.,* 1999b]. K4 correlator began to work as normal geodetic correlator since 2000 and the pulsar gating function worked effectively from the beginning of 2001. After the correlation processing, bandwidth synthesis software "KOMB" was used to synthesize all channels of data and to derive group delays and delay rates. The obtained observables (group delay and phase delay rate) were used for astrometry analysis described in Chapter 6. Principle of correlation processing, procedure to derive the observables, and correlation amplitude of pulsar data after pulsar-gating processing were given in this Chapter.

3.2 Correlation Processing

3.2.1 Correlation Process of Each Channel

A correlator is an instrument to measure the arrival time delay of radio signal observed at two stations by cross correlation. The principle of cross correlation is expressed by convolution integral of two signals. Normalised cross correlation function is given as

$$R(\tau) = \frac{\int x(t)y(t+\tau)dt}{\sqrt{\int x^2(t)dt \int y^2(t)dt}}, \tag{3.1}$$

where $x(t)$ and $y(t)$ are the observed signals at two stations X and Y. Since a radio signal emitted from a radio source at a time arrives at two stations at different time epochs, the observed signals are expressed as $x(t) = s(t) + n_x$ and $y(t) = s(t - \tau_g) + n_y$, where $s(t)$ is the signal departed from the radio source, n_x and n_y are the noise received at the two stations, and τ_g is the arrival time delay at station Y in relation to station X. Source coordinates on the celestial sphere can be determined by measurements of the delay τ_g.

Formula (3.1) is rewritten by using Wiener-Khintchine's relation as

$$R(\tau) = \int X(\omega)Y^*(\omega)e^{-j\omega\tau}d\omega/|X||Y|, \tag{3.2}$$

where $X = S + N_x$ and $Y = Se^{+j\omega\tau_g} + N_y$ are the Fourier counterparts of *x(t)* and *y(t)*. When we observe the source of a flat spectrum with bandwidth B (radian/sec), the term of signal from the star in formula (3.2) is rewritten as

$$\begin{aligned} R(\tau) &= \frac{1}{|X||Y|}\int_0^B S^2 e^{j\omega(\tau_g-\tau)}d\omega \\ &= \frac{S^2B}{|X||Y|}e^{j\omega\frac{B}{2}}\mathrm{sinc}[\frac{B}{2}(\tau_g-\tau)], \end{aligned} \tag{3.3}$$

where the sinc function is $\mathrm{sinc}(t) = \sin(t)/t$. The half width of the first null of cross correlation function (3.3) is $4\pi/B$. The delay resolution function becomes narrower as the bandwidth increases and approaches the shape of delta function. Effective expansion of the bandwidth is performed by synthesis of multiple channel data separated in frequency domain. This bandwidth synthesis technique is described in the next Section.

The phase of product of *x(t)* and *y(t+τ)* is given from formula (A7) or (A8) as

$$ARG = \Delta\phi + \omega'(\tau - \tau_g) - \omega_y(\tau_g^0 + \tau_g^{(1)}t + \frac{1}{2}\tau_g^{(2)}t^2) + \omega_{\mathrm{LO}}\Delta r t, \tag{3.4}$$

where $\omega' = (\omega - \omega_y)$ is video frequency, $\Delta\phi = \phi_y - \phi_x$ is the initial phase difference of local oscillators, $\Delta r = r_x - r_y$ is the clock-rate difference of atomic standards, and τ_g is expressed by a Taylor series up to the second order.

A correlator is a digital processor specially designed to integrate the products of two signals (equation (3.4)) of VLBI observation data. The radio signal arrival time difference at two stations are modeled by correlator delay model. The correlator model includes the geometrical delay, ionosphere and troposphere propagation delay, and clock difference between two stations. The correlator compensate for the actual delay τ_g with hardware delay controlled in accordance with the correlator delay model (delay tracking). Although, the delay tracking compensates for the actual delay with keeping $\tau_g - \tau$ within 0.5 bit, it is not enough to keep coherence of the fringe. Because the phase of the correlation coefficient changes with time (fringe rotation) as seen in equation 3.4. And the correlated signal fade out rapidly as the correlation coefficient is integrated with time. This fringe rotation is originated from frequency down conversion of the received signal at observation as explained in Appendix A. To prevent the degradation of correlated signal, up to the second order of fringe rotation is compensated by hardware phase rotation during correlation integration (see equation (7.15) and appendix A).

Initial phase differences among local oscillators of each channel and intermediate frequency (IF) signal transmission cable delay in the each antenna are also added in the fringe phase in actual conditions. These additional phase differences among the channels are mostly compensated by using a phase-calibration signal (P-cal). However, absolute phase cannot be calibrated by the P-cal. Thus, the argument of $\Delta\phi$ will include such offset phase, too.

Concerning the hardware fringe rotation compensation, there are two ways: baseband fringe rotation (BBFR) and band center fringe rotation (BCFR). BCFR has the advantage of a smaller loss of coherence but rather complicated $\pi/4$ phase jump (see Appendix A) is required. Both BBFR and BCFR were available by using the KSP and the K4 correlators, and we used BCFR to minimize the coherence loss.

The observed VLBI data at Kashima and Kalyazin stations were recorded in magnetic tapes and sent to the Kashima Space Research Center for correlation processing. The recorded data

were played back and processed by KSP correlator at first without pulsar-gating function. Since the beginning of 2001, all the observed data were re-processed by using the K4 correlator with pulsar-gating function. Then precise group delay was derived by bandwidth synthesis described in the next Section.

3.2.2 Bandwidth Synthesis for Determining Precise Group Delay

Expanding the recording bandwidth is an approach to increase the sensitivity and delay measurement accuracy [*Nakajima et al.,* 2001]. However, recording bandwidth is limited by recording instruments. To over come this limitation, A. Rogers (1970) developed bandwidth synthesis (BWS) technique, which expands effective bandwidth by allocating multiple narrow band channels in a widely distributed frequency range. The BWS technique is similar to the idea of radio interferometer itself, which increases special resolution by synthesizing the beam from multiple antennas.

As a result of integration of data with hardware delay tracking and fringe rotation, complex correlation coefficients are output at every parameter period (PP) and for each frequency channel. A synthesised correlation function is obtained by integrating correlator outputs expressed by equations (A13) (BBFR) or equations (A18)(BCFR). In the case of the baseband rotation, the synthesized signal is represented by

$$\begin{aligned} D(\Delta\tau) &= \sum_{i=1}^{n} \int_0^B g_{x,i} g_{y,i} s_{0,i}^2 \exp j\{\Delta\phi_i + \omega'\Delta\tau + \omega_{\mathrm{LO,i}}\Delta\tau + \omega_{\mathrm{LO,i}} r_y \tau_g\} + n_x n_y] d\omega' \\ &= B e^{j\frac{B}{2}\Delta\tau} \mathrm{sinc}(\frac{B}{2}\Delta\tau) \sum_{i=1}^{n} g_{x,i} g_{y,i} s_{0,i}^2 \exp j\{\Delta\phi_i + \omega_{\mathrm{LO,i}}(\Delta\tau + r_y\tau_g)\} + N_{xy}, , (3.5) \end{aligned}$$

where $\Delta\tau = \tau_c + \delta\tau - \tau_g$, N_{xy} is a noise component, B is bandwidth of each channel, and i is a suffix for channel number. Frequency channel dependency of antenna gain $g_{x,i}, g_{y,i}$ and source flux $s_{0,i}^2$ were taken into account in the equation. Synthesized correlation function in the case of the BCFR can be derived in the same manner from equation (A18). The bandwidth synthesis (which also called as fringe fitting) determines $\Delta\tau$ which maximizes equation 3.5, and that $\Delta\tau$ is also a unbiased maximum-likelihood estimator of the group delay residual [Rogers, 1970; *Whitney,* 1974; *Kondo and Kunimori,* 1984]. It can be shown that the delay search by BWS is equivalent to LSQ estimation of τ_g by using the fringe phase as an observable (Appendix B). The BWS software KOMB developed by Kondo [*Kondo and Kunimori*, 1984] was used for determining group delay.

3.3 Correlation Amplitude and SNR Improved by the Gating Function

The correlation process has done by the K4 correlator for all observation data. And pulsar-gating function was applied for pulsar data. The pulsar-gating function improved the effective pulsar's flux density and signal to noise ratio (SNR). This Section shows the results of improved correlation amplitude and the time variation of the the pulsar signal in each VLBI experiment. Correlation amplitudes, which is in proportion to the flux density of the source, of some pulsars showed large time variation in contrast to those of reference sources. This flux time variation is an evidence of interstellar scintillation (ISS).

3.3.1 March 1995 VLBI Experiment

The VLBI experiment in March 1995 was the first one between Kalyazin and Kashima. Eight pulsars were observed as listed in Table 2.3, and four pulsars (B0329+54, B0355+54, B1933+16, and B2021+51) were detected. Detection of the letter three pulsars was owing to SNR improvement by pulsar gating function of the K4 correlator.

Figure 3.1 shows time variation of correlation amplitude (SNR) of pulsars and reference sources, 0300+470 and 2022+542, which were observed alternatively with the pulsars.

PSR B0329+54 showed a quite strong amplitude variation up to several hundreds times increase or decrease in about one hour. Also larger amplitude variation both over 16 channels of frequency band was observed. (Figure 3.1(a)). It was obviously property of pulsar signal, since the correlation amplitude (SNR) of reference sources 0300+470 was quite stable (Figure 3.1(b)). Variation differences among channels corresponds to narrow scintillation (de-correlation) bandwidth caused by interstellar scattering. The shorter scintillation time scale and narrower scintillation bandwidth implies larger spatial electron density irregularity of ISM in the line of sight. Both PSR B0355+54 and PSR B1933+16 (Figure 3.1(c) and (d))showed amplitude variation in the range of several times magnitude increase or decrease during 30 minute. However they could not be compared directly since correlation amplitudes of B0355+54 were sometimes below the detection limit (SNR 7).

PSR B2021+51 (Figure 3.1(e)) showed amplitude increase with time scale of more than 2.5 hours. This was not due to a variation of the observation system because the correlation amplitude of reference source 2022+542 is almost constant during the same time span (Figure 3.1 (f)). This slow intensity variation should be also a phenomenon of the ISS. The longer scintillation time scale and wider scintillation bandwidth imply smaller electron density irregularity in line of the sight. (See the thin screen model of ISS in Chapter 5 for more detailed explanation).

3.3.2 May 1996 VLBI Experiment

Two pulsars, B0329+54 and B0950+08, were observed in this experiment and fringes were detected for both pulsars. Fringes of B0950+08 were not detected without the pulsar gating function.

PSR B0329+54 showed large amplitude variation in time and frequency, as in the results of the March 1995 experiment (Figure 3.2 (a)). The correlation amplitude of 0300+470 varied during the observation; however, the reason for this is still un-resolved yet (Figure 3.2 (b)). It might be due to gradual change of system temperature during the observation. In any way, it was obvious that the time scale of amplitude variation and variation in frequency channel was completely different between PSR B0329+54 and 0300+470. Thus the amplitude variation of the pulsar should be a phenomenon of ISS.

The amplitude variation of PSR B0950+08 (Figure 3.2 (c)) could not be directly connected with ISS phenomena, because of few data points and low SNR. Correlation amplitude of reference source 4C39.25 is plotted in Figure 3.2 (c) to indicate system variation during that observation period.

3.3.3 May 1997 VLBI Experiment

The Main target of this experiment was PSR B2111+46 and PSR B0329+54, although B2111+46 was not detected even after the correlation with pulsar gating. PSR B0329+54 showed correlation amplitude variation, which would be caused from the ISS (Figure 3.3).

3.3.4 May 1998 VLBI Experiment

The observation frequency was changed from L-band to S-band for this experiment, because the L-band receiver of the Kashima 34-m antenna was suffered from strong artificial interference

from mobile communication. Variation of pulsar's correlation amplitude Figure 3.4 (a) was in contrast with stable amplitude of 0300+540 Figure 3.4 (b). The correlation amplitude of PSR B0329+54 shows a similar time variation due to scintillation as the other experiment results. The SNR of the correlation amplitude was smaller than the other experiments because of negative spectrum index characteristic of the pulsar.

3.4 VLBI Data Analysis

3.4.1 Ionospheric Delay Correction

Propagation delay of microwave measurements consists of the following several components. The dry and wet components of a neutral atmosphere have no frequency dependency in the radio region. Ionospheric delay has a dispersion characteristic and is proportional to f^{-2}, where f is radio observation frequency. Figure 3.5 shows several components of propagation delay in the zenith direction. A pulsar is usually observed below 5 GHz because of its steep spectrum characteristic. The frequency range from 400 MHz to 2.3 GHz is sometimes used for pulsar astrometry VLBI observations. The most significant error source in these propagation effects at this frequency region is the ionospheric delay component. The single dot-dashed line in the Figure 3.5 indicates three ionospheric conditions. The ionospheric delay is proportional to the total number of free electrons in the observation line of sight. The total number of free electrons in the line of sight per square meter is called total electron content (TEC) and its unit is $10^{16} electrons/m^2$(=1 TEC unit:TECU). The upper (blue) line in the figure represents 150 TECU. This is almost equal to the maximum of the Earth's ionospheric TEC. The middle (yellow) and lower (pink) lines correspond to 100 and 50 TECU, which is in the vertical TEC variation range in the middle latitude region in maximum solar activity phase.

Since our pulsar VLBI observations were performed in the 1.4-2.3 GHz frequency range, the ionospheric delay must be corrected to reduce systematic error. Ordinary geodetic VLBI observation uses 2.2 and 8.3 GHz simultaneously to measure and compensate for the ionospheric delay. However, pulsar observation cannot use this method, because a pulsar's flux decreases very rapidly at higher frequency. We thus investigated to use GPS-based ionosphere measurements for ionospheric delay correction in pulsar VLBI observation. A similar approach is now being investigated by Chatterjee and Cordes (2000). We have tested local ionosphere TEC estimation by using our own GPS receivers, however, it was not completely successful because of coarse delay resolution of the GPS receivers and lack of GPS observation points. And we found that the global ionosphere map generated by the Bern University was quite useful and it had high correlation with real ionospheric delay measured by VLBI. The detail of accuracy evaluation of the GPS-based global ionosphere map is described in Chapter 4. The results of GPS-based TEC application to pulsar astrometric observation are described in Chapter 6.

3.4.2 Least-square Estimation with the CALC/SOLVE

Group delays and phase delay rates of each scan were determined by the bandwidth synthesis technique (Section 3.2.2), and together with observation related parameters such as weather data, planetary ephemeris, Earth orientation parameters, and frequency table, were stored in the Mark-III database system. After that ionospheric delay parameters calculated from the GIM/CODE (see chapter 4) were included in the database. And precise delay model and partial derivatives of the observables were computed by using the CALC, which is a precise VLBI delay model calculation software developed by the Goddard Space Flight Center (GSFC) of the NASA.

Absolute astrometric analysis with group delays and delay rates was performed by the SOLVE, which is a least square square estimation software for geodesy and astrometry developed by the GSFC/NASA. Interferometric parameters such as clock offset, clock rate difference,

and atmospheric parameters were estimated by using reference sources, which were observed alternatively with the target pulsars.

Earth orientation parameters are very important for absolute astrometry, because the International Terrestrial Reference Frame (ITRF) on the Earth and the International Celestial Reference Frame (ICRF) fixed to quasars are linked by theory of IAU 1976 Precession, IAU 1980 Nutation, and the Earth orientation parameters (EOP): (XWOB, YWOB, UT1-UTC) and Celestial Pole Offsets (CPO): ($\delta\Delta\psi, \delta\Delta\epsilon$). The CPO was introduced to compensate for the difference between celestial pole position defined by the model (IERS conventions *McCarthy,* 1996) and that observed by VLBI. The IAU 1980 nutation model thus needs to be corrected by adding the CPO parameters. Details of the ICRF can be found in http://hpiers.obspm.fr/icrs-pc/ and the link between ICRF and ITRF is described in IERS Conventions [*McCarthy*, 1996]. The EOP and CPO parameters are reported in the IERS bulletins every month. The author used Bulletin B to get the standard solutions of EOP and CPO for our analysis.

3.5 Summary

Correlation processing and bandwidth synthesis technique used to determine the group delays were described. The ionospheric delay as the most significant error source of our observation was introduced. Correlation amplitude of pulsars improved by pulsar gating function and their time variation were demonstrated. The CALC and the SOLVE analysis package developed by the GSFC/NASA were used to derive pulsar coordinates in the ICRF. The Earth orientation parameters and celestial pole offsets, which are important for our absolute astrometry, were used from the Bulletin B of the IERS report.

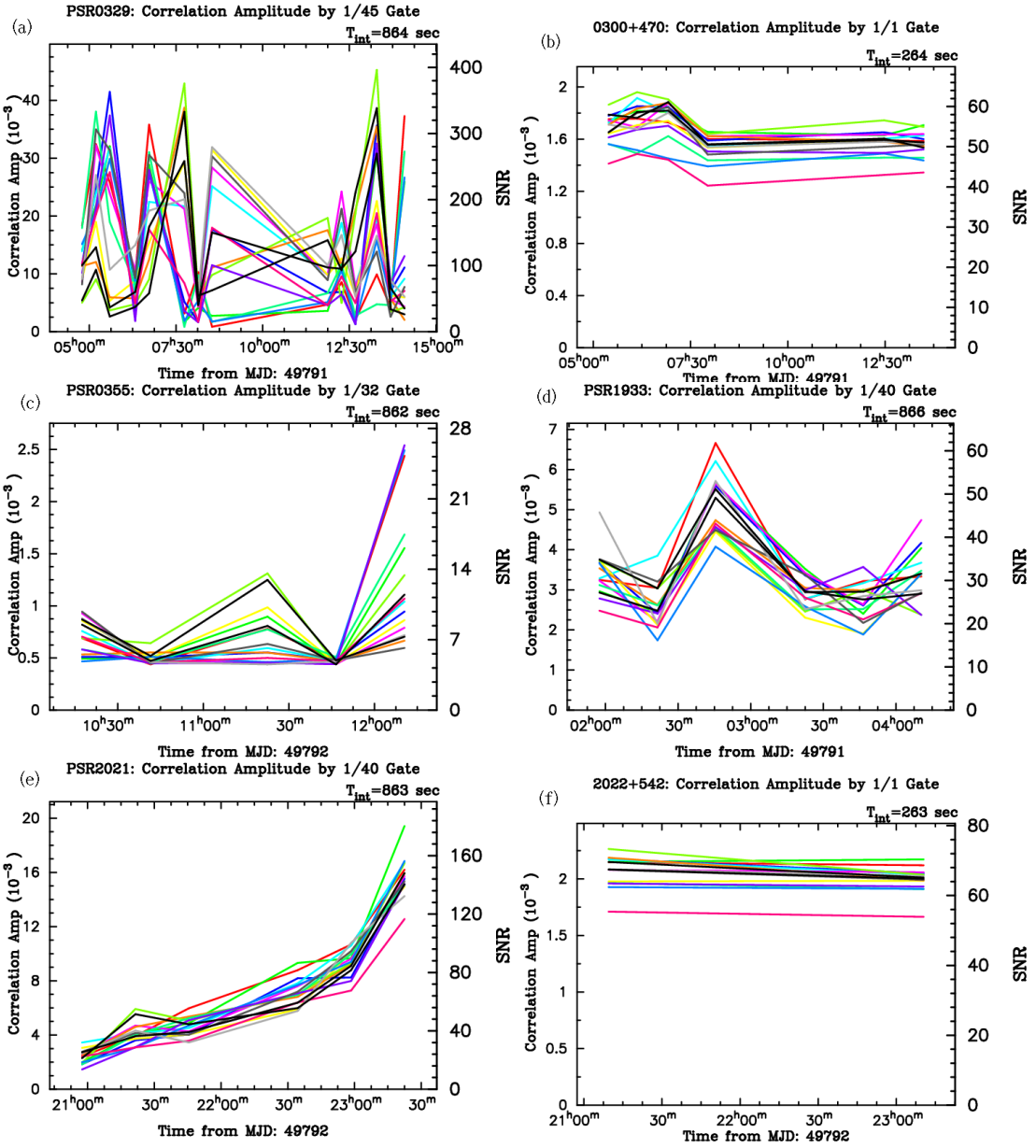

Figure 3.1: Time variation of correlation amplitudes and SNRs of pulsars and reference sources in March 1995 VLBI experiment. Pulsar-gating was applied in correlation processing of pulsars' data ((a) PSR B0329+54:gate width=15.9 ms; (b) 0300+470; (c) PSR B0355+54: gate width=4.9 ms; (d) PSR B1933+16: gate width=9.0 ms; (e) PSR B2021+51: gate width=13.2ms; (f): 2022+542). Each coloured solid line corresponds to a each frequency channel with a 2-MHz bandwidth.

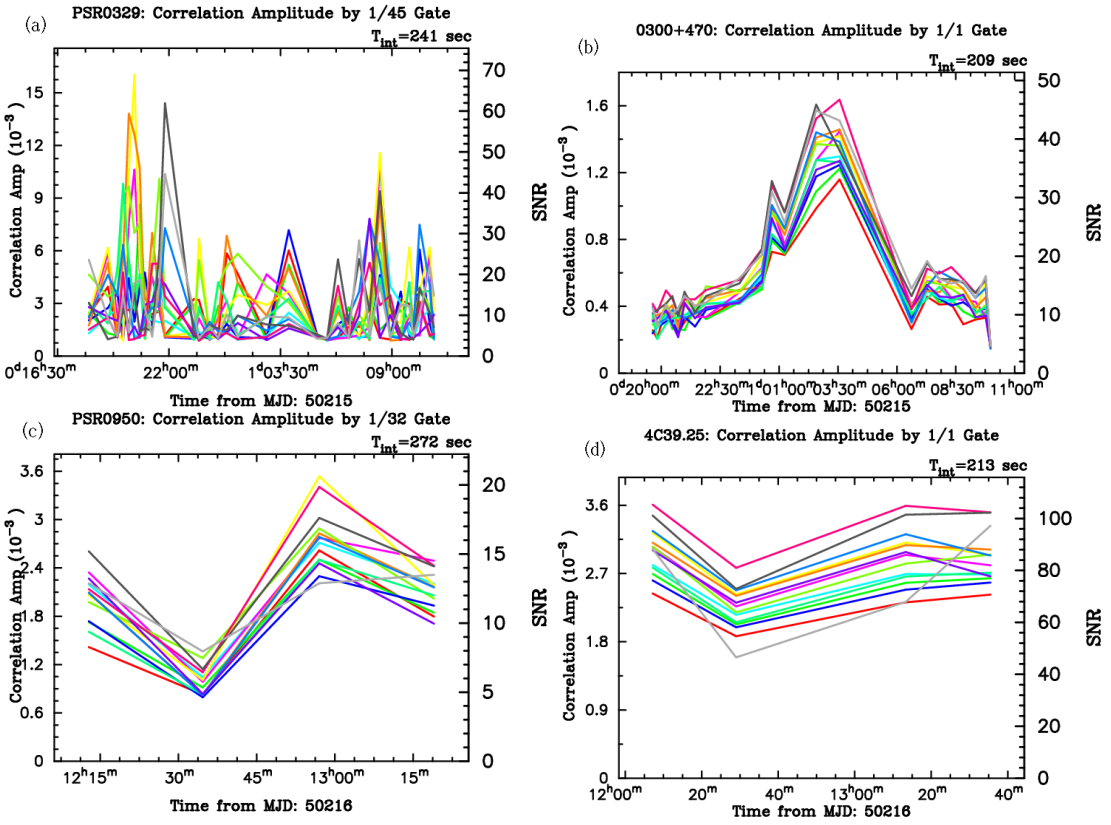

Figure 3.2: Correlation amplitudes and SNRs of pulsars in May 1996 experiment Pulsar-gating was applied in correlation processing of pulsars' data ((a) PSR B0329+54: gate width=15.9 ms; (b)0300+470; (c) PSR B0950+08: gate width=7.9ms; (d) 4C39.25). Each colored solid line corresponds to a frequency channel of 2-MHz bandwidth.

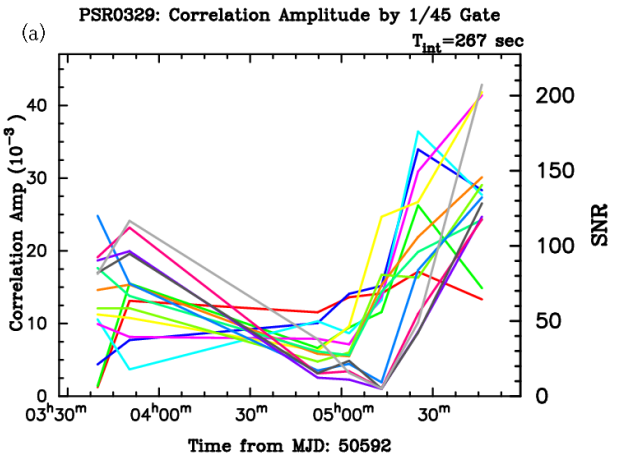

Figure 3.3: Correlation amplitude and SNR of PSR B0329+54 in May 1997 experiment. PSR B0329+54's data was processed with pulsar-gating with gate width 15.9 ms. Each colored solid line corresponds to a frequency channel of 2-MHz bandwidth.

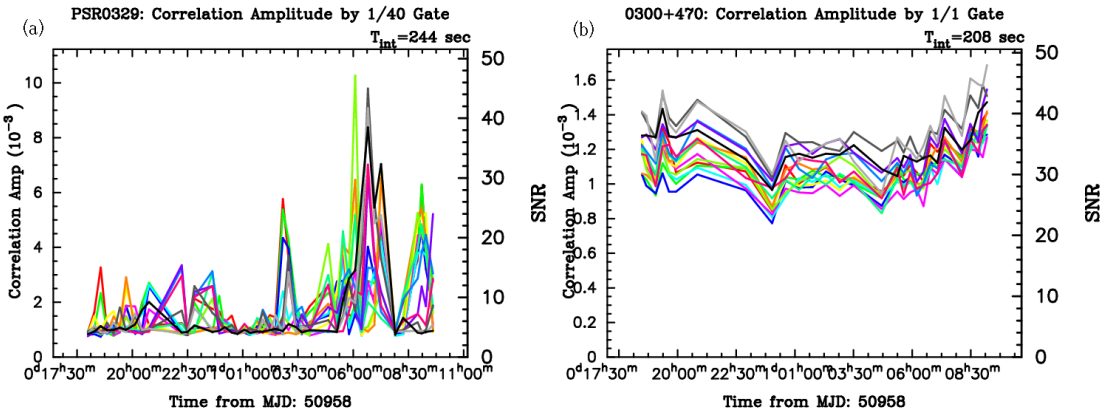

Figure 3.4: Correlation amplitude and SNR of pulsars in May 1998 experiment. PSR B0329+54's data was processed with pulsar-gating with gate width 15.9 ms. Each colored of solid line corresponds to a frequency channel of 2-MHz bandwidth.

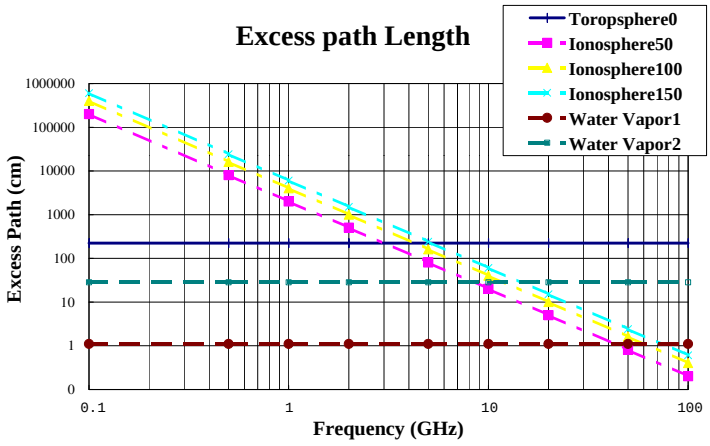

Figure 3.5: Atmosphere propagation excess path length of radio signal. The solid flat line indicates the dry component of standard atmosphere. The dashed lines indicates the components of water vapor. The upper (green) dashed line represents the case of 80% relative humidity at 30°C, and the lower (brown) dashed line represents the case of 50% relative humidity at -15°C. The three solid dotted lines represent ionospheric zenith delays. The upper (blue), middle (yellow), and lower (pink) solid dotted lines correspond to ionospheric total electron contents of 150, 100 and 50 TECU.

Chapter 4

Evaluation of GPS-based TEC Measurement Accuracy

4.1 Introduction

The ionospheric plasma of the Earth is a cause of disturbance in space measurement technology, such as GPS, VLBI, and spacecraft navigation, using microwave signal. Geodetic VLBI, which measures over a baseline length of several thousands of kilometers at an accuracy of a few centimetres or less, uses total electron content (TEC) measurement with simultaneous 2/8GHz (S/X band) observation for ionospheric delay correction [*Clark et al.,* 1985]. Although this technique is not applicable to all kinds of VLBI observations because, for example, a pulsar has steep spectrum of negative spectrum index from -2 to -3, observation in X-band is thus difficult. In astrometric VLBI observation of a pulsar, lower frequency observation is preferable from viewpoint of a higher signal to noise ratio, since a pulsar's flux density decreases rapidly as frequency increases. From viewpoint of delay, the ionospheric delay uncertainty is one of the most significant error sources in low frequency observation. The Earth's ionosphere uncertainty is also an error source for high-precision spacecraft navigation using range and range rate. High-accuracy ionosphere TEC data will thus contribute to improvement of space navigation accurate.

Global positioning system (GPS) technology has been developed drastically over the last decade, and GPS observation stations have been distributed all over the world. Now they can be a tool not only for geodesy but also for monitoring the Earth's environment such as the troposphere and ionosphere [*Beutler,* 1998; *Feltens and Schaer,* 1998]. When a microwave propagates in the ionosphere, ionospheric dispersive excess delay is proportional to the total number of free electrons in the ray path (TEC) and is inversely proportional to the square of radio frequency. The GPS satellites broadcasting the P-code on L1 (=1.57542 GHz) and L2 (=1.22760 GHz) signals. And TEC in line of sight can be obtained by measurements of arrival time difference between the GPS-emitted signals L1 and L2, as geodetic VLBI uses S and X band for measurement of TEC in the line of sight. Dual-frequency GPS receivers can be thus good sensors for ionosphere monitoring [*Lanyi and Roth,* 1988; *Wilson et al.,* 1995; *Ho et al.,* 1997; *Schaer*, 1999]. And the TEC measured by using GPS signal can be applicable to ionospheric delay correction in a microwave measurement system, such as a single frequency GPS receiver, VLBI astrometry, and space navigation.

GPS-based TEC measurements were used for ionospheric delay correction in VLBI with an accuracy of 9 - 14 TECU (1 TECU = $10^{16} electrons/m^2$) [*Kondo and Imae,*1993]. Ros et al. (2000) and Pérez-Torres et al. (2000) achieved sub-millisecond accuracy in astrometry with 8.4 GHz by using GPS-derived TEC correction in 3.5 - 6 TECU accuracy. However, the 3.5 - 6 TECU correspond to 2.4 - 6 ns delay error at 1.4 GHz. Thus, more accurate TEC data is required in pulsar VLBI observation in L-band.

In this chapter, we evaluated the accuracy of two types of ionosphere total electron content maps by comparison with TEC value measured by S/X dual-band VLBI observation. One is a regional ionosphere map estimated from TECMETER, which is special GPS receiver for TEC measurement. The other is the Global Ionosphere Map (GIM) generated by CODE (Center for Orbit Determination in Europe) at Bern University, which is one of the IGS (International GPS Service) Analysis Centers.

4.2 Basis of GPS-based Ionospheric TEC Evaluation

When an electromagnetic wave propagates in a plasma, the refractive index of the plasma is expressed by Appleton-Hartree's formula [e.g., *Maeda and Kimura,* 1984].

$$n^2 = 1 - \frac{2X}{2(1-jZ) - \frac{Y^2\sin^2\theta}{1-X-jZ} \pm \sqrt{\frac{Y^4\sin^4\theta}{(1-X-jZ)^2} + 4Y^2\cos\theta}}, \tag{4.1}$$

where θ is the angle between magnetic field $\mathbf{B}$ and the direction of radio wave propagation, $X = \omega_p^2/\omega^2$, $Y = \Omega_e/\omega$, $Z = \nu/\omega$, and $\omega_p = \sqrt{\frac{N_e e^2}{\varepsilon_0 m}}$ is plasma frequency, $\Omega_e = eB/m$ is cyclotron frequency, $\omega = 2\pi f$ is angular frequency of radio signal, and N_e is electron density.

If the radio frequency of the electromagnetic wave is much higher than both geomagnetic cyclotron frequency and plasma frequency of the Earth's ionosphere, the refractive index of the plasma is approximated as

$$n = 1 - \frac{N_e e^2}{2\varepsilon_0 m\omega^2}, \tag{4.2}$$

and excess delay due to propagation in the dispersive medium is approximately expressed as

$$\tau_{ion} = \frac{e^2}{8\pi^2 m\varepsilon_0 c}\frac{TEC}{f^2}. \tag{4.3}$$

Here e is elementary charge, ε_0 is the dielectric constant of vacuum, c is the speed of light, f is observation frequency, and TEC is total electron content in the propagation path.

VLBI and GPS techniques use two distant frequencies for TEC measurement along the line of sight. Let f_1 and f_2 be the two observation frequencies ($f_1 < f_2$) and let $\Delta\tau_{ion}$ be excess delay difference between the two frequencies, TEC is thus derived as follows:

$$TEC = \frac{f_1^2 f_2^2}{(f_2^2 - f_1^2)}\frac{\Delta\tau}{A} = \left(\frac{f_c}{2\Delta f} - \frac{\Delta f}{8f_c}\right)\frac{\Delta\tau_{ion}}{A}, \tag{4.4}$$

where $A = \frac{e^2}{8\pi^2 m\varepsilon_0 c}$, $f_c = (f_1 + f_2)/2$, and $\Delta f = (f_2 - f_1)$. This equation shows that as the observation frequency (f_c) decreases and frequency distance (Δf) increases, the TEC error decreases. The value in the right bracket of formula (4.4) is about 0.3 in VLBI using S/X dual-band and is about 2 in GPS using L1/L2. When the errors of observables (group delays of VLBI and phase delays of GPS) are supposed to be almost in the same level in both VLBI and GPS measurements, accuracy of VLBI-based TEC measurement is superior than that of GPS, because the value in the bracket of right term in the equation (4.4) is 0.28 in S/X dual band VLBI and . Actually, the mean VLBI-measured TEC error is less than 1 TECU, i.e., typically 0.6 TECU for a thousands kilometers baseline. Therefore VLBI-measured TEC is close to true ionospheric TEC than that of GPS, the accuracy of GPS-based TEC models can be evaluated by comparison with VLBI-based TEC measurements.

The observed TEC value is different between GPS and VLBI: the GPS measurement gives the TEC along the ray path from an observation station, whereas VLBI measurement gives the difference of TEC between two stations. Then TEC measured by VLBI and that measured by

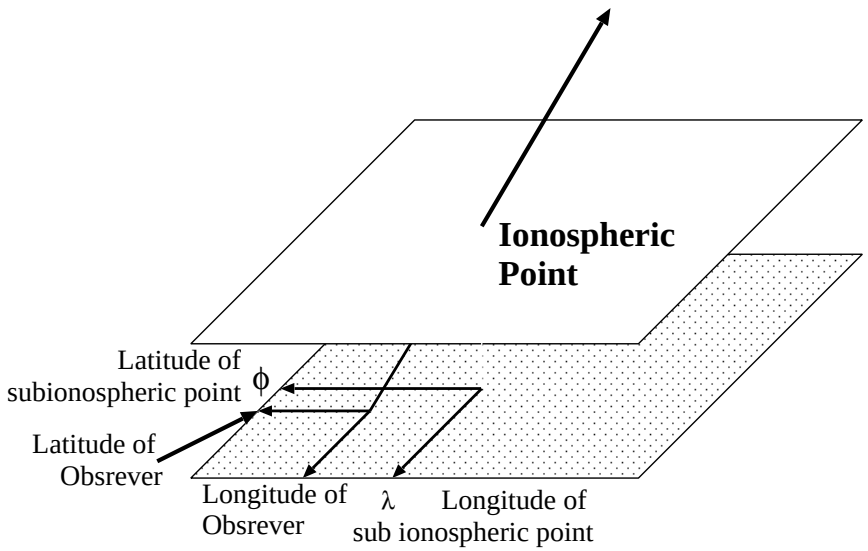

Figure 4.1: Schematic view of ionospheric point (ISP)

GPS were compared by the following steps. (i) The TEC map above the station was estimated from GPS observation data (Section 4.3.1). (ii) The coordinates of ionospheric point (ISP), where the line of sight to the radio source from the VLBI observation station is across the ionospheric layer (see Figure 4.1), is calculated at each VLBI observation epoch. Then vertical TEC values are computed from TEC maps mentioned in Section 4.3.1 or Section 4.3.2. (iii) Vertical TEC is converted to slant TEC by using mapping function and difference between the slant TECs from the two stations: $VTEC_y Fm(El^y, H) - VTEC_x Fm(El^x, H)$, is computed. (iv) Finally, VLBI-measured TEC and the computed TEC taken from GPS-based TEC maps are compared. Step (i) can be skipped in case of the GIM/CODE data, since we used the global ionosphere map provided from Bern University.

4.3 GPS-based Ionosphere Map

4.3.1 Local Ionosphere Map Estimated from TECMETER

TECMETER Observations

TECMETER is a kind of special GPS receiver [*Imae et al.*, 1991], that measures TEC in the line of sight to a GPS satellite by measuring the arrival time difference between P-code of the L1 and L2 signals. The bit rate of the P-code is 10.23 MHz (clock width is about 98 ns), and its time resolution is lower than that of a geodetic GPS receiver, which uses carrier phase as observable. However, TECMETER is very convenient to get rough TEC value without additional data processing. Two sets of TECMETERs were placed at the Kashima and Koganei Key Stone Project (KSP [*Yoshino,* 1999]) VLBI stations. The baseline between these two stations is about 100 km in the east-west direction. TECMETER observation was performed at the same time with dual-band geodetic VLBI observation of the Kashima-Koganei baseline from 7th to 17th April 2000. The data acquisition interval was three minutes, and the elevation cut-off angle of the TECMETER observation was 30 degrees in order to reduce the multi-path effect, whereas VLBI observation elevation cut-off angle was seven degrees.

Calibration of Instrumental Differential Code Biases of Satellites and Receivers

The observed delay difference between P-code of the L1 and L2 GPS signals contains not only the ionospheric dispersive delay of equation (4.4) but also instrumental hardware biases. Differential code biases of each GPS satellite (DCBS) and each GPS receiver (DCBR) are the main error source in estimating absolute TEC by using dual-frequency code observation [*Coco et al.,* 1991, *Sardón et al.,* 1994]. DCBSs differ from satellite to satellite and they are in the order of several nanoseconds [e.g., *Coco et al.,* 1991; *Sardón* , 1994]. Taking into account the DCBSs and DCBRs, the TECMETER output data is expressed as follows:

$$\tau^l_{i,k} = A(\frac{1}{f_1^2} - \frac{1}{f_2^2})VTEC_i \times Fm(El) + \tau^l_{\mathrm{DCBS}} + \tau_{k,\mathrm{DCBR}} \tag{4.5}$$

$$Fm(El, H) = \frac{1}{\cos\{\sin^{-1}[\frac{R}{R+H}\cos(El)]\}} \tag{4.6}$$

where $\tau^l_{i,k}$ is observed delay difference between L1 and L2 in the i_{th} observation along the line of sight from station k to the GPS satellite l. $Fm(El, H)$ is the mapping function of the single-layer spherical ionosphere model, where El is the elevation angle of the observation, R is the Earth's radius, and H is the height of the Ionosphere from the Earth's surface, τ^l_{DCBS} is the DCBS of satellite l, and $\tau_{k,\mathrm{DCBR}}$ is the DCBR of receiver k.

It was not impossible to estimate the DCBS of each GPS satellite from our observation data, but the estimated value was not so stable because of the limited number of observation stations. We thus used the DCBS values provided by the Deutsches Zentrum für Luft- unt Raumfahrt (DLR) [*Sardón et al.,* 1994]. The DLR is one of the institutes analysing GPS data for geodesy and for producing a regional ionospheric map above Europe. The DCBS is obtained as a by-product of the procedure generating the regional TEC map. When the DCBS data provided by the DLR is used for calibration of differential code bias, it is necessary to be aware that the DCBS data are not absolute values but relative values in reference to the mean of them. The reason of the relative DCBS data are provided is that DCBS and DCBR are easily coupled and it is difficult to estimate them separately.

After the DCBSs were subtracted from the TECMETER observation data, $\tau_{k,\mathrm{DCBR}}$ was estimated by least-square analysis using TECMETER data over two weeks. The data recorder during nighttime was used for the estimation, because ionosphere TEC is more stable at nighttime than in daytime. Consequently, the DCBRs were derived as -10.8 $\pm$ 0.6 ns for Kashima and -7.9 $\pm$ 0.8 ns for Koganei.

Estimation of Ionosphere Map

The Earth's ionosphere consists of D, E, and F layers of plasma. The maximum electron density occurs in the F layer at a height between 200 and 500 km. The electron density decreases rapidly with distance from the F-layer. Thus, most of the electrons in the ionosphere's plasma are assumed to be concentrated in a thin layer at the first approximation. We used a single-layer spherical shell model based on this approximation for the ionosphere structure. Daily change of ionospheric height was ignored and a constant ionospheric height (300 km) was used for simplicity.

The vertical TEC value ($VTEC_i$) at an ionospheric point (ISP) is obtained from equation (4.5) after calibration of the DCBSs and DCBRs. When the ISP coordinates are expressed as (λ, φ), it is useful to use local time λ in the longitude direction, because ionosphere TEC maximum longitude is almost fixed with reference to the Sun and TEC distribution can be approximated by slowly changing TEC model in the sun-fixed coordinate system. The local time λ is $UT + \lambda^g$, where λ^g stands for geographical longitude at the ISP. Hence λ has two

meanings: axis of space coordinates in the longitude direction and the axis of time at the observation point. And φ indicates the coordinate of geographical latitude.

Lanyi and Roth introduced a thin-shell ionosphere model expressed with two dimensional polynomials [*Lanyi and Roth,* 1988]. Wilson et al. proposed a model with spherical harmonics expansion (1995) instead of polynomials to express global TEC distribution. In our case, the GPS data received at only two stations covers a very narrow belt shaped region of about 10 degrees width in latitude. Kondo and Imae (1993) used a mixed model of Fourier expansion plus a linear trend in one dimension in the longitude (time) direction. We expanded from the one dimension model of Kondo and Imae to two-dimensional VTEC distribution model, which is expressed by the product of independent longitudinal and latitudinal functions on a thin ionospheric layer. The model is expressed as follows:

$$\begin{aligned} VTEC(\lambda,\varphi) &= f(\lambda)\times g(\varphi) \\ f(\lambda) &= c_0 + c_1\lambda + \sum_{k=1}^{4} a_k \cos(\frac{2\pi k}{T}\lambda) + b_k \sin(\frac{2\pi k}{T}\lambda) \qquad (4.7) \\ g(\varphi) &= 1 + c_2\varphi \qquad (\mathrm{T} = 24 \text{ hours}). \qquad (4.8) \end{aligned}$$

Constant offset, linear trend, and 4th order of harmonic variation as a function of longitude (time) is represented by a function $f(\lambda)$. And constant offset and linear trend as a function of latitude is simply represented by a function $g(\varphi)$. Since ionospheric area, which can be observed from single GPS station, is in a narrow belt-shaped region of about 10 degrees width in latitude (it is seen in the TEC map in Figure 4.2), linear trend or polynomial modeling in latitude direction will be appropriate in this case for simplicity. Then, free eleven parameters $(a_i, b_i : (i = 1..4), and\ c_j : (j = 0..2))$ of equation (4.7) solved by Gauss-Newton non-linear least square method with observed TECMETER data $VTEC_i$

We have tested two ways to handle the TECMETER data sets. In case I, ionospheric maps were obtained from the Kashima and Koganei TECMETER data sets, separately. In case II, the data sets of both stations were combined and a common TEC map was produced, because the distance between the two observation sites was only about 100 km and the ionospheric conditions were almost the common above both stations. An example TEC map obtained in the case II is shown in Figure 4.2.

4.3.2 Global Ionosphere Map Generated by CODE

Global Ionosphere Model

CODE determines precise GPS orbit by using IGS network observation data and provides precise orbit information for world wide GPS users. And CODE has been routinely generating global ionosphere maps (GIMs) on a daily basis since 1 January 1996 [*Schaer et al.,* 1998a; *Schaer,* 1999] by using more than 130 IGS stations' data. These GIMs have the advantage that instrumental delay biases are not included in the observable, since double difference of pseudo range measured by carrier phase is used in the GPS data analysis. CODE uses single-layer spherical shell model for the ionosphere structure and the shell height is assumed to be constantly 450 km. The GIM provided by the CODE (GIM/CODE) is modeled with 149 coefficients of spherical harmonic expansion up to 12 degrees and 8 orders. A solar-geomagnetic reference frame or a solar-geographic reference frame is used to express the GIM/CODE. Twelve GIMs in two-hour intervals (12 maps per day) are included in a GIM/CODE data. And the data is provided in two sorts of formats: IONEX [*Schaer et al.,* 1998b] and Bernese ION file. Daily GIM data from 1 January 1995 and related subroutines are provided on the Internet

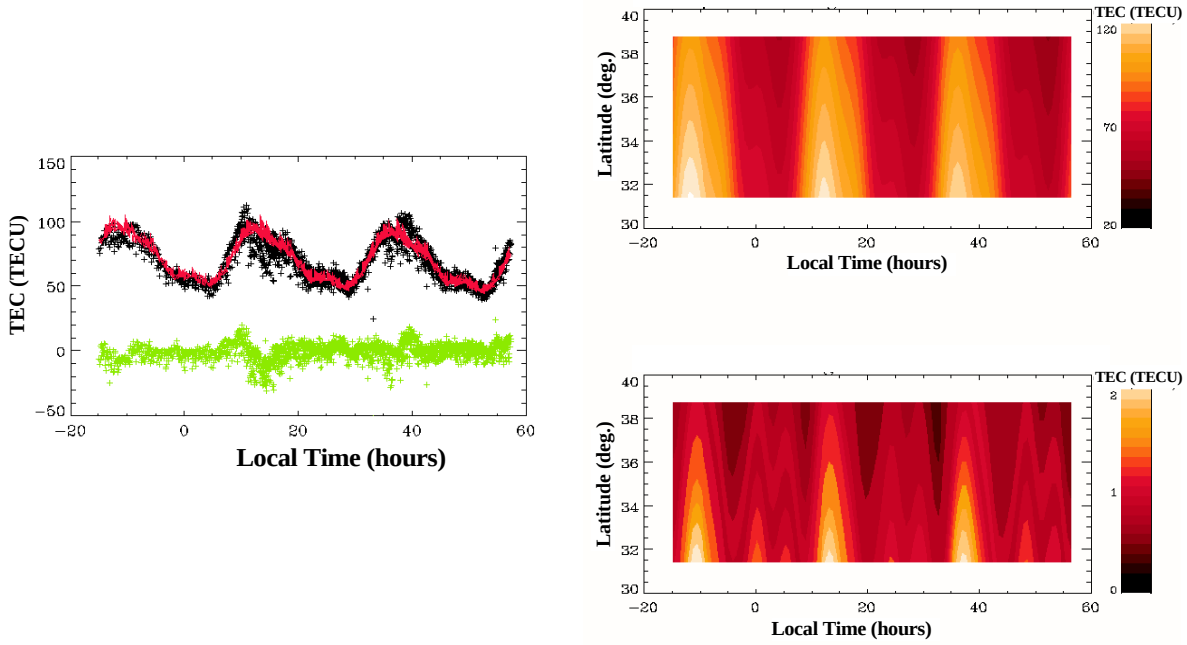

Figure 4.2: Results of least-square model fitting a 2D ionosphere model to combined data sets (Kashima and Koganei TECMETER data obtained from 7 to 9 of April 2000) (case II; see text). The left panel shows the result of fitting a 2D ionosphere model (see text) to vertical TEC (VTEC) data on the local time-latitude plane. The black '+' mark, red line, and the green '+' mark respectively indicate the VTEC data, fitted model, and residual. The upper right panel shows a VTEC map above the Kashima and Koganei stations. The origin of the horizontal coordinate is local time 0 o'clock of April 08. The lower right panel shows the VTEC model error-map calculated from correlation matrix of the least-square analysis.

(http://www.aiub.unibe.ch/ionosphere.html). Figure 4.3 is an example of GIM and its error map on 5 July 2000. It is expressed in the geographical coordinate system, and it can be seen that the TEC structure is meanders along the geomagnetic equator.

Computation of TEC in VLBI Observation by Using the GIM/CODE

We computed the ionospheric delays of VLBI observations from the GIM model (hereafter referred to case III) and compared them with the dual-frequency VLBI observations below.

One set of GIM/CODE data contains 12 GIMs with 2-hour intervals in a day. Recent GIM/CODEs are expressed in the Sun-fixed geomagnetic reference frame, which takes the z-axis in the direction of the geomagnetic pole and the x-axis is fixed in the direction to the Sun. Vertical TEC at arbitrary epoch t at geographical coordinates (λ, φ) is calculated by linear interpolation using the nearest two GIM data by the following formula.

$$VTEC(\lambda,\varphi) \quad = \quad GIM(l(t),\varphi_m,t_k)\frac{t_{k+1}-t}{t_{k+1}-t_k} + GIM(l(t),\varphi_m,t_{k+1})\frac{t-t_k}{t_{k+1}-t_k}, \qquad (4.9)$$

where t_k and t_{k+1} are earlier and later nearest epoch to t in the GIM data, respectively. Coordinates (λ, φ) in the geographical reference frame at epoch t correspond to the coordinates $(l(t), \varphi_m)$ in the sun-fixed geomagnetic reference frame.

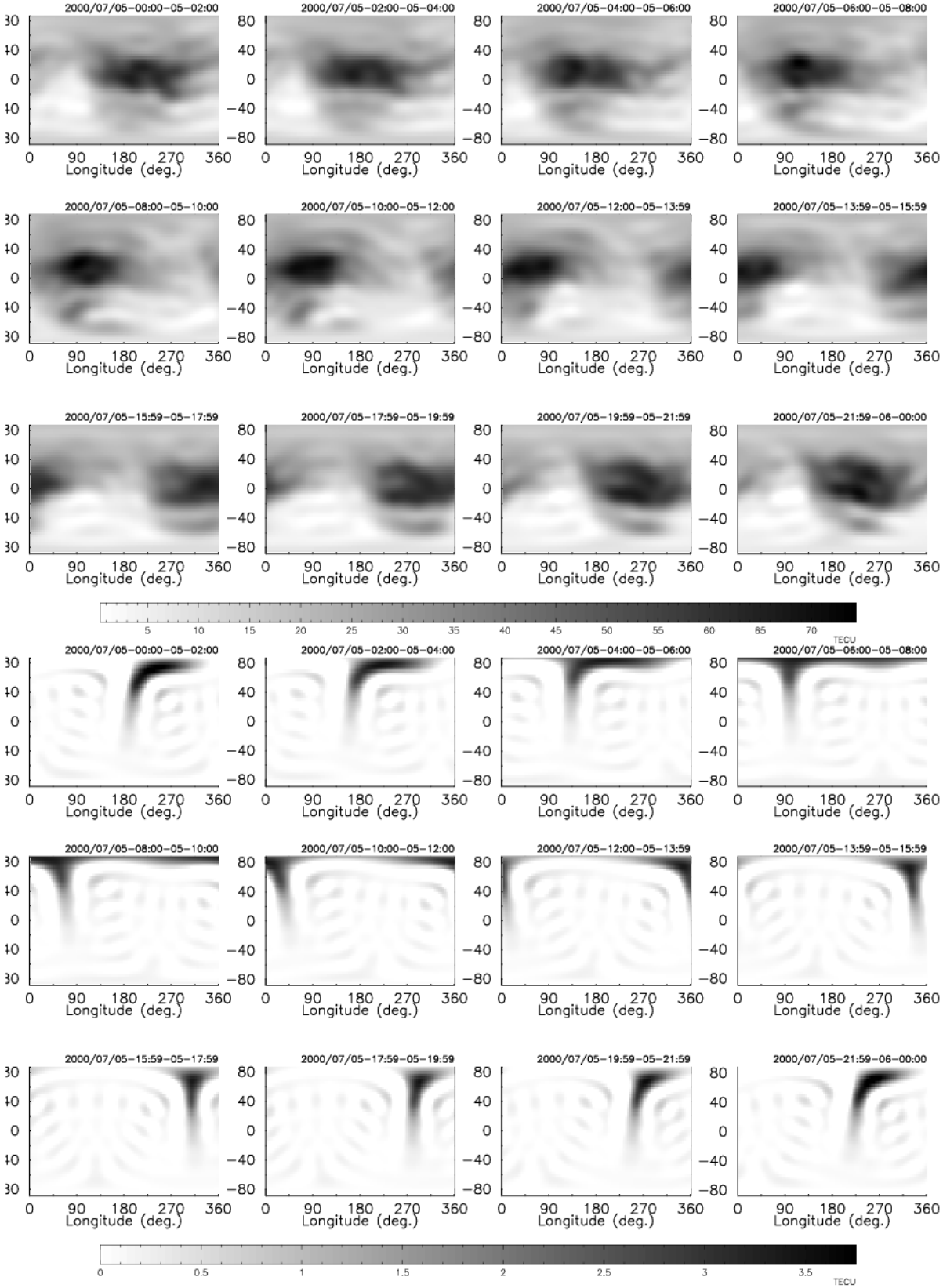

Figure 4.3: Global ionosphere map data on 5 July 2000 generated by the CODE (upper panel) and the TEC estimation error (lower panel). Horizontal axis is geographical longitude and vertical axis is geographical latitude.

4.4 Evaluation of GPS-based TEC Accuracy

4.4.1 Comparison between VLBI-derived TEC and Local Ionosphere Map Generated by TECMETER Observation

Two TEC estimations, case I and II, by using TECMETER data were compared with TEC data measured by dual-band KSP-VLBI 100-km baseline observation. The total number of scans used for the comparison was 2862. The results of these statistical comparisons are listed in Table 4.1. In case that common ionosphere map was estimated with joint data set (case II), the local TEC map data showed about 80% of correlation with VLBI-measured TEC, and the root mean square (RMS) of the difference between VLBI-based TEC and local TEC map (case II) was about 1.2 TECU. This RMS value corresponds to an excess path delay of 23 ps at 8.3 GHz. Figure 4.4 shows comparison between VLBI and GPS-based measurement of the case II on 7 April 2000 as an example. Thus ionospheric delay obtained from GPS observation (case II) can be used for the ionospheric delay calibration with error of a few tens of picoseconds at 8.3 GHz on short (100-km) baseline.

However, when local ionosphere map was estimated using single station's TECMETER data set (case I), RMS difference between VLBI-based TEC and that derived from TECMETER observation was about 7 TECU, and correlation between them was about 0.2. In spite of the same TECMETER observation data were used, the results of the comparison with VLBI data were quite different. The reason of the such drastic change of comparison results between cases I and II is that common error in the TEC map generated from joint data set are cancelled in case II, whereas errors in the TEC maps generated at each stations do not correlate each other in case I. Figure 4.5 shows elevation dependency of the RMS difference of cases I and II. The data set was divided into subsets by 10-degree intervals of elevation angle and RMS was computed for each subsets. Since differences between elevation angles of the two VLBI observations were less than one degree on the KSP 100-km baseline, uncorrelated error ($\sigma_{u,x}$ of equation (C6)) in the TEC map can be evaluated from Figure 4.5, in which RMS TEC difference shows elevation dependency of uncorrelated TEC map error as expressed by equation (C6) in Appendix C. Broken lines in the Figure indicate constant error (1.5, 4.5, and 7.5 TECU in case I (upper panel) and 0.15, 0.45, and 0.75 TECU in case II (lower panel)) magnified by mapping function (formula (4.6)). The differences between TEC map and VLBI data in case I is about one order larger than that in case II. The distribution of RMS in relation to the elevation angle is similar in both cases, i.e., error increases faster than the factor of mapping function as elevation angle decreases. This means the TEC map accuracy decreases as the ISP becomes far from the observation station. TEC map accuracy is discussed in more detail in Section 4.6.

4.4.2 Comparison between VLBI-derived TEC and the Global Ionosphere Map of the CODE

Comparison on 100-km Baseline

Results of comparison between TEC data derived from KSP VLBI experiments for 6 days (24 hours a day; 2862 scans) and the GIM/CODE data on the same dates are summarised in Table 4.1. Examples of scattered plot and a difference residual plot are shown in Figure 4.6. The GIM/CODE data show better coincidence with VLBI-measured TEC than TECMETER measurement in case II. The correlation is more than 0.9 and RMS difference is about 0.8 TECU. Proportionality factor was almost unity. The offset between the GIM/CODE data and VLBI TEC data is 2.5 TECU, i.e., the same as in case II. Since GIM/CODE data does not contain instrumental bias in principle, this offset corresponds to signal transmission delay difference between X-band and S-band of the VLBI receiver system. The offset 2.5 TECU correspond to

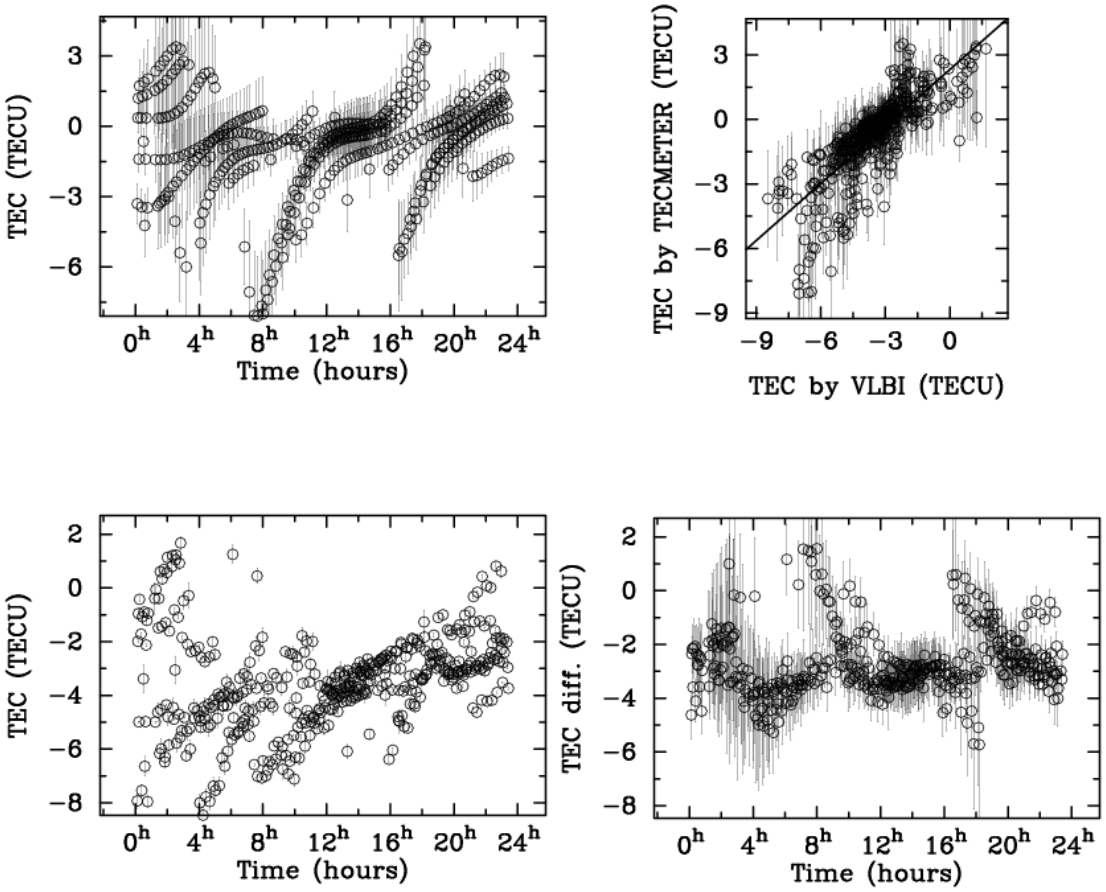

Figure 4.4: Comparison of ionospheric TEC measured by VLBI and by TECMETERs (case II) on 7 April 2000. The lower left panel shows the ionospheric TEC difference measured by dual-band VLBI observation and the upper left panel is the corresponding difference computed from the TEC map generated from the combined TECMETER data from two stations (case II; see text). The upper right panel shows the correlation between the TEC measured by VLBI and the TEC measured by the TECMETERs. The correlation coefficient, proportionality factor, and offset are respectively 0.79, 0.88, and 2.3 TECU. The lower right panel shows the difference between the VLBI and TECMETER observations. The RMS of the residual is 1.2 TECU.

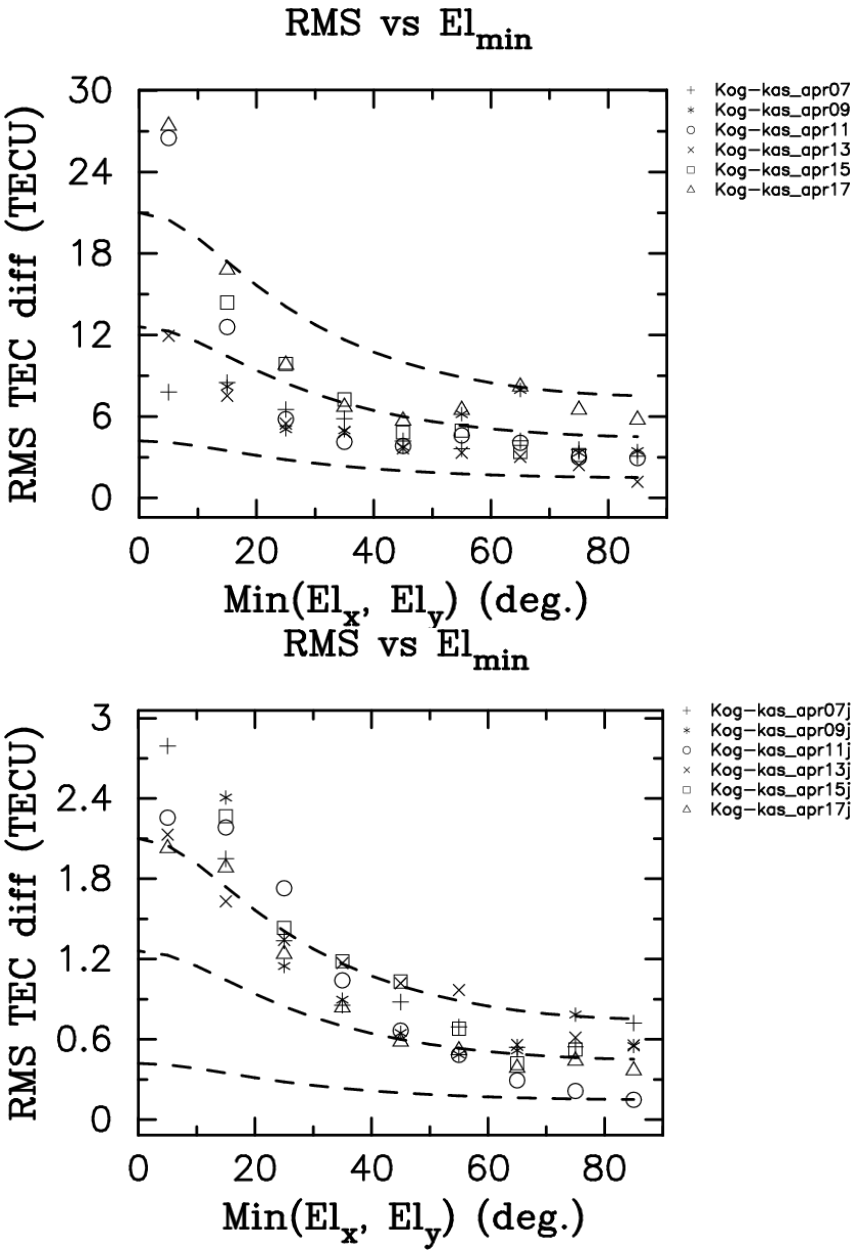

Figure 4.5: The RMS difference between TEC measured by VLBI and TECMETER on a short baseline (100 km) plotted as a function elevation angle. The elevation angles at both VLBI stations are almost the same. Each RMS was computed from data subsets divided by 10-degree steps of elevation angle. Upper panel is the case I and lower panel is the case II. Broken lines indicate constant error magnified by a mapping function factor (Equation (4.6)). The lines respectively correspond to constant error of 1.5, 4.5, and 7.5 TECU from the bottom in the upper panel, 0.15, 0.45 and 0.75 TECU from the bottom in the lower panel. Symbols indicate the observation data on 7, 9, 11, 13, 15, and 17 April 2000.

Table 4.1: Comparison of TEC measured by VLBI and three cases of GPS-based TEC measurements on the KSP (100-km) baseline. In case I, two TEC maps were generated from TECMETER observations at each VLBI station. In case II, the TECMETER data from two stations were combined and a single TEC map was generated. In case III, the global ionosphere map model produced by CODE was used. The difference between the TEC along the lines of sight from the pair of VLBI stations was compared with the corresponding TEC value for each case of GPS-based TEC measurements. The root mean square of the difference, correlation coefficient, proportionality factor , and offset are computed. The Kp indexes, which represent geomagnetic disturbance, of each day are listed in the bottom line [*Rasmussen et al.*, 2000].

Date		4/7-8	4/9-10	4/11-12	4/13-14	4/15-16	4/17-18	Mean
Case I (TECMETER)	RMS (TECU)	5.6	5.6	7.4	5.0	8.2	9.7	6.92
	Correlation	0.39	0.0	0.12	0.35	0.15	0.0	0.17
	Offset (TECU)	5.0	-3.6	-1.5	2.0	-0.66	19.8	3.51
	Proportionality factor	1.35	-0.2	0.56	1.1	0.88	-0.1	0.60
Case II (TECMETER)	RMS (TECU)	1.2	1.2	1.3	1.2	1.3	1.0	1.20
	Correlation	0.79	0.75	0.78	0.80	0.76	0.84	0.79
	Offset (TECU)	2.32	2.59	2.90	2.0	2.38	2.93	2.52
	Proportionality factor	0.88	0.87	0.98	0.86	1.08	1.01	0.95
Case III (GIM/CODE)	RMS (TECU)	0.70	0.89	0.75	0.73	0.82	0.69	0.76
	Correlation	0.92	0.88	0.91	0.92	1.00	0.92	0.93
	Offset (TECU)	2.3	2.9	2.32	2.40	2.68	2.48	2.51
	Proportionality factor	0.83	1.07	1.01	0.95	1.11	1.02	1.00
Kp index		40+	23	17	10	12	19	-

0.65 ns delay difference between 2.2 GHz and 8.4 GHz. This hardware delay offset between S and X band VLBI receivers has not been aware in normal geodetic VLBI observation, because it couples with station clock offset and is removed from analysis. This offset needs to taken into accounted in VLBI experiments for precise time transfer.

The upper panel of Figure 4.7 shows elevation dependency of the RMS differences on the 100-km baseline. Horizontal axis indicates minimum elevation angle of the pair of VLBI stations (represented by Min(Elx, Ely)). Broken lines in that panel indicate constant TEC error of 0.3, 0.4, 0.5, and 0.6 TECU magnified by the mapping function (equation (4.6)). Elevation dependency of error coincides well with these lines. This means that the ionosphere TEC map error is constant regardless of the distance from the observation point to ISP. This conclusion is reasonable, since the GIM/CODE data have no relation with the VLBI observation station position. As described in Section 4.4.1, one of the reasons for the small RMS difference between VLBI and the GIM/CODE is cancellation effect of common error, since the baseline is short and most part of the ray path in the Earth's ionosphere is shared by both VLBI stations. The uncorrelated GIM/CODE data error on 100-km baseline is estimated to be no larger than 0.35 ($=0.5/\sqrt{2}$) TECU from this figure.

Comparison on Intercontinental (several thousands km) Baseline

Intercontinental geodetic VLBI experiment data were obtained from the International VLBI Service (IVS) data center, and 36 baselines (total 38,845 scans) were used for TEC comparison with the GIM/CODE data. The names of the VLBI experiments used for the comparison are listed in Table 4.2. The VLBI TEC measurement error was less than 1 TECU, typically 0.6 TECU. An example of a scattered plot and a difference residual plot are shown in Figure 4.8.

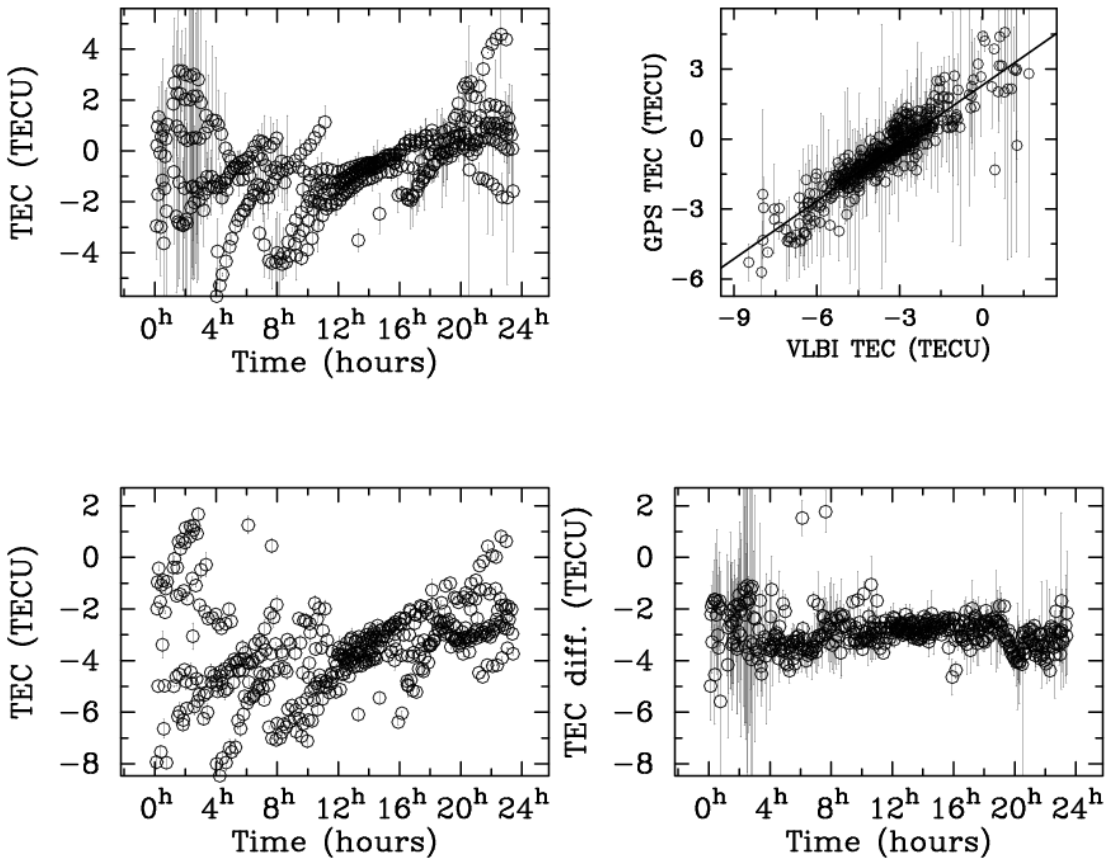

Figure 4.6: Comparison of the ionospheric TEC measured by VLBI and the global ionosphere map model by the CODE (case III) on 7 April 2000. The lower left panel shows TEC difference measured by dual band VLBI observation of KSP (100-km) baseline. The upper left panel is the corresponding difference computed from the global ionosphere map by the CODE. The upper right panel shows the correlation between the TEC measured by VLBI and the TEC derived from the GIM/CODE model. The correlation coefficient, proportional coefficient, and offset were respectively 0.92, 1.01, and -2.9 TECU. The lower right panel is the difference between the VLBI-measured TEC and the TEC derived from the GIM/CODE model. The RMS of the difference is 0.7 TECU.

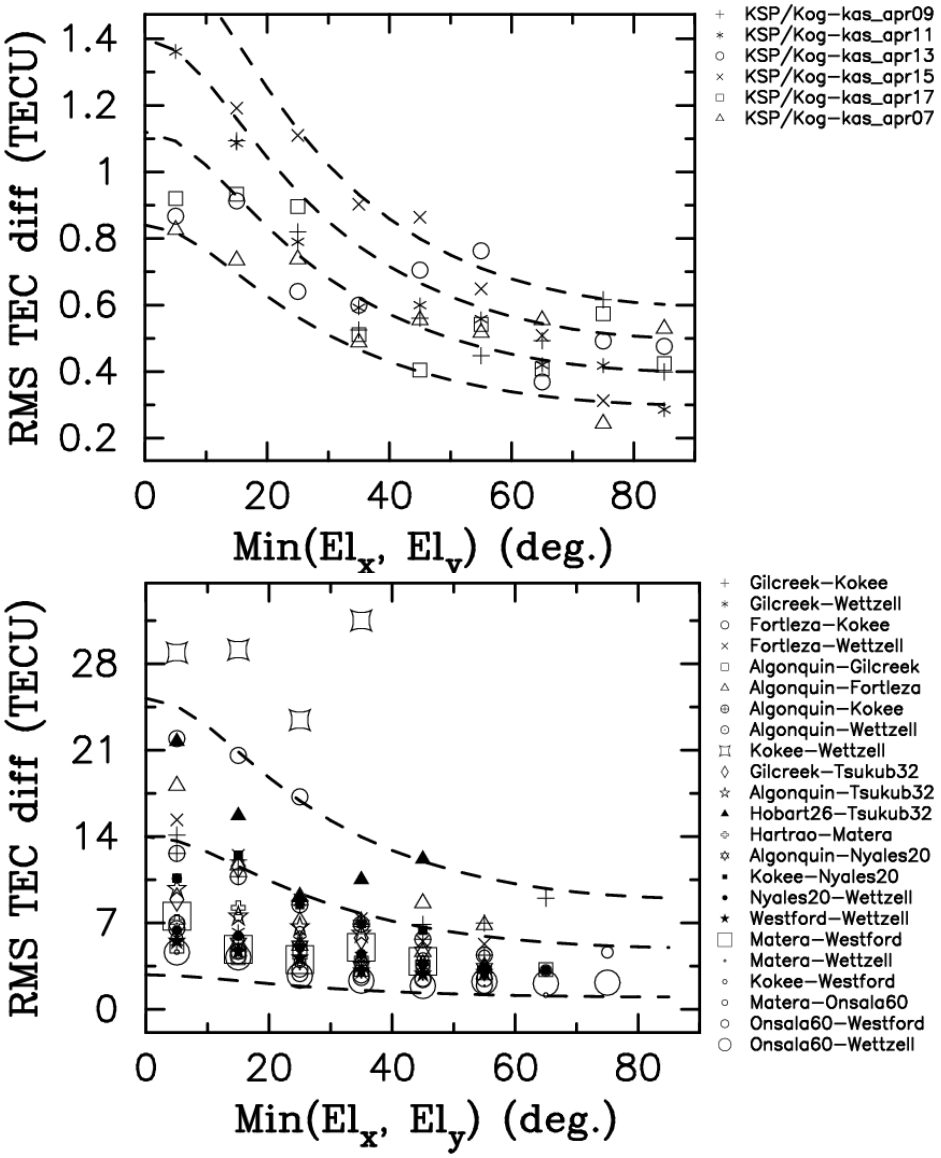

Figure 4.7: RMS difference between TEC measured by VLBI and that computed from GIM/CODE data are plotted as a function of minimum elevation angles at the two observation stations. The upper panel represents the RMS difference on the 100-km baseline and the lower panel represents that on the intercontinental baseline. Broken lines indicate constant error magnified by mapping function factor (equation (4.6)). The lines in the upper panel respectively correspond to constant errors of 0.3, 0.4, 0.5, and 0.6 TECU from the bottom. And the lines in the lower panel respectively correspond to error of 1, 5, and 9 TECU error from the bottom. Each symbol indicates a different baseline.

Table 4.2: Intercontinental VLBI experiments used for TEC comparison

Date	Experiment name	Station names
2000/7/5-6	NEOS-A375	Algonquin, Fortleza, Kokee, Wettzell, Gilcreek
2000/7/10-11	CORE-1001	Algonquin, Gilcreek, Hartrao, Hobart, Matera, Tsukuba
2000/7/11-12	NEOS-A376	Algonquin, Fortleza, Kokee, Nyales, Wettzell
2000/7/12-13	CORE-3001	Gilcreek, Kokee, Onsala, Westford, Wettzell
2000/7/18-19	NEOS-A377	Algonquin, Fortleza, Kokee, Wettzell, Gilcreek
2000/7/25-26	NEOS-A378	Algonquin, Fortleza, Kokee, Nyales, Wettzell

Since two radio signals share almost no common ray path in the Earth's ionosphere on the intercontinental VLBI baseline, the variation range of excess delay became larger on a longer baseline. As indicated in Figure 4.9(a), the correlation coefficient approached unity as the baseline became longer.

The lower panel of Figure 4.7 shows elevation dependency of RMS TEC difference between GIM/CODE and VLBI. Minimum elevation angle of the pair of VLBI stations (represented by Min(Elx, Ely)) was used as a horizontal axis of the figure. The whole data set was divided into data subsets separated by 10-degree intervals by the Min(Elx, Ely). Then RMS of difference (GPS-VLBI) was computed for each data subset. The summation of the RMS was taken in respect to each baseline regardless of the difference of experiments. Since the error in VLBI-based TEC measurement is less than 1 TECU, the difference mainly comes from error in the GIM/CODE model. And the difference between the elevation angle of the pair of the VLBI stations is mostly larger on longer baseline. That is to say, one station observes at low elevation while the other station observes at high elevation angle. Vertical TEC error is magnified by mapping function at low elevation angle: thus the error budget is mostly dominated by TEC error of lower elevation station. Hence Figure 4.7 approximately indicates elevation dependency of the Global ionosphere map TEC error from a single station. Broken lines in the figure indicate 1, 5, and 9 TECU error magnified by the mapping function (equation (4.6)). Error distribution follows the elevation dependency of the mapping function. This again implies that vertical TEC error is constant regardless the distance of ISP from the observation point. The error is larger for longer baseline than shorter baseline (upper panel) is because long baseline data does not contain common error as a shorter baseline does. Thus, the accuracy of the absolute TEC value of the GIM/CODE data is estimated as 1 - 5 TECU from this plot.

Figure 4.9(b) shows baseline dependency of the RMS difference. It is clear that the RMS difference increases with baseline length. Figure 4.9(c) plots the ratio of the RMS error to the TEC variation range. The ratio is almost completely in the range of 3 to 10% for any baselines. This ratio is an indicator of the ionospheric TEC correction accuracy, when the GIM/CODE

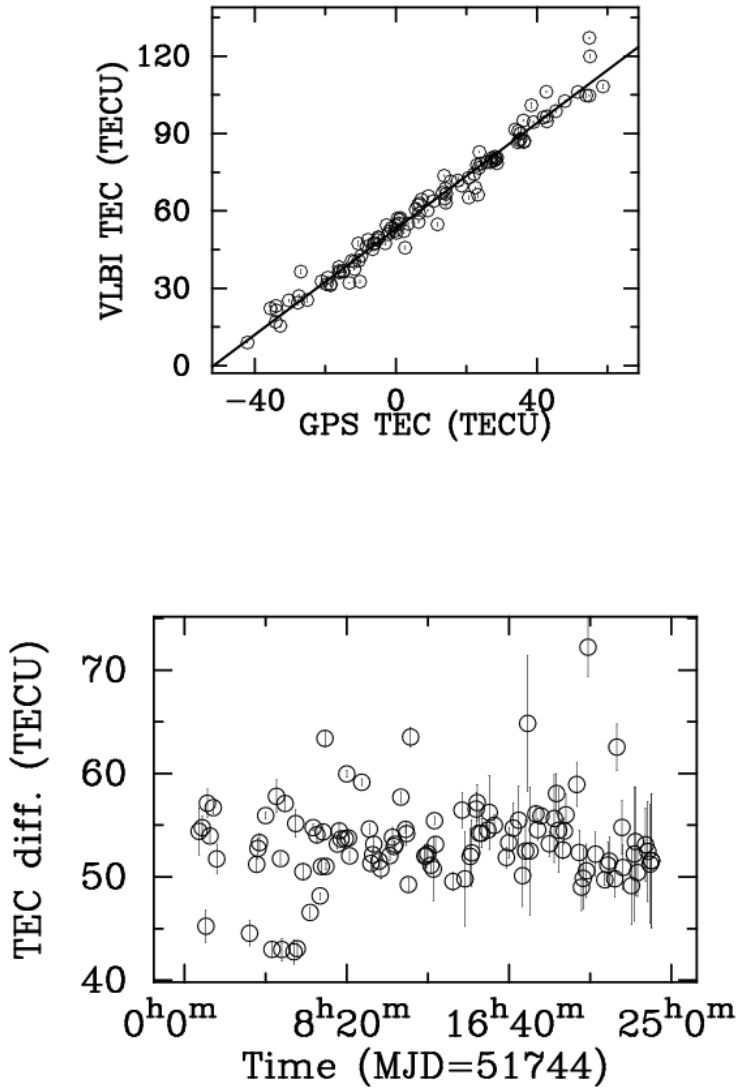

Figure 4.8: Comparison of ionospheric TEC measured by VLBI and the GIM/CODE model on 18 July 2000 (Algonquin-Wettzell baseline, about 6000-km). Upper panel shows scatter plot of TEC measured by VLBI and GPS. Correlation coefficient, proportionality factor, and offset are respectively 0.99, 1.03, and 52.7 TECU. Lower panel is plot of difference between VLBI-measured TEC and the GIM/CODE model. The RMS of the difference is 4.2 TECU.

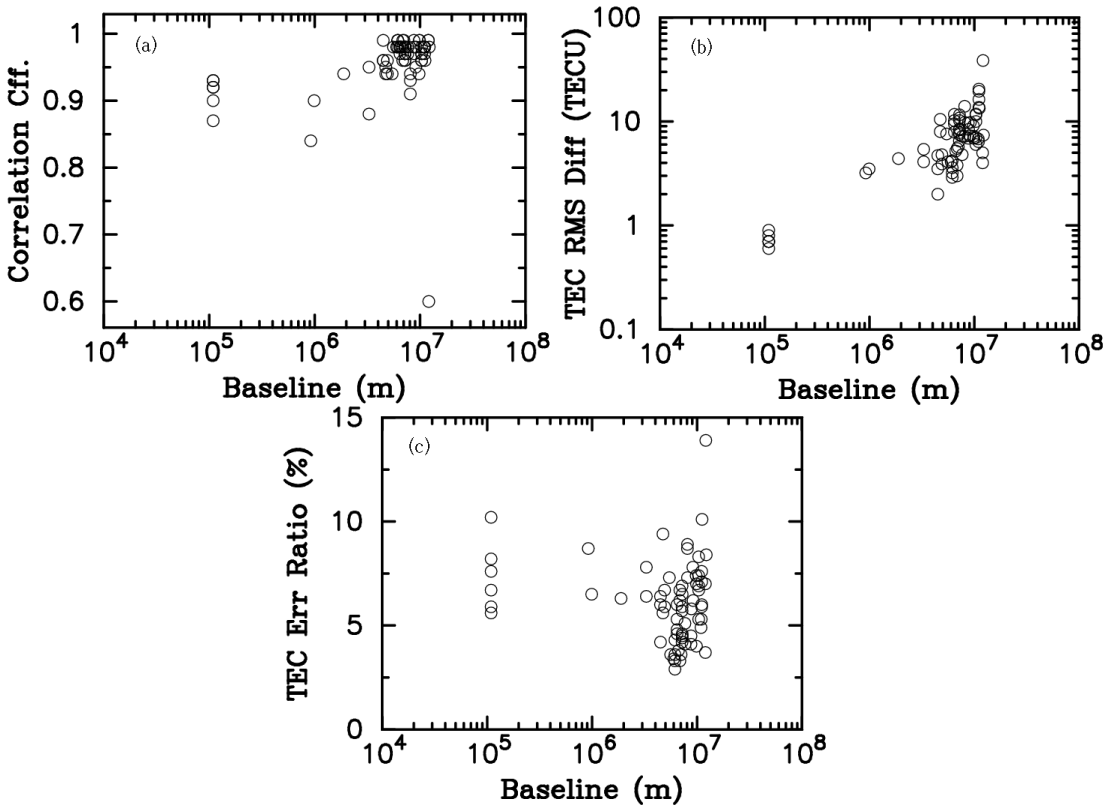

Figure 4.9: Correlation, RMS difference, and ratio of TEC error to the TEC variation range on that baseline are plotted in relation to the baseline length. (a): Correlation of TEC measured by VLBI and that computed from GIM/CODE is plotted in relation to the baseline length. (b): RMS TEC difference between TEC measured by VLBI and that computed from GIM/CODE data is plotted as a function of baseline length. (c): Ratio of the TEC error (RMS difference between TEC measured by VLBI and that computed from GIM/CODE data) to the TEC variation ranges is plotted in relation to baseline length. The VLBI data used for this comparison were KSP-VLBI data in Table 4.1 and IVS data in Table 4.2.

TEC map is used for ionospheric delay correction in VLBI data analysis. That is, the global ionosphere map of the CODE can compensate for more than 90% of ionospheric delay in VLBI observation.

4.5 Comparison of Phase Delay Rate Derived from GPS-based TEC and VLBI

Phase delay rate caused by TEC of the Earth's ionosphere is also disturbance in several kinds of space measurements with microwave. The SELENE project [*Matsumoto et al.,* 1999, *Heki et al.,* 1999] is one of those project, in which velocity of the spacecraft need to be determined at accuracy of 0.1 mm/s or less at S-band. The accuracy correspond to delay rate measurement accuracy of 0.3 ps/s. Since this order of rate change can be cause by TEC changing rate of 1 milli-TECU/s at 2.2 GHz, phase delay change rate due to the Earth ionosphere needs to be corrected in such project.

VLBI can measure phase delay rate caused by the ionosphere, which corresponds to TEC change rate (hereafter referred to TEC rate) in the line of sight. We compared the TEC rates determined by VLBI measurements and those computed from GIM/CODE data. VLBI-measured TEC rate consists of the TEC time variation and spatial change of the line of sight due to tracking of the radio source. We computed TECs in the line of sight to the radio source at the desired epoch, and at four other epochs with 10-minute intervals before and after the desired epoch. Then TEC rate was computed by numerical derivation of the 5 points of TEC data.

The TEC rates were compared on the short baseline (KSP) and on the intercontinental baseline (Table 4.2). Unfortunately, correlation between VLBI-measured TEC rate and TEC rate computed from GIM/CODE was almost zero for the short (100-km) baseline. Even though correlation of around 0.6 to 0.8 was found in longer baselines, the GIM/CODEs had not enough accuracy for phase delay rate correction. Figure 4.10 shows an example of the result of TEC rate comparison on the Algonquin-Wettzell baseline on 18 July 2000. RMS difference of TEC rate between the GIM/CODE and VLBI was several milli-TECU/second, whereas accuracy of TEC rate measured by VLBI was less than 1 milli-TECU/sec. The reason of the poor coincidence of TEC rate is understood by following two reasons. First, the GIM/CODE data consists of 12 global ionosphere maps with two-hour intervals. Thus short time scale TEC variation is not included in the data. Second, the GIM/CODE data is expressed by spherical harmonics components up to 12 degrees and 8 orders. And ionospheric TEC structure expressed with that model is limited to the scale of about 2500-km in longitude and about 1700-km in latitude. Thus a scale smaller than those is not included in that model. However, those small scale structure is important in delay rate, because the derivative operation to derive the TEC rate is equivalent to high pass filtering to suppress lower frequency components and to enhance higher frequency components. Thus contribution of small scale component is magnified by the derivative operation.

As an conclusion, the GIM/CODE data do not contain higher frequency component in both time and space domain, so TEC rate derived from the GIM/CODE shows poor coincidence with actual VLBI-measured TEC rate.

4.6 Discussion

4.6.1 Accuracy of TEC Map Derived by Analysis Cases I and II

As explained in appendix A, the relation between ensemble average of the RMS difference (GPS-VLBI) and uncorrelated error of TEC map is expressed by equation (C6), when the elevation angles of the two observation stations are almost the same. This condition is satisfied on short

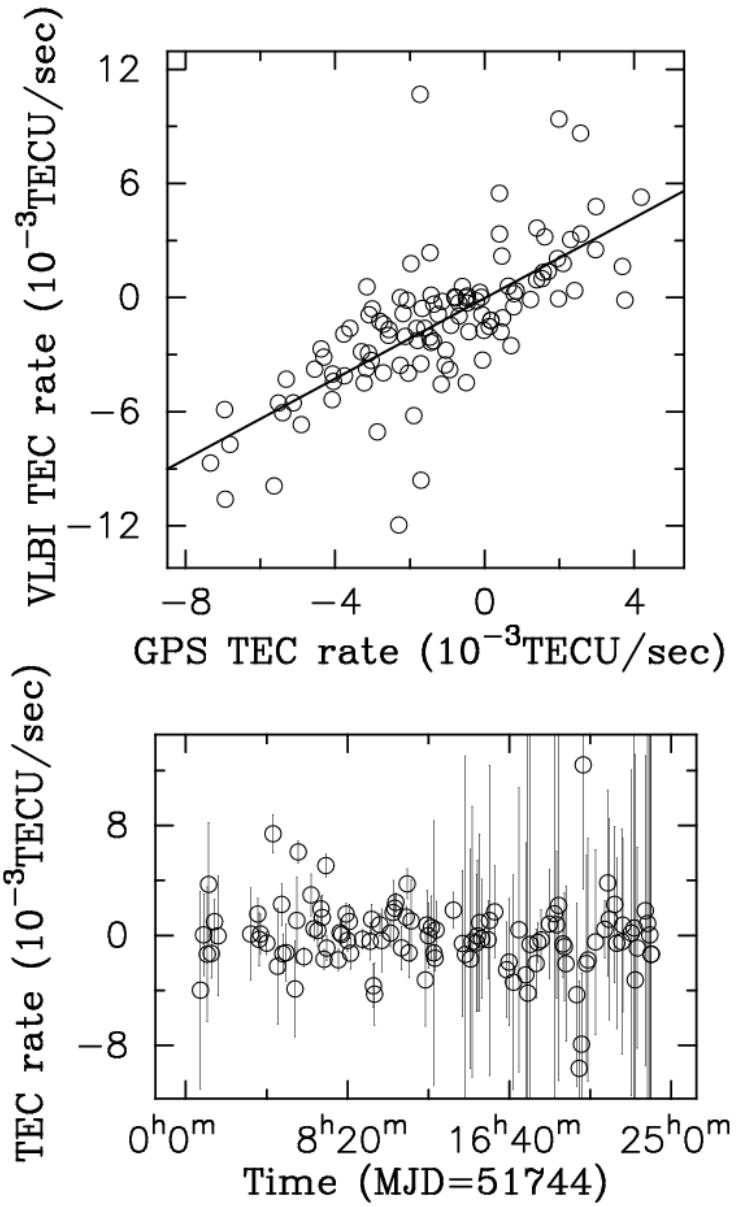

Figure 4.10: Comparison of TEC rate derived from VLBI and the GIM/CODE. TEC rate data on 18 July 2000 (Algonquin - Wettzell baseline). The upper panel shows a scatter plot of TEC rate measured by VLBI and corresponding rate computed from GIM/CODE. The lower panel is a difference residual plot of the TEC rates determined by VLBI and by the GIM/CODE model. Correlation between the TEC rates determined by VLBI and by the GIM/CODE is 0.7 and the RMS residual is 2.6×10^{-3}.

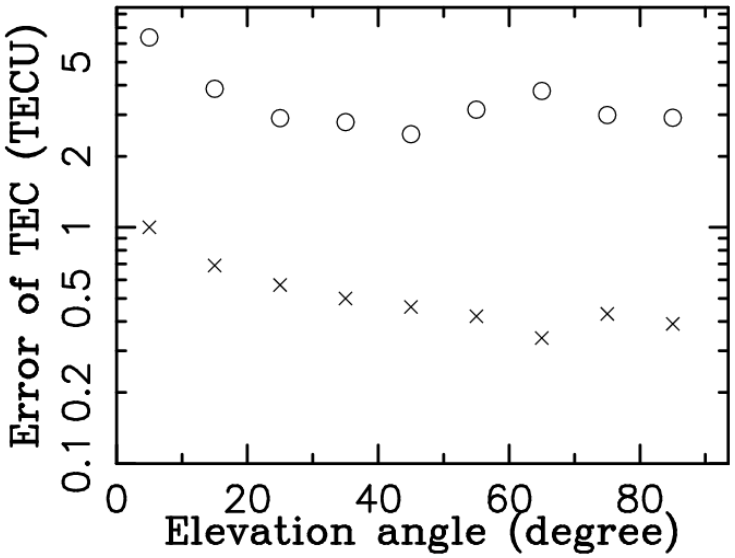

Figure 4.11: Uncorrelated error of TEC map generated by TECMETER observation in case I and II (100-km baseline) is plotted against elevation angle. Whole data set was divided into subsets by 10-degree interval by minimum elevation angle of the pair of VLBI stations. The mark ◯ represents TEC map estimation from TECMETER data of the case I and × represents that of the case II.

baselines such as the KSP-VLBI baseline. The elevation angle difference is no larger than one degree on Kashima-Koganei baseline. Then equation (C6) can be used to estimate uncorrelated TEC map error generated by TECMETER observation in case I and II.

The GPS-VLBI difference data set was divided into nine subsets by 10-degree steps of elevation angle. And ensemble average $< Fm^2 El_x >$, instead of $Fm^2(El_x)$ in equation (C5), was computed in each subset . The uncorrelated error is plotted in relation to elevation angle in Figure 4.11 for cases I and II. It is seen that elevation dependency due to the mapping function is removed and uncorrelated error level is obviously seen in that figure. As discussed in Section 4.4.1, the error still increases at lower elevation in cases I and II. The reason is that the error increases as the ionospheric point become far from observation point. Rather rapid increase of the error below 30 degrees should be caused by the elevation cut-off angle 30 degrees in the TECMETER observation. From average of the results at elevation angle range 40 – 90 degrees, uncorrelated errors were estimated as 3.1 TECU in case I and 0.41 TECU in case II. Since two stations TEC maps in case I were estimated independently from independent data set, two sets of errors were added in case I. Hence the uncorrelated error of 3.1 TECU represents the accuracy of our TEC map estimation method described in Section 4.3.1. This accuracy of the TEC map produced by TECMETER measurements is inferior to that of GIM/CODE data as described in the next section. It is because of the following reasons: the precision of observable (group delay) by the TECMETER is inferior to regular geodetic GPS receiver's (hereafter GGR) observable (carrier phase), which is used to produce GIM/CODE. TECMETER measures group delay difference between two frequencies in the line of sight to GPS satellites every 3 minutes interval, whereas GGR observes carrier phase differences between the two frequencies in lines of sight to several GPS satellites almost simultaneously. Thus, the number of data obtained by GGR is much larger than TECMETER. GIM/CODE is generated by using world-wide GPS network observation data, whereas TECMETER data from only one or two stations were used to produce the local TEC map. Consequently, the TEC map error (cases I and II) increases as elevation angle decreases (Figure 4.5 and Figure 4.11).

4.6.2 Accuracy of the GIM/CODE

The relation between GIM/CODE TEC error and the RMS difference compared the GIM/CODE and VLBI-based TEC measurements is approximately expressed equation (C8). The data set, including IVS and KSP, was divided into nine subsets of 10-degree intervals according to Min(Elx, Ely), which is minimum of elevation angles of the pair of VLBI stations. Each data subset was divided again into three groups according to baseline length: (1) 0-4000 km, (2) 4000 - 8000 km, and (3) longer than 8000-km. An ensemble average $< (Fm^2(El_x) + Fm^2(El_y)) >$ was computed for each data subset instead of $\{Fm^2(El_x) + Fm^2(El_y)\}$ in equation (C8). The estimated σ_{GPS} is plotted in the upper panel of Figure 4.12. As it was expected from Figure 4.7, Figure 4.12 shows that estimated GIM/CODE TEC error is constant with respect to the elevation angle when baseline length is less than 8000-km. That implies that GIM/CODE TEC error is constant regardless of the distance of ISP from the observation point.

The increase of estimated error at elevation angle of more than 60 degrees in case (ii) is due to the larger deviation caused by smaller number of data used for the computation. The Figure 4.12 shows that the estimated error increases with baseline length. This is because ray paths share less part of ionosphere as the baseline becomes longer.

To determine how the estimated error changes with baseline length, the whole data set was divided into subsets by 1000-km intervals of baseline length. Summation in computation of RMS difference was taken for each data subsets and are plotted against the baseline length (lower panel of Figure 4.12). Three cases of elevation cut-off test was performed with 20, 40, and 60 degrees of elevation limit. The figure indicates that error increases rapidly below 2000-km range and is almost constant at baseline larger than 2000-km. This implies that the ionosphere path is no more shared at longer baseline than 2000 km. The reason of the increase of error at longer than 8000 km is not obvious. One reason is due to ray path bending effect, which is not taken into account in the mapping function (formula (4.6)). Since occurrence of lower elevation is more frequent at longer baseline, the error due to the ray-path-bending effect appears more clearly at longer baseline than short baseline, where that effect is averaged out. Another reason of the error increase at longer baseline is larger deviation due to the smaller number of data to be averaged.

Error in GIM/CODE was estimated as 2.5 TECU by averaging the error over a baseline range of 2000-6000 km. This error is a little larger than expected from GIM/CODE error map (Figure 4.3) except for the larger error around the North Pole. One source of the GIM/CODE TEC error is that the GIM/CODE is modeled by 12-degree 8-orders spherical harmonics, thus smaller scale than approximately 2500 km in longitude and 1700 km latitude is not included in the model. Although small (100 km) scale traveling ionospheric disturbances (TIDs) with amplitude of 1 TECU from peak to peak arise frequently [*Saito et al.,* 1998], such small scale disturbances are not modeled in the GIM/CODE. The incomplete modeling of ionosphere is one reason of error in the absolute TEC data of GIM/CODE. The second reason of the error in the GIM/CODE is that many baselines used in this comparison crossed the North Pole, where the error in GIM/CODE is larger. When larger error around the North Pole and the lack of high frequency component in the GIM/CODE are taken into account, the estimated error in the GIM/CODE can be concluded reasonable.

In spite of several disadvantages of TECMETER described in Section 4.6.1, the accuracy of GIM/CODE (2.5 TECU) is little different from TEC map by TECMETER (3.1 TECU). This result can be explained by following reasons. The GGR used for GIM/CODE has potential to measure the small scale structure and temporal changes of TEC in high time resolution, but the GIM/CODE model is not including high spatial frequency components in the model. Also the interval of the GIM/CODE is two hours and the temporal change of TEC is averaged out. In spite of the large difference of the number of stations and data used to generate the TEC

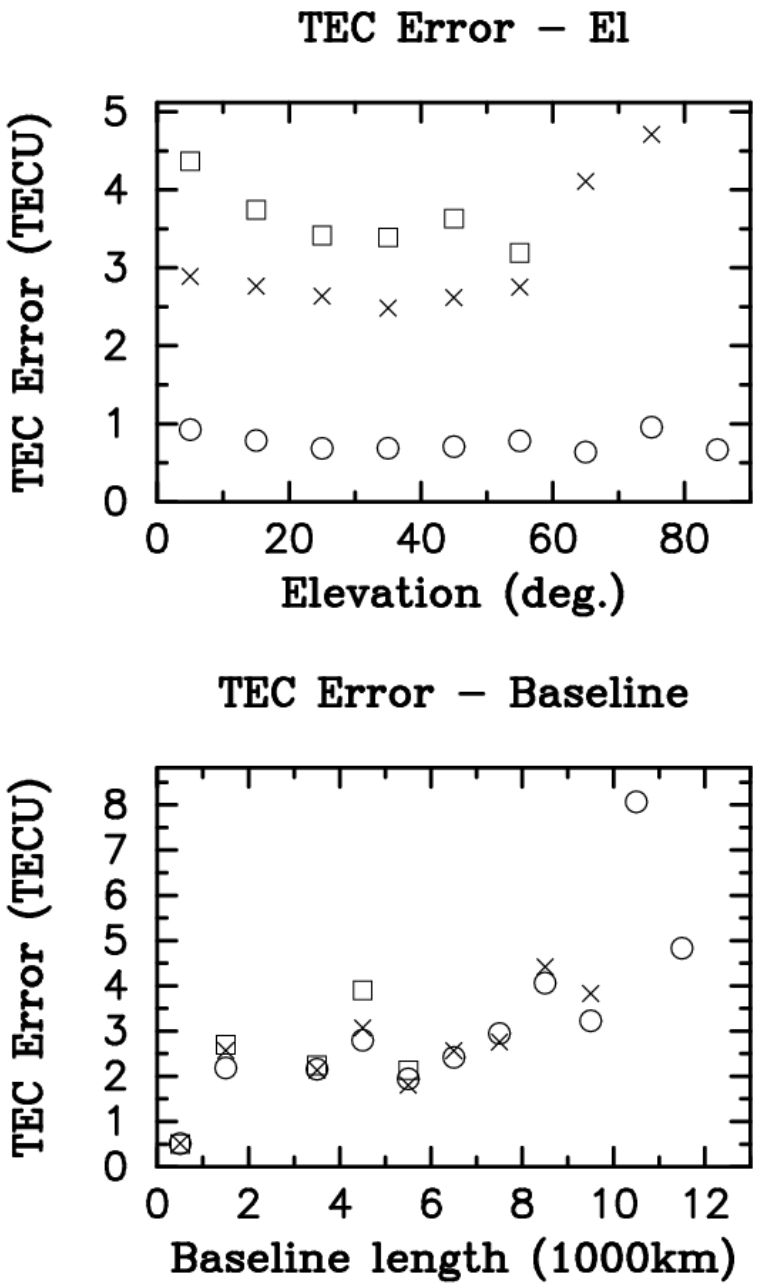

Figure 4.12: Estimated GIM/CODE TEC error is plotted in relation to elevation angle (upper panel). Whole data set of TEC difference (GPS-VLBI) was divided into data subsets by 10 degrees intervals by minimum elevation angle of two VLBI stations. The data subsets were again divided into three groups according to the baseline length: ◯, 0 - 4000-km; ×, 4000 - 8000-km; and □, longer than 8000-km. The GIM/CODE error was computed from Equation (C8). Estimated GIM/CODE errors are plotted against baseline length in the lower panel. Whole data set was divided into subsets by 1000-km intervals of baseline length. Elevation cut-off test was also performed at an elevation limit of 20 (◯), 40 (×), and 60 (□) degrees.

map between TECMETER (case II), which used only two stations, and GIM/CODE, which used moire than one hundred, there were not so large difference in the comparison with VLBI data; RMS difference was 1.2 TECU in the case of TECMETER (case II) and that was 0.76 TECU in the case of GIM/CODE (Table 4.1). The rather small difference of accuracies can be understandable since the IGS stations probing the sky over Japan are only two: Tsukuba and Usuda, and also two stations data was used in TECMETER observation.

4.7 Summary

Accuracies of GPS-based ionosphere TEC map produced in two sorts of technique were evaluated by comparison with VLBI TEC measurements from 100-km baseline (2,862 scans) to intercontinental baselines (38,845 scans). One uses TECMETER observation and the other uses a global ionospheric map generated by the CODE (GIM/CODE).

In former case, local TEC maps were estimated by TECMETER observation and compared with VLBI TEC data on the KSP (100 km) baseline. The TEC map estimated with joint data set (case II in section 4.3.1) demonstrated about 80% correlation with VLBI TEC data. The local TEC map produced by this method is applicable to ionospheric delay correction in single band short baseline VLBI observations with 1.2-TECU (i.e., 23 ps at 8.3 GHz) accuracy level, which is comparable with RMS residual of the latest geodetic VLBI delay analysis [*KSP,* 2000]. The accuracy of this TEC map estimation method was evaluated as about 3.1 TECU.

In the latter case, the global ionosphere map generated by the CODE was more accurate than the TECMETER observation presented here. The difference of the TEC compared with VLBI data was about 0.7-0.8 TECU on 100-km short baseline and 3-10 TECU on the intercontinental baseline. These TECU values respectively correspond to delays of 14-16 ps and 57-190 ps delay at 8.3 GHz. The latter range is the same level of accuracy with that of Ros et al. (2000) and Pérez-Torres et al.(2000). The advantage of the GIM/CODE data is that TEC map is available at any time and any place on the Earth without having to measure the ionosphere TEC, since the GIM/CODE is provided everyday without interruption. The GIM/CODE data is useful to remove biases caused by ionospheric delay uncertainty from single-frequency VLBI data, especially at low frequency.

TEC rates derived from GIM/CODE were compared with VLBI-measured TEC rates. Unfortunately, the correlation between them was not so high and TEC rate derived from GIM/CODE is not accurate enough for TEC rate correction in space-measurement techniques. The reason of the low accuracy of the TEC rate data can be attributed to a lack of high-frequency TEC variation modeling in the GIM/CODE model in both time and space domains.

Saito et al. (1998) measured TEC above Japan by using the Japanese dense GPS network (GEONET) [*Miyazaki et al,* 1997], and demonstrated that real ionospheric TEC has 100-km scale traveling ionosphere disturbances (TIDs) with an amplitude of about 1 TECU from peak to peak. A more precise TEC map including such small scale and short time variation should be required, if the GPS-based TEC measurement data is used for ionospheric delay rate correction in precise space navigation (e.g., SELENE project [*Matsumoto et al.,* 1999]).

Precise ionospheric information is useful for VLBI astrometry, especially for pulsar VLBI observation. Also, such information is good for accurate geodetic measurement with a single-frequency GPS receiver, which is often employed for dense array geodetic observation after earthquakes or volcanic eruptions. A more accurate TEC map with high time and spatial resolution will also contribute to improvement of space navigation.

Chapter 5

Interstellar Scintillation in VLBI Observation

5.1 Introduction

Optical scintillation is well known as twinkling of stars. Radio scintillation is also observed from small diameter radio sources. Both interplanetary scintillation (IPS) and interstellar scintillation (ISS) are observed at radio frequencies below hundreds of megahertz. And ISS is dominant in the microwave region, except in the area very close to the Sun.

A pulsar is a quite small object of about 10-km radius and its angular diameter is about 0.3 pico radians when it is observed from 1 kpc away. Consequently, the spatial frequency of the signal from a pulsar has very coherent characteristics. After signals departed from the same emission origin of the pulsar separately propagated into the space, they are scattered and changed the direction of the propagation by interstellar medium (ISM). Then they may come together on the observer plane by chance. This is a brief explanation of the ISS and a thin screen ISM model is illustrated in Figure 5.1.

Scintillation observation of pulsar has been done for a long time since discovery of pulsars by single dish observation. Such scintillation observation of pulsars has been used for investigation of ISM and velocity of pulsars [e.g., *Galt at al.,* 1972]. More over Lyne measured orbital parameters of binary pulsar B0655+64 from scintillation observation (1984). Figure 5.2 shows an example of ISS of PSR B0329+54 observed for by using 408-MHz by Rickett (1969). The ISS has a typical scale of modulation pattern in both frequency and time domains, and the scales are called decorrelation bandwidth B_s and scintillation time scale τ_s. A review of ISS is written by Rickett (1977; 1990) and an overview of ISS can be found in several books [*Lyne and Smith,* 1998; *Thompson et al.,* 1994].

VLBI observation of pulsars is distinguished from ordinary continuum radio sources by the presence of ISS phenomena Because ordinary continuum radio sources such as quasars have a large diameter emission region, they do not show scintillation phenomenon. There are two distinct differences between VLBI observation results of pulsar and quasars. (1) The cross correlation spectra are modulated in both frequency and time domains, (2) Probability distribution of correlation amplitude occurrence is different from that of quasars [*Gwinn et al.,* 1998]. Based on the thin screen model, Gwinn discussed a distinct characteristic of pulsar VLBI observation [*Gwinn et al.,* 1998] and demonstrated a quite unique approach to resolve Vela pulsar's emission region by using ISS phenomena in pulsar VLBI observation [*Gwinn et al.,* 1997; 2000a, 2000b, 2000c]. ISS has also been observed in our VLBI observation, especially in observations at 1.4 GHz. Although the actual angular size of a pulsar is quite small, the image of a pulsar is broadened by ISS to form a scattering disk. And the size of this scattering disk is an error source for astrometry of pulsars.

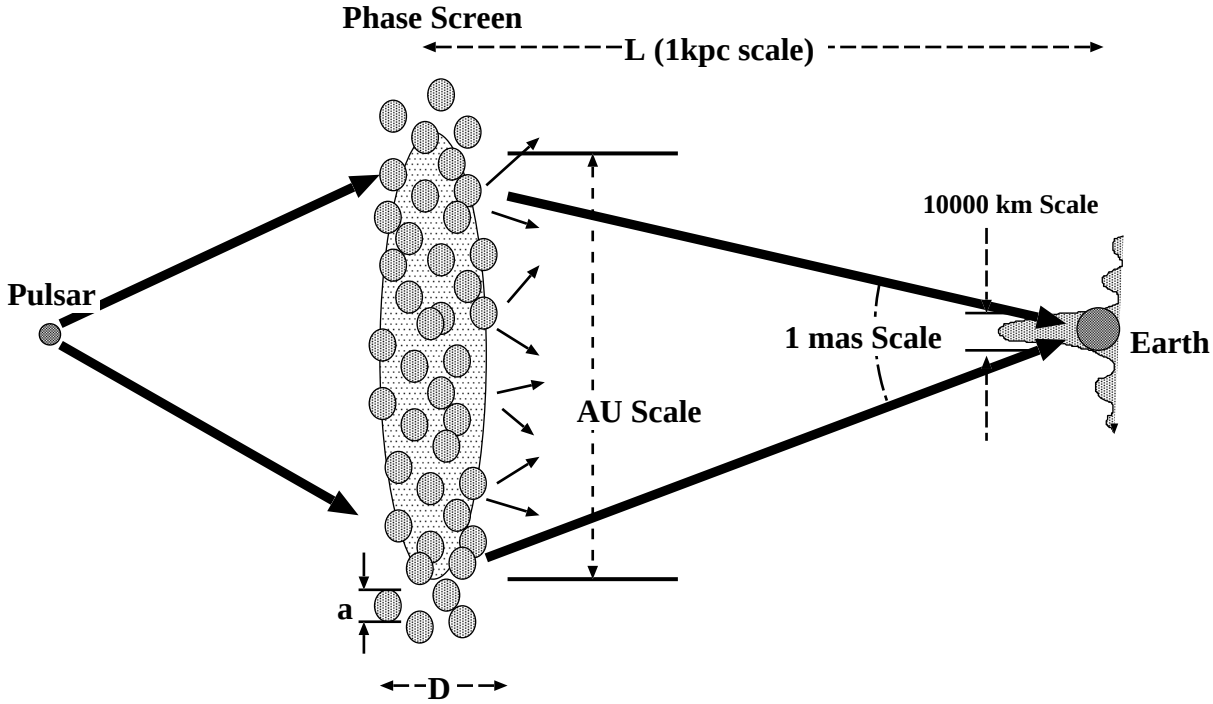

Figure 5.1: Schematic view of the thin screen model of interstellar scintillation. Distribution of free electron density irregularities with a diameter of a is assumed to be concentrated in a screen of width D at the distance L from the observer plane. Let'us suppose the screen of ISM plays a role of a lens with a diameter of 1 AU, and the ray from the pulsar focuses on the observer plane. When scattering angle is 1 mas, the size of diffraction pattern is 4×10^4 km at 1 kpc distance.

5.2 Thin Screen Model

The thin screen model of ISM is in practice useful for most of the analysis of pulsar scintillation. Figure 5.1 illustrates the thin-screen model of interstellar scattering. The model assumes that random irregularities of refractive index are found between source and observer. They are effectively concentrated in a thin screen roughly middle way along the propagation path. The irregularities have a typical diameter a and the thickness of the screen is D. The mean refractive index n is close to unity and a variation δn extending over a length a changes the phase of a wave by an amount $\delta\phi = (2\pi/\lambda)a\delta n$. Since the refractive index of cold plasma is expressed by formula (4.2), the phase change for a wave traversing a single irregularity is

$$\delta\phi = ar_e\Delta N_e\lambda, \tag{5.1}$$

where r_e is classical electron radius and is given by $e^2/4\pi\varepsilon mc^2 = 2.82\times10^{-13}$, and ΔN_e is the fluctuation in electron density corresponding to δn.

The total phase shift after passing through the screen depth D is given by $\Delta\phi = \sum\delta\phi$. Since deviation of the $\Delta\phi$ is derived from the theory of statistics as $<\Delta\phi^2>=(D/a)<\delta\phi^2>$, the difference between the phase perturbations of rays separated laterally by more than a becomes

$$\Delta\phi \approx \left(\frac{D}{a}\right)^{1/2}\delta\phi = (Da)^{1/2}r_e\Delta N_e\lambda \tag{5.2}$$

when phase perturbation $\Delta\phi$ in lateral distance a causes change of propagation direction by

$$\theta_{\rm scat} \approx \frac{\Delta\phi\lambda}{2\pi a} = \frac{1}{2\pi}\left(\frac{D}{a}\right)^{1/2} r_e\Delta N_e\lambda^2. \tag{5.3}$$

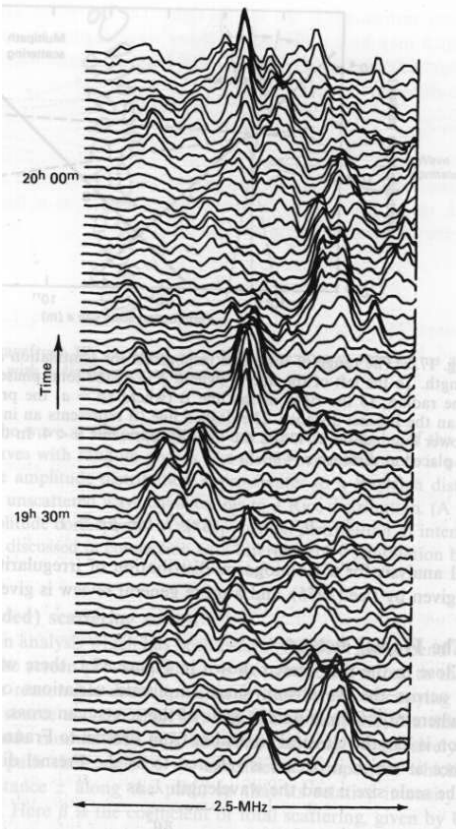

Figure 5.2: Example of ISS phenomena of PSR0329+54 observed by Rickett (1970) at 408 MHz.

This is the apparent angular size of the source seen through the screen.

Wavefront has no amplitude variation immediately after the thin screen. As the distance from the screen increases the amplitude variation is build up through interference between rays from various paths of the corrugated wavefront. The ray path length will differ by length $\frac{1}{2}\theta_{\rm scat}^2 L$, which may be a difference of many wavelengths. The interference between rays will therefore differ at different wavelengths. Since excess phase due to the ray path is given by $\psi = \frac{\pi}{\lambda}\theta_{\rm scat}^2 L = \frac{\pi}{c}\theta_{\rm scat}^2 Lf$ (see Figure 5.3). Then frequency band width Δf, where the phase differs by 2 π, is expressed by formula (5.3) as

$$\Delta f = \frac{2c}{\theta_{\rm scat}^2 L} \tag{5.4}$$

$$= \frac{8\pi^2 ac}{DLr_e^2(\Delta N_e)^2\lambda^4}. \tag{5.5}$$

We assume the scale of D is the same order as the distance to the screen, L, so the decorrelation (scintillation) bandwidth is expressed as

$$B_s = \frac{8\pi^2 ac}{D^2 r_e^2(\Delta N_e)^2\lambda^4}. \tag{5.6}$$

When temporal angular size of the pulsar is $\theta_{\rm scat}$ and the distance between the phase screen and observer is L, the scattering disk size on the screen is in the order of $\theta_{\rm scat} L$. The size of the diffraction pattern (S: *scintle*) on the observer plane formed by a lens with diameter $\theta_{\rm scat} L$ at distance L is given by $\lambda/\theta_{\rm scat}$, and sometimes $S = \lambda/2\pi\theta_{\rm scat}$ is used. When either the phase screen, pulsar, or observer moves in this system, the *scintle* scans observer and causes time

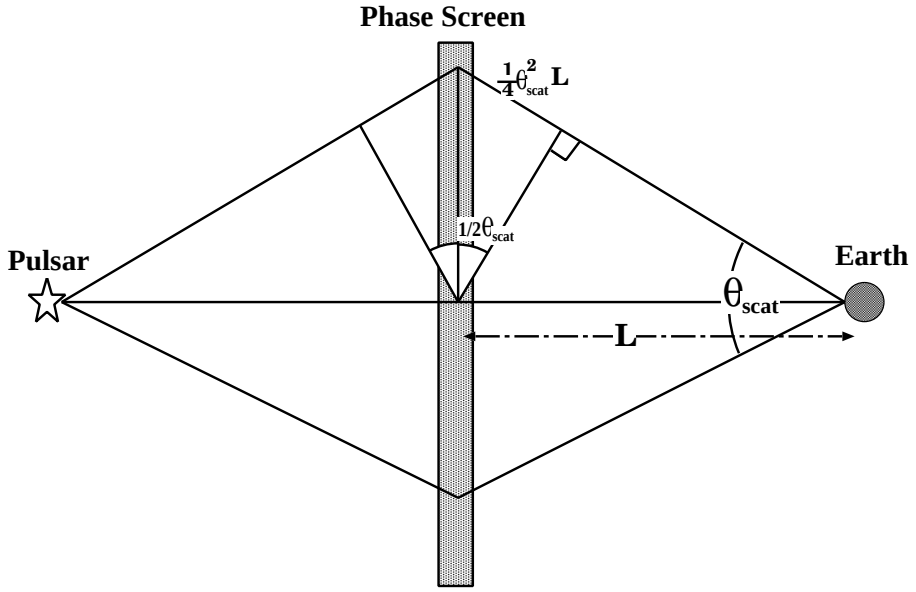

Figure 5.3: Excess ray path of interstellar scattering

variation of observed signal. The velocity of the *scintle*, $V_{\rm sci}$ is governed by three factors:

Motion of the pulsar, $V_{\rm sci(1)} = -\frac{L_s}{L_p - L_s} V_{\rm psr}$;

Motion of the phase screen, $V_{\rm sci(2)} = \frac{L_p}{L_p - L_s} V_{\rm scr}$;

Motion of the Earth, $V_{\rm sci(3)} = -V_{\rm Erth}$;

Here, L_p and L_s are the distance to the pulsar and the distance to the screen from observer; $V_{\rm psr}$, $V_{\rm scr}$, and $V_{\rm Erth}$ are velocity of the pulsar, velocity of the screen, and velocity of the Earth. We assume that these motions are in the same plane for simplicity, so the observed velocity of the *scintle* is a summation of these velocities:

$$V_{\rm sci} = \frac{L_s V_{\rm scr} - L_s V_{\rm psr}}{L_p - L_s} - V_{\rm Erth}. \tag{5.7}$$

Then scintillation time scale is expressed by using Equation (5.3) as

$$\tau_s = \frac{S}{V_{\rm sci}} = \frac{\lambda}{2\pi\theta_{\rm scat} V_{\rm sci}} \tag{5.8}$$

$$= (\frac{a}{D})^{1/2} \frac{1}{V_{\rm sci} r_e \Delta N_e \lambda}. \tag{5.9}$$

Equations (5.3), (5.6), and (5.9) indicate the essential features of scintillation, that is, the apparent angular size of the pulsar, $\theta_{\rm scat} \propto \lambda^2$, decorrelation band width, $B_s \propto \lambda^{-4}$, and scintillation time scale, $\tau_s \propto \lambda^1$. Lee and Jokipii (1976) compared models in which sizes of irregularities are concentrated around a single value, being spread only by a Gaussian distribution, and a model of power law distribution. The power law indices of frequency dependence on ISS, in terms of $\theta_{\rm scat}$, B_s, and τ_s computed from two irregularity distribution models, Gaussian and Kolmogorov, are listed in Table 5.1.

Attention to the definition of scintillation bandwidth or decorrelation bandwidth is important for comparison between theory and observation. Several kinds of bandwidth had been proposed such as B defined by half-width at e^{-1} of the spectral correlation, f_ν defined by frequency separation where the autocorrelation falls to 1/2, and so on. Normally the definition of f_ν gives the decorrelation bandwidth. Relations of various scintillation bandwidth is described by Cordes et al. (1985). The time scale τ_s is usually measured as the time lag where the autocorrelation falls to e^{-1}.

Table 5.1: Power-law index of frequency dependencies on ISS.

		Gaussian	Kolmogorov
Scattering angle	$\theta_{\rm scat}$	-2	-2.2
Bandwidth	B_s	+4	+4.4
Time scale	τ_s	+1	+1.2

5.3 ISS in Pulsar VLBI Observation

Examples of ISS features observed in our pulsar VLBI observations on each sources are shown in Figure 5.4 and explained below.

PSR B039+54 ISS of PSR B0329+54 observed in March 1995 experiment in L-band is demonstrated in Figure 5.4(a). The scintillation characteristic is clearly seen with high SNR in dynamic spectrum plot (a-1). The enhanced flux is extended over the channels. The time variation of correlated power is displayed for each channels in the dynamic fringe plot (a-2).

Decorrelation bandwidth B_s and scintillation time scale τ_s were estimated as about 15 MHz and several hundred seconds, respectively. The Figure 5.4(a-3) shows that fringe amplitude is modulated by ISS; however, the fringe phase slope in the frequency domain (group delay) is not affected. The data was processed with the K4 correlator with pulsar gating function (gate width = 15.9 ms).

PSR B0355+54 ISS of PSR B0355+54 observed in March 1995 experiment in L-band is demonstrated in Figure 5.4 (b). Dynamic cross power spectrum (b-1) shows that narrow scintillation pattern are drifting from higher frequency to lower frequency around 1397 MHz. The time scale of the ISS is more clearly seen in the dynamic fringe plot in Figure 5.4(b-2). The scintillation bandwidth is in the order of 1 MHz and the scintillation time scale is around 200 seconds. The data was processed by the K4 correlator with pulsar gating (gate width = 4.9 ms).

PSR B0950+08 ISS of PSR B0950+08 observed in May 1996 experiment in L-band is demonstrated in Figure 5.4 (c). The ISS pattern is not obvious because of lower SNR, although scintillation band width seems to be wider than 43 MHz bandwidth. The correlation processing was done by the K4 correlator with the gating function (gate width = 7.9 ms). The reason for peaks around 1410 MHz and 1430 MHz is not obvious.

PSR B1933+16 ISS of PSR B1933+16 observed in March 1995 experiment in L-band is demonstrated in Figure 5.4 (d). The dynamic cross power spectrum plot (d-1) clearly shows scintillation in both the time and frequency domains. Narrow scintillation bandwidth and short time scintillation pattern implies large electron density irregularity (ΔN_e) or large distance of the phase screen, as it is inferred from formula (5.6) and (5.9). The lower limit of the distance to the pulsar was estimated by HI absorption observation as 3.5 kpc, and adopted distance was 7.9 kpc [*Frail and Weisberg,* 1990]. The observed ISS characteristic in our observation consistent with the far distance. Frequency drifting of the pattern is seen and it is also the feature of the ISS. The decorrelation bandwidth was a few hundreds kilohertz and scintillation time scale was about 100 seconds. The cross power spectrum integrated for 860 seconds in time direction is shown in Figure 5.4(d-3). A few narrow peaks caused by the ISS were also seen within a 2-MHz bandwidth of each channel.

PSR B2021+51 ISS Characteristic of PSR B2021+51 observed in March 1995 are indicated in Figure 5.4(e). In contrast to the two former pulsars, PSR B2021+51 does not show clear ISS feature in the 35-MHz bandwidth. This implies smaller irregularity of electron density in the ISM (ΔN_e) or shorter distance to the pulsar from the observer, as it is inferred from formula (5.6) and (5.9). The distance of this pulsar is estimated as 1.2 kpc. from dispersion measure obtain by pulsar timing observation. Comparing with PSR B0329+54, its distance from the Earth is estimated as 1.4 kpc. Although B0329+54 and B2021+51 are located at almost the same distance from the Earth, ISS characteristic is fairly different. This result suggest that ISM irregularity in the direction to B2021+51 is smaller than that in direction to B0329+54.

3C84 Cross-power-spectrum characteristic of 3C84 observed in March 1995 is indicated in Figure 5.4(f). The figure shows the typical characteristics of the signal from a quasar: flat spectrum in frequency axis and constant amplitude in time axis.

5.4 Discussion

5.4.1 Scattering Disk Size

Equation (5.4) indicates the relation between scattering disk size $\theta_{\rm scat}$ and decorrelation bandwidth B_s, and equation (5.8) shows the relation between $\theta_{\rm scat}$ and scintillation time scale τ_s. The scattering disk size can be estimated from the visibility as a function of UV length for normal radio sources, however, this method was difficult to apply in our observation results owing to two folded reasons. One reason is that the radio flux of a pulsar varies rapidly with time due to the scintillation, as it is shown in Figures 3.1 – 3.4. Then visibility changes not only as a function of UV but also changes randomly with time. The second reason is that only one data of visibilities are taken at one time, since we used only one baseline. Therefore enough samples of visibilities at different UV distances are not taken within the scintillation time scale, in which the radio flax is treated as constant.

The ISS parameters for each pulsars are listed in Table 5.2. Scintillation time scale (τ_s) and decorrelation band width (B_s) are cited from literatures ("Ref." column). And τ_s and B_s are scaled to the values at 1.4 GHz by assuming the Kolmogorov law ($\tau_s \propto f^{1.2}$; $B_s \propto f^{4.4}$). The last two columns are scattering disk size derived from τ_s and B_s by using equations (5.4) and (5.8), respectively.

Our observed dynamic spectra were consistent with the ISS parameters of τ_s and B_s given in the literature. Scattering disk sizes computed from τ_s were smaller than those from B_s. This is because we used pulsar velocity for $V_{\rm sci}$ according to the assumption that the screen is at the middle point between the observer and pulsar ($L_s = 1/2L_p$). The source size is a function of distance to the screen L_p as $\theta'_{\rm scat} = \theta_{\rm scat} L_p/2(L_p - L_s)$. If the screen is quite close to the observer (less than 20 % of distance to the pulsar), the disk size would be more than 3 time larger than current estimation. Although dense ionised medium is sometimes found in supernova remnant located near the pulsar or widely distributed between observer and pulsar. Hence the estimated $\theta_{\rm scat}$ should be appropriate.

The scattering disk sizes may have to be taken into account the error budget of our astrometry results. However the scattering disk sizes were less than 1 mas for most pulsars at 1.4 GHz. Thus, they will not so much affect the final error of the pulsar coordinates.

Table 5.2: ISS Parameters of Pulsars at 1.4 GHz

Pulsar	τ_s (sec.)	B_s (MHz)	Ref.	$\theta^*_{\rm scat}$ (mas)	$\theta^\dagger_{\rm scat}$ (mas)
B0392+54	871	17	a	0.05	0.33
	841	17	b	0.02	0.33
	1206	24	c	0.02	0.28
	700	15	f	0.082	0.35
B0355+54	487	7.9	c	0.16	0.46
	172	4.6	e	0.28	0.61
	200	1	f	0.26	0.13
B0950+08	2647	759	b	0.03	0.17
B1933+16	49	0.07	e	0.34	2.2
	-	-	d	–	0.60‡
	60	0.15	f	0.12	1.5
B2021+51	1920	67.7	c	0.065	0.18
	1154	87	b	0.026	0.16

Notes:
a: Gupta et al., 1994; b: Gupta, 1995; c: Lyne and Smith, 1982; d: Gwinn et al., 1993; e: Cordes, 1986; f: our results.
$*$: θ_{scat} was computed from τ_s, V_{iss}, and distance D by using relation (5.8). When $V_{\rm sci}$ was not available, pulsar velocity computed from proper motion and distance was used.
†: θ_{scat} was computed from B_s and D by using equation (5.4).
‡: Gwinn et al. measured the scattering disk size (15.2 mas) by VLBI at 326 MHz. The disk size was scaled to the value at 1.4 GHz by assuming Kolmogolov's law ($\theta_{\rm scat} \propto f^{-2.2}$).

5.4.2 Does ISS influence Group Delay Determination by Bandwidth Synthesis?

Pulsar VLBI data contains frequency modulation pattern with typical bandwidth. This is a different feature from quasars. Does ISS feature introduce additional error into the group delay measurement in bandwidth synthesis (BWS)?

As shown in Appendix B, BWS is equivalent to weighted least square (LSQ) estimation of phase slope in the frequency domain, where amplitudes are the weights of each frequency channel in the LSQ. Thus, the low amplitude implies only low weight and does not affect the phase slope. A simple simulation of BWS is demonstrated in Figure 5.5. The black solid line corresponds to a flat spectrum, and the green single-dotted line and red dashed line correspond to the cross power spectra with distorted amplitude. The phase of them are not modulated (set to 0) as the same with real pulsar VLBI data, whose cross power spectrum amplitudes are modulated by the ISS but the phases are not modulated (Figure 5.4(a)-(e)). The simple simulation (Figure 5.5) shows that even if there is amplitude modulation in the cross spectrum, the estimated group delay is not affected as long as the phases are not modulated. But it results in degradation of delay resolution through narrowing of effective bandwidth. The effect of amplitude distortion cause narrowing of effective band width and modulation of weight in the LSQ estimation of group delay. And these effects might degrade the group delay measurement accuracy, but these error increases are included in group delay error. Thus, the ISS effect on the group delay is not necessary to be especially taken into account.

5.5 Summary

Interstellar scintillation (ISS) in dynamic cross power spectrum was observed by the Japan-Russia VLBI observations. The decorrelation bandwidth and scintillation time scale obtained from our observation were compared with the other ISS measurements data in literatures. And these parameters of our measurements were almost consistent with others. Scattering disk sizes of PSRs B0329+54, B0355+54, B0950+08, B1933+16, and B2021+51 were computed from the ISS parameters with based on a thin screen model, and they were almost less than 1 mas at 1.4 GHz. These disk sizes are taken into account in the error budget of astrometry results. The effect of the ISS amplitude modulation on the group delay determination in BWS was discussed, and it was made clear that this modulation effect need not be additionally taken into account in the error budget of pulsar coordinates, since it is already included in group delay error as the modulation of weight in our weighted-LSQ estimation of group delay.

If the projected baseline length is larger than the size of *scintle*, the characteristic of ISS observed by VLBI would show new feature. It contains information on the structure or distribution of interstellar free electrons. By using this sort of data, an approach to resolve pulsar emission reason was shown by Gwinn et al. (1997). The size of *scintle* is, however, larger than the baseline in our observation, the scintillation phenomena observed in our VLBI experiments were not so much different from those of single dish observation.

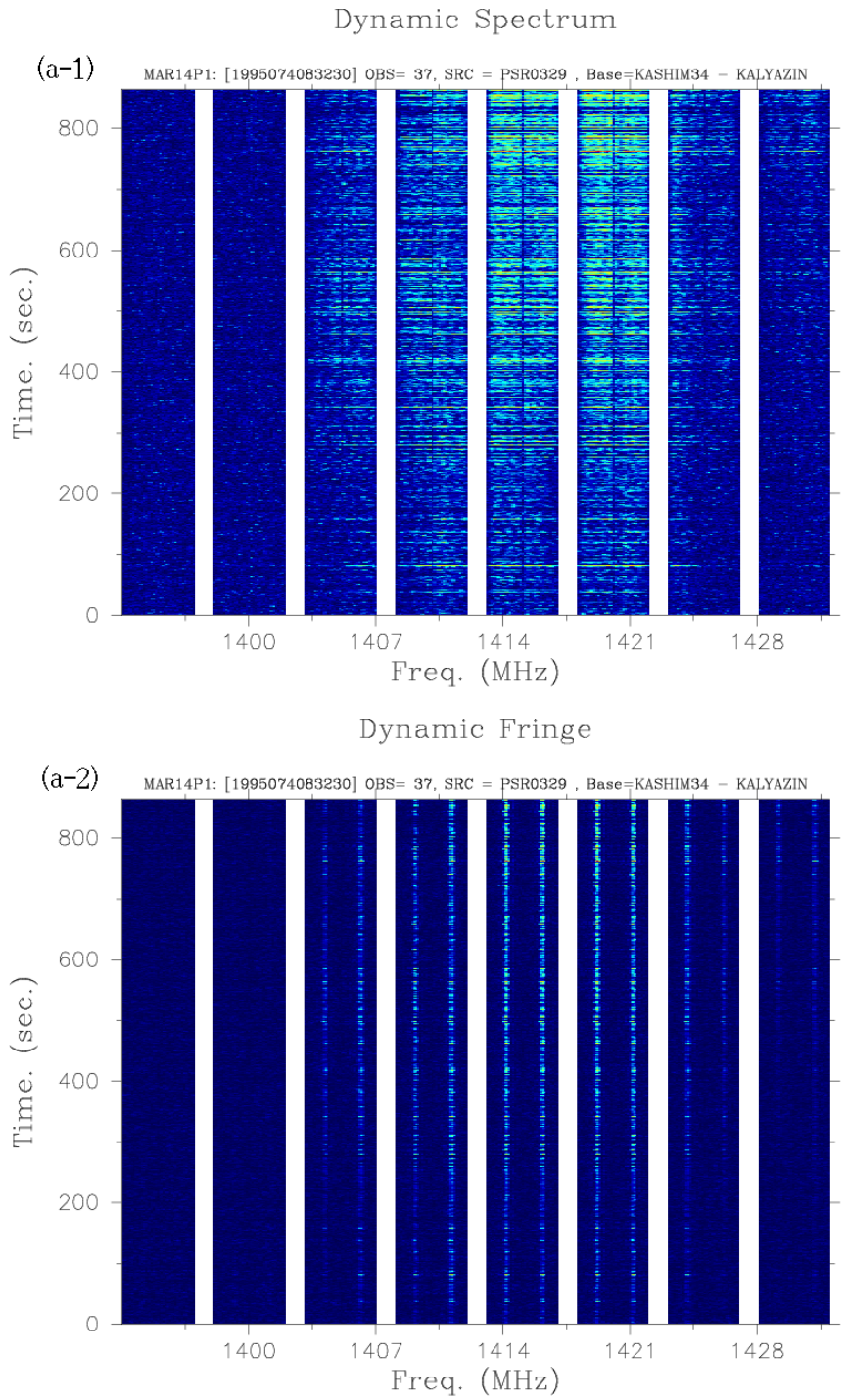

Figure 5.4: (a) ISS feature of PSR B0329+54 observed in March 1995 experiment. (a-1): Dynamic cross power spectra: Integration time was 1 second for each bin. (a-2): Dynamic fringe: Cross spectra were integrated in the frequency direction of each channel and were aligned at the corresponding frequency channels. (a-3): Cross power spectrum integrated for 860 seconds. Correlation processing was done by the K4 correlator with pulsar gating function, where the gate width was 1/45 pulse period.

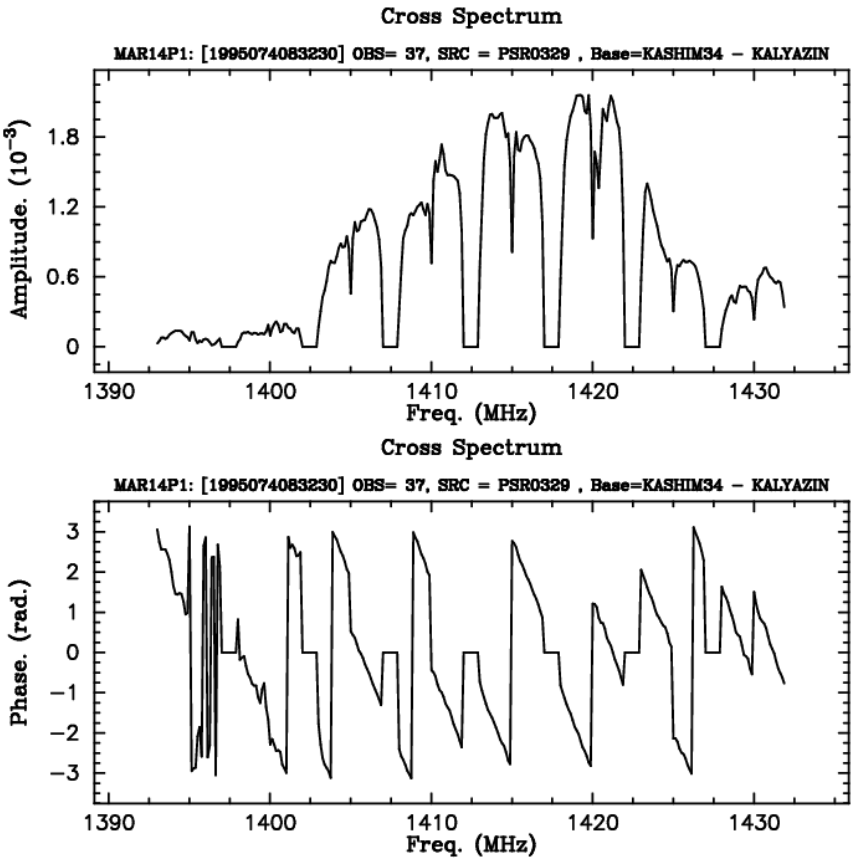

Figure 5.4: (a) ISS feature of PSR B0329+54 (Continued)

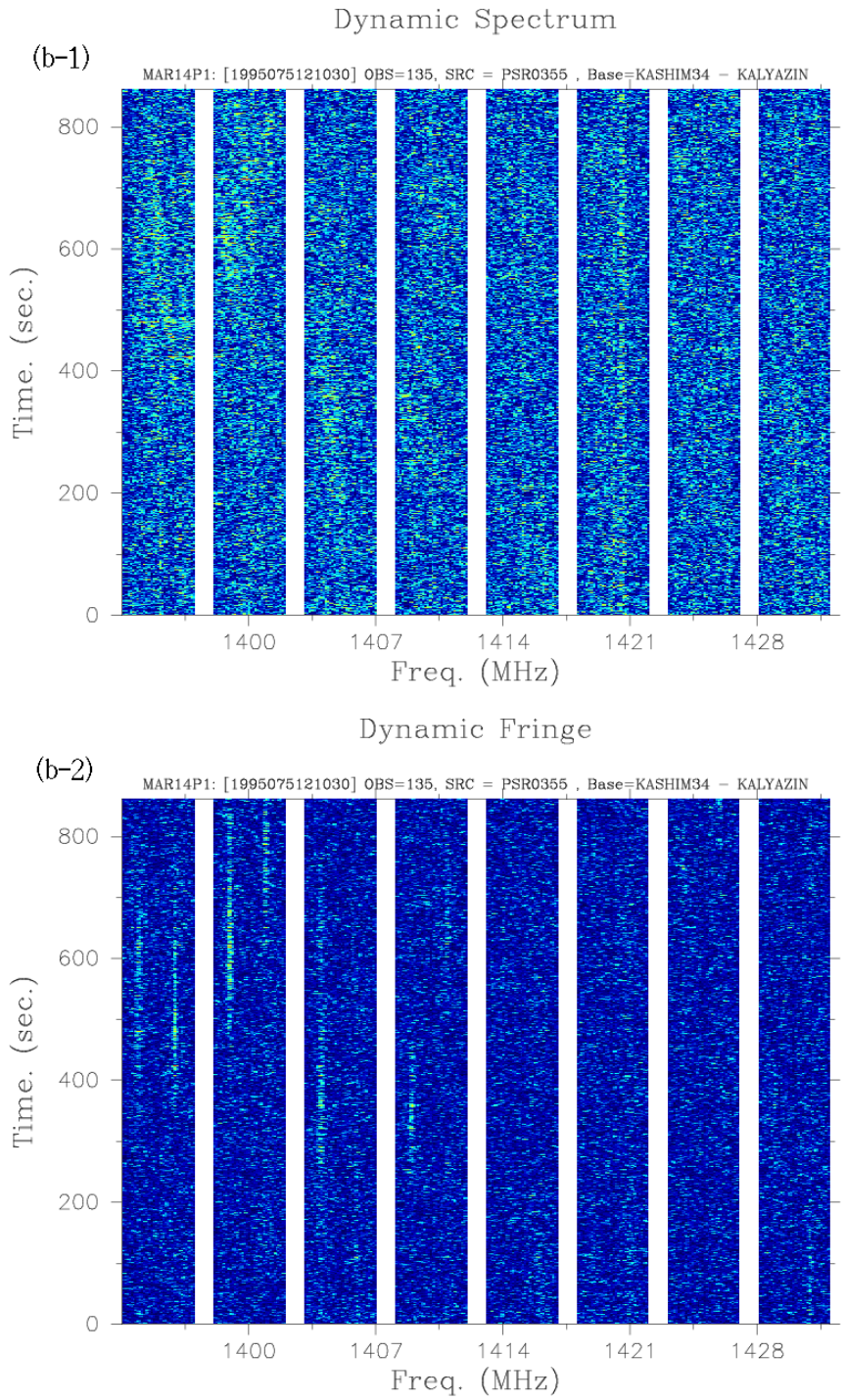

Figure 5.4: (b) ISS feature of PSR B0355+54 observed in March 1995 experiment. (b-1): Dynamic cross power spectra: Integration time was 1 second for each bin. (b-2): Dynamic fringe: Cross spectra were integrated in the frequency direction for each channel and were aligned at corresponding frequency channels. (b-3): Cross power spectrum integrated for 860 seconds. Correlation processing was done by the K4 correlator with the pulsar gating function, where gate width was 1/32 pulse period.

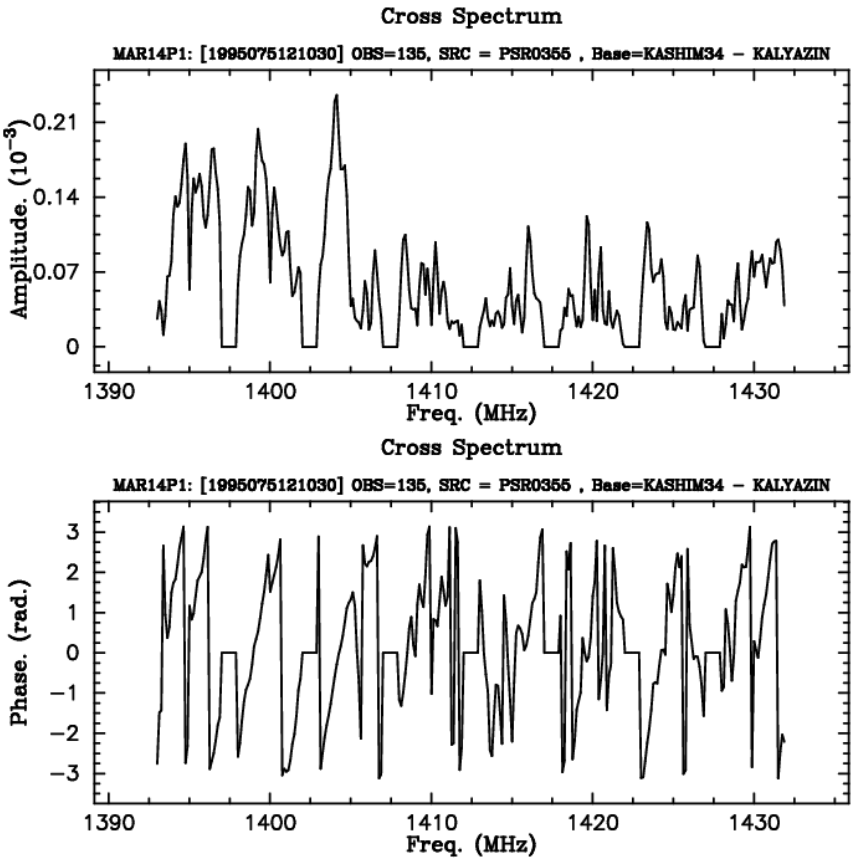

Figure 5.4: (b) ISS feature of PSR B0355+54 (Continued)

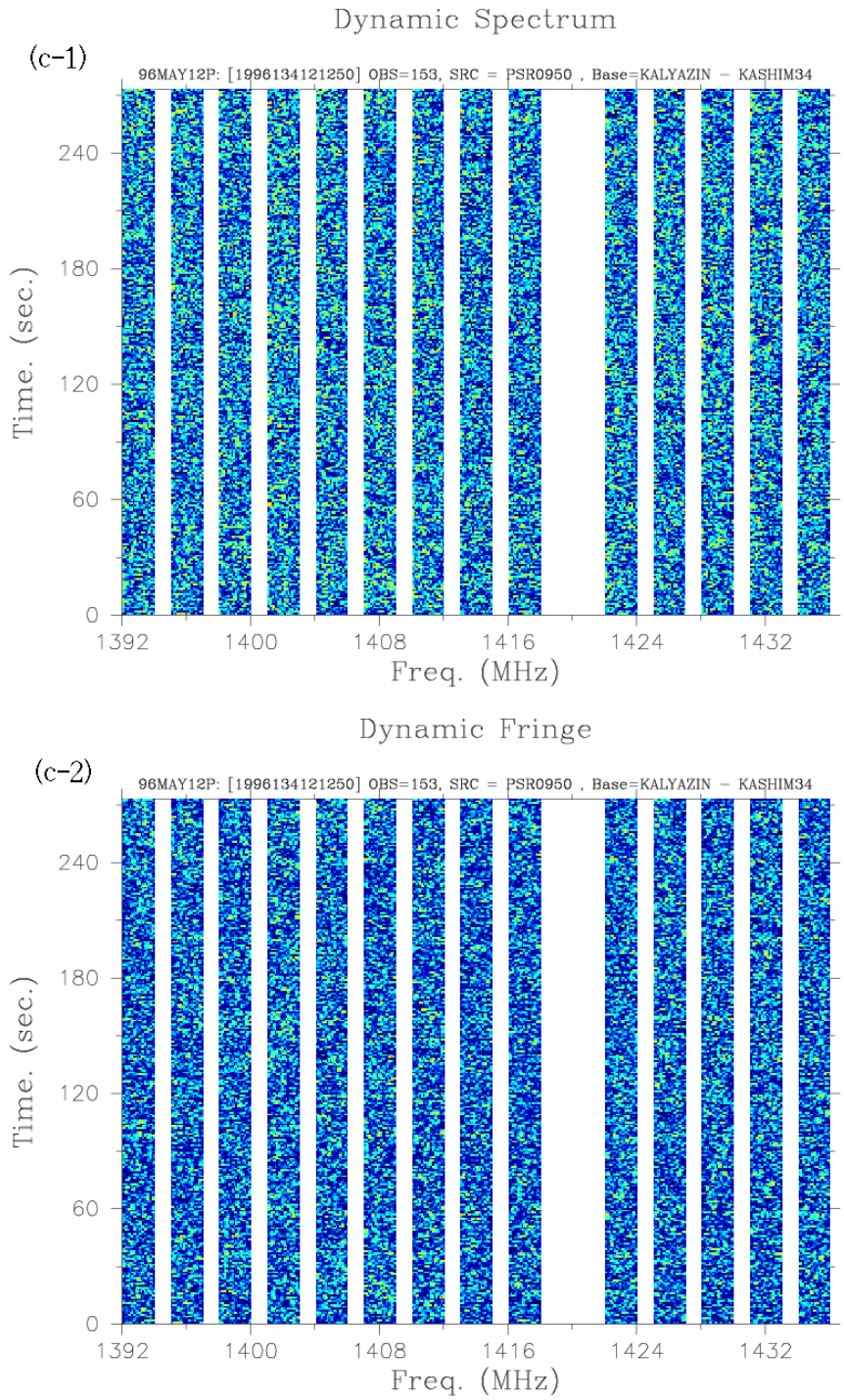

Figure 5.4: (c) ISS feature of PSR B0950+08 observed in May 1996 experiment. (c-1): Dynamic cross power spectra: Integration time was 1 second for each bin. (c-2): Dynamic fringe: Cross spectra were integrated in the frequency direction for each channel and were aligned at corresponding frequency channels. (c-3): Cross power spectrum integrated for 860 seconds. Correlation processing was done with the pulsar gating function of the K4 correlator,where the gate width was 1/32 pulse period.

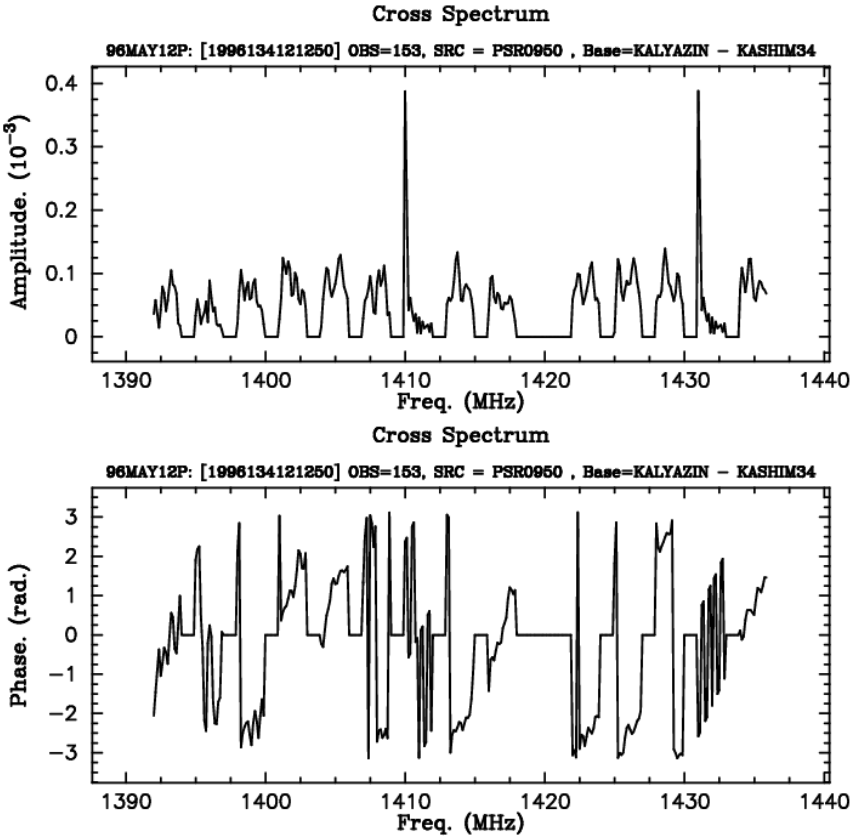

Figure 5.4: (c) ISS feature of PSR B0950+08 (continued)

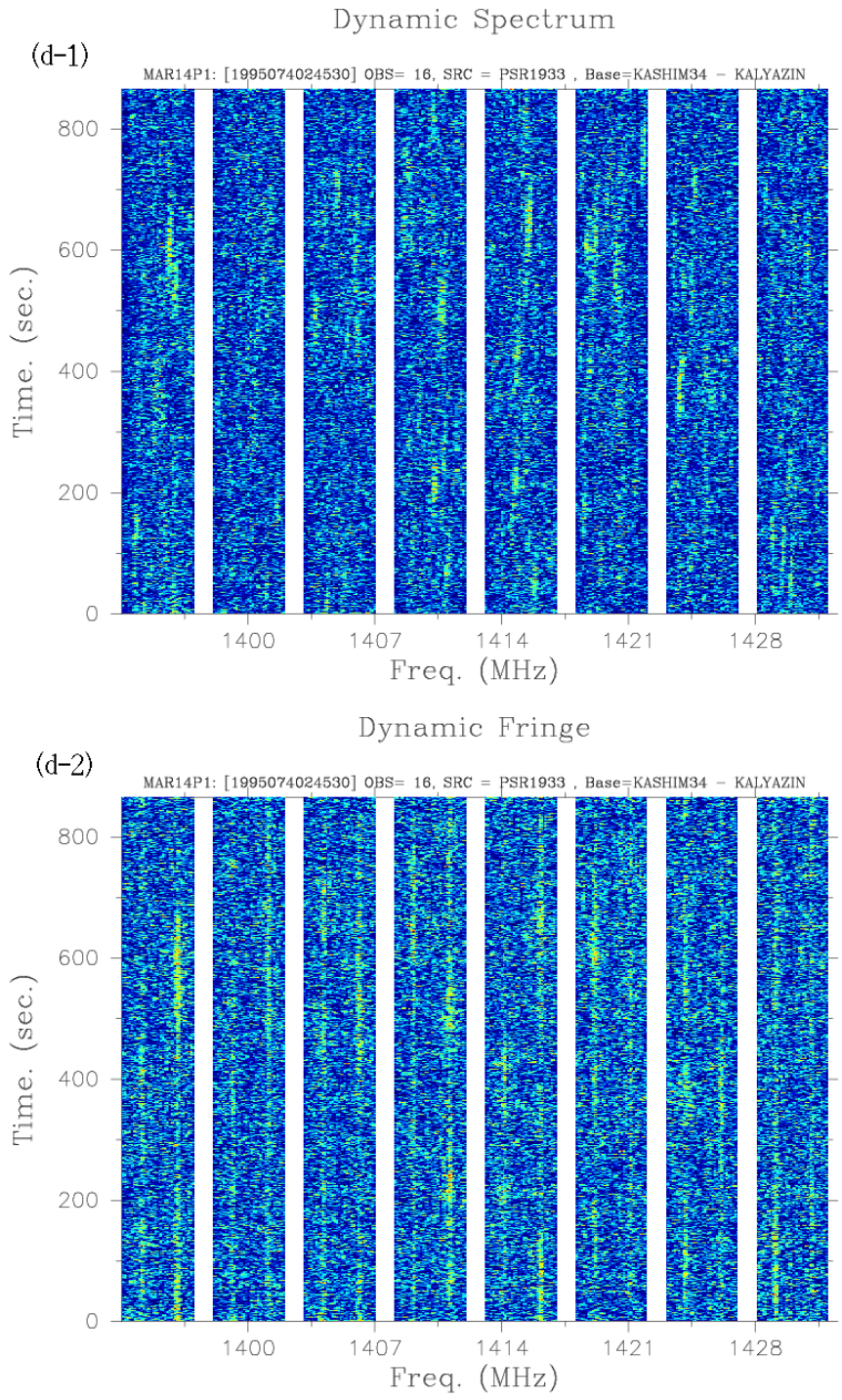

Figure 5.4: (d) ISS feature of PSR B1933+16 observed in March 1995 experiment. (d-1): Dynamic cross power spectra: Integration time was 1 second for each bin. (d-2): Dynamic fringe: Cross spectra were integrated in the frequency direction for each channel and were aligned at corresponding frequency channels. (d-3): Cross power spectrum integrated for 860 seconds. Correlation processing was done by the K4 correlator with the pulsar gating function, where the gate width was 1/40 pulse period.

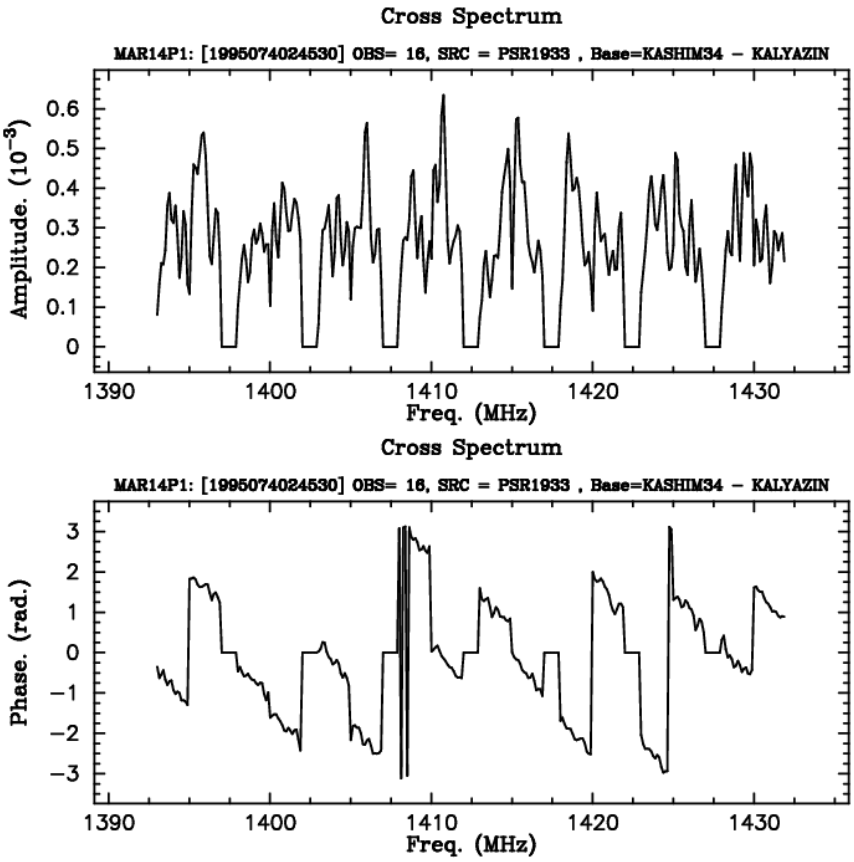

Figure 5.4: (d) ISS feature of PSR B1933+16 (continued)

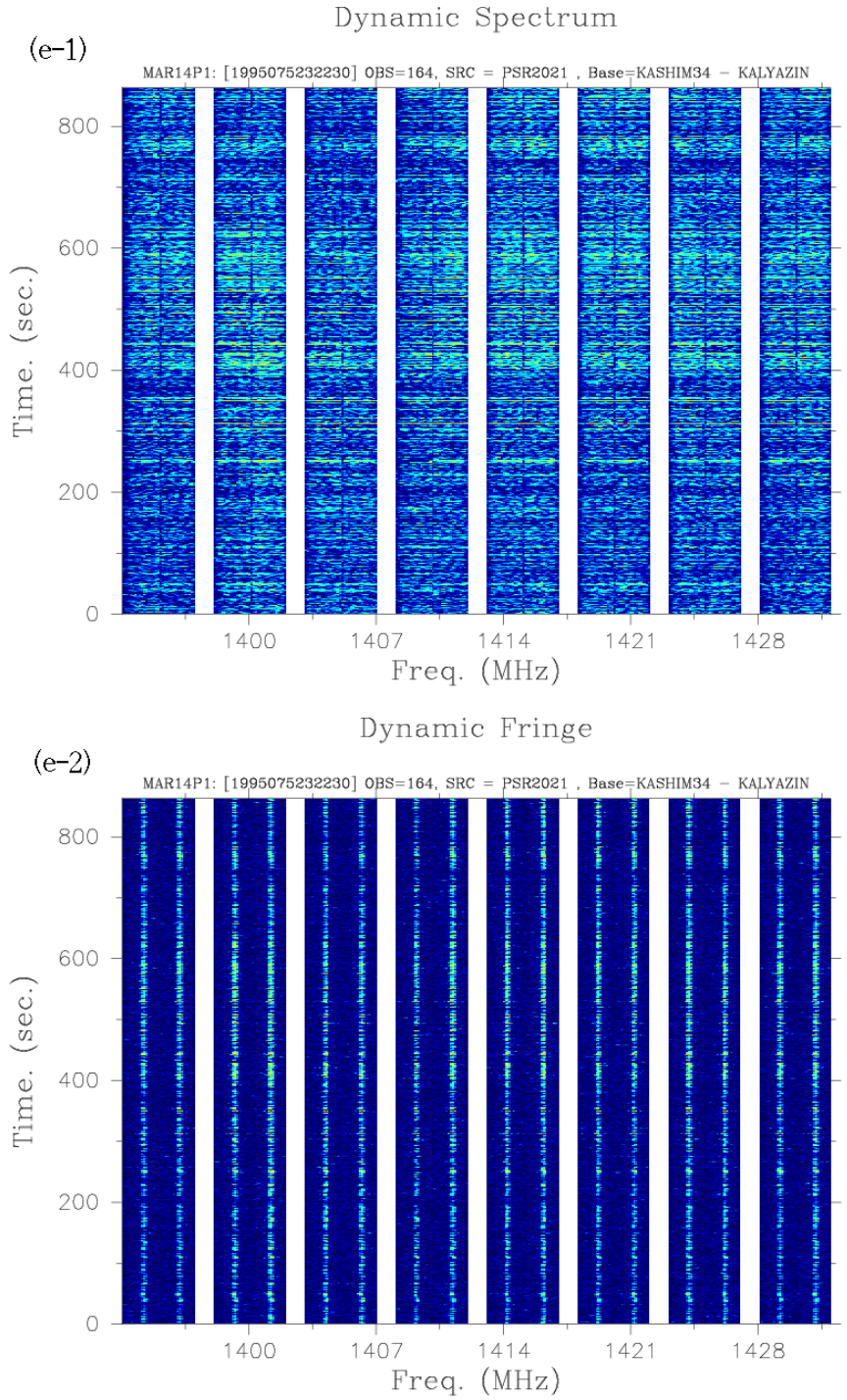

Figure 5.4: (e) ISS feature of PSR B2021+51 observed in March 1995 experiment. (e-1): Dynamic cross power spectra: Integration time was 1 second for each bin. (e-2): Dynamic fringe: Cross spectra were integrated in frequency direction for each channel and were aligned at corresponding frequency channels. (e-3): Cross power spectrum integrated for 860 seconds. Correlation processing was done by the K4 correlator with the pulsar gating function, where the gate width was 1/40 pulse period.

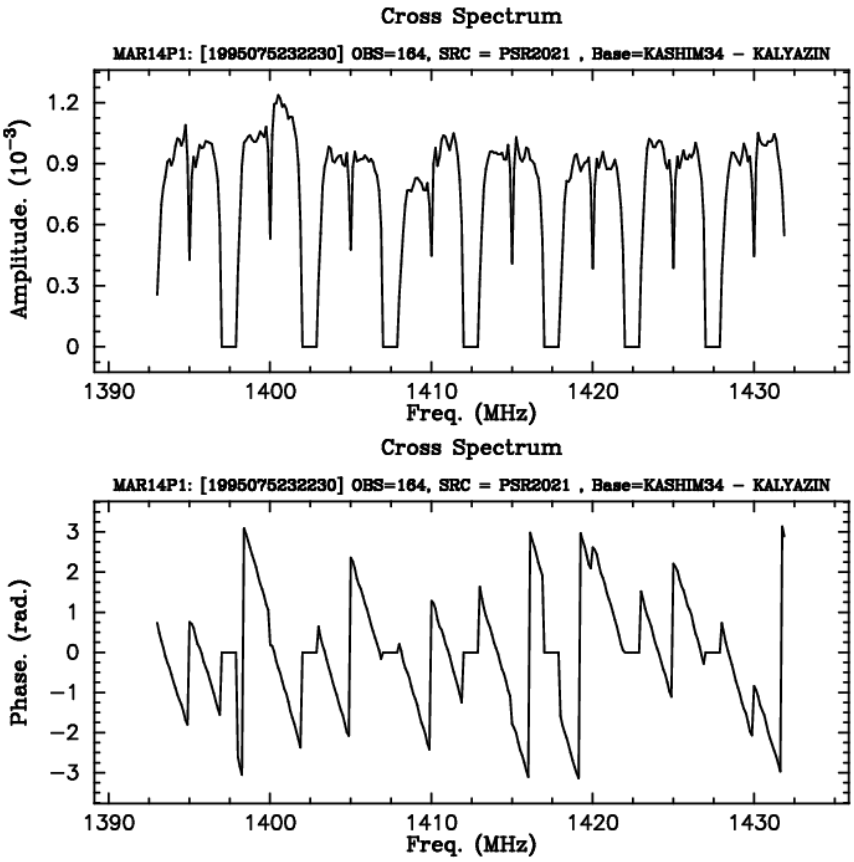

Figure 5.4: (e) ISS feature of PSR B2021+51 (continued)

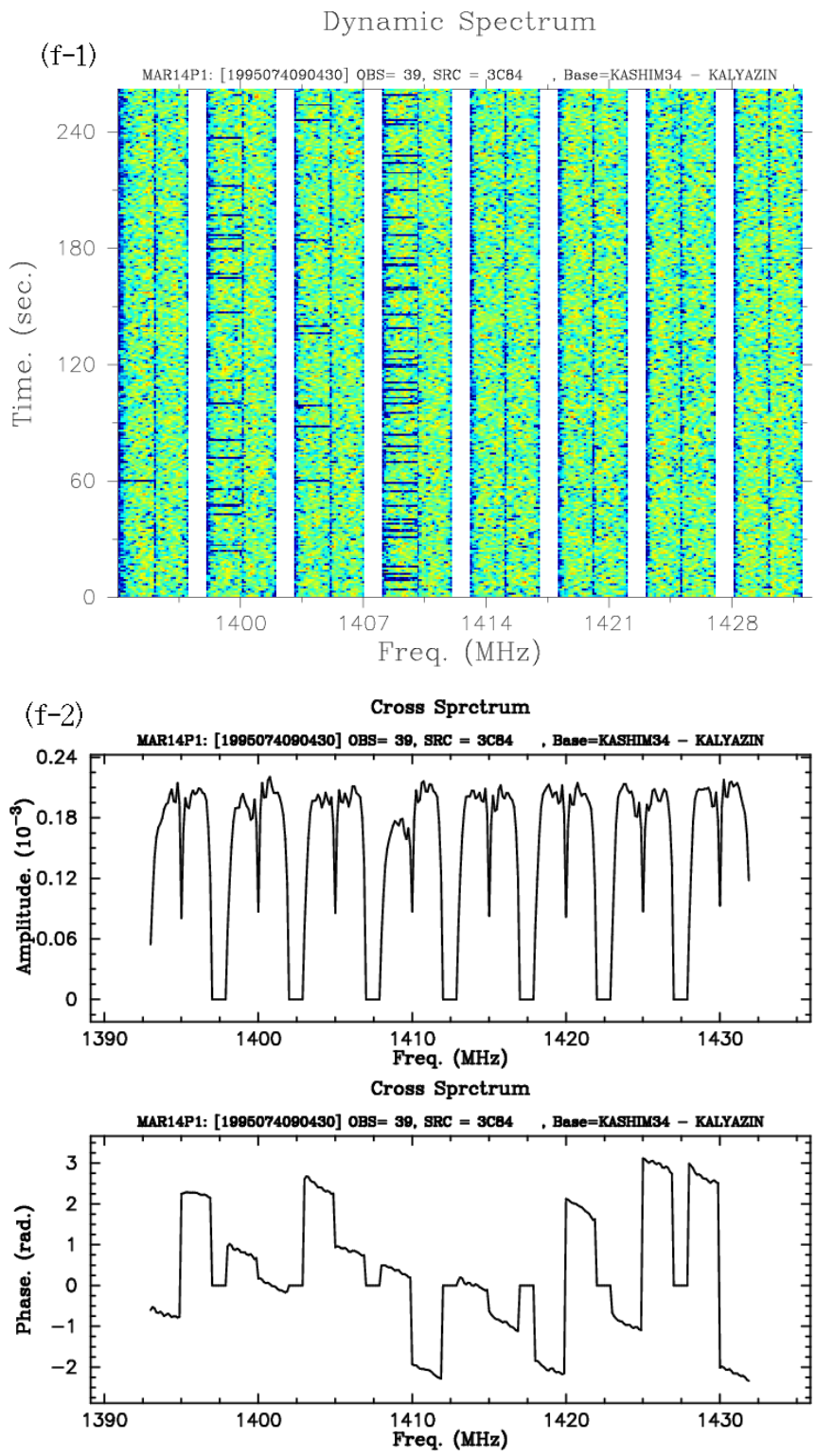

Figure 5.4: (f) Cross power spectrum of 3C84 is displayed to show the contrast between ISS phenomena in pulsar VLBI data and quasar's data without ISS . This data was observed in the March 1995 experiment. (f-1): Dynamic cross power spectrum. (f-2): Cross power spectrum integration for 262 seconds. The intensity was very flat over the frequency band and ISS feature was not seen.

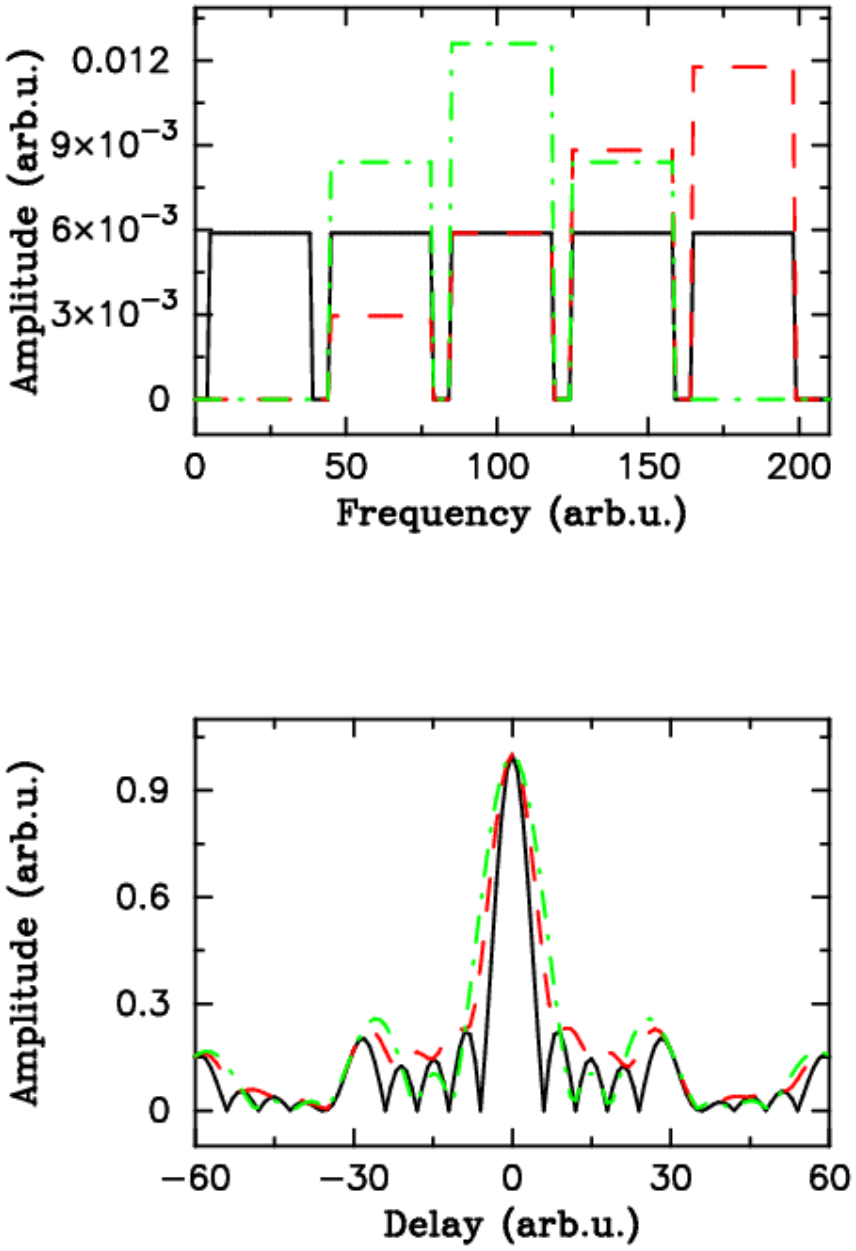

Figure 5.5: A simple simulation of bandwidth synthesis with modulated amplitude. The upper panel shows cross power spectrum in the frequency domain. Black solid line indicates uniform amplitude distribution. Red dashed line indicates spectrum biased at higher frequency, and green single-dotted line corresponds to a spectrum biased at the center of band. Phase of each frequency components are zero for all cases. The lower panel indicates synthesized delay resolution function computed from the spectra in the upper panel. The difference of the spectrum amplitude modulation results in broadening of delay resolution function. The units of the axes in both upper and lower panels are arbitrary unit.

Chapter 6

Pulsar VLBI Astrometry

6.1 Introduction

VLBI is the most precise method for measuring radio source positions. VLBI observations of pulsars determine their coordinates in the ICRF (International Celestial Reference Frame), which is defined by VLBI observations of extragalactic objects [*Ma et al.,* 1998]. On the other hand, a pulsar timing observation determines a pulsar's coordinates in a dynamical reference frame (e.g., DE200, and DE405), which is based on the planetary orbit. Especially for millisecond pulsars, a timing position accuracy of 30–60 μ arc sec has been achieved (e.g., *Kaspi et al.,* 1994; *Cognard et al.,* 1995a). Thus, a pulsar is a very important object for a frame tie between the quasar reference frame and a dynamical reference frame (e.g. *Dewey et al.,* 1996; *Bartel et al.,* 1996).

Astrometric parameters are also important for investigation of pulsars. Proper-motion measurements of pulsars will help us to understand the association between pulsars and their progenitors–super nova remnants. Nice and Taylor (1995) reported that an proper motion affects the derived value of the intrinsic pulsar spin-down rate, $\dot{P}_{\rm int}$. If the proper motion is wrong, it will cause an incorrect estimation of the characteristic age of a pulsar. Thus, a pulsar timing observation requires independent measurements of the astrometric parameters.

The Communications Research Laboratory (CRL) in Japan and the Pushchino Radio Astronomy Observatory (PRAO) of the Lebedev Physical Institute in Russia started joint VLBI observations of pulsars in 1995. Our purposes were two-fold. One was to obtain astrometric parameters of pulsars by using the interferometric method. The other was to contribute to the frame tie between the extra-galactic reference frame measured by VLBI and the dynamical reference frame of ephemeris.

6.2 VLBI Observations

VLBI observations were performed from March 1995 to May 1998. The individual VLBI experiments and observed pulsars are listed in Table 2.3. Generally, because pulsars have rather large spectral index (typically -2 – -3) their flux density decreases rapidly as the frequency increases. A lower frequency observation is preferable for a higher signal-to-noise ratio, although the radio-wave propagation delay through the Earth's ionosphere becomes the most significant error source at lower frequency. Because the magnitude of the ionospheric delay is inversely proportional to the square of the radio frequency, a higher frequency observation is superior from the viewpoints of smaller ionospheric disturbances and higher angular resolution. The frequency band of 1.4 GHz (L-band) was chosen to compromise these two restrictions. However, radio interference caused by mobile communication becomes severer day by day especially at 1.5 GHz. Thus, we changed the observation frequency to 2.2 GHz (S-band) since May 1998 experiments.

6.2.1 March 1995 Experiment

The first VLBI experiment was carried out on March 14 1995. The observation frequency range was 1395–1425 MHz. The signal in radio frequency was converted to sixteen channels of signal at video frequency region, and sampled by a VLBI sampler with 1 bit quantization. Eight video channels were upper side band (USB) signal and the same number of other video channels were lower side band (LSB) signals. The total 16 video channels were allocated with 5 MHz frequency intervals in the radio frequency band. The sampled data were recorded with the K4 VLBI data acquisition system (K-4 DAS) (Kiuchi et al., 1993; *Kiuchi et al.,* 1997). Extragalactic radio sources, which were chosen from the IERS catalogue (ICRF92), and target pulsar were observed alternatively. Since the coordinates of sources in the IERS catalogue have been determined accurately by intercontinental geodetic and astrometric VLBI observations, they are suitable for the calibrating atmospheric and clock parameters in VLBI data analysis. The pulsars detected in this experiment are as follows:

B0329+54: The radio sources 0300+470, 0316+413 (3C 84), and 0355+508 (NRAO 150) are not so far from PSR B0329+54 and they are appropriate as reference sources for that pulsar. The angular distances from the pulsar were 8.6, 13.2, and 5.5 degrees for 0300+470, 3C 84, and NRAO 150, respectively. Two observation sessions were carried out, one during 4:40–8:40 and the other during 11:45–14:13 on 74 DOY (day of the year) in UT, and the total observation time was 6.5 hours. The radio source NRAO 150 was not detected in this experiment.

B0355+54: This pulsar was observed during 10:10–12:45 on 75 DOY (UT). The same reference sources with PSR B0329+54 were used.

B1933+16: This pulsar was observed during 01:50–04:20 on 74 DOY for about 2.5 hours with reference sources 1923+210, 1929+226, 1932+204, and 1934+207. However, fringes were not detected for 1932+204 and 1934+207. Thus 1929+226, 1923+210, and reference sources for the other pulsars were used for clock parameters and atmospheric delay estimation.

B2021+51: This pulsar was observed during 20:50–23:30 on 75 DOY (UT). 2022+542 and ICRF source 2037+511 were observed as nearby reference sources.

The observation cycle was 15 minutes for the pulsar and 5 min for the reference sources.

6.2.2 April 1995 Experiment

This experiment was conducted to survey the detectability of pulsars by using our baseline. Observation frequency was the same as the March experiment and the K-4 DAS was used for VLBI observation. Strong interference from mobile communications affected the observation and sometimes it caused trouble in the correlation process. The K-4 DAS uses a time stamp and a synchronization code for reproducing the observation time code and for synchronized playing back of magnetic tapes for correlation processing. Strong interference sometimes causes saturation in the back-end system, occasionally making all observed bits "high". Since sync code "FFFF" is used to recognise the beginning of time stamp data, all "high" bits caused by interference are mis-read by the play-back system. One simple solution to avoid this kind of trouble is terminating the 16th channel input port of the K4 VLBI input interface (DFC-1100) by using a 50-Ohms load.

In spite of the loss of the data, some pulsars were detected without gating function in correlation process. The Table 6.1 lists the pulsars detected in the April 1995 experiment. Correlated flux computed from the SNR and system sensitivity was almost consistent with flux of pulsars listed in Table 2.4.

Table 6.1: SNR of pulsars detected in the April 1995 experiment after correlation processing without the gating function and BWS processing. The integration time was about 500 seconds and integrated bandwidth was 14 MHz. Flux S in the fourth column is the correlated flux computed from correlation amplitude and equation (2.2).

PSR Bname	SNR	Correlation ρ (10^{-4})	Flux S (mJy)
B1929+10	15.4	2.3	34
B2020+28	12.9	1.7	25
B0950+08	44.5	5.6	82
B0809+74	7.9	0.93	13

6.2.3 May 1996 Experiment

The observation frequency range was 1392–1436 MHz except for the 1418–1421 MHz range, to minimize influence of radio interference. Fourteen channels of USB signals with 2 MHz bandwidth were arranged at 3-MHz frequency intervals. And these signals were sampled and recorded with the K4 VLBI system.

B0329+54: This pulsar was observed between 18:00 – 22:00 on 133 DOY, 23:00 on 133 DOY – 04:00 on 134 DOY , and 05:00 – 11:00 on 134 DOY in UT. The total observation time was about 15 hours. The reference sources were also principally chosen from the IERS catalogue for the same reason as described in subsection 6.2.1. Reference sources for B0329+54 are listed in Table 6.2. In addition to the former reference sources, 0333+321 (NRAO 140), 0429+415 (3C119), and 0518+165 (3C138) are added. The pulsar and a few reference sources were observed alternatively, and the duration of the observation time was 5 min. for PSR B0329+54 and 4 min. for the reference sources.

B0950+08: This pulsar was observed from 12:10 to 13:22 of 134 DOY in UT for about one hour. 1003+351 (3C236), 0923+392 (4C39.25), and 0954+556 (4C55.17) were observed as nearby reference sources.

6.2.4 May 1997 Experiment

B2111+46: This pulsar was selected as a target for two several reasons: it was a high latitude source and its proper motions had not been measured. We observed this source for rather a long time and expected to get fringes, but the observations were not successful.

B0329+54: This pulsar was observed from 3:37 to 07:20 of 144 DOY in UT for about three hours 40 min. The reference sources are listed in Table 6.2. Observation frequency was set at the same as that of the May 1996 Experiment.

6.2.5 May 1998 Experiment

To avoid radio interference, we changed the observation frequency to the S-band in spite of the lower flux density. The observation frequency channels were allocated in the range of 2199.99–2286.99 MHz with a 5-MHz spacing. Fifteen channels of the K-4 DAS were used for data acquisition and the 16th channel of DFC-1100 was terminated to avoid the time-code problem as described in sections 6.2.2 and 2.2.2. Pulsars observed in this experiment were as follows:

Table 6.2: Pulsars (B0329+54, B0355+46, B0950+08, and B1933+16) and their reference sources observed in the experiments. Angular distances between pulsars and reference sources and number of scans used for least square analysis are listed. The numbers in the column for each experiment indicate numbers of scans used for analysis / total number of scans.

Source name	1995 Mar.	1996 May	1997 May	1998 May	Angular distance (deg.)	ICRF remarks(1)	Structure Index (S)(2)
0133+476	-	13/13	-	16/16	19.2	D	2
0212+735	-	18/18	-	21/22	20.7	O	2
0300+470	6/6	20/25	6/6	29/30	8.6	O	1
3C 84	8/8	13/13	-	18/19	13.2	O	-
NRAO 140	-	8/8	-	3/3	22.3	O	-
NRAO 150	0/11	-	-	-	5.4	O	-
3C 119	-	12/13	-	1/1	16.3	-	-
3C 138	-	8/8	-	-	43.3	D	4
B0355+54	5/5	-	-	-	3.8	-	-
B0329+54	14/14	26/33	8/8	39/45	0.0	-	-
3C245	-	-	-	11/11	12.9	D	-
OK290	-	-	-	0/5	17.3	O	1
4C39.25	-	4/4	-	6/6	31.7	D	-
B0950+08	-	4/4	-	11/11	0.0	-	-
1923+210	3/7	-	-	-	5.4	C	-
1929+226	2/2	-	-	-	6.5	C	1
1932+204	0/5	-	-	-	4.3	C	1
1934+207	0/2	-	-	-	4.6	-	-
B1933+16	6/6	-	-	-	0.0	C	-
2022+542	2/2	-	-	-	2.6	-	-
2037+511	2/2	-	-	-	2.5	D	-
B2021+51	6/6	-	-	-	-	-	-

(1) Character indicating category of extragalactic source in ICRF catalogue. D indicates it is a defining source of the ICRF, O indicate that they failed to clear some criteria as a defining source, but they are still useful for frame tie or for the other astrometric purposes [*Ma et al.,* 1998].
(2) Source structure index of S-band is cited from C. Ma et al.(1998). The index 1 implies very good source for reference frame and 4 implies extended source and not so good for astrometric purposes.

B0392+54: This pulsar was observed from 17:57 to 21:00 of 145 DOY, and from 22:00 of 154 DOY to 09:40 of 146 DOY. The total observation time was 14 hours 40 min. The reference sources are basically the same as the May 1996 experiment as listed in Table 6.2

B0950+08: This pulsar was observed from 10:10 of 145 DOY to 13:28 for three hours 18 min. ICRF sources 1040+123 (3C245), 0923+392 (4C39.25), and 0953+254 (OK290) were used as reference sources.

6.3 VLBI Data Analysis for Astrometry

6.3.1 Data Processing

Correlation processing was performed by using the KSP correlator [*Kiuchi et al.*, 1999] at Headquarter of CRL and the K-4 correlator at the Kashima Space Research Center. The group delay and the phase delay rate were derived by using the bandwidth synthesis software "KOMB" [*Takahashi et al.,* 1991; *Takahashi et al.,* 2000]. The data were stored together with ground

weather data in the Mark-III database. The data reduction procedure is described in Chapter 3. For details of the K4 correlator, refer to Chapter 7.

6.3.2 Least Square Estimation of Pulsar Coordinates

Precise VLBI delay model calculation and least square analysis were done by CALC and SOLVE software packages developed by the GSFC/NASA. The CALC ver. 8 was used to calculate the delay model for VLBI data in the Mark-III database system and SOLVE 5.25 was used for least square estimation of pulsar coordinates.

The Earth orientation parameters (EOPs) are very important for absolute astrometry, since the orientation of the VLBI baseline fixed on the Earth is connected to the celestial reference frame by these parameters. Thus, the final solution of EOP values and celestial pole offset (CPO) provided by the IERS Earth Orientation Center (http://hpiers.obspm.fr/eop-pc/) (Bulletin-B) were used in the analysis.

Weighted-least square analysis was carried out with the software SOLVE. Absolute source position estimation from the group delay and phase delay rate was performed in the same way as in the geodetic VLBI measurement.

Since the ICRF source's positions used in the experiments were determined very accurately (the accuracy is usually no more than 1 mas), they were useful for calibrating the interferometer parameters, such as the clock parameters and atmospheric parameters. In general, the clock offset and rate must be calibrated with reference sources in VLBI analysis, because time-synchronization or time comparison between UTC and a local time standard is not enough. The accuracy of the time differences between UTC (GPS time) and the local atomic standard clock at each station is typically sub-micro seconds, where the delay measurement precision in VLBI is from a few nanoseconds to several tens of picoseconds. Calibration of the clock offsets, clock rates, and atmospheric delays were performed by using reference sources.

6.3.3 Ionospheric Delay Correction

Ionospheric Delay Correction with GIM/CODE data

Excess delay caused by the Earth's ionosphere is the most significant error source in our experiment (Figure 3.5), so the author developed a technique to use GPS-based ionosphere data for VLBI ionospheric delay correction (hereafter referred to as ion-correction). The accuracy of GPS-based TEC measurements was examined in Chapter 4. This technique was applied to the pulsar astrometry described in this Chapter. Ionosphere TEC calculation software CODTEC was developed. A brief overview of the ion-correction is given as follows. The CODTEC software calculates the TEC value in the lines of sight to the radio source from two VLBI observation stations at every epoch (PRT) of VLBI scans, and the TEC difference between the two VLBI stations is output. Then the obtained TEC value of each scan is converted to excess delay at a specified observation radio frequency and stored in the Mark-III database. This ion-correction data are used in astrometric analysis with the SOLVE.

Test of ion-Correction and Additional Error

To make sure the ion-correction really improves the accuracy of source coordinates estimation in single band VLBI analysis, we tested it. The test was performed by estimating the reference source position (hereafter referred to as the 'test source'), whose position is known. Enough number of other reference sources should be remain in the VLBI data except for the test source, because they are necessary to calibrate interferometer parameters such as clock and atmospheric parameters. Then the May 1996 experiment was used for the test. Two ICRF sources, 0133+476 and 0212+735, were used as the test source, alternatively.

Cold plasma such as Earth ionosphere and interstellar medium has dispersive characteristic, that affect electromagnetic wave propagation delay in the opposite sense for group delay and phase delay. In other words, phase delay is negative whereas group delay is positive. Observables of VLBI observation were group delay and phase delay rate. so if the ionospheric dispersive delays are not appropriately compensated, the two observable, group delay and phase delay rate , will conflict and cause an increase of residual. We took two sorts of combination of observables, group delay only (D) and group delay + phase delay rate (DR), in the LSQ analysis with SOLVE, since discrepancy between the two solutions becomes an indicator of the ion-correction. Thus two cases of analyses, D and DR, were applied to VLBI data with ionospheric delay correction (Cion) and that without the correction (Nion). Therefore, total four cases of analyses (Cion-DR, Cion-D, Nion-DR, and Nion-D) were examined to see how the GPS-based TEC data could fix the ionospheric excess delay error.

Figure 6.1 shows the estimated coordinates of the two test sources. In both cases, the solutions of Cion-D and Cion-DR are almost identical and close to the true position (origin of the coordinates). On the contrary, the solutions of Nion-D and Nion-DR differ each other and they have offset from the true position. These results shows that GPS-based ion-correction successfully removes the large offsets from estimated coordinates of radio sources.

Estimated position of 0133+476 coincides with true position within error of one σ. 0133+476 is 'definition source' of the ICRF and its position is determined more than 0.1 mas accuracy by X-band. Estimated position of 0212+735 shifted from catalog position by more than one σ, however. 0212+735 is categorised as 'other source' in the ICRF catalog and it has double peak structure in S-band. A possible reasons for the deviation of 0212+735's position from the ICRF catalog coordinates are the difference of source structure, thus difference of source mean position between X-band and L-band and imperfectness of the GPS-based ion-correction. Generally, the source structure and source position as mean point of source structure are different between X-band and L-band. And double peak structure of 0212+735 in S-band is known [Fey et al., 1996; http://rorf.usno.navy.mil/rrfid.shtml] and these two peaks are separated by about 10 mas. This angular distance of double peak structure is not enough to explain the about 40 mas deviation from the true coordinates, although, the source structure in L-band might more largely extended.

As a conclusion of the test, it was shown that ion-correction by using GPS-based TEC map is useful to remove the most part of systematic error caused by ionospheric excess delay. However, the precision of astrometry may be limited to several mas level by the error introduced by the ion-correction.

Comparison of ionospheric Delay Effect on PSR B0329+54's Coordinates

Since PSR B0329+54 was observed four epochs, it is good for testing the repeatability of our measurements and for examining the effect of the ion-correction. The pulsar's coordinates were estimated in two cases of combination of observables, with group delay only (D) and with both group delay and phase delay rate (DR), because the difference of solutions between D and DR will be good indicator how much ionospheric excess delays are remain in the observables. Analyses were performed with VLBI data with ion-correction (Cion) and without ion-correction (Noion), thus, total four solutions of pulsar coordinates were obtained.

The coordinates solutions and formal errors of B0329+54 are shown in Figure 6.2. This figure shows that the solutions by ion-correction (Cion) have smaller error than those without correction (Noion). And discrepancy of solutions between the D and DR is smaller in the case of Cion. This result indicates the inconsistency between group delay and phase delay rates was reduced by the ion-correction by using the GPS-based TEC data.

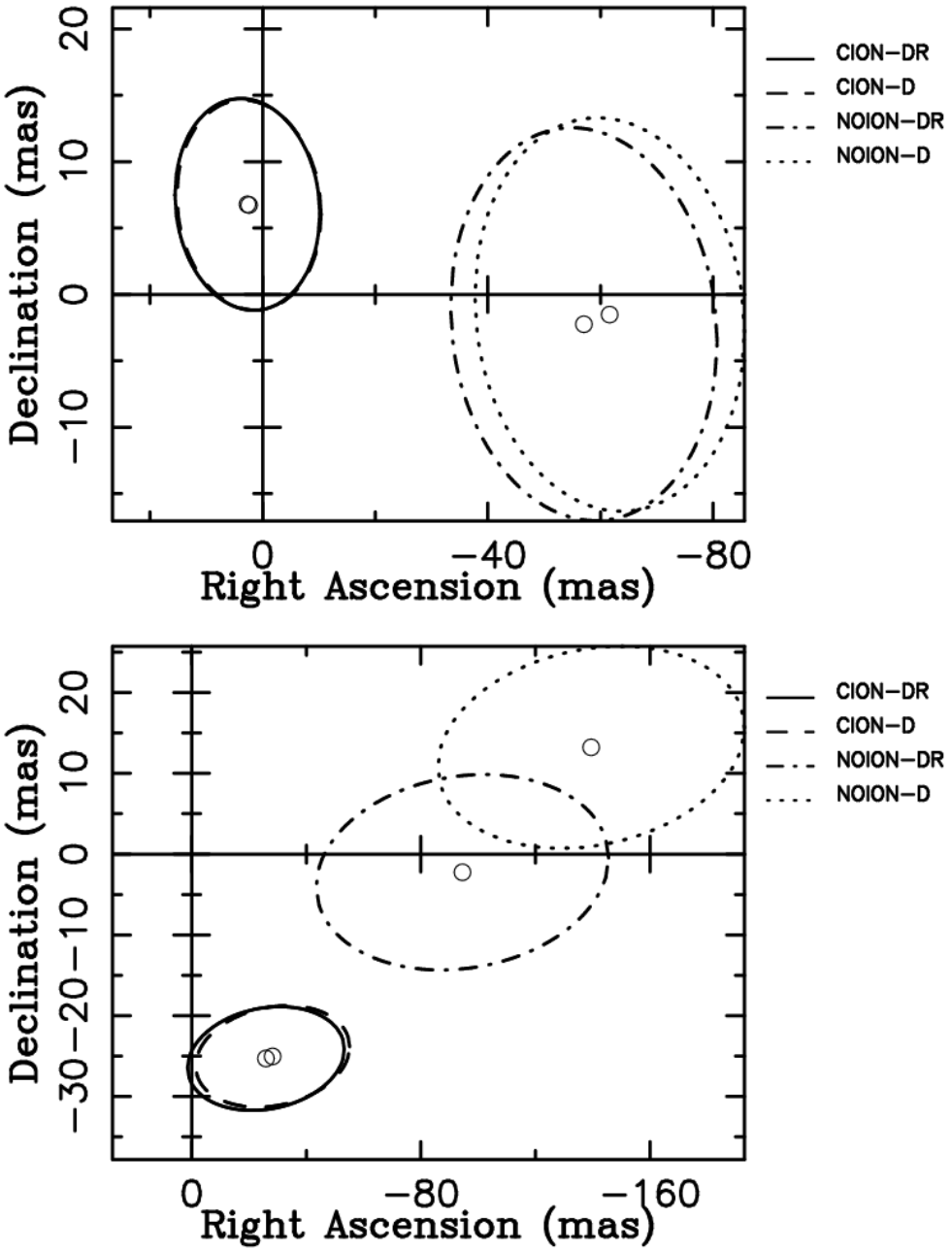

Figure 6.1: Coordinates of ICRF sources estimated by single (L) band VLBI data in May 1996 experiment. The notations of solutions, 'Cion' and 'Noion', represent the solutions from the data with ion-correction and without ion-correction, respectively. The latter half notations 'D' and 'DR' mean two cases of observable combinations, group delay only and group delay + phase delay rate, used in source coordinates estimation. The upper panel (a) shows the coordinates of 0133+476, and the ellipsoid represent one sigma error of the coordinates. The lower panel (b) shows the coordinates of 0212+735 estimated in the four cases of analysis conditions. The origin of the axes are source coordinates in X-band published in the ICRF catalog [*Ma et al.*, 1998], thus, the differences between the estimated coordinates and those of the ICRF catalog are plotted.

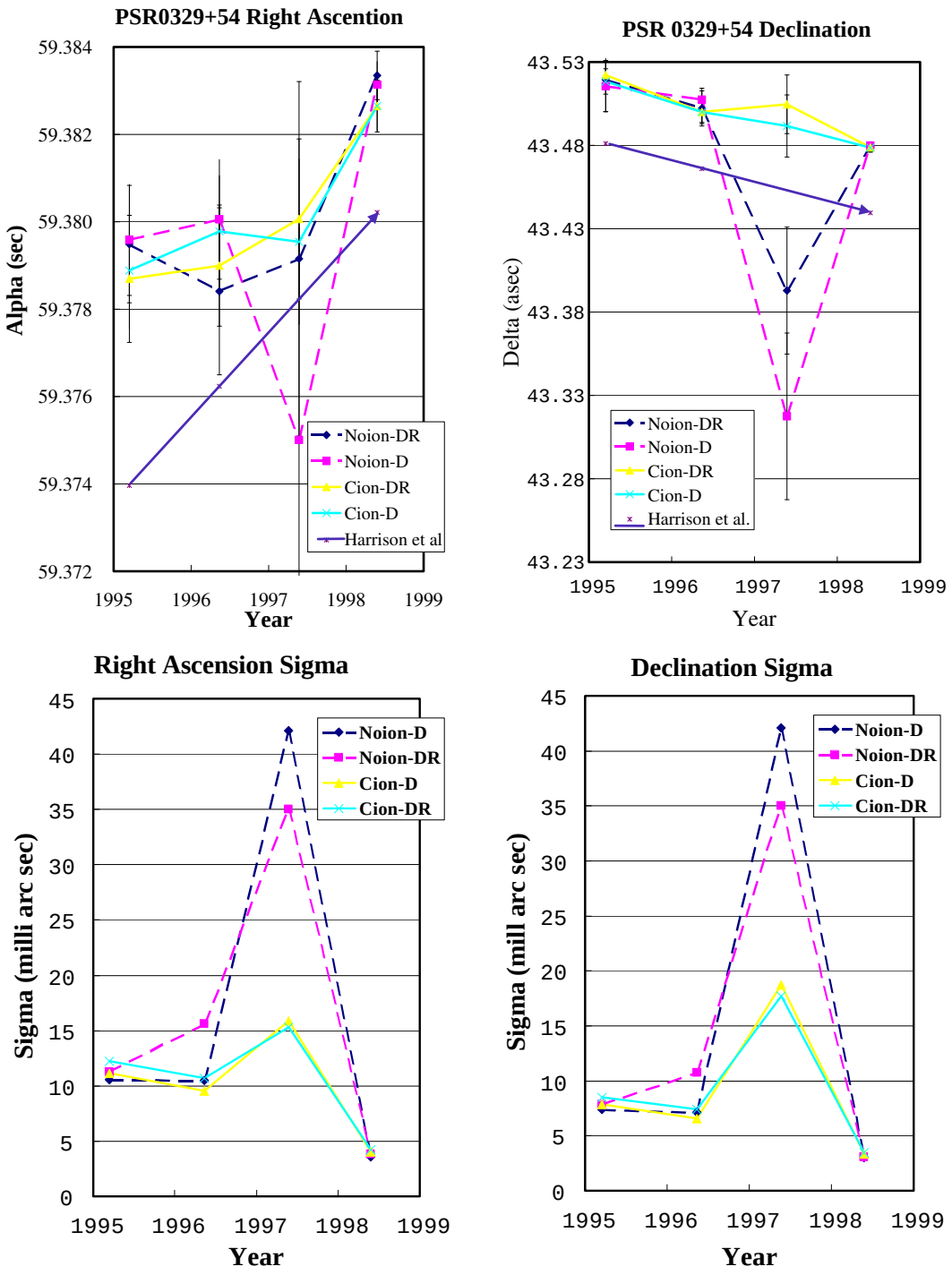

Figure 6.2: Coordinates and errors of PSR B0329+54 at four epochs. Coordinates of right ascension (upper left) and declination (upper right) and the errors of least square (LSQ) analysis are plotted at epochs 1995.20, 1996.36, 1997.39, and 1998.40. The notations, Cion and Noion, indicates two sorts of analysis conditions, with ion-correction and without ion-correction, respectively. The other notations, D and DR, imply two cases of data set used in the analysis, "group delay only" and "group delay + delay rates", respectively. The dashed lines indicate Noion and solid lines Cion. The arrows in the upper panels show proper motion ($\mu_\alpha = 17 \pm 1 mas/yr$, $\mu_\delta = -13 \pm 1 mas/yr$) measured by Harrison et al (1993).

6.3.4 Radio Source Coordinates and Error Analysis

Error Sources in Radio Source Coordinate Estimation

Station Coordinates Error The station position of the Kashima 34-m antenna was measured very accurately in the International Terrestrial Reference Frame (ITRF) by intercontinental geodetic VLBI experiments. However, the position of the Kalyazin 64-m antenna was only measured with GPS before the May 1995 experiments. The errors of the Kalyazin station position measured by GPS were 3 cm in horizontal plan and 15 cm in vertical direction in the WGS-84 coordinate system (Table 2.1). And the WGS-84 system measured by GPS is identical to ITRF within 10 cm [*ITRF,* 2001]. Thus, error of source coordinates due to station position uncertainty and terrestrial reference frame tie are 4 mas and 3 mas, respectively, at 7000 km baseline. To reduce the error of Kalyazin station position on ITRF, we conducted the first geodetic VLBI observation including Kalyazin station in June of 2001, however, it was failed probably because of antenna tracking error at Kalyazin station. We are going to organized the next geodetic VLBI experiment in this fall, and are expecting that the accuracy of Kalyazin station coordinates on ITRF will be improved soon.

Effect of ISS Influence of the amplitude modulation caused by ISS on the group delay measurement was discussed in Section 5.4.2. According to the discussion in that section, amplitude modulation does not affect the group delay directly but just reduce the effective bandwidth. The effect of reduced bandwidth by ISS is included in an error of the group delay by "KOMB", so the amplitude modulation effect need not be taken into account in the error budget additionally.

However, the scattering disk of the ISM should affect the observed group delay. The angular size of the pulsar itself is quite small, but its image on the phase screen fluctuates and changes its position over the area of scattering disk size. The scattering disk size becomes larger at lower frequency. Thus, the scattering disk size needs to be taken into account the error budget of radio source coordinates, especially at low radio frequency observation. As discussed in Chapter 5, the scattering disk sizes of the five pulsars were evaluated from 0.1 up to one milliarcsecond at 1.42 GHz (Table 5.2). These scattering disk sizes have to be added to the error budget of pulsars' positions.

Effect of Reference Source Structure The effect of the radio source structure is not only important especially in the phase referenced method but also in the group delay measurement. Charlot (1990) analyzed the effect of the radio source structure on VLBI group delay and delay rates. According to his analysis, the structure effects of extended sources on group delay reaches to 100 ps. Fey and Charlot (1997) defined source a structure index (1-4) based on the effect of the radio source structure on group delay. The structure index of S-band is indicated in Table 6.2 for the reference sources, whose structure index is known. Most of the reference sources used in our experiment were definition sources of the ICRF or their structure indexes are 1. Since the reference sources used in our experiments were suitable for astrometric purposes, the effect of source structure is less than a few tens of picoseconds. It corresponds to 0.3 mas on a 7000-km baseline.

Ionospheric Delay Correction As discussed in the Section 6.3.3, ion-correction with global ionosphere TEC map works effectively to remove large part of the systematic error caused by the Earth's ionosphere. Although, the global TEC map contains 3-5 TECU of error in zenith direction (Chapter 4). It corresponds from 60 cm to 1 m at 1.42 GHz and 25 - 42 cm at 2.2 GHz. Thus some amount of remaining ionospheric delay or newly introduced error come from the GIM/CODE data should be taken into account in error budget. And it should be larger at lower frequency.

As mentioned in Section 6.3.3, the difference between two sorts of analysis solutions 'DR' and 'D' can be an indicator of the remaining uncorrected ionospheric excess delay. Of course the inconsistency of the two observables will increase the formal error of solution 'DR', thus it should be partly included in formal error. For conservativeness of the solution, however, we used standard deviation of two solutions ('DR' and 'D') as error component of remaining ionospheric delay. And the standard deviation of each coordinate was added in root sum square manner, respectively.

And weighted average of the two solutions was used as final coordinate solution of our measurements.

Summary of Error Budget

The sources of error in our VLBI astrometry observation discussed here are summarized as follows:

1. Station coordinates errors in WGS84 coordinate system are evaluated 4 mas.
2. Error due to terrestrial reference frame tie between WGS84 and ITRF is about 3 mas.
3. The scattering disk size of the ISS at 1.4 GHz was estimated in Table 5.2. And the scattering disk size at 2.2 GHz was computed by using the scaling law of $\theta_{scat} \sim f^{-2.2}$.
4. The effect of source structure difference between X-band and L-band will be taken into account by 1 mas error, for conservativeness in this report.
5. Pulsar coordinates errors caused from uncalibrated ionospheric excess delay error were represented by standard deviation of two sorts of solutions ('DR' and 'D') for each coordinate. And weighted average of the two solution was used as final solution.

Since errors (term 1 - 4) affect equally in both right ascension and declination, the root sum square multipled by factor $1/\sqrt{2}$ was used as error of each coordinate. And ionospheric error (term 5) was added to α and δ, respectively, by root sum square manner. For example, the extra error of B0329+54's right ascension coordinate in March 1995 experiment (1.4-GHz) was $\sigma_{\rm ext} = \sqrt{(4^2 + 3^2 + 0.3^2 + 1^2)/2 + 1.2^2} = 3.8$ mas. The evaluated errors and total extra errors are summarized in Table 6.3 for each pulsar. These external errors were added to the formal error for each coordinate by root sum square manner.

6.4 Results and Discussion

6.4.1 Pulsar Coordinates by Our Measurements

PSR B0329+54

As discussed in the previous section, deviation of Cion-DR and Cion-D is used to represent remaining ionospheric delay error, and average of solutions Cion-DR and Cion-D is designated as final solution by our measurements hereafter. PSR B0329+54's coordinates by our measurements are summarized in Table 6.4. The reason of higher accuracy measurement at 1998.4 than that of other epochs is two folds. (1) The angular resolution of the observation was improved by using S-band (2.2GHz), where L-band (1.4GHz) was used in the observations at the other epochs. (2) Ionospheric effect was smaller since the magnitude of the ionospheric delay decreases in inversely proportional to the square of radio frequency as the frequency increases. The coordinates obtained by May 1997 experiment were less accurate than that of other epochs, because number of scans for this pulsar were small in this experiment.

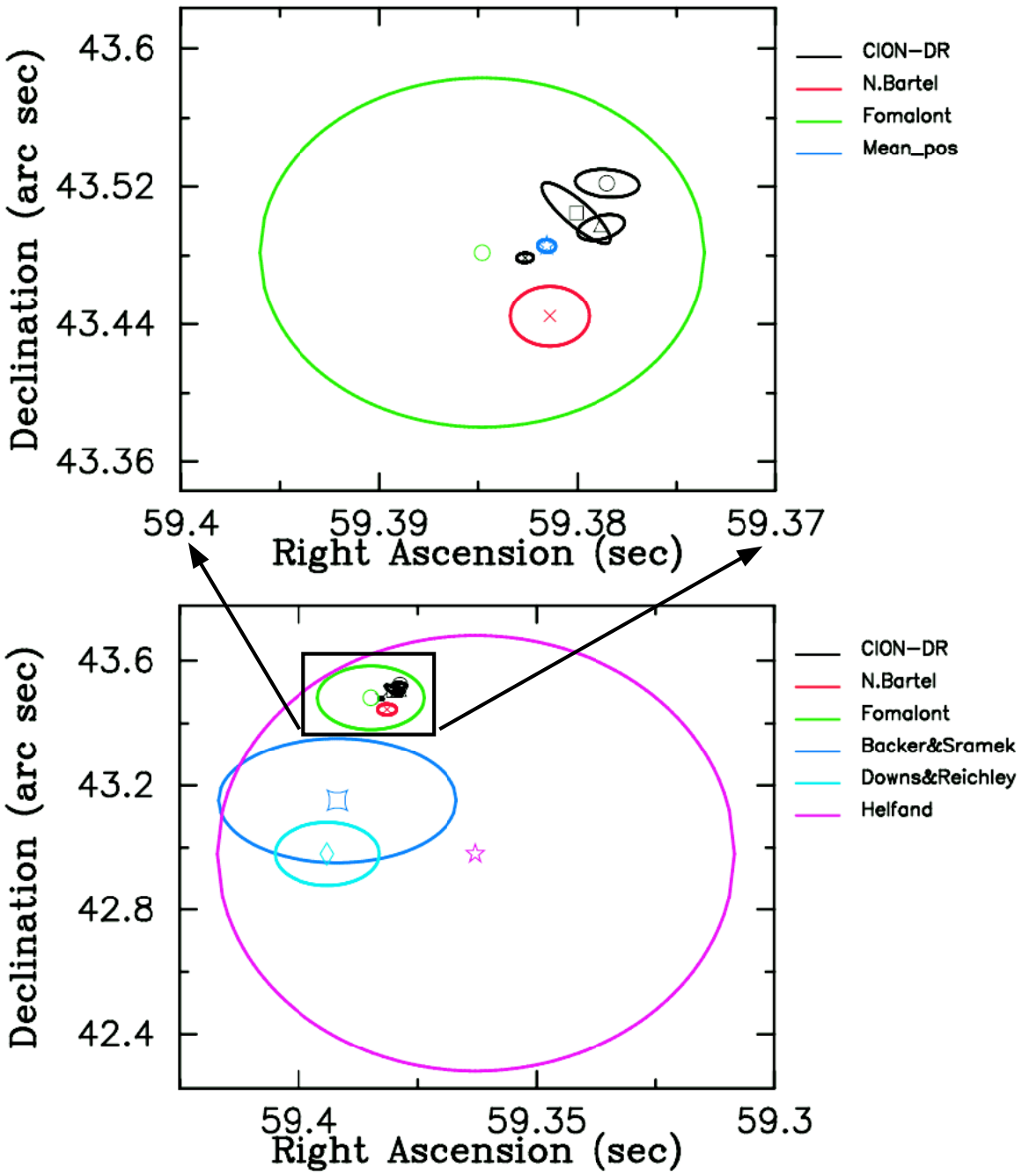

Figure 6.3: Coordinates comparison of PSR B0329+54's measured by interferometer and pulsar timing. The black colored marks are results by our measurements at 4 epochs (see Table 6.5): open circle: at 1995.20, open triangle: at 1996.36, open box: at 1997.39, cross: at 1998.40. The other colored marks are results by other measurements as follows: the pink colored open star: Helfand et al.(1980; timing), the blue open box: Backer and Sramek (1981; NRAO 35 km interferometer), the water colored open diamond: Downs and Reichley (1983; timing), the red cross: Bartel, et al.(1985a; VLBI), the green open circle: Fomalont et al.(1984; VLA). The exact coordinates values are listed in Table 6.6. Upper panel indicates magnified view around our results. The blue color open star is mean of our measurements results at reference epoch 1998.0. All the data except for ours are cited from a paper by Bartel et al.(1985a) and those coordinates are propagated to a epoch at 1998.0 by using proper motion by Harrison et al.(1993). The error of the proper motion was taken into account in the epoch conversion with root-sum-square manner. Each ellipsoid indicates one sigma error of the position.

Table 6.3: Error budget of source coordinates except for formal error of the LSQ analysis. Unit of the error is milliarcsecond.

Error source		B0329+54	B0355+54	B0950+08	B1933+16	B2021+51
Station in WGS84		4	4	4	4	4
Frame tie WGS84&ITRF		3	3	3	3	3
ISS	1.4 GHz	0.3	0.8	0.17	1.4	0.17
	2.2 GHz	0.1	0.3	0.06	0.7	0.06
Ref. source structure		1	1	1	1	1
ion	Mar. 1995	(1.2, 2.7)	(27, 111)	-	(88, 271)	(47,10)
(α, δ)	May 1996	(4.8, 0.05)	-	(202, 808)	-	-
	May 1997	(3.2, 9.2)	-	-	-	-
	May 1998	(0.01, 0.1)	-	(21, 73)	-	-
Total	Mar. 1995	(3.8, 4.5)	(27, 111)	-	(88, 271)	(47,11)
Error	May 1996	(6.0, 3.6)	-	(202, 808)	-	-
(α, δ)	May 1997	(4.8, 9.9)	-	-	-	-
	May 1998	(3.6, 3.6)	-	(21, 73)	-	-

Table 6.4: Coordinates of PSR B0329+54 from our measurements are listed. The source coordinates system is based on the International Celestial Reference Frame (ICRF).

Epoch	α (J2000)†		δ (J2000)†		$C^{\ddagger}_{\alpha\delta}$
1995.20	59.3789	± 0.0014	43.520	± 0.009	0.23
1996.36	59.3794	± 0.0013	43.500	± 0.008	-0.36
1997.39	59.3798	± 0.0019	43.498	± 0.021	0.86
1998.40	59.3827	± 0.0006	43.479	± 0.004	-0.040

†: Right ascension coordinate value larger than second are 03^h32^m. Declination coordinate value larger than arc second are $54^o34'$.
‡: Correlation between right ascension and declination.

Proper motions and mean positions at epoch 1998.0 were estimated by using four epochs of our measurements results, where covariance matrix of each solutions are used as weights. The obtained mean solution and proper motion is listed in Table 6.5. The pulsar coordinates by ours and other measurements from literatures are compared in Figure 6.3. The pulsar coordinates and proper motion data used in the comparison are summarized in Table 6.6.

The Figure 6.3 shows that interferometric results (ours, Bartel et al., and Fomalont et al.) coincide quite well each other. The coordinates measured by pulsar timing coincide with our results within the error. The larger error of timing measurements comes from timing noise, which cannot be fitted by ordinary pulsar parameters. Due to the systematic behaviour of the pulsar timing residual, a planetary system around this pulsar was suspected (e.g. *Shabanova,* 1995; *Konacki et al.,* 1999). However, existence of planet around this pulsar has not proved yet. The large timing noise is thought to be due to spin irregularity of young pulsar at present.

The proper motion derived from our four epochs of measurements (13.5 ± 3.6, -12.1 ± 2.7) (mas/yr) is almost consistent with former measurement by Harrison et al.(13± 1, -17 ± 1) (mas/yr) within 3 sigma error. Further discussion on proper motion are described in section 6.4.2.

Table 6.5: Coordinates and proper motions of PSR B0329+54 determined from our four epochs of VLBI observations. Reciprocal square of coordinates error and correlation between α and δ from astrometry analysis of each epoch were used in weight matrix in weighted-least-square estimation of mean coordinates and proper motion. The reference epoch of the mean coordinates is 1998.0. Only coordinates in seconds and arc seconds are listed. Significant coordinates values of PSR B3029+54 are α: 03^h32^m, and δ: $54^o34'$.

	Solution and error			Correlation Matrix			
				α	δ	μ_α	μ_δ
α	03^h	32^m	$59^s.3816 \pm 0.0005$	1.0	0.047	0.343	-0.004
δ	54°	34'	43".486 ± 0.004	-	1.0	-0.013	0.437
μ_α			12.6 ± 3.5 (mas/yr)	-	-	1.0	0.038
μ_δ			-11.8 ± 2.7 (mas/yr)	-	-	-	1.0

Table 6.6: PSR B0329+54's coordinates obtained by our VLBI observation are listed. Pulsar coordinates by other measurements were cited from Bartel et al.'s paper (1985a). And those pulsar positions were propagated to epoch of 1998.0 by using proper motions by Harrison et al.(1993). The error of proper motion was taken into account in the position error at the destination epoch.

Method	α (J2000)		δ (J2000)		Epoch	Reference
VLBI	03^h 32^m	$59^s.3816 \pm 0.0005$	54° 34'	43".486 ± 0.004	1998.0	a
VLBI		$59^s.3486 \pm 0.0005$		43".663 ± 0.005	1981.21	b
		$59^s.381 \pm 0.002$		43".445 ± 0.018	1998.0	c
VLA		$59^s.352 \pm 0.01$		43".70 ± 0.1	1981.21	d
		$59^s.394 \pm 0.01$		42".99 ± 0.1	1998.0	e
35km		$59^s.359 \pm 0.023$		43".37 ± 0.2	1981.21	f
Interferometer		$59^s.391 \pm 0.025$		43".15 ± 0.2	1998.0	g
Timing		$59^s.362 \pm 0.01$		43".2 ± 0.1	1981.21	h
		$59^s.394 \pm 0.01$		42".99 ± 0.1	1998.0	i
Timing		$59^s.33 \pm 0.05$		43".2 ± 0.7	1981.21	j
		$59^s.36 \pm 0.05$		42".98 ± 0.7	1998.0	k

a: Mean coordinates of our measurements
b: Bartel et al.(1985a)
c: Bartel et al.(1985a) + proper motion by Harrison et al. (1993)†
d: Fomalont et al.(1984)
e: Fomalont et al (1984) + proper motion by Harrison et al (1993) †
f: Backer and Sramek (1981)
g: Backer and Sramek (1981) + proper motion by Harrison et al.(1993) †
h: Downs and Reichley (1983)
i:Downs and Reichley (1983) + proper motion by Harrison et al.(1993)†
j: Helfand et al.(1980)
k: Helfand et al.(1980) + proper motion by Harrison et al.†
†: Proper motion (μ_α= 17 ± 1 mas/yr, μ_δ =-13 ± 1 mas/yr) by Harrison et al.(1993) was used for epoch conversion.

Table 6.7: Coordinates of PSR B0355+54 by our measurement and those of other measurements from literatures. All the possible extra errors discussed in Section 6.3.4 are included in the error of our data by root sum square manner.

Method	α (J2000)	δ (J2000)	$C_{\alpha\delta}^{(1)}$	Epoch (year)	Reference
VLBI	$03^h\ 58^m\ 53^s.713 \pm 0.003$	$54°\ 13'\ 13".75 \pm 0.1$	0.43	1995.20	a
VLA	$53^s.705 \pm 0.004$	13.58 ± 0.03	-	1986.39	b
	$53^s.718 \pm 0.005$	13.624 ± 0.04	-	1995.20(2)	c
	$53^s.710 \pm 0.0056$	13.633 ± 0.04	-	1995.20(3)	d
Timing	$53^s.707 \pm 0.003$	13.62 ± 0.04	-	1991.35	e
	$53^s.709 \pm 0.0034$	13.63 ± 0.042	-	1995.20(3)	f

a: This paper
b: Fomalont et al.(1992)
c: Fomalont et al.(1992) + (proper motion) Fomalont et al.(1997)
d: Fomalont et al.(1992) + (proper motion) Lyne et al.(1982)
e: Arzoumanian et al.(1994) f: Arzoumanian et al.(1994) +(proper motion) Lyne et al.(1982)
(1) Correlation of parameters between right ascension and declination.
(2) Pulsar coordinates were propagated to the reference epoch by proper motion ($\mu_\alpha = 13 \pm 3$ mas/yr, $\mu_\delta = 5 \pm 4$ mas/yr) by Fomalont et al.(1997).
(3) Pulsar coordinates were propagated to the reference epoch by proper motion ($\mu_\alpha = 5 \pm 4$ mas/yr, $\mu_\delta = 6 \pm 3$ mas/yr) by Lyne et al.(1982).

PSR B0355+54

PSR B0355+54 was observed only in the March 1995 experiment, the coordinates are obtained at one epoch. Coordinates by our measurements and other interferometric measurements from literatures are compared in Figure 6.4 and the data used in the comparison are listed in Table 6.7. Figure 6.4 shows the interferometric and pulsar timing measurement results are consistent within about 30 mas. Since the error of the celestial reference frame used by VLA is thought to be coincide with ICRF within accuracy of 20 mas [*Fomalont et al.,* 1992], the absolute coordinates of PSR B0355+54 measured by Fomalont by VLA (1992) are coincide with the ICRF within that level. The proper motion by Lyne et al. explains rather well the shift from the coordinates of Fomalont et al. to our position. So Lyne's proper motion is likely more correct than that of Fomalont et al.(1997). The next absolute astrometry measurement of this pulsar will solve the question of proper motion.

PSR B0950+08

PSR B0950+08 was observed at two epochs (May 1996 and May 1998), and the pulsar's coordinates were obtained at two epochs. Pulsar coordinates by our results are compared with combinations of pulsar's position and proper motions measured by Fomalont et al.(1992), Lyne et al.(1982), Gwinn et al.(1986), and Brisken et al.(2000), and these data are plotted on Figure 6.5. And the data used in the plot are listed in Table 6.8. The result of May 1996 experiment (L-band) has larger error than that at May 1998 (S-band). The reasons of this are (1) higher resolution with S-band (2.2GHz) observation and (2) smaller influence of ionospheric delay than L-band (1.4GHz). Additionally the declination of this source is close to the equator and our observation used East-West single baseline. consequently the solution of parameters (α, δ) have 99 % of correlation (Table 6.8), then the error ellipsoid is elongated in North-East and South-West direction.

The proper motion and parallax of this pulsar was measured by Gwinn et al.(1986) by VLBI observation with phase delay for the first time. That proper motion coincide well with

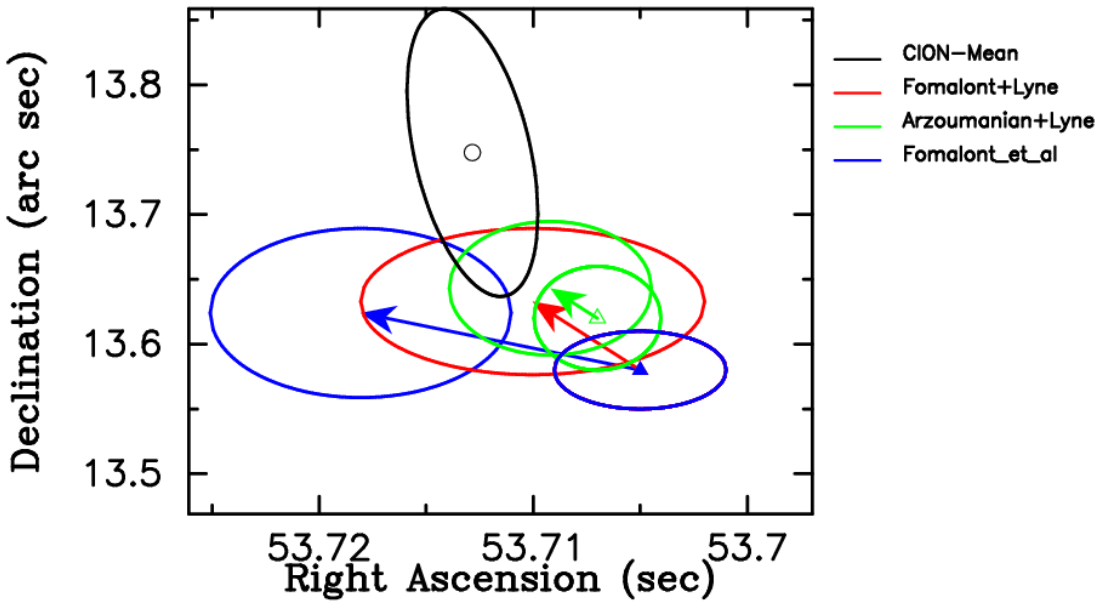

Figure 6.4: Coordinates comparison of PSR B0355+54 measured by interferometers and pulsar timing. The black open circle indicates our measurement result at epoch 1995.20. The blue closed triangle is VLA measurement result by Fomalont et al.(1992), and the coordinates are propagated to the reference epoch 1995.20 by using two proper motions by Fomalont et al.(1997) by VLA (blue arrow) and by Lyne et al.(1982) by Radio link interferometer (red arrow). The green open triangle and the same colored arrow indicate position and proper motion measured through pulsar timing observations by Arzoumanian et al.(1994). The ends of the arrows correspond to the coordinates at the reference epoch 1995.20. The error of the proper motion was taken into account in the epoch conversion with root-sum-square manner. Each ellipsoid indicates one sigma error of the position.

Table 6.8: Coordinates of PSR B0950+08 from our observation results and the other measurements results from literatures are listed. The possible extra errors discussed in subsection 6.3.4 are included in the error by root sum square manner.

Method	α (J2000)		δ (J2000)		$C_{\alpha\delta}^{(1)}$	Epoch (year)	Reference
VLBI	$09^h\ 53^m$	$9^s.30 \pm 0.01$	$7^\circ\ 55'$	$35".8 \pm 0.8$	0.99	1996.36	a
VLBI		$9^s.309 \pm 0.001$		$36".154 \pm 0.07$	0.98	1998.40	b
VLA		$9^s.316 \pm 0.003$		$35".60 \pm 0.04$	-	1986.39	c
		$9^s.328 \pm 0.007$		$35".97 \pm 0.07$	-	1998.40 (2)	d
		$9^s.331 \pm 0.004$		$36".035 \pm 0.06$	-	1998.40 (3)	e
		$9^s.3147 \pm 0.003$		$35".954 \pm 0.04$	-	1998.40 (4)	f

a: Our observation at 1996.36
b: Our observation at 1998.40
c: Fomalont et al.(1992)
d: Fomalont et al.(1992) + proper motion by Lyne et al.(1982)
e: Fomalont et al.(1992)+ proper motion by Gwinn et al.(1986)
f: Fomalont et al.(1992)+ proper motion by Brisken et al.(2000)
(1) Correlation of parameters between right ascension and declination
(2) Pulsar coordinates were propagated to the reference epoch by proper motion (μ_α = 15 $\pm$ 8 mas/yr, μ_δ= 31 $\pm$ 5 mas/yr) by Lyne et al.(1982).
(3) Pulsar coordinates were propagated to the reference epoch by proper motion (μ_α = 18.7 $\pm$ 3.1 mas/yr, μ_δ= 36.2 $\pm$ 4.2 mas/yr) by Gwinn et al.(1986).
(4) Pulsar coordinates were propagated to the reference epoch by proper motion (μ_α = -1.6 $\pm$ 0.4 mas/yr, μ_δ= 29.5 $\pm$ 0.5 mas/yr) by Brisken et al.(2000).

the measurement by Lyne et al.(1982). In 2000, Brisken et al.(2000), however, claimed that Gwinn et al.'s observation mistook the beam ambiguity, and they published new proper motion and parallax measurement results based on VLBA phase referenced mapping by using in-beam calibration technique. If the absolute coordinates measured by Fomalont et al.(1992) are correct within 20 mas level [Fomalont et al., 1992], our measurements results (May 1998) support the proper motion by Brisken et al. The magnitude of proper motion of this pulsar seems to be about 30 mas/year, a few years interval of absolute astrometry VLBI observation promise to give the definite answer to this question.

Here author wish to emphasise the importance of absolute astrometry. In general, absolute position measurement is difficult with phase delay observation. Then the source positions measured by phase differential astrometry are not transfered to the other researcher, hence each researcher has to use only their own measurement data for astrometric parameter derivation. The absolute source position determination has advantage that the source coordinates measured in the past time can be used for further proper motion derivation and tracking the pulsar's motion for a long time span, and it might enable a detection of acceleration or deceleration of the pulsar motion.

PSR B1933+16

PSR B1933+16 was observed only in March 1995 VLBI experiment, and the coordinates were obtained at the single epoch. Coordinates of PSR B1933+16 obtained by our observation are plotted in Figure 6.6 with other measurements result from literatures. The pulsar's coordinates and proper motion data plotted in Figure 6.6 are listed in Table 6.9.

Figure 6.6 indicates that our measurement result is fairly consistent with those by Fomalont et al.(1992,1997). In contrast to the consistency among interferometric results, pulsar timing position by Downs & Reichley seems to be rather different from interferometric results on both

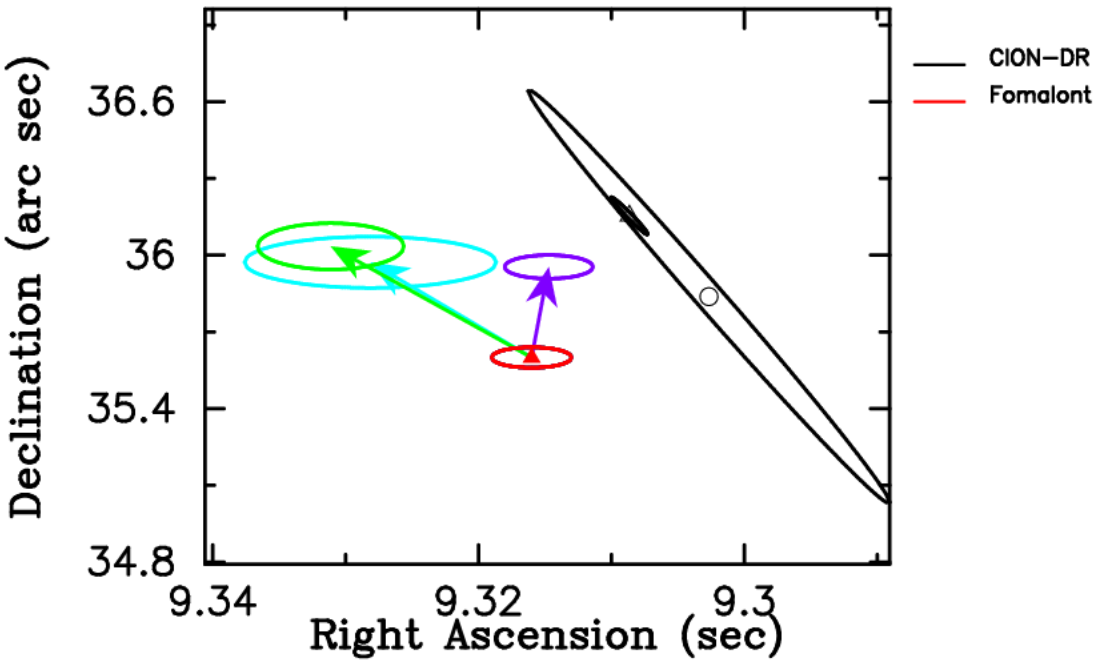

Figure 6.5: Coordinates compassion of PSR B0950+08 measured by interferometers. The black open circle indicates our coordinates at 1996.36, and black open triangle shows our coordinates at 1998.40. The red closed triangle indicates pulsar coordinates at epoch 1986.39 measured by Fomalont et al.(1992) measured using VLA. This position was propagated to the reference epoch 1998.40 using proper motions by Lyne et al.(water colored arrow), Gwinn et al.(green arrow), and Brisken et al.(violet arrow), respectively. The error of the proper motion was taken into account in the epoch conversion with root-sum-square manner. Each ellipsoid indicates one sigma error of the position.

Table 6.9: Coordinates of PSR B1933+16 obtained by our observation and the other measurements results cited from literatures are listed. Since the coordinates by Downs & Reichley were originally in B1950.0 system, we cited the coordinates in J2000.0 from Taylor's catalog [*Taylor et al.,* 1993]. Also since the pulsar position by Fomalont et al.(1992) was given in B1950.0 system, the coordinates were converted to J2000 by following a procedure described by Aoki et al.(1983).

Method	α (J2000)		δ (J2000)		$C^{(1)}_{\alpha\delta}$	Epoch (year)	Reference
VLBI	$19^h\ 35^m$	$47^s.824 \pm 0.006$	16° 16'	40".07 ± 0.27	0.98	1995.20	a
VLA		47.830 ± 0.004		40".16 ± 0.05	-	1986.39	b
		47.825 ± 0.006		39".975 ± 0.07	-	1995.20(2)	b
		47.829 ± 0.004		40".05 ± 0.056	-	1995.20(3)	c
Timing		47.835 ± 0.003		40".59 ± 0.05	-	1968.98	d
		47.840 ± 0.007		39".92 ± 0.13	-	1995.20(4)	e

a: Our data
b: Fomalont et al.(1992)
c: Fomalont et al.(1992) + proper motion by Fomalont et al.(1992)
d: Fomalont et al.(1992) + proper motion by Fomalont et al.(1992)
e: Fomalont et al.(1992) + proper motion by Fomalont et al.(1997)
f: Downs and Reichley (1983)
f: Downs and Reichley (1983) + proper motion by Downs and Reichley
(1) Correlation of parameters between right ascension and declination.
(2) Pulsar coordinates were propagated to the reference epoch by proper motion (μ_α = -8 ± 8 mas/yr, μ_δ= -21 ± 6 mas/yr) by Fomalont et al.(1992).
(3) Pulsar coordinates were propagated to the reference epoch by proper motion (μ_α = -1 ± 3 mas/yr, μ_δ= -13 ± 3 mas/yr) by Fomalont et al.(1997).
(4) Pulsar coordinates were propagated to the reference epoch by proper motion (μ_α = 2.6 ± 3.4 mas/yr, μ_δ= -25.7 ± 4.8 mas/yr) by Downs and Reichley et al.(1983).

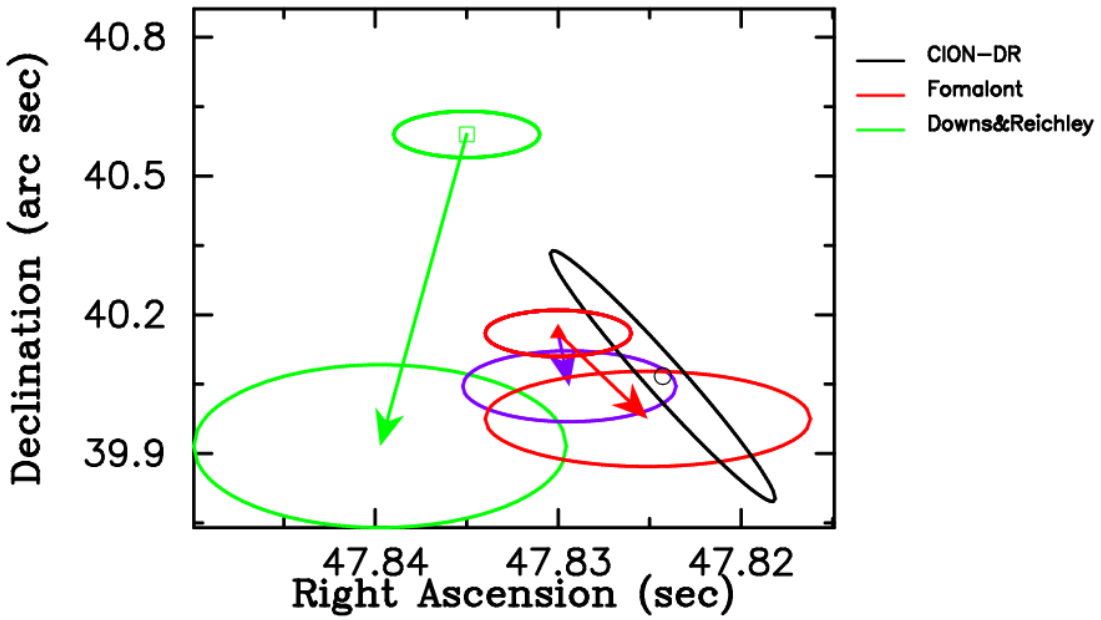

Figure 6.6: Coordinates comparison of PSR B1933+16 measured by interferometer and pulsar timing. Our measurement at 1995.20 is plotted with the black open circle. The red closed triangle shows VLA measurement result by Fomalont et al.(1992) at 1986.39. Two kinds of proper motions are used to propagate till to the reference epoch 1995.20. The red colored arrow indicates proper motion by Fomalont et al.(1992) and the violet colored arrow indicates improved proper motion by Fomalont et al.(1997). The green colored open box is pulsar coordinates at epoch 1968.98 measured by Downs & Reichley (1983) through pulsar timing observation. The same colored arrow indicates proper motion derived from their pulsar timing analysis. Since their coordinates were originally in the B1950.0 system, we cited the coordinates data in J2000 system from Taylor's catalog [*Taylor et al.,* 1993]. The ends of the arrows correspond to the coordinates at the reference epoch 1995.20. The error of the proper motion was taken into account in the epoch conversion with root-sum-square manner. Each ellipsoid indicates one sigma error of the position.

Table 6.10: Coordinates of PSR B2021+51 obtained by our observation and the other measurements from literatures are listed. Pulsar coordinates in J2000.0 system of Downs & Reichley's measurements were cited from Taylor's catalog (1993). Also pulsar coordinates by Fomalont et al.(1984) were converted to those on J2000.0 system in accordance with a procedure described by Aoki et al.(1983). The possible extra error discussed in Section 6.3.4 are included in the error of our data by root sum square manner.

Method	α (J2000)	δ (J2000)	$C^{(1)}_{\alpha\delta}$	Epoch (year)	Reference
VLBI	$20^h\ 22^m$ $49^s.866 \pm 0.005$	$51°\ 54'$ $50".302 \pm 0.01$	0.36	1995.20	a
VLBI	$49^s.87031 \pm 0.00004$	$50".2913 \pm 0.0003$	-0.37	1992.723	b
	$49^s.86814 \pm 0.00008$	$50".3245 \pm 0.0007$	-0.37	$1995.20^{(2)}$	c
VLA	$49^s.85 \pm 0.02$	$50".10 \pm 0.15$	-	1981.0	d
	$49^s.86 \pm 0.02$	$50".33 \pm 0.16$	-	$1995.20^{(3)}$	e
Timing	$49^s.867 \pm 0.006$	$50".31 \pm 0.05$	-	1991.35	f
	$49^s.864 \pm 0.006$	$50".36 \pm 0.05$	-	$1995.20^{(2)}$	g
Timing	$49^s.900 \pm 0.002$	$50".06 \pm 0.02$	-	1970.08	h
	$49^s.915 \pm 0.01$	$50".48 \pm 0.09$	-	$1995.20^{(4)}$	i

a: Our data
b: Campbell et al.(1996)
c: Campbell et al.(1996) + proper motion by Campbell et al.(1996)
d: Fomalont et al.(1984)
e: Fomalont et al.(1984) + proper motion by Lyne et al.(1982)
f: Arzoumanian et al.(1994)
g: Arzoumanian et al.(1994) + proper motion by Campbell et al.(1996)
h: Downs and Reichley, (1983)
h: Downs and Reichley, (1983) + proper motion by Downs and Reichley (1983)
(1) Correlation of parameters between right ascension and declination.
(2) Pulsar coordinates were propagated to the reference epoch by proper motion (μ_α = -8.11 $\pm$ 0.24 mas/yr, μ_δ= 13.41 $\pm$ 0.25 mas/yr) by Campbell et al (1996).
(3) Pulsar coordinates were propagated to the reference epoch by proper motion (μ_α = 6 $\pm$ 4 mas/yr, μ_δ= 17 $\pm$ 4 mas/yr) by Lyne et al (1982).
(4) Pulsar coordinates were propagated to the reference epoch by proper motion (μ_α = 5.6 $\pm$ 4.1 mas/yr, μ_δ= 16.6 $\pm$ 3.5 mas/yr) by Downs and Reichley et al (1983).

the direction and magnitude of proper motions. The reason of this in-consistency should be partly caused from systematic noise (red noise) in the pulsar timing data [e.g., *Cognard, et al.,* 1995b; *Kopeikin,* 1999]. And it is partly due to difference of reference frame, i.e., difference of the ICRF of VLBI and planetary ephemeris of pulsar timing.

PSR B2021+51

PSR B2021+51 was observed only in March 1995 experiment and the coordinates were obtained at this one epoch. Coordinates by our observation are plotted in Figure 6.7 with other measurement results cited from literatures. And the data used in Figure 6.7 are listed in Table 6.10.

Recently published pulsar coordinates of both interferometric measurements and timing measurements are almost consistent each other as seen in upper panel of Figure 6.7. Campbell et al. had made excellent phase delay measurement by VLBI and obtained very precise proper motion and parallax of PSR B2021+51. Usually absolute position measurements are difficult with delay measurement, however, they successfully estimated the absolute pulsar coordinates in reference to the nearby reference source. Their pulsar coordinates at reference epoch 1995.20

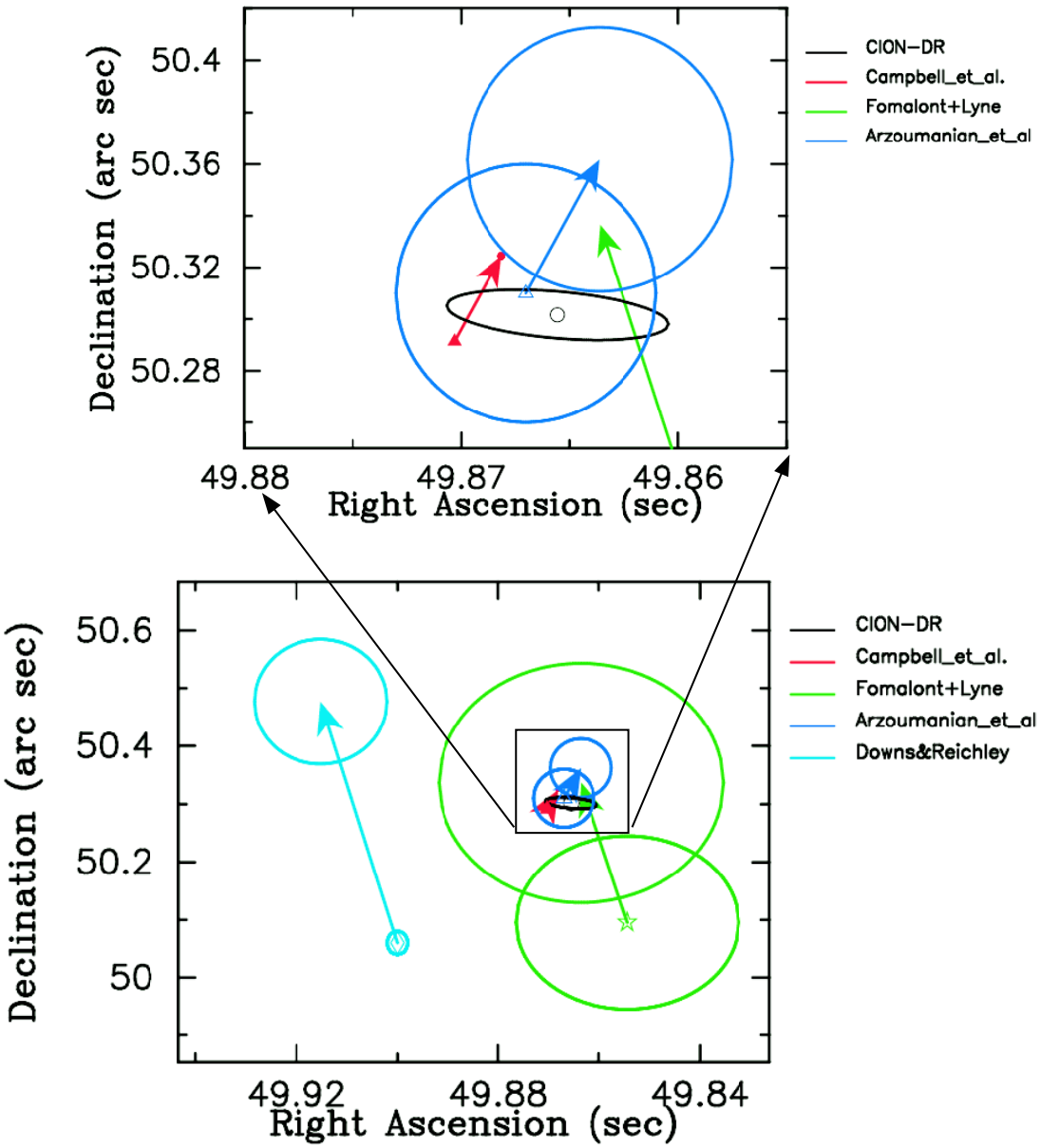

Figure 6.7: Coordinates comparison of PSR B2021+51 measured by interferometer and pulsar timing. The black open circle is our measurement result at epoch 1995.20. The red colored closed triangle and arrow show coordinates and proper motion measured by Campbell et al.(1996) at 1992.72 with VLBI phase delay measurement. The green open star indicates VLA measurement result by Fomalont et al.(1992) at epoch 1986.39, and their position was propagated till to the reference epoch 1995.20 using proper motion (green arrow) by Lyne et al.(1982). The water colored open diamond and the arrow are position and proper motions results by Downs & Reichley(1983) from pulsar timing observation. The blue colored open triangle and the arrow indicate position and proper motion determined through pulsar timing by Arzoumanian et al.(1994). The ends of all the arrows are positions at the reference epoch 1995.20. The error of the proper motion was taken into account in the epoch conversion with root-sum-square manner. And all the ellipsoids indicate one sigma error of the position.

Table 6.11: Coordinates and proper motions of PSR B0329+54 derived from joint data set: "Ours+Bartel" and "Ours+Fomalont". Correlation matrixes are also listed to show the estimation errors and correlation between parameters correctly. The reference frame is the ICRF and the reference epoch is 1995.0.

		Solutions (J2000)	Correlation Matrix $\alpha^{(1)}$	$\delta^{(2)}$	μ_α	μ_δ
"Ours+Bartel"	α	$59^s.37589 \pm 0.0004$	1.0	0.063	0.483	0.034
	δ	$43".5171 \pm 0.003$	-	1.0	0.041	0.318
	μ_α	17.3 ± 0.35	-	-	1.0	0.022
	μ_δ	-10.6 ± 0.4	-	-	-	1.0
"Ours+Fomalont"	α	$59^s.37710 \pm 0.001$	1.0	0.055	-0.899	-0.033
	δ	$43".521 \pm 0.007$	-	1.0	-0.038	-0.876
	μ_α	13.3 ± 3	-	-	1.0	0.029
	μ_δ	-12.0 ± 2.5	-	-	-	1.0

(1): Digits of Right ascension coordinates larger than second are 03^h32^m.
(2): Digits of Declination coordinates larger than second are $54^o34'$.

are consistent with our result within our two sigma error level.

Also the pulsar coordinates derived from timing measurements by Arzoumanian et al.(1994) are consistent with our result within their two sigma error level. The coordinates of VLA measurements by Fomalont et al. also coincide with the coordinates described above, when the position is propagated to the reference epoch 1995.20 using proper motion by Lyne et al. Although, the proper motion between Lyne et al.(1982) and Campbell et al.(1996) are rather different, they still keep consistency among these data set, since the error of the coordinates measurement by VLA [*Fomalont et al.,* 1984] is large.

Campbell et al.'s proper motion is likely to be the most correct at present. But phase measurement has potential to mistake wrong ambiguity, as the case of Gwinn et al.(1986) pointed by Brisken et al.(2000), definite answer about the proper motion will be given by repetition of absolute astrometry with several years interval.

6.4.2 Proper Motion and Coordinates Estimation of PSR B0329+54 by using Joint Data

As it was seen in Figure 6.3, the pulsar coordinates measured by Fomalont et al.(1984: hereafter referred to as FM84) and by Bartel et al.(1985a: hereafter referred to as BR85) are quite consistent with our results (Figure 6.3). Then, more precise proper motion can be derived from two cases of joint analysis with our data and that of FM84 or BR85.

The pulsar coordinates of the BR85 were measured with reference to the coordinates of NRAO 150 (0355+508). The NRAO150 is one of the ICRF source categorized as "Other source"[*Ma et a.,* 1998], which cannot clear some criteria as the ICRF defining source, but they are sill useful for frame tie. The coordinates of NRAO 150 which Bartel et al. used differ from that of the ICRF by 0.14 ms of time in right ascension and minus 0.5 mas for declination. So that we corrected Bartel et al.'s pulsar coordinates by these amounts Then BR85's pulsar coordinates are thought to be almost on the ICRF.

The VLA coordinates system, in which Fomalont et al. determined the pulsar position, was consistent with FK5 within 0.1 arc sec [*Fomalont et al.,* 1984], and the ICRF is identical with FK5 within uncertainty of 0.1 arc sec. [*Lindegen et al.,* 1995]. Thus the pulsar coordinates determined by Fomalont et al.(1984) are thought to be on the ICRF within 0.1 arc sec uncertainty.

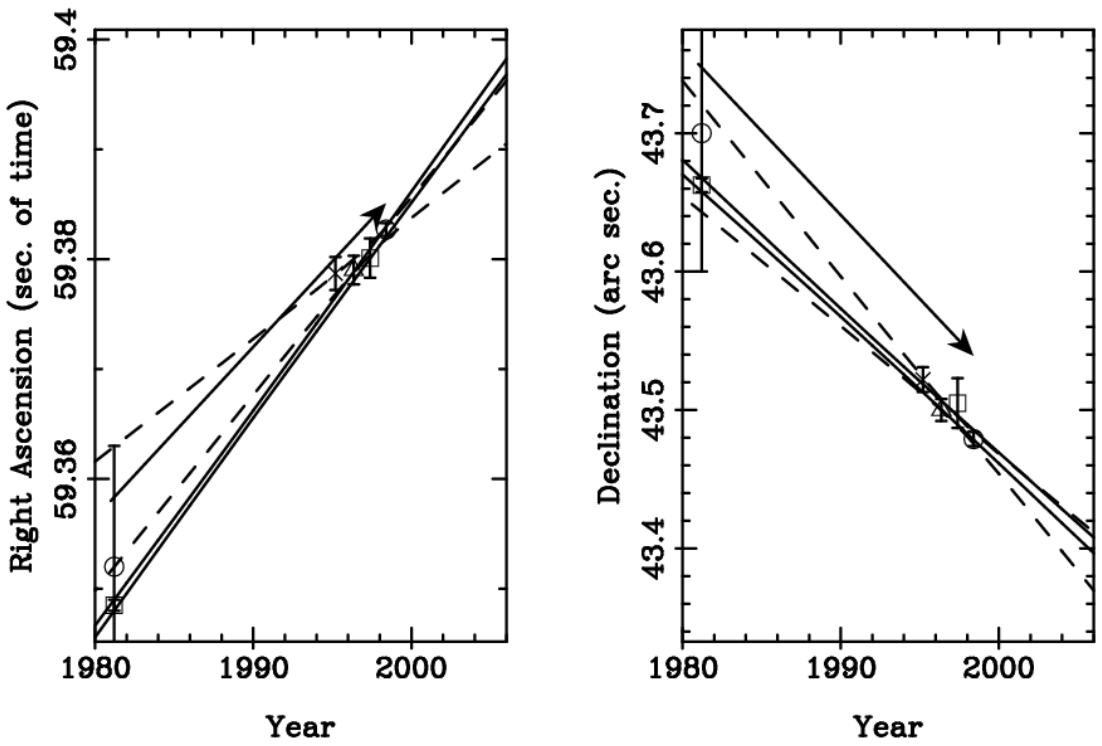

Figure 6.8: Proper motion and coordinates of PSR B0329+54 used for joint data analysis are plotted. Left panel indicates proper motion in right ascension and right panel shows proper motion in declination. Each four points around the center of the two panels are our results (cross: 1995.20; open triangle: 1996.39; open box: 1997.39; open circle: 1998.40), and each two marks are the left side of two panels are data of Fomalont et al.(open circle) and Bartel et al.(open box). Each arrow of the two panel shows proper motion derived from only our four epochs of measurements. The area closed by dashed (solid) curves shows one sigma area, where pulsar is found with probability 68.4%, derived from analysis with joint data set "Ours+Fomalont" ("Ours+Bartel").

Figure 6.8 shows the relation between proper motion and the data set used for joint analysis. The arrows in the Figure 6.8 indicate proper motion derived from four epochs of our observation data. The proper motion coincide with the data of FM84, BR85. Thus, by joining the pulsar coordinates of ours to that of Fomalont et al.(referred to as "Ours+Fomalont") and joining our data to that of Bartel et al.(referred to as "Ours+Bartel"), two sorts of more precise proper motion and mean coordinates of pulsar were estimated by least square analysis. Where the magnitude of error of each pulsar position was used as weight and correlation between α and δ (Table 6.4) were taken into account in weight matrix in weighted-least-square-analysis. The derived coordinates at reference epoch 1995.0, proper motions, errors, and correlation matrix are listed in Table 6.11.

The area closed by the dashed hyperbolic curves in the Figure 6.8 indicates the region where pulsar is found with one sigma (68.4%) probability. It was derived by joint data analysis of "Ours+Fomalont", The area closed by solid hyperbolic curves is also one sigma probability region derived from joint data set of "Ours+Bartel".

The two cases of the one sigma probability areas are consistent in declination, however, those in right ascension are slightly different. It is caused by the rather larger coordinates of α in the result of March 1995 experiment, but at present we don't have any reason to reject or down wait the data. In any cases, both solutions are consistent each other within two sigma (95.6%) error level.

Table 6.12: Pulsar coordinates (VLBI, Timing) used for frame tie.

PSR name	Epoch (MJD)	Right Ascension		Declination		Reference
VLBI coordinates						
B0329+54	50814	$03^h\ 32^m$	$59^s.3816 \pm 0.0005$	54° 34'	43".486 ± 0.004	a
B0355+54	49791	$03^h\ 58^m$	$53^s.713 \pm 0.003$	54° 13'	13".75 ± 0.1	a
B1257+12	48794	$13^h\ 0^m$	$3^s.05005 \pm 0.00005$	12° 40'	56".7043 0.003	b
B1937+21	46854	$19^h\ 39^m$	$38^s.5613 \pm 0.0004$	21° 34'	59".130 ± 0.003	c
B2021+51	49058	$20^h\ 22^m$	$49^s.8703 \pm 0.0004$	51° 54'	50".291 ± 0.0003	d
Pulsar timing coordinates						
B0329+54	40621	$03^h\ 32^m$	$59^s.3107 \pm 0.008$	54° 34'	43".657 ± 0.099	e
B0355+54	48382	$03^h\ 58^m$	$53^s.707 \pm 0.003$	54° 13'	13".62 ± 0.04	f
B1257+12	49750	$13^h\ 0^m$	$3^s.0578 \pm 0.00004$	12° 40'	56".478 ± 0.001	g
B1937+21	47530	$19^h\ 39^m$	$38^s.560210 \pm 0.000002$	21° 34'	59".14166 ± 0.00006	h
B2021+51	48382	$20^h\ 22^m$	$49^s.867 \pm 0.06$	51° 54'	50".31 ± 0.05	f

a: Our measurements; b: Nunes and Bartel (1998); c: Bartel et al.(1996); d: Campbell et al.(1996); e: Rodin, personal communication. He analyzed the published data of Downs & Reichley (1983) with time-of-arrival analysis software TIMAPR [*Doroshenko and Kopeikin,* 1990]; f: Arzoumanian et al.(1994); g: Wolszczan (1994); h: Kaspi et al.(1994);

Table 6.13: Proper motions of pulsars used for frame tie.

PSR Name	μ_α (mas/yr)	μ_δ (mas/yr)	Reference
B0329+54	17.2 ±0.3	-10.5 ± 0.4	This paper
B0355+54	5 ±4	6 ± 3	Lyne et al.(1982)
B1257+12	46.4 ± 0.6	-82.9 ± 0.9	Wolszczan (1994)
B1937+21	-0.130 ± 0.008	-0.464 ± 0.009	Kaspi et al.(1994)
B2021+51	-8.11 ± 0.24	13.41 ± 0.25	Campbell et al.(1996)

The proper motion derived from the data set 'Ours+Bartel' are the most precise one ever achieved for this pulsar. When it is compared with that of Harrison et al.(1993: $\mu_\alpha = 17 \pm 1 mas/yr, \mu_\delta = -13 \pm 1$ mas/yr), the proper motion in declination is consistent within 3 sigma level of their result, and that in right ascension is quite consistent and ours have higher precision.

6.4.3 Reference Frame Tie

Reference frame tie is one of the purposes of our measurements. Here we tried to estimate the rotation matrix between the ICRF and the DE200 by using coordinates of five pulsars. Two pulsars' VLBI coordinates (PSR B0329+54 and PSR B0355+54) were used from our measurements. And other three pulsar's VLBI coordinates (PSR B1257+12, PSR B1937+21, and PSR B2021+51) and pulsar timing coordinates of the five pulsars are cited from literatures. The coordinates of the pulsars are summarized in table 6.12.

All pulsar's coordinates were converted to those at reference epoch 1998.40 (MJD 50958) by using the proper motion data listed in in Table 6.13. Then Cartesian coordinates components of the unit vector toward each pulsar were computed for both VLBI and pulsar timing coordinates.

A vector in the ICRF $\mathbf{x}_{ICRF}$ and a vector in the DE200 $\mathbf{x}_{DE200}$ are related by a rotation matrix $\mathbf{A}^{\rm ICRF}_{\rm DE200}$ as:

$$\mathbf{x}_{\rm ICRF} = \mathbf{A}^{\rm ICRF}_{\rm DE200}\mathbf{x}_{\rm DE200}, \tag{6.1}$$

where the frame rotation matrix $\mathbf{A}^{\rm ICRF}_{\rm DE200}$ is

$$\mathbf{A}^{\rm ICRF}_{\rm DE200} = \begin{pmatrix} 1 & \theta_z & -\theta_y \\ -\theta_z & 1 & \theta_x \\ \theta_y & -\theta_y & 1 \end{pmatrix}. \tag{6.2}$$

Here the rotation angle is assumed to be much smaller than unity ($\theta_i (i = x, y, z) << 1$). By using a vector $\mathrm{d}\mathbf{x} = \mathbf{x}_{\rm ICRF}$-$\mathbf{x}_{\rm DE200}$ and $\mathbf{\Theta} = (\theta_x, \theta_y, \theta_z)^T$, the equation (6.1) is rewritten as

$$\mathrm{d}\mathbf{x} = \mathbf{B}(x_{\rm DE200})\Theta, \tag{6.3}$$

where the design matrix $\mathbf{B}(\mathbf{x}_{\rm DE200})$ is expressed by Cartesian components (x_i, y_i, z_i) of unit vector toward pulsar i in DE200 coordinates system as follows:

$$\mathbf{B}(\mathbf{x}_{\rm DE200}) = \begin{pmatrix} 0 & -z_1 & y_1 \\ z_1 & 0 & -x_1 \\ -y_1 & x_1 & 0 \\ 0 & -z_2 & y_2 \\ \cdots & \cdots & \cdots \end{pmatrix}. \tag{6.4}$$

Consequently, weighted least square solution of the rotation vector $\mathbf{\Theta}$ obtained by using the pulsar coordinates data in the Table 6.12 and observation equation (6.3) is.

$$\mathbf{\Theta} = \begin{pmatrix} -7.4 & \pm 3 & mas \\ -11.9 & \pm 5 & mas \\ -9.1 & \pm 3 & mas \end{pmatrix} \tag{6.5}$$

Reciprocal square sum of VLBI and pulsar timing coordinates errors was used as weight of the weighted-least-square analysis. Errors of the solution represent only formal error. Figure 6.9 shows the angular differences of the directions to the pulsars between the two reference frames. Also rotation angles of the solution and residuals of the analysis are plotted in the figure. This figure shows that the last two pulsar's residuals are quite small comparing with those of first three pulsars. This is because the coordinates of two pulsars are measured very accurately by both VLBI and timing observation. Then, those two pulsars' data have larger weight in the LSQ analysis. VLBI coordinates accuracy of PSR B0329+54 and PSR B2021+51 are enough, but the coordinates accuracy from pulsar timing are not enough and need to be improved. In case of PSR B0355+54, both VLBI and pulsar timing coordinates needs to be improved.

The frame rotation vector estimated by Folkner et al.(1994) was

$$\mathbf{\Theta} = \begin{pmatrix} -2 & \pm 2 & mas \\ -12 & \pm 3 & mas \\ -6 & \pm 3 & mas \end{pmatrix} \tag{6.6}$$

The frame tie with pulsars was tied by Rodin and Sekido (2000) by using 4 pulsars with trigonometric formulation. In this study, formulation was done by using rectangular coordinates and precision of rotation angle was improved. The trial of the frame tie in this time was not enough to improve the result of Folkner et al., however, it was consistent within two sigma error level, even in the case of only 5 pulsars (effectively 2 pulsars) were used for rotation angle estimation. This result indicates that pulsar coordinates comparison between VLBI and pulsar timing is useful for frame tie between the ICRF and planetary ephemeris. And the accuracy of frame tie expected to be improved by using larger number of pulsars data.

Now new planetary ephemeris DE406 is widely used and it is announced that consistency with the ICRF is improved much better than DE200. Although most of pulsar coordinates from timing measurements are still based on DE200 ephemeris. To examine the consistency between the new ephemeris (DE406) and the ICRF, accurate pulsar coordinates on the new ephemeris are desirable.

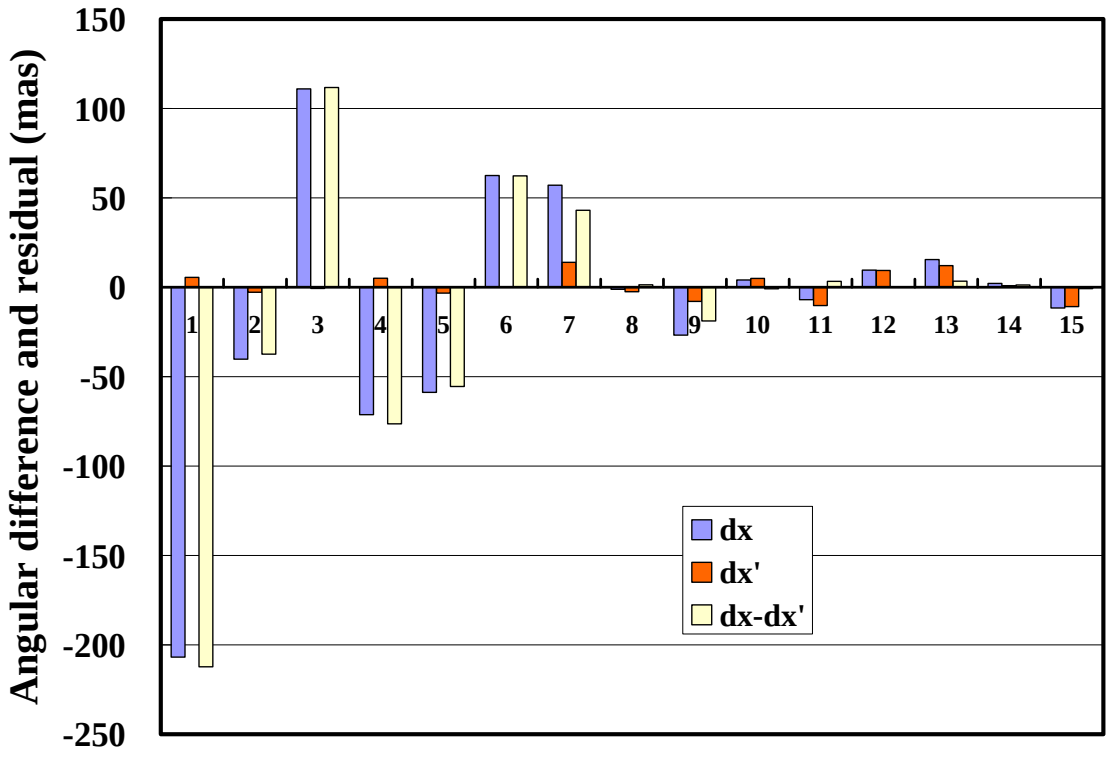

Figure 6.9: Angular differences and residuals of DE200-ICRF rotation angle estimation. The vertical axis indicates angular difference, rotation angle of a solution, and residual. The blue colored bars (denoted by dx) are angular differences of "VLBI - timing" of each Cartesian coordinates components toward the pulsars. The red colored bars (denoted by dx') are rotation angles of a solution, and yellow colored bars (denoted by dx-dx') are residuals of angles. The horizontal axis indicates the components of Cartesian coordinates of unit vector toward the pulsars used for frame tie. The each group of three numbers from 1, 2, 3 till to 13, 14, 15 correspond to the coordinates x, y, z of each pulsar: PSR B0329+54, PSR B035+54, PSR B2021+51, PSR B1257+12, and PSR B1937+21 in this order.

6.5 Summary

Astrometry analysis

Five pulsars' (PSR B0329+54, PSR B0355+54, PSR B0950+08, PSR B1933+16, and PSR B2021+51) coordinates are determined on the ICRF by using Japan - Russia VLBI observation. Absolute astrometry technique with group delay was used because it determines fiducial coordinates of pulsar on the ICRF.

Ionospheric excess delay correction technique by using the GIM/CODE (Chapter 4) was applied in VLBI analysis, and the usefulness of our method was confirmed by the test using ICRF source. The test of the ion-correction demonstrated that about 60 mas of systematic error, which included in the solution, was corrected. The pulsar VLBI data and ion-correction data were stored in Mark-III database system and analyzed with precise VLBI delay model calculation software CALC and least-square analysis software SOLVE. Following pulsars' coordinates were determined by our observations.

B0329+54 were observed at four epochs from 1995 to 1998. Then mean coordinates and proper motion of this pulsar were derived from our results within 4 mas and 3.5 mas/year precision, respectively. The derived pulsar coordinates and proper motions were consistent with the other interferometric and pulsar timing measurements within one-sigma error. Additionally, VLA measurement result by Fomalont et al.(1984) and VLBI coordinates by Bartel et al.(1985a) were used together with our data for proper motion derivation. The Bartel's coordinates were almost identical with those on the ICRF, and the most accurate proper motion for this pulsar (0.3 mas/year) was derived from the joint data set "Ours+Bartel". This proper motion agreed with that of Harrison et al.(1993) within three sigmas error range.

B0355+45's coordinates were determined at reference epoch 1995.20 with L-band observation within 20-50 mas precision. The success of the coordinate measurement is greatly owing to the signal-to-noise ratio improvement by pulsar gating function of the K4 correlator.

Interferometric coordinates of Fomalont et al.(1992) and pulsar timing coordinates by Arzoumanian et al.(1994) were consistent with our results within one-sigma error. The lower precision of this pulsar was due to insufficient observation time in March 1995 experiment. We will improve the measurement precision by following observations.

B0950+08 was observed at epoch 1996.36 and 1998.4 with L-band and S-band, respectively and pulsar coordinates were determined with precision of 90-350 mas at 1993.36 and 15-60 mas at 1998.40. The low precision result at 1996.36 was because of insufficient observation time for this pulsar. The larger ionospheric influence and larger beam size at L-band than S-band were partly responsible for the lower precision. Large correlation between right ascension and declination is owing to observational limitation of single baseline observation in east-west direction.

Gwinn et al.(1986) made the first parallax and proper motion measurement on this pulsar by VLBI. And the proper motion was almost consistent with that of Lyne et al.(1982), Although Brisken et al.(2000) claimed that Gwinn et al.'s proper motions are likely wrong due to mis-choice of side-lobe. Room of an argument remains on proper motion of this pulsar. It should be worthwhile to note that all of these measurements (Lyne et al.(1982), Gwinn et al.(1986), and Brisken et al.(2000)) were based on phase delay measurement. Thus it is potentially possible to take wrong choice of ambiguity in those analysis. The author believes that we are hopefully able to give a definite answer to the question on proper motion by following absolute astrometry observations.

B1933+16 was observed at epoch 1995.2 in L-band and its coordinates were measured with precision 50-150 mas. A combination of pulsar's coordinates and proper motion obtained by Fomalont et al.(1992) with VLA are consistent with our position within one sigma error. The proper motion derived through pulsar timing [*Downs and Reichley*,] 1983) are likely to be different from interferometric ones. The true proper motion will become obvious by following absolute astrometry observations, but not with the single Kashima-Kalyazin baseline. Since the single baseline observation produce elongated error ellipsoid in the same direction with that of expected proper motion (Figure 6.6), then multiple baseline observation should be desirable.

B2021+51 was observed at epoch 1995.2 in L-band and its coordinates were measured with 45-10 mas precision. The observation time was not sufficient for this source in the March 1995 experiment.

Both interferometric coordinates [*Campbell et al.,* 1996]) and timing ones [*Arzoumanian et al.,* 1994] are consistent with our result. Although interferometric proper motions are

inconsistent between Campbell et al. and Lyne et al.(1982). Both measurements are also based on phase delay measurements. Since March 1995 experiment was the first Kashima-Kalyazin VLBI observation, most of the pulsar were observed only for short time. And low correlation between the α and δ is possible with long time observation even with only single baseline, because the declination of this pulsar is high. So more improvement of the coordinates precision is promising.

Frame tie

Reference frame tie by using pulsar coordinates were performed with five pulsars including our results of PSR B0329+54 and PSR B0355+54. The rotation angle of reference frame from the DE200 to the ICRF was estimated with 3-5 mas precision. And it was almost consistent with results of Folkner et al.(1994). Unfortunately our pulsar coordinates did not make significant contribution for frame tie because of insufficient precision of pulsar timing coordinates, PSR B0329+54, PSR B2021+51, and insufficient precision of both methods, PSR B0355+54. But our trial demonstrated that pulsars are useful for frame tie. More accurate link of the reference frames should be possible if we could use larger number of accurate pulsars' coordinates on both reference systems.

Chapter 7

K4 Correlator and Pulsar Gating Function

7.1 Introduction

The Communications Research Laboratory has been developed data acquisition systems and correlation processing systems for VLBI since 1980s. The K3 VLBI system [*Kiuchi et al.,* 1991; *Hama et al.,* 1991; *Takahashi et al.,* 1991; *Kondo et al.,* 1991] was developed from 1979 to 1983 as a compatible system with the Mark-III VLBI system [*Whitney et al.,* 1976; *Clark, et al.,* 1985] developed by the Haystack observatory. It was successfully used for domestic and international geodetic VLBI experiments and measured the Pacific plate motion [*Koyama,* 1991] and east direction motion of the Chinese continent. The K3 correlator is a part of the K3-VLBI system. It has a gating function for a second-period pulsar signal and it effectively worked to increase the SNR of pulsar data observed in the Kashima-Usuda baseline pulsar VLBI experiment [*Hama et al.,* 1994; *Sekido et al.,* 1994]. However, the K3 correlator was designed to open the pulsar gate once in a parameter period (PP) and the minimum PP was 1 sec. The PP is an interval of time, where a set of hardware correlation parameters are used, and correlation integration is performed in this period. Thus, gating function of the K3 correlator was not effective for improvement of SNR of millisecond pulsar data. The K4-VLBI system was developed as upgraded VLBI system by using a cassette-type data recorder [*Kiuchi et al.,*]. The K4 correlator was developed as a part of the K4-VLBI system.

7.2 Overview of the K4 Correlation System

The K4 correlation processing system consists of K4 VLBI recorders, VLBI output interfaces, a host computer, and a data switcher. A block diagram and picture of the K4 correlation system are shown in Figure 7.1. Parameters of the K4 correlator and a comparison with the K3 correlator are summarised in Table 7.1.

The data processing performance for geodesy is almost the same on both correlators. The advanced features of the K4 correlator are its smaller size, lighter weight, intelligent CPU system, high rate network data output capability, two-bit sample data processing capability, and pulsar gating function adaptive to millisecond pulsar data. The volume of the K4 correlator is about 17 times smaller than the K3 correlator because of its integrated circuit technology, comprising custom LSIs and programmable logic-gate arrays. The K4 correlator employed a VME-bus system in the backplane and equipped with multi purpose CPU board (Motorola 68040) for delay-model calculation and for overall control of the correlator. Its Ethernet interface is used for data output via network file system (PC-NFS). Correlation output data is directly written

Table 7.1: Parameters of the K4 correlator and the K3 correlator.

Parameters	K3 correlator	K4 correlator
Logic IC	Standard monolithic logic IC	Custom LSI and Programmable logic gate array
Number of corr. units	14	16
Number of lags/unit	8 lags	18 lags
Clock rate	4, 8 MHz	4, 8 MHz
Min. parameter period	1 sec.	1 sec.
Fringe rotation performance		
Phase resolution	0.02 μradian	0.02 μradian
Max fringe rate	15.5 kHz (K=16)	15.5 kHz (K=16)
Max fringe rate acceleration	466 Hz/s	466 Hz/s
Pulsar gating period	Once in a PP	Any times in a PP
Data distribution mode[a]	No	Yes
Two bit mode	No	Yes
CPU	Z80	Motorola 68040
Data bus	Flat cable	VME-bus
Control line	GP-IB	GP-IB
Data output	GP-IB	Ethernet (NFS)
Size W/H/D (mm)	760/1800/800	450/315/450

to a hard disk of the PC-NFS server (host computer) at each PPs. Its GP-IB interface is used for communication with the host computer. The host computer manages correlation processing of all scans in a experiment and it sets up correlation processing parameters at the beginning of every scan.

The procedure of correlation processing for one scan is as follows. The host computer sets up correlation parameters (e.g., station coordinates, source coordinates, clock parameters, earth orientation parameters, and so on.) in the K4 correlator. Then the host computer sends commands to the K4 output interface (DFC-1100) to synchronise the data recorders (DIR-1000). After the recorders are synchronized, correlation processing starts and continues until scan end time or until time code data disappears in the data stream. The output data format of the K4 correlator is described in Appendix D.

7.3 Delay Model of K4 Correlator

7.3.1 Geometrical Delay

We assume $\mathbf{B}$ as the baseline vector in the International Terrestrial Reference Frame (ITRF) and let $\mathbf{S}$ be a unit vector in the direction of the radio source in the International Celestial Reference Frame (ICRF). When $\mathbf{B}$ is denoted by $\mathbf{B}'(t)$ in the ICRF, $\mathbf{B}'(t)$ is expressed with $\mathbf{B}$ as

$$\mathbf{B}'(t) = \mathbf{P}(t)\mathbf{N}(t)\mathbf{R}(t)\mathbf{W}(t)\mathbf{B}, \tag{7.1}$$

where $\mathbf{P}(t)$, $\mathbf{N}(t)$, $\mathbf{R}(t)$, and $\mathbf{W}(t)$ are coordinates rotation matrixes of precession, nutation, diurnal motion, and wobble, respectively. The IAU 1976 precession [*Liske et al.,* 1977] and IAU 1980 theory of nutation [*Seidelmann,* 1982; *Wahr, 1981*] are used to calculate $\mathbf{P}(t)$ and $\mathbf{N}(t)$. It is known that there are differences between the Earth rotation theory (IAU 1976 Precession and IAU 1980 Theory of Nutation) and the actual Earth orientation measured by VLBI. Thus, correction of nutation angle in longitude $\Delta\psi$ and obliquity $\Delta\epsilon$ called "celestial pole offset" (CPO) is necessary when the Earth rotation theory used. Each value of this correction is reported in IERS bulletin as dpsi and deps. Since the correction is in the order of a few tens of mas and

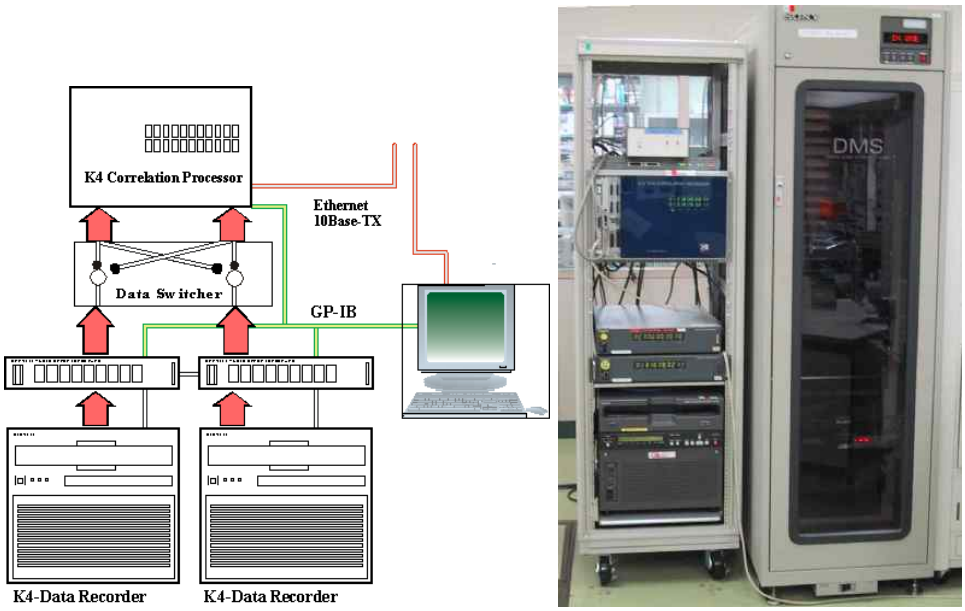

Figure 7.1: K4 correlation system

corresponds to a few nanosecond of delay on an inter-continental baseline, it is not so important for ordinary correlation processing, but it have to be be taken into account for the purpose of precise astrometry and geodesy. Wobble parameters and offset of UT1-UTC are taken from IERS bulletin B (final solutions of the Earth orientation by the IERS). More detailed on the procedure for transformation between the celestial and terrestrial systems is described in IERS conventions (1996) [*McCarthy,* 1996]. After the baseline vector fixed on the Earth is transformed to a vector in the celestial system, change of a radio source direction caused by aberration effect needs to be taken into account. Let $\mathbf{S}$, $\mathbf{S}'$, and $\mathbf{V}_{\rm obs}$ be a unit vector to the radio source in the ICRF, apparent direction of the radio source, and velocity of the observer (X-station) on the Earth in the solar barycentric coordinates system, respectively. The apparent direction of radio source $\mathbf{S}'$ is calculate by

$$\mathbf{S}' = \frac{\mathbf{S} - \mathbf{V}_{\rm obs}/c}{|\mathbf{S} - \mathbf{V}_{\rm obs}/c|}. \tag{7.2}$$

Then geometrical delay model used in the K4 correlator is computed by

$$\tau_{\rm GEO} = \mathbf{S}' \cdot \mathbf{B}'(\mathbf{t})/c. \tag{7.3}$$

7.3.2 Propagation Delay

VLBI observables contain several propagation delay components caused from ionosphere and neutral atmosphere of the Earth. Neutral atmospheric delay is composed of a dry-air component and water-vapour (wet) component. When n is refractive index, refractivity N ($=10^6(n-1)$) is expressed with the following formula [e.g., Thompson et al., 1994]

$$N = 77.6\frac{p_{\rm d}}{T} + 64.8\frac{p_{\rm v}}{T} + 3.776 \times 10^5 \frac{p_{\rm v}}{T^2}, \tag{7.4}$$

where $p_{\rm d}, p_{\rm v}$, and T are partial pressure of dry air, that of water vapor in hectopascals, and atmosphere temperature, respectively. This formula is accurate to better than 1% for frequency below 100 GHz [*Thompson et al.*, 1994]. By using densities of total air ($\rho_{\rm T}$) and water vapour ($\rho_{\rm v}$) in g/m^3, equation (7.4) is approximated around room temperature as follows

$$N \approx 0.2228\rho_{\rm T} + 1763\frac{\rho_{\rm v}}{T} = N_{\rm d} + N_{\rm v}, \tag{7.5}$$

Since hydrostatic equilibrium in the atmosphere can be assumed, a parcel of gas in static equilibrium between pressure and gravity obeys the equation

$$\frac{dP}{dh} = -\rho_{\mathrm{T}} g, \tag{7.6}$$

where g is the acceleration due to gravity, and h is the height above the Earth's surface. Under the condition of hydrostatic equilibrium, the excess pass length caused by the dry component does not depend on the height profile of the density, but only on the surface pressure P_0, given by

$$P_0 = g \int_0^\infty \rho_{\mathrm{T}}(h) dh. \tag{7.7}$$

By using equations (7.5) and (7.7) the excess path length caused from the dry component in the zenith direction is

$$L_{\mathrm{d}} = 10^{-6} \int_0^\infty N_{\mathrm{d}} dh = A P_0, \tag{7.8}$$

where A = 0.228 cm/hPa.

To take into account the contribution of dry troposphere component to propagation delay in VLBI observation, the K4 correlator delay model uses mapping function proposed by Chao (1970) and the zenith-delay model of Moran (1981). Thus, propagation delay due to the dry component at elevation angle El is

$$\tau_{\mathrm{dry}} = \frac{L_{\mathrm{d}}/c}{\sin(El) + \frac{0.00143}{\tan(El)+0.0445}}, \tag{7.9}$$

where c is the speed of light.

Because water vapour is poorly mixed in the troposphere, the propagation delay due to the wet component is not so accurately estimated from ground-based weather measurement data. And the magnitude of the delay is about one order smaller than that of the dry component, so the wet-component delay model is not included in the K4 correlator delay model. A ionospheric delay model is not also implemented in correlator delay model at present. To use phase delay as an observable for accurate astrometry, fringe phase connection between scans without ambiguity is essential. A correlator model is required to be as accurate as possible for such an application, since residual fringe rate must be kept as small as possible. We will continue to improve the correlator model by taking into account the gravitational bending due to the Sun, standard ionosphere model, and more sophisticated troposphere models [*Daivis et al.,* 1985; *Herring,* 1992; *Niell,* 1996].

7.3.3 Interpolation to Derive Correlator Delay Model

The K4 correlator integrates the data observed at the two stations by compensating the delay (described above) and fringe rate (Appendix A). This integration is performed during a short interval called the parameter period (PP), and the results are output every PP. The correlator updates the hardware correlation parameter set (see Table 7.2) in the every PP. Available parameter period is in the range from 1 to 8 seconds. To quickly calculate the hardware parameter set at every PP, the a priori delay models are calculated at five points separated by equal time intervals in a scan in advance of the start of processing. Then a fourth-order polynomial is fitted to the correlator-model delays at five points, and this polynomial and its derivatives are used for delay rate and acceleration computation.

$$\tau_{\mathrm{model}}(t) = a_4(t - t_{\mathrm{PRT}})^4 + a_3(t - t_{\mathrm{PRT}})^3 + a_2(t - t_{\mathrm{PRT}})^2 + a_1(t - t_{\mathrm{PRT}}) + a_0 \tag{7.10}$$

$$\frac{d\tau_{\mathrm{model}}}{dt}(t) = 4a_4(t - t_{\mathrm{PRT}})^3 + 3a_3(t - t_{\mathrm{PRT}})^2 + 2a_2(t - t_{\mathrm{PRT}}) + a_1 \tag{7.11}$$

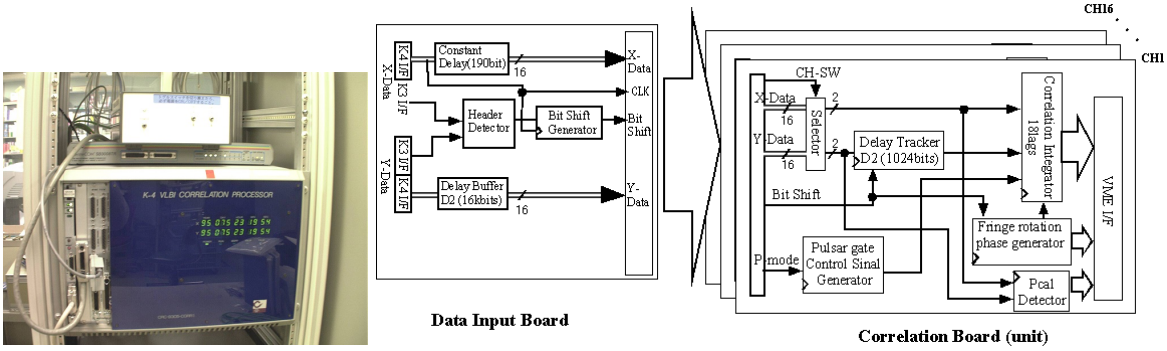

Figure 7.2: The K4 Correlator and its function block diagrams

$$\frac{d^2\tau_{\rm model}}{dt^2}(t) \quad = \quad 12a_4(t-t_{\rm PRT})^2 + 6a_3(t-t_{\rm PRT}) + 2a_2 \tag{7.12}$$

A time-point in each scan is defined as parameter reference time (PRT), which is usually middle point of each scan, and it is used for the reference epoch of the delay measurement.

7.4 K4 Correlator Hardware Architecture

The K4 correlation processor consists of a CPU board, a data input board, and 16 correlation boards. All of these board are connected to a backplane VME-bus, which is widely used high performance bus system. Figure 7.2 shows a photo of the K4 correlator (left) and its function block diagram (right). The three main functions of the correlator are delay compensation, fringe rotation, and integration.

7.4.1 Hardware Parameters

Delay compensation is accomplished by using three buffers: (1) a data synchronization function of VLBI output interfaces (DFC-1200), which enables two data-streams synchronization with certain amount of delay offset in one data stream with respect to another, (2) a common delay buffer (D1) on data input board of the K4 correlator, and (3) a delay tracker (D2) on each correlator board. Buffer (1) is realized by a function of DFC-1200 and the adjustable delay resolution is one-bit. The delay offset is set at the tape synchronization and is fixed during processing of one scan. Buffer (2) is a 16-kbit common delay buffer for all correlator boards. This delay buffer is also set at the beginning of correlation processing for each scan, and is fixed during the scan except for the case buffer (3) reached to the end of buffer (1024 bit). This buffer has not bit shift function, but only when the delay tracking by buffer (3) is not sufficient, the buffer (2) is used for delay tracking with combination with the buffer (3). Buffer (3) has 1024 bits delay with bit shift function.

Summarizing the above, the buffer (1) absorbs the large delay difference including geometrical delay and clock offset between two stations. The buffer (2) and (3) compensate for the dynamic change of delay in accordance with the correlator delay model (Section 7.3).

Fringe stopping (see Appendix A) is realized by multiplexing three-level-approximated sine and cosine functions. The fringe rotation phase is generated with taking into account up to the acceleration of the fringe phase. Delay tracking and fringe rotation architecture of the K4 correlator is basically the same as that of the K3 correlator [*Sugimoto and Hama,*, 1984; *Sugimoto et al.,* 1991]. Hardware parameters are listed in Table 7.2.

Delay tracking hardware parameters, T1 and ΔT (see Table 7.2 and Figure 7.3), are related

Table 7.2: K4 correlator hardware parameters

Parameter name	Description
T1	Number of bits until first bit shift occurs during PP (bit)
ΔT	Bit shift period (bit)
BSsign	Direction of bit shift (+1/-1)
ϕ_0	Initial phase of fringe rotation at beginning of PP
$\Delta\phi_0$	Initial fringe phase increments (0 - 2^{28})
K	After K-bit clock is counted, fringe phase increment by dϕ
B	After B-Byte clock is counted, dϕ increment 1 bit (2^{-28})
Jpol	Direction of $\pi/4$ jump, when fringe rotation is performed at the center of the video band
S_K	Sign of up/down of K-bit counter
S_B	Sign of up/down of B-Byte counter
P1	After P1 bit clock is counted, pulsar gate is open (bit)
ΔP	Pulsar gate is open, during ΔP bit clocks (bit)
P2	Interval time during pulsar gate is closed (bit)

with physical parameters, delay and delay rate $(\tau, \dot{\tau})$, as follows:

$$\Delta T = 1/|\dot{\tau}| \tag{7.13}$$

$$T1 = \begin{cases} |(0.5 - fbit)/\dot{\tau}| & (\dot{\tau} > 0) \\ |(0.5 + fbit)/\dot{\tau}| & (\dot{\tau} < 0) \end{cases} . \tag{7.14}$$

Where fbit is fractional bit difference between correlator delay model and actual digital delay tracking at the beginning of PP. The bit delay tracking is schematically drawn in Figure 7.3. Also a block diagram of the fringe-rotator's phase generator is shown in the right panel of Figure 7.3. The fringe-rotator's phase is expressed by 28 bits. Thus phase resolution is $(2\pi/(2^{28}-1) =)$ 11.7 nano radians per bit. Fringe rotation frequency is controlled by a K-bit counter and fringe rate acceleration is controlled by a B-byte counter. The fringe rotator phase (ϕ) and fringe frequency (Fr) are expressed by the hardware parameters as

$$\begin{aligned} \phi &= \frac{2\pi}{2^{28}}\{\phi_0 + (\Delta\phi_0 + S_B\frac{Sr}{8B}t)S_K\frac{Sr}{K}t\} \\ &= \frac{2\pi}{2^{28}}(\phi_0 + S_K\Delta\phi_0\frac{Sr}{K}t + S_KS_B\frac{(Sr)^2}{8KB}t^2) \end{aligned} \tag{7.15}$$

and

$$Fr = 2^{-28}(S_K\Delta\phi_0\frac{Sr}{K} + S_KS_B\frac{Sr^2}{4KB}t), \tag{7.16}$$

where, ϕ_0 is the initial phase of the fringe rotator at the beginning of PP ($\phi_0 = 1 \sim 2^{28}-1$), Sr is Sampling rate (Samples/sec.),B is a B-byte counter (B=1 $\sim 2^{25}-1$), K is K-bit counter (K=1 $\sim$ 16), S_K is the up/down sign of K bit counter, S_B is the up/down sign of the B-byte counter, and $\Delta\phi_0$ is initial phase increment ($\Delta\phi_0 = 1 \sim 2^{28}-1$). Fringe rotator phase and fringe rate are related with the delay parameters as follows:

$$\phi = f_{\rm RF} \times \tau_{\rm model} \tag{7.17}$$

$$Fr = f_{\rm RF} \times \dot{\tau}_{\rm model}. \tag{7.18}$$

$f_{\rm RF}$ is radio frequency of the observation. Correlator delay model $\tau_{\rm model}$ and $\dot{\tau}_{\rm model}$ are described in Section 7.3. Then hardware parameters are determined from equations (7.15), (7.16), (7.17), and (7.18).

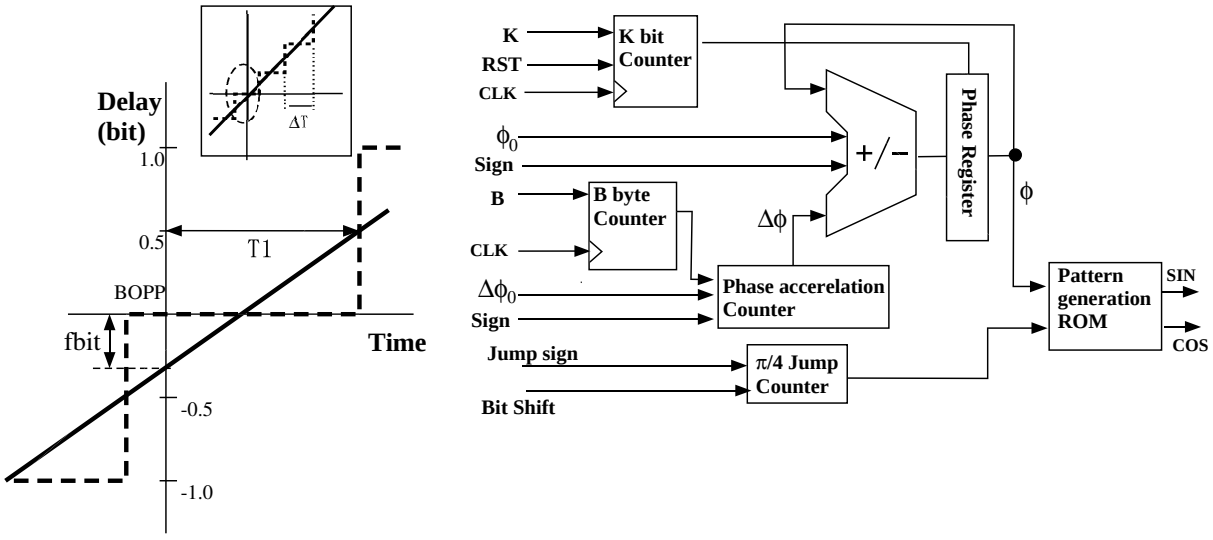

Figure 7.3: Schematic view of delay tracking and fringe rotation block diagrams. Left: solid line indicates the correlator delay model and dashed line indicates delay tracking by bit shifts. "fbit" is fractional delay difference between correlator delay model and actual delay tracking at the beginning of the parameter period (BOPP). Right: block diagram of the fringe-rotation phase generation circuit. The K bit counter and $\Delta\phi$ are used to generate fringe frequency and the B byte counter is used to generate fringe acceleration (see text).

7.4.2 Hardware Components

Each component of the correlation processor is described as follows:

Data Input Board Its basic function is buffering of the Y data for delay tracking (buffer (2) in Section 7.4.1) and generating a bit-shift signal. Its function block diagram is indicated in the right panel in Figure 7.2.

Correlation Board One board has function of a cross correlation unit with fringe stopping, pulsar gating, and p-cal signal detection for a pair of data steams. Each correlator board has 18 lags of delay window. Sixteen correlator boards (units) are implemented in one correlator and 16 simultaneous channels of correlation processing are possible. The selector block (Figure 7.2) has the capability to choose one pair of 16 data-pairs streams. This function is useful for fringe search mode and for high-resolution spectrum monitoring, in which 18 lags of 16 correlation units are arranged in series, and it works as a one-channel correlator with 288 lags. The pulsar gating function is used to increase signal-to-noise ratio of the pulsar data. More detail of pulsar gating is described in Section 7.6.

CPU Board Real-time OS pSOS on a Motorola 68040 CPU is used for control overall of the K4 correlator and calculation of correlator delay model. When the K4 correlator is switched on, the correlator downloads the system program from the host computer by using a tftpboot protocol through a local area network (LAN). Thus, software can be upgraded very easily by simply replacing the boot-up file on the host computer. Commands and status communication for the correlation process with host computer are performed via a GP-IB interface. Correlation output data is directly written to the hard disk of the host computer by a network file system (NFS) through the LAN. The console communication port with an RS-232C interface is also connected to the host computer and is used for status monitoring of the correlator as well as switching to debug mode.

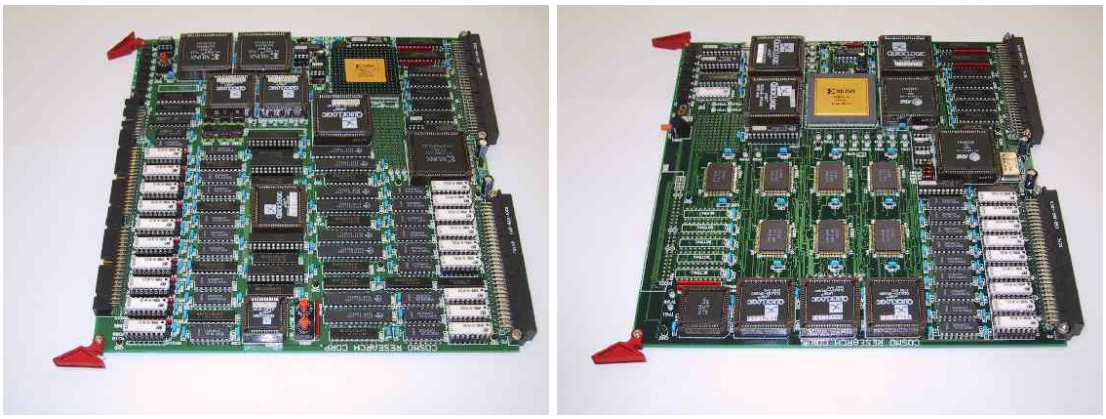

Figure 7.4: The K4 correlator data input board (left) and correlation board (right).

7.5 K4 Correlator Functions

7.5.1 Processing Modes

Geodetic correlation mode (G-mode) This is most basic operation mode, in which 16 pairs of data streams from two data recorders are fed to 16 correlation units and cross correlation processing of 16 data channels are performed in parallel.

Fringe search mode (S-mode) Delay lags are arranged in series with all correlation units. One pair of data channels is selected from 16 pairs of data channels. Then one channel pair are processed with 288 (=16x18) lags. This mode is useful for fringe search when the clock offset of the observation station is unknown. It is also useful for monitoring a radio source spectrum or a video band characteristic with high frequency spectrum resolution. When video bandwidth is 2 MHz, the frequency resolution is about 13 kHz.

Pulse Search mode (PS-mode) When pulsar gating is applied to pulsar VLBI observation data, pulse phase has to be determined before actual correlation processing with pulsar gating function. The PS-mode is used to find a pulsar fringe and to determine pulse phase offset.

In pulse search mode, one pair of data streams is delivered to 16 correlation units as the same as in S-mode. The delay arrangement is the same with G-mode, and pulse gate opening timing differs by one pulse gate width from one correlation unit to the other. Normally we use pulse period divided by integral number, $P/N_{\rm div}$, as the gate width. For example, when $N_{\rm div}$ equals 16, the pulse gate width is $\Delta P = P/16$. In this case, the whole pulse period is covered by 16 correlation units by using PS-mode. If fringe is detected at unit i, $(i-1)/N_{\rm div}$ is the pulse phase offset. Figure 7.5 shows gate timing of the PS-mode schematically.

Pulsar mode (PN-mode) After pulse offset $P1$ and optimum division numbers ($N_{\rm div}$) for each pulsars are determined by using PS-mode, pulsar data is processed in PN-mode. Each 16 pairs of data channels are cross-correlation processed by the pulsar gating function in parallel. Difference of pulse arrive time caused from dispersion of the ISM is taken into account in the gate opening timing of each channel.

Auto correlation mode (A-mode) Auto correlation is possible by using a data switcher (left picture in Figure 7.2), which selects a data stream from X and Y as the input for the correlator. This mode is useful to check power-spectrum characteristic of the video channels of each station.

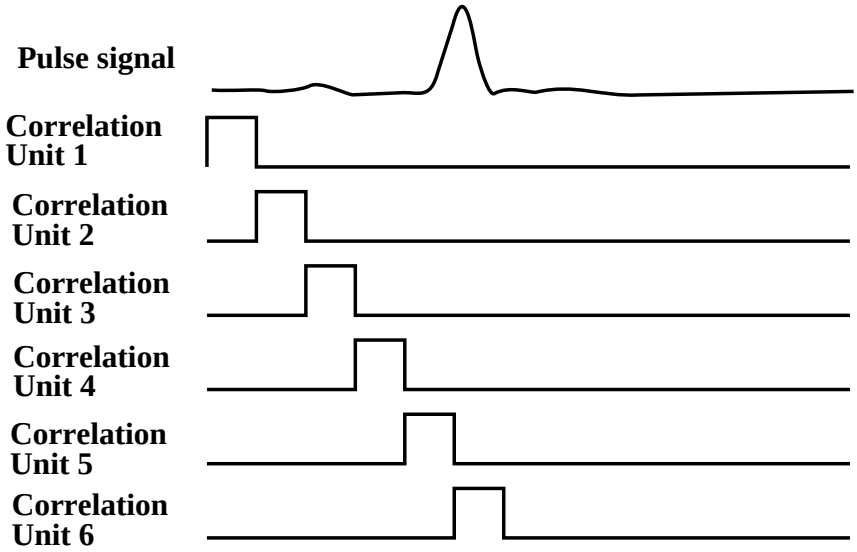

Figure 7.5: Gate timing of pulse search mode of the K4 correlator. Horizontal direction is time and the most upper line indicate pulsar signal schematically. The following lines indicate gate timing of pulse search mode. The gate opening timing differs sequentially from one correlator unit to the other by the gate width.

7.6 Pulsar Gating Function

The power of pulsar signal is concentrated on its pulse. Thus, pulsar gating is essential to increase the signal-to-noise ratio in correlation processing of pulsar VLBI data. To control the pulsar gate synchronously with observed pulses, we need to know pulse arrival time and its period precisely. The high-precision pulse period and pulse-phase calculation software CALP was developed for the K4 correlator gating function by Dr. Alexander E. Rodin of Lebedev Physical Institute and the author. The relative accuracy of pulse period calculation by CALP is better than 10^{-9}. This precision is enough to keep the pulse signal from millisecond pulsar for half a day within the gate width of several μ seconds.

7.6.1 Required Accuracy of Pulsar Period

Cross correlation process of VLBI data is performed by updating the set of hardware correlation parameters (Table 7.2) at every PP. The number of pulses in observation time (T) is T/P, where P is the pulsar period. Pulsar gating is a function that integrates the data only part of the pulsar's pulse by applying a gate synchronously with the pulse arrival time. Let W be width of the pulsar gate window. When ΔP is error of pulse period to control the pulsar gate, the shift of timing relation between the pulsar gate and actual pulse arrival time is $\Delta P \times T/P$. Since the pulse signal in the data have to be kept within the gate width, W, of the K4 correlator. That is express as $\Delta P \times T/P << W$. Here, T is larger than at least the time of one scan (i.e., 120-1000 sec), the relative accuracy of the pulsar period has to satisfy the following condition:

$$\frac{\Delta P}{P} < \frac{W}{T}. \tag{7.19}$$

For example, we consider pulsar PSR 1937+21 with period P of 1.6 ms. We assume the pulse width is 1% of pulse period ($W = 0.01P = 1.6 \times 10^{-5}$ sec) and $T = 1000$ sec. Then $\Delta P/P < 1.6 \times 10^{-8}$.

The shift of pulse with respect to the gate window can arise not only from errors of pulsar period but also from pulsar period changes due to acceleration of the observer caused by the

Table 7.3: Allowable time interval $T_{\rm limit}$ to use pulsar gating with constant pulse period. The pulse period P of 1.6 ms and binary motion period $T_{\rm bin}$ of 0.1 day are assumed here.

α (m/s^2)	$T_{\rm limit}$ (s)	$\Delta P/P$	Comment
6×10^{-3}	$1789\sqrt{\frac{P}{1.6ms}}$	3.2×10^{-6}	Earth rotation
3×10^{-2}	$565\sqrt{\frac{P}{1.6ms}}$	1.5×10^{-5}	Earth evolution
3×10^{2}	$5.6\sqrt{\frac{P}{1.6ms}}T_{\rm bin}$	5.6×10^{-6}	Pulsar binary motion

Earth's rotation, the Earth's orbital motion, or acceleration of the pulsar, which is large when the pulsar is in a binary system. The change of a pulsar period δP during time interval t can be evaluated as

$$\frac{\delta P(t)}{P} \sim \frac{v}{c} = \frac{\alpha\, t}{c}, \tag{7.20}$$

Where, α is acceleration caused from the above reasons, and c is the speed of light. The pulse-phase drift during integration time ($T_{\rm limit}$) must be less than W. The following condition is then derived.

$$\frac{1}{P}\int_0^{T_{\rm limit}} \delta P {\rm d}t = \frac{\alpha}{c}\int_0^{T_{\rm limit}} t\,{\rm d}t < W, \quad T_{\rm limit} < \sqrt{\frac{2Wc}{\alpha}} = \sqrt{\frac{2Pc}{N_{\rm div}\alpha}}. \tag{7.21}$$

Where, we assumed the gate width W equals $P/N_{\rm div}$. Consequently, pulse changes its phase by W in the time scale of $\sqrt{\frac{2Pc}{N_{\rm div}\alpha}}$. The orders of acceleration contributions from the Earth's rotation, Earth's motion around the Sun, and binary pulsar motion (0.1-day orbital period is assumed) are $6 \times 10^{-3}, 3 \times 10^{-2}$, and 3×10^{2} m/sec^2, respectively. Table 7.3 lists examples of the time interval limit $T_{\rm limit}$ and change of period P when we assume $N_{\rm div} = 100$ and P=1.6 ms (PSR 1937+21). This table indicates that integration time of correlation processing by using fixed pulsar period is limited up to several hundreds seconds even if it is single pulsar. In the case of binary pulsar (0.1 day binary period), the pulsar period must be updated very frequently.

7.6.2 Calculation Software for Pulsar Phase and Period

Algorithm

A comprehensive theory of single pulsar timing has been given by Doroshenko and Kopeikin (1990), and the analysis of pulsar motion in a binary system has been worked out in several studies [*Blandford,* 1976; *Damour and Deruelle,* 1986; *Haugan,* 1985]. We used the theory of these studies to construct pulsar timing calculation software. The algorithm for calculating pulsar phase and pulsar period consists of the following steps:

1. Conversion of the pulse time of arrivals (TOA) from the UTC time scale to the terrestrial time scale (TT) and the barycentric time scale (TB).

2. Calculation of several correction terms, so called Roemer correction, which compensates for the Earth's motion around the solar system barycenter (SSB), Shapiro delay (the relativistic delay of the radio signal in the gravitational field of the solar system), and the dispersion delay due to propagation of the radio signal through interplanetary and interstellar plasma. Calculation of observer's velocity with reference to the SSB.

3. In case of a binary pulsar, the software must be able to calculate corrections inherent in pulsar motion around the barycenter of the binary system, and calculate pulsar velocity with reference to the barycenter of the binary system.

4. Calculation of pulsar phase and pulsar period.

Time Scale Conversions

Since pulsar phase and period are calculated in TB (Time of SSB) time scale, the time scale on the Earth has to be converted to TB scale. The UTC (Coordinated Universal Time) and the TAI (International Atomic Time) time scale are related by the formula

$$\mathrm{TAI} = \mathrm{UTC} + k, \tag{7.22}$$

where k - is an integral number of seconds introduced to keep the difference UT1-UTC within 0.5 second. The actual value of k can be taken from the IERS (International Earth Rotation Service) bulletin. The relation between TAI and TT (Terrestrial Time) is

$$\mathrm{TT} = \mathrm{TAI} + 32.^s184, \tag{7.23}$$

where a shift of 32.184 sec is caused for historical reasons.

TT and TB time scales differ only by periodic and mixed terms as

$$\mathrm{TB} = \mathrm{TT} + \sum_i (A_i + B_i T + C_i T^2 + D_i T^3 + E_i T^4) \sin(\omega_i T + \varphi_i), \tag{7.24}$$

where A_i, B_i, C_i, D_i, E_i, ω_i, and φ_i are constants, and $T = (JD - 2451545)/325250$ in TT time scale. Relation (7.24) is expressed in ready computational form in several works [*Fairhead and Bretagnon,* 1990; *McCarthy,*, 1996].

Pulsar Phase

The pulsar phase observed by a fictional observer at the SSB in the empty space is expressed by the formula

$$N(t) = \nu_0 \Delta t + \frac{1}{2}\dot{\nu}\Delta t^2 + \frac{1}{6}\ddot{\nu}\Delta t^3 + \ldots, \tag{7.25}$$

where $\Delta t = t - t_0$, t_0 is the initial epoch of observations taken from the pulsar catalog [*Taylor et al.,* 1993], t is time of arrival of the pulse phase $N(t)$ to the the solar system's barycenter in TB scale, and ν_0, $\dot{\nu}$, and $\ddot{\nu}$ are the pulsar frequency, and its 1st and 2nd derivative respectively at epoch t_0 (ν_0, $\dot{\nu}$, and $\ddot{\nu}$ are taken from the pulsar catalog). The moment of arrival at the barycenter t is related to the TOA t_{OBS} to observer with barycentric coordinates $\mathbf{x}_{\mathrm{OBS}}$ by the formula as follows,

$$\begin{aligned} t = \; & t_{\mathrm{OBS}} + \frac{1}{c}(\mathbf{k}\cdot\mathbf{x}_{\mathrm{OBS}}) - \frac{1}{2Rc}|\mathbf{k}\times\mathbf{x}_{\mathrm{OBS}}|^2 + \sum_a \frac{2GM_a}{c^3}\ln(r_{\mathrm{OBS,a}} + (\mathbf{r}_{\mathrm{OBS,a}}\cdot\mathbf{k})) + \\ & \Delta_{\mathrm{orb}} - 10^{-2}\left(\frac{1}{f_r^2} - \frac{1}{f_0^2}\right)\frac{DM}{2.41}, \end{aligned} \tag{7.26}$$

where t_{OBS} is in TB time scale and is obtained after a conversion of the actual pulse observation time $t_{\mathrm{OBS,UTC}}$ from the UTC time scale to the TB one by means of formulae (7.22)-(7.24)[*Doroshenko and Kopeikin,* 1990]. And $\mathbf{r}_{\mathrm{OBS,a}} = \mathbf{x}_{\mathrm{OBS}} - \mathbf{x}_{\mathrm{a}}$ and $\mathbf{x}_{\mathrm{a}}$ are the coordinates of the graviting body calculated at time t_{a}, i.e.;

$$t_{\mathrm{a}} = t_{\mathrm{OBS}} + \frac{1}{c}(\mathbf{k}\cdot\mathbf{r}_{\mathrm{OBS,a}}). \tag{7.27}$$

In equations (7.26), $r_{\mathrm{OBS,a}} = (\mathbf{r}_{\mathrm{OBS,a}}\cdot\mathbf{r}_{\mathrm{OBS,a}})^{1/2}$, $\mathbf{k}$ is a unit vector directed towards to the pulsar corrected for its proper motion, f_r is the frequency in gigahertz of a radio emission received at

time $t_{\rm OBS}$, f_0 is the reference frequency in the barycenter coordinate system, DM is dispersion measure in pc/cm^3, and $\Delta_{\rm orb}$ is the correction for the motion of a pulsar in a binary system.

The term $\frac{1}{c}(\mathbf{k}\cdot\mathbf{x}_{\rm OBS})$ is called the Roemer delay. The term $\frac{1}{2Rc}[\mathbf{k}\times\mathbf{x}_{\rm OBS}]^2$ expresses the effect that the pulsar's signal is not a plane wave but a spherical one. Its value is approximately 1.2 μs when R is 1 kpc. The term $\sum_a \ldots$ is called the Shapiro delay. The term with DM in equation (7.26) is the dispersion delay of the radio signal in interstellar and interplanetary plasma. $\mathbf{x}_{\rm OBS}$ and $\Delta_{\rm orb}$ are calculated in the following paragraph.

Coordinate Transformation

The coordinates of antenna $\mathbf{x}_{\rm OBS}$ are given by

$$\mathbf{x}_{\rm OBS} = \mathbf{x}_{\rm be} + \mathbf{w}, \tag{7.28}$$

where $\mathbf{x}_{\rm be}$ is the vector from barycenter to geocenter given from an ephemeris, and $\mathbf{w}$ is the vector from geocenter to antenna, calculated by formula

$$\mathbf{w} = \mathbf{NPS}\,\mathbf{y}, \tag{7.29}$$

where **N, P,** and **S** are the matrixes of nutation, precession, and diurnal rotation, respectively. $\mathbf{y}$ is the vector of the antenna in a coordinate system rigidly fixed to the Earth (in the ITRF). Matrixes **N** and **P** are necessary for transformation of the antenna coordinates to celestial ones in the same epoch (usually J2000.0) with the ephemeris. We referred to IERS conventions (1996) [*McCarthy,* 1996] for the coordinates transformation. These matrixes are expressed as follows:

$$\mathbf{N} = \mathbf{p}(-\epsilon_0 - \Delta\epsilon)\,\mathbf{r}(-\Delta\psi)\,\mathbf{p}(\epsilon_0), \tag{7.30}$$

$$\mathbf{P} = \mathbf{r}(-z_A)\,\mathbf{q}(\theta_A)\,\mathbf{r}(-\zeta_A), \tag{7.31}$$

$$\mathbf{S} = \mathbf{r}(-S). \tag{7.32}$$

Here, $\mathbf{p}$, $\mathbf{q}$, and $\mathbf{r}$ are rotation matrixes around coordinate axis x, y, and z by arbitrary angle a.

$$\mathbf{p} = \begin{pmatrix} 1 & 0 & 0 \\ 0 & \cos a & \sin a \\ 0 & -\sin a & \cos a \end{pmatrix}, \tag{7.33}$$

$$\mathbf{q} = \begin{pmatrix} \cos a & 0 & -\sin a \\ 0 & 1 & 0 \\ \sin a & 0 & \cos a \end{pmatrix}, \tag{7.34}$$

$$\mathbf{r} = \begin{pmatrix} \cos & \sin a & 0 \\ -\sin a & \cos a & 0 \\ 0 & 0 & 1 \end{pmatrix}. \tag{7.35}$$

The nutation in longitude $\Delta\psi$ and obliquity $\Delta\epsilon$ is computed by using IAU 1980 Theory of Nutation [*Seidelmann,* 1982; *Wahr, 1981*].

ζ_A, z_A, and θ_A are the precession parameters from the IAU 1976 model. Their expressions are taken from the paper by Lieske et al. (1977).

$$\begin{aligned} \zeta_A &= 2306''.2181\ T + 0''.30188\ T^2 + 0''.017998 T^3, \\ z_A &= 2306''.2181\ T + 1''.09468\ T^2 + 0''.018203 T^3, \\ \theta_A &= 2004''.3109\ T - 0''.42665\ T^2 - 0''.041833 T^3, \end{aligned} \tag{7.36}$$

here $T = ({\rm JD} - 2451545)/36525$. Greenwich true sidereal time is necessary for transformation of the antenna coordinates from a coordinate system rotating with the Earth to a coordinate

system fixed to the equinox. The Greenwich mean sidereal time at 0^h UT1 is calculated by the formula

$$S_0 = 6^h 41^m 50^s.548\,41 + 8\,640\,184^s.812\,866\,T' + 0^s.093\,104\,T'^2 - 6^s.2 \cdot 10^{-6}\,T'^3, \tag{7.37}$$

where $T' = \frac{JD'-2451545.0}{36525}$, and JD' is the Julian date at 0^h UT1. The Greenwich true sidereal time S at UT1 is expressed as

$$S = S_0 + r[(\mathrm{UT1} - \mathrm{UTC}) + \mathrm{UTC}] + d\alpha, \tag{7.38}$$

where

$$r = 1.0002737909350795 + 5.9006 \times 10^{-11}\ T' - 5.9 \times 10^{-15}\ T'^2. \tag{7.39}$$

The nutation in right ascension (equation of equinox) $d\alpha$ can be found by formula

$$d\alpha = d\psi \cos\epsilon_0, \tag{7.40}$$

where $d\psi$ is the nutation in longitude, and ϵ_0 is the mean obliquity given by

$$\epsilon_0 = 23^\circ 26' 21''.448 - 46''.8150\,T - 0''.000\,59\,T^2 + 0''.001\,813\,T^3, \tag{7.41}$$

where T is the same as that in formulae (7.36).

Delay for Binary Orbit

The correction Δ_{orb} compensates for the pulsar motion around the barycenter of the binary system. A derivation of Δ_{orb} with sufficient accuracy has been done by Blandford and Teukolsky [*Blandford and Teukolsky,* 1976]:

$$\begin{aligned}\Delta_{\mathrm{orb}} = \quad & -\alpha(\cos E - e) - (\beta+\gamma)\sin E \\ & - \frac{(\alpha \sin E - (\beta+\gamma)\cos E)[\alpha(\cos E - e) + (\beta+\gamma)\sin E]}{\mathcal{P}(1 - e\cos E)},\end{aligned} \tag{7.42}$$

where

$$\alpha = x\sin\omega, \quad \beta = (1-e^2)^{1/2} x\cos\omega, \mathrm{and} x = a_1 \sin i. \tag{7.43}$$

Here, ω is angular distance of the periastron from the line of nodes, x is projection of semi-major axis a_1 to line of sight, and i is inclination angle of the orbit. And γ is given by

$$\gamma = \frac{M_2^2(M_1 + 2M_2)\mathcal{P}e}{a_1(M_1+M_2)^2}. \tag{7.44}$$

Here, $\mathcal{P} = P/2\pi$, P is the orbital period, e is the orbital eccentricity, and M_1 and M_2 are the masses of the pulsar and companion, respectively. Eccentric anomaly E can be found from the solution of Kepler equation:

$$E - e\sin E = (t - t_\Pi)/\mathcal{P}, \tag{7.45}$$

where t_Π is the time of periastron passage. The values t_Π, x, e, ω, and γ are taken from the pulsar catalog [*Taylor et al,* 1993].

Pulsar Period

Principally, pulsar period at the observer is calculated as a derivative of pulse phase. It is expressed as the first derivative of equation (7.25) with UTC. This equation is expressed in TB time scale. To calculate pulsar period in such a way, the coefficient of dt_{TB}/dt_{TT} has to be taken into account. Another way to calculate the apparent pulsar period is to calculate the Earth's velocity from ephemeris DE405. Below, this latter method is used. Derivative of the third term in the right hand side of equation (7.26) is of the order 10^{-12}, which is negligible. The derivative of the fourth term in the right hand side of equation (7.26) with respect to TB, in the case of small angular distance from the Sun to pulsar, is of the order 10^{-9}. Usually pulsars are observed at large angular distances from the Sun, so this terms becomes much smaller and it is negligible for the purpose of pulsar gating. (When angular distance between a pulsar and the Sun is 10 degrees, this term is in the order of 10^{-11}.) Hence, the Doppler effect due to the Earth's motion around the SSB and binary pulsar motion are taken into account in the pulsar-period calculation.

The apparent rotational frequency of the pulsar $\nu_{\rm app}$ is calculated by the following formula instead of a numerical derivation of pulsar phase.

$$\nu_{\rm app} = \nu(1 + \mathbf{V} \cdot \mathbf{k}/c)^{-1}. \tag{7.46}$$

$\mathbf{V}$ is relative velocity between the pulsar and the observer ($\mathbf{V} = \mathbf{V}_{\rm psr} - \mathbf{V}_{\rm obs}$), and $\mathbf{k}$ is unit vector from the observer to the pulsar. The velocity of antenna $\mathbf{V}_{\rm obs}$ is calculated as the sum of the velocity of the Earth's center of mass $\mathbf{V}_{\rm be}$ around the SSB and the velocity of the antenna $\mathbf{V}_{\rm A}$ relative to the Earth's center of mass:

$$\mathbf{V}_{\rm obs} = \mathbf{V}_{\rm be} + \mathbf{V}_{\rm A}. \tag{7.47}$$

Velocity $\mathbf{V}_{\rm be}$ is taken from the planetary ephemeris. Velocity $\mathbf{V}_{\rm A}$ is calculated by

$$\mathbf{V}_{\rm A} = \mathbf{PN}[\omega \times \mathbf{Sy}], \tag{7.48}$$

where **P, N, S,** and **y** have the same meaning as in equation (7.29), ω is the angular rotational speed of the Earth, and $[\mathbf{a} \times \mathbf{b}]$ denotes the cross product of vectors **a** and **b**.

$\mathbf{V}_{\rm psr}$ can be found by taking the time derivative of formula (7.42):

$$\begin{aligned}\frac{\mathbf{V}_{\rm psr}}{c} = \quad & \frac{\alpha \sin E - (\beta + \gamma)\cos E}{\mathcal{P}(1 - e\cos E)} - \\ & \frac{(\alpha \cos E + (\beta + \gamma)\sin E)(\alpha(\cos E - e) + \beta \sin E) - (\alpha \sin E - (\beta + \gamma)\cos E)^2}{\mathcal{P}^2(1 - e\cos E)^2} + \\ & \frac{(\alpha \sin E - (\beta + \gamma)\cos E)(\alpha(\cos E - e) + (\beta + \gamma)\sin E) e \sin E}{\mathcal{P}^2(1 - e\cos E)^3}.\end{aligned} \tag{7.49}$$

Formula (7.49) takes into account $\frac{dE}{dt} = \frac{1}{\mathcal{P}(1 - e\cos E)}$.

Comparing Software CALP with Other Software

On the basis of above formulae, a software CALP was developed to calculate pulsar's phase and period. It takes pulsar name, epoch, reference frequency, and observation station coordinates in the ITRF as input parameters. Then it outputs pulse phase and pulse period. In order to ensure the correctness of the calculation, comparison of pulse phase and pulse frequency were made with reference to timing software TEMPO [*Taylor and Weisberg,* 1989], and TIMAPR

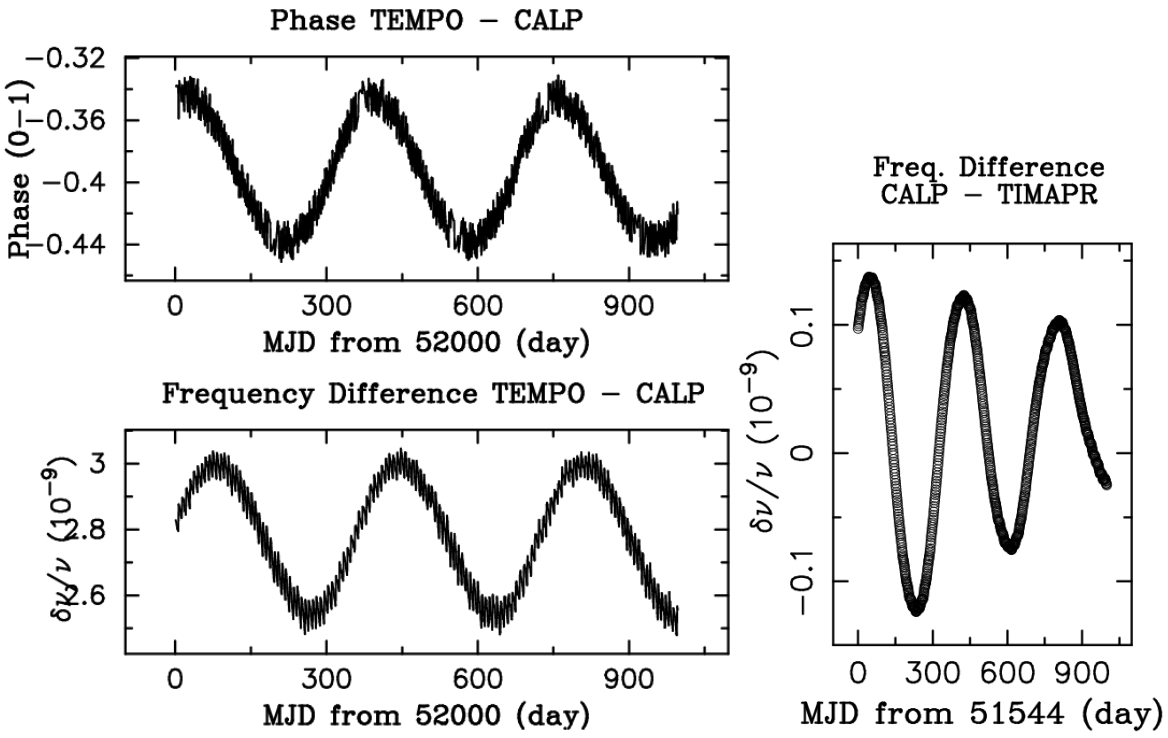

Figure 7.6: Comparison of pulsar phase and frequency computed by CALP and those TEMPO and TIMAPR (PSR B1937+21). Left two panels indicates pulse arrival phase (upper) and pulse period (lower) compared between CALP and TEMPO. Right panel shows pulsar period comparison between CALP and TIMAPR.

[*Doroshenko and Kopeikin,* 1990; *Doroshenko and Kopeikin,* 1995]. Figure 7.6 shows pulse period comparison on single pulsar PSR B1937+21. Difference of pulse period between CALP and TIMAPR is about 3 $^{-9}$ and that between CALP and TIMAPR is 1 $\times 10^{-10}$. Deviation of pulse period by 3 $\times 10^{-9}$ correspond to keep the pulse within 30 μsec (= 1/40 pulse period) for 3.6 hours. Figure 7.7 shows pulse period comparison on binary pulsar PSR B1855+09. Difference of pulse period between CALP and TIMAPR is up to 8 $^{-9}$ and that between CALP and TIMAPR is 4 $\times 10^{-10}$. Deviation of pulse period by 8 $\times 10^{-9}$ correspond to keep the pulse within 134 μsec (= 1/40 pulse period) for 4.6 hours. These precisions are enough for the gating function to find a fringe and use the pulse phase for a few hours without re-adjustment. Reasons of the difference of predicted pulse periods among those software are caused from difference of binary orbit model and ephemeris used in each software.

Pulsar Gate Control Software

The pulsar gate is controlled by hardware parameters P1, P2, and Δ P in unit of bits. The relation between these parameters is shown in Figure 7.8. Here, P1 is the interval from the beginning of PP until to first pulsar gate is opened. ΔP is gate width, and P2 is the bit interval during which the gate is closed. Pulsar period and hardware parameters are thus related as follows:

$$P1 = (1 - \psi_{\rm BOPP})PSr, \tag{7.50}$$

$$\Delta P = W \times Sr, \tag{7.51}$$

$$P2 = (P - W)Sr, \tag{7.52}$$

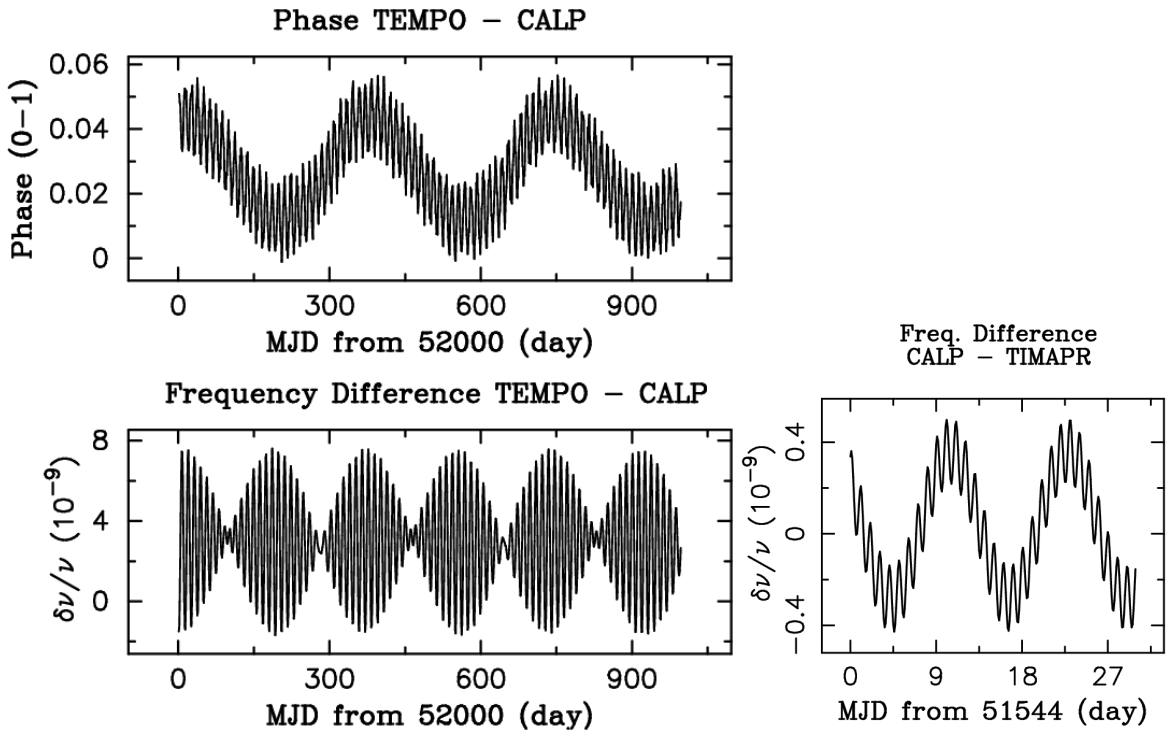

Figure 7.7: Comparison of pulsar phase and frequency computed by CALP, TEMPO, and TIMAPR for binary pulsar PSR1855+09. This pulsar's pulse period is 5.3 ms and orbital period is 12.3 days, respectively.Left two panels indicates pulse arrival phase (upper) and pulse period (lower) compared between CALP and TEMPO. Right panel shows pulsar period comparison between CALP (excluding higher order term of pulsar binary motion) and TIMAPR.

where P is pulse period (sec), W is pulse width (sec), and $\psi_{\rm BOPP}$ is pulse phase (0.0 - 1.0) at the beginning of PP. Dispersion delay caused by the interstellar medium are taken into account for each frequency channel. The K4 correlator receives parameters listed in Table 7.4 and calculates hardware parameter P1, P2, and ΔP for each unit in accordance with the processing mode described in Section 7.5.1. Optimum gate width and pulse phase at a certain epoch is determined by pulse search mode (PS-mode).

7.6.3 Improvement of Signal-to-Noise Ratio by Gating Function

The pulsar-gating function can improve correlation amplitude and signal-to-noise ratio (SNR) of pulsar data. Figure 7.8 (right) shows the relation between pulsar signal and gate function schematically. We assume the pulsar signal has an ideal rectangular shape with period P (sec.), pulse width W (sec.) and pulse flux $S_{\rm PLS}$ (Jy). When this signal is processed without a gating function, energy concentrated in the pulse is averaged over the pulse period and effective flux $\bar{S}_{\rm pls}$ is given by $S_{\rm pls}W/P$ as a result of correlation processing.

When gate function with width $P/N_{\rm div}$ is applied and gate offset is adjusted so that the pulse signal is included inside the gate (Figure 7.8), the observed flux is expressed by

$$S_{\rm gate} = \begin{cases} S_{\rm pls}\frac{WN_{\rm div}}{P} & (W \le P/N_{\rm div}) \\ S_{\rm pls} & (W > P/N_{\rm div}). \end{cases} \tag{7.53}$$

Correlation amplitude of the signal is expressed as

$$\rho = \frac{\pi D_1 D_2}{8k_{\rm B}} S \sqrt{\frac{\eta_1\eta_2}{T_{sys,1}T_{sys,2}}}, \tag{7.54}$$

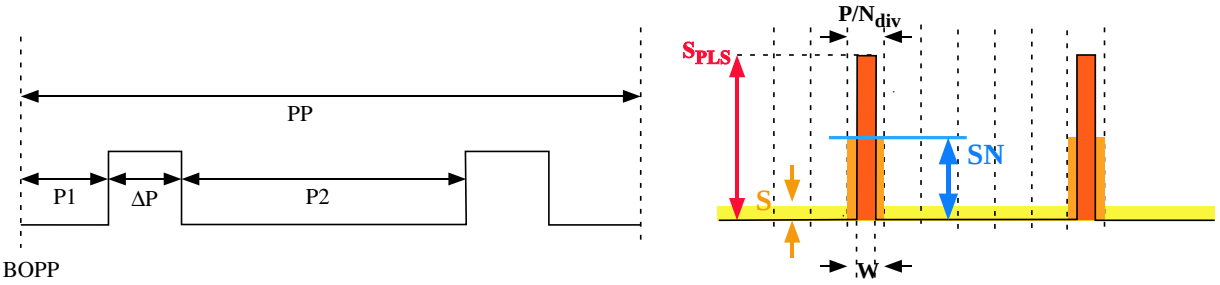

Figure 7.8: Relation among pulsar gate hardware parameters P1, P2, and ΔP is indicated in the left panel. ΔP is width of gate in bits. P1 is the interval from beginning of PP (BOPP) to the first gate opening timing; P2 is time interval between gates. The right panel shows how the pulsar gate increases the effective flux density. The red rectangular represents the signal from pulsar with peak flux density S_{PLS}. When this signal is processed in the usual way, the average flux level (S) decreases as low as the magnitude is indicated by yellow bar. If the gate function is applied so as the gate width (P/N_{div}) is no less than the pulse width (W) and it includes the pulse signal, the effective flux density increases as indicated by the orange colored area (SN_div).

Table 7.4: Pulsar gate control parameters. P and $PHS_{\rm pls}$ at the beginning of scan are given from pulse phase calculation software CALP at frequency $F_{\rm Ref}$ with dispersion measure DM. Gate width is determined by number of divisions $N_{\rm div}$. Gate offset OFST is fixed empirically by pulse search in PS-mode.

Parameter	Description
P	Pulsar period
DM	Dispersion measure
$\rm PHS_{pls}$	Pulse phase at $F_{\rm Ref}$ calculated by CALP
$F_{\rm Ref}$	Reference radio frequency
$N_{\rm div}$	Number of division of pulse period
OFST	Offset of pulse phase

where D_1, D_2, η_1, η_2, and $T_{sys,1}, T_{sys,2}$ are diameters, efficiencies, and system temperatures of two antennas, respectively; $k_{\rm B}$ is the Boltzmann constant and S is flux density in W/m^2/ Hz. Noise amplitude is $1/\sqrt{N}$, where N is number of samples contributing to the integration. The pulsar signal is a continuum emission, so N equals 2BT, were B is bandwidth and T is integration time. If pulsar gating is applied with $P/N_{\rm div}$ width, integration time is reduced by a factor $1/N_{\rm div}$, so N equals $BT/N_{\rm div}$. Signal-to-noise ratio (SNR) of pulsar data with gating function is

$$SNR_{\rm gating} = \begin{cases} AS_{\rm pls}\frac{W}{P}\sqrt{2BTN_{\rm div}} & (W \le P/N_{\rm div}) \\ AS_{\rm pls}\sqrt{\frac{2BT}{N_{\rm div}}} \end{cases} . \qquad (7.55)$$

Figure 7.9 shows examples of the correlation amplitude ρ and SNR improvement by the gating function of the K4 correlator. Upper panels of the Figure 7.9 shows the ρ and SNR of PSR B0329+54, and lower panels are those of PSR B1933+16. ρ of PSR B0329+54 continue to increase over 100 of $N_{\rm div}$ and the increasing rate of the ρ is less than that proportional to $N_{\rm div}$. These results imply that the pulse is not an ideal rectangular shape but, has a tail component and the peak of pulse is sharp. In contrast to the data of PSR B0329+54, ρ of PSR B1933+16 increased almost in proportion to $N_{\rm div}$ and it becomes almost constant from $N_{\rm div}$ equals 64. These suggests that the pulse profile of PSR B1933+16 is close to the rectangular shape with pulse width a few percents ($\approx 1/64$). Actual pulse profiles of PSR B0329+54 and B1933+16 observed Seiradakis et al. (1995) are displayed in Figure 7.10. Signal of PSR B0329+54 observed

by the 100 m diameter radio telescope shows extended pulse up to 7 % of pulse period and sharp main pulse profile. Signal of PSR B1933+16 in Figure 7.10 shows box shape pulse profile with about 2 % of pulse period, as they are inferred from the results of pulsar gating. The SNR is expected to decrease inversely proportional to $\sqrt{N_{\rm div}}$, when the pulse shape is rectangular and gate width is narrower than the pulse width. The actual data of PSR B1933+16 shows this tendency when $N_{\rm div}$ is larger than 64.

7.7 Summary

The K4 correlator was developed as a part of the K4 VLBI system for geodetic and astrometric VLBI observations. It has simultaneous cross correlation processing capability of 16 channels with 4 or 8 Mbps data rate for each channel. Architecture of the K4 correlator is described in this chapter. Except for this basic function, this correlator has fringe search mode (288 lags), autocorrelation mode, and pulsar gate mode. Its pulsar-gating function is suitable for millisecond pulsars and can improve correlation amplitude and signal-to-noise of pulsar VLBI data. High precision pulse arrival period prediction software is inevitable for the pulsar gating function. For this purpose, a pulse phase prediction software CALP was developed by Rodin and the author, and its precision was evaluated by comparison with other pulser timing software TEMPO and TIMAPR. The relative accuracy of the computed pulse period by CALP is required to be accurate at least 10^{-9}, and this criteria was satisfied by CALP on millisecond pulsar B1937+21 and binary pulsar B1855+09. Correlation amplitude and SNR improvement was demonstrated for PSR B0329+54 and PSR B1933+16, and contributed to improvement of SNRs for five pulsars in VLBI data of Japan-Russia baseline (Chapter 6).

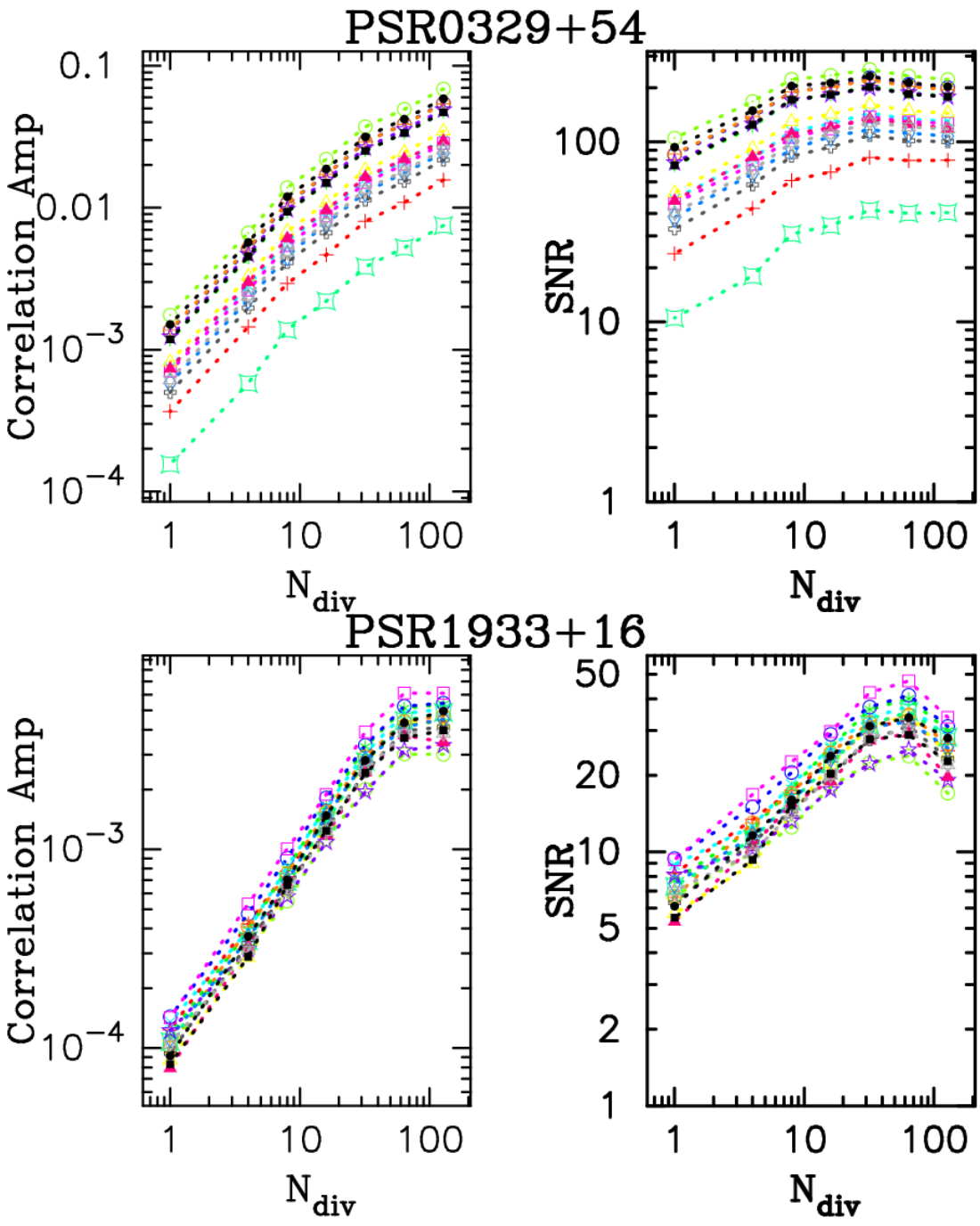

Figure 7.9: Improvement of correlation amplitude and SNR of PSR B0329+54 and B1933+16 by gating function. PSR B0329+54 (upper panels) and B1933+16 (lower panels) were processed by changing the gate width division number $N_{\rm div}$ from one to 128. The integration time was about 860 sec and bandwidth was 2 MHz (4MHz sampling). Left panels show the correlation amplitude. When a rectangular-shaped pulse is assumed, correlation amplitude is expected to increase in proportion to the number of divisions until the gate width becomes smaller than the pulse width. Right panels indicate SNR. Also in the case of a rectangular-shaped pulse, the SNR increases in proportion to $\sqrt{N_{\rm div}}$. If the gate width becomes smaller than the pulse width, SNR decreases in proportion to $1/\sqrt{N_{\rm div}}$.

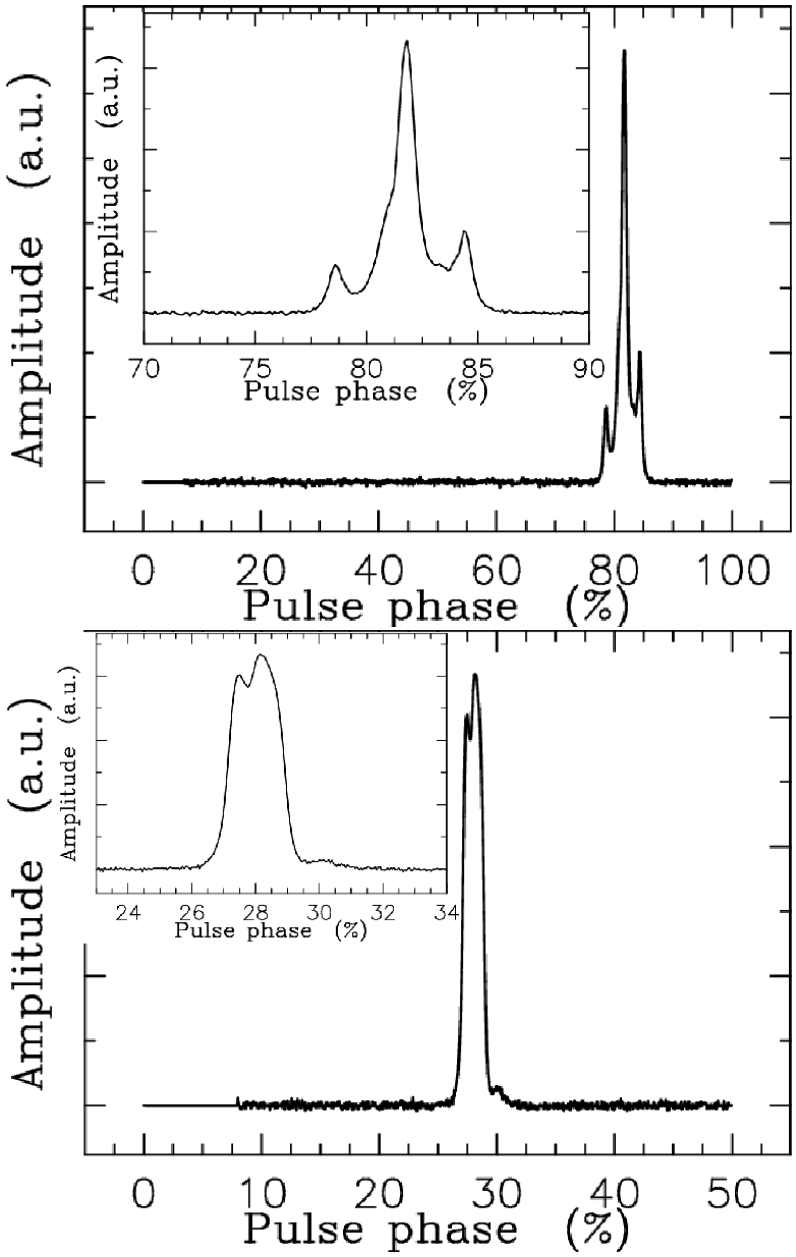

Figure 7.10: Pulse profiles of PSRs B0329+54 (upper panel) and B1933+16 (lower panel) at 1.4GHz taken from the data base of published pulse profiles maintained by the European Pulsar Network, available at: http://www.mpifr-bonn.mpg.de/pulsar/data/. Pulse profile data observed by Seiradakis et al. (1995) with 100 m diameter radio telescope of the Max-Planck Institut für Radioastronomie.

Chapter 8

Summary and Conclusions

8.1 Research Work Performed in This Study

8.1.1 Observations

Japan-Russia Pulsar VLBI observation was performed from 1995 to 1998 to determine pulsar coordinates on the International Celestial Reference Frame. The 64 m-diameter antenna (RT-64) at Kalyazin (Russia) and the 34 m diameter antenna at Kashima (Japan) were used for the observations. The K4 VLBI data acquisition system was installed in both stations and used during this project. The VLBI experiment in March 1995 was successful in spite of that it was the first VLBI observation for the RT-64. Then following 6 times of VLBI experiments were performed (Table 2.3).

We used absolute astrometry based on group delay measurement for pulsar coordinates measurements. The reasons are (1) group delay measurement is conservative technique but it can determine absolute coordinates of pulsar on the sky without phase ambiguity, thus the coordinates can be used as fiducial point. (2) group delay measurement, which can take longer integration time than antenna switching observation for phase measurement, is suitable for large diameter antennas, because they cannot move so fast; (3) consequently, group delay measurement output steady output than phase measurements. Measurement of absolute pulsar's coordinates is important for many purposes. Frame tie and identification of pulsar with object at other wavelength require accurate coordinate of pulsars. Absolute coordinates data of pulsar with several years of interval enable accurate proper motion determination.

Totally 26 pulsars were observed in 5 times of VLBI experiments (March 1995, April 1995, May 1996, May 1997, May 1998), and most of the experiments were successful. Only April 1995 experiment was partly suffered from radio interference of commercial communication. Observation frequency band was L-band (1.4 GHz) until May 1997 and S-band (2.2 GHz) was used from May 1998. Observed data were processed by K4 correlator with gating function. Fringes of 8 pulsars (PSR B0329+54, PSR B0355+54, PSR B0950+08, PSR B1933+16, PSR B2021+51, PSR B1929+10, PSR B2020+18, PSR B0809+74) were detected. The post correlated data are fed to bandwidth synthesis program and group delay and phase delay rate observables are extracted and stored in Mark-III database system.

8.1.2 Calibration of Ionospheric Delay with GPS-based TEC measurement

The most significant error source of pulsar VLBI astrometry at L-band is the Earth ionospheric delay uncertainty. Because ionospheric delay is larger at lower frequency in proportional to the square of radio frequency. The excess delay introduced by the ionosphere is proportional to the total number of free electrons in line of sight. For the purpose to compensate for the ionospheric delay in pulsar VLBI observation, we have investigated ionospheric total ionospheric

content (TEC) measurement by using GPS signal. We have estimated local ionospheric TEC by using GPS receivers, which are locally installed at VLBI stations (Kashima and Koganei). Although, the generated local TEC map could not achieve enough accuracy due to following reasons: uncertainty of satellites and receivers differential code biases introduced bias error into vertical TEC measurements; the delay measurement resolution of our GPS receiver was insufficient because it used code delay. Widely distributed GPS receivers were necessary to improve the accuracy and for more dense scanning line of ionosphere.

International GPS Service (IGS) analysis centers have been involved in measurement of ionospheric total electron content by using GPS signal. A Global Ionosphere Map (GIM) provided from Bern University (CODE) of Switzerland has following advantages: (1) GIM is suitable for ionosphere delay correction on intercontinental baseline observation, since VLBI stations are also globally distributed and GIM data provides TEC data of any places on the Earth with almost uniform precision; (2) the GIM of the CODE (GIM/CODE) has higher accuracy than TECMETER observation; (3) GIM/CODE data from January 1995 up to today are freely available through the Internet and the data is continuous without interruption in that period.

To use the GIM/CODE data for our VLBI observation data calibration, we evaluated the absolute accuracy of the GIM/CODE by comparison with domestic and international dual-frequency VLBI data. And we determined that the absolute accuracy of the GIM/CODE data was about 3-5 TECU (10^{16} electrons/m^2) in zenith direction and we concluded that about 90% of the ionospheric delay effect could be compensated by the GIM/CODE TEC model.

A test of the ionospheric delay correction, was performed by estimating accurately known quasars' coordinates with VLBI. Then it was shown that 60-100 mas bias error, which was introduced in source coordinates estimation without ION-correction, was calibrated (Figure6.1). Finally, ionospheric delay data derived from the GIM/CODE were applied for the calibration in the pulsar VLBI astrometry analysis.

8.1.3 Improvement of SNR of Pulsar Data by pulsar gating and Development of K4 correlator

The K-4 correlation processor was developed for astrometry VLBI observations. It has a pulsar-gating function applicable to millisecond pulsar data. To apply the pulsar gating function effectively to pulsar data, pulse arrival period need to be accurately known (Section 7.6). For this purpose, precise pulse-arrival-time calculation software CALP was developed under the collaboration with the Pushchino Radio Astronomy Observatory of the Lebedev Physical Institute of Russia. The accuracy of the pulse period prediction software was confirmed to be accurate within about 10^{-9} by comparison with other pulsar timing software TEMPO and TIMAPR. Pulsar-gating function is essential to improve signal-to-noise ratio of pulsar data in correlation processing. Actually, the SNR of pulsar data was improved by factor 4 - 5 with the pulsar-gating function, and fringes of PSR B0355+54, B0950+08, B1933+16, and B2021+51 were successfully detected and these data could be used for coordinates analysis.

8.1.4 Interstellar Scintillation in Pulsar VLBI Observation

Interstellar scintillation phenomena were observed on pulsar data as the consequence of interstellar scattering of pulsar signal. The interstellar scattering also cause smearing of source image called "Angular broadening" especially in case of compact radio source. The size of the angular broadening (scattering disk size) increases inversely proportional to about square of radio frequency as the frequency decreases. So the angular broadening will affect to precision of astrometry especially at lower frequency. For the purpose to estimate the scattering disk size ($\theta\{\mathrm{scat}\}$), decorrelation bandwidth (B_s) and scintillation time scale (τ_s) were estimated for each pulsar.

Thin phase screen model was assumed for derivation of the relation among $\theta_{\rm scat}$, $B_{\rm s}$ and $\tau_{\rm s}$. The decorrelation bandwidth $B_{\rm s}$ and scintillation time-scale $\tau_{\rm s}$ were derived from the dynamic cross power spectrum of pulsar data. The obtained $B_{\rm s}$ and $\tau_{\rm s}$ were almost consistent with the data in literatures. In other words, the ISS phenomena observed by VLBI were almost the same with that in single dish observation in our case. The reason was that the baseline length of our observations were smaller than the size of *scintle* on the observer plane. If we observed pulsars with longer baseline than the size of *scintle*, the ISS feature of VLBI observation would differs from single dish observation and it also depends on the baseline length. These observation must be interesting from view point of investigation of ISM and could be extended to resolve pulsar emission region as Gwinn et al.(1997, 2000) have done. Scattering disk size was evaluated from $B_{\rm s}$ and $\tau_{\rm s}$ based on thin phase screen model, and 0.1 - 1.4 mas of scattering disk size was estimated at 1.4 GHz. The scattering disk size data were included in the error of pulsar coordinates in the astrometric results.

8.1.5 Pulsar Astrometry

After VLBI data reduction procedure of correlation processing and bandwidth synthesis, the obtained group delay and phase delay rate were stored in the Mark-III database system and analyzed by using precise VLBI delay model calculation software CALC and least-square analysis software SOLVE. Ionospheric delay computed from the GIM/CODE TEC model was also stored in the database and used for ionospheric delay calibration. The inconsistency among the group delay and phase delay rates were reduced by the ionospheric delay correction, and formal error of LSQ analysis was decreased.

Pulsar coordinates of B0329+54, B0355+54, B0950+08, B1933+16, and B2021+51 were obtained by these VLBI observations. The other 3 pulsars (B0809+74, B1929+10, B2020+28) were detected but their coordinates were not determined due to insufficient data.

PSR B0329+54 Pulsar coordinates and proper motion were derived from four epochs (1995.20, 1996.36, 1997.39, 1998.40) of observations as:

$$\left\{\begin{array}{lrrrll} \alpha: & 03^h & 32^m & 59^s.3816 & \pm 0.0005 & \text{at 1998.0} \\ \delta: & 54^\circ & 34' & 43''.486 & \pm 0.004 & \\ \mu_\alpha: & & 12.6 & \pm 3.5 & \text{(mas/year)} & \\ \mu_\delta: & & -11.8 & \pm 2.7 & \text{(mas/year)} & \end{array}\right.$$

This coordinates of PSR B0329+54 is based on the ICRF. When the coordinates are propagated to a epoch 1981.21 by using our proper motion, the pulsar positions measured by Bartel et al. (1985) and Fomalont et al. (1984) were consistent with our results. Bartel et al. determined coordinates of this pulsar with reference to NRAO150, which is included in the ICRF source categorized as "Other source". Thus Bartel's pulsar position can be connected with that on the ICRF by correction of difference of reference source(NRAO150)'s coordinates between the ICRF and those used by Bartel et al.

Then, we could derive more accurate proper motion and mean coordinates by using joint data sets 'Ours+Bartel' as:

$$\left\{\begin{array}{llrrrll} \textit{'Ours + Bartel'} & \alpha: & 03^h & 32^m & 59^s.37577 & \pm 0.0004 & \\ \text{at 1995.0} & \delta: & 54^\circ & 34' & 43''.5179 & \pm 0.003 & \\ & \mu_\alpha: & & 17.3 & \pm 0.35 & \text{(mas/year)} & \\ & \mu_\delta: & & -10.6 & \pm 0.37 & \text{(mas/year)} & \end{array}\right.$$

This proper motion was the most accurate one for this pulsar. And it is consistent with proper motion data measured by Harrison et al. (1993) within 3 sigma error level.

PSR B0355+54 Coordinates of B0355+54 were obtained at epoch 1995.20.

$$\begin{cases} \alpha: & 03^h & 58^m & 53^s.713 & \pm 0.003 \\ \delta: & 54^\circ & 13' & 13''.75 & \pm 0.1 \end{cases}$$

Pulsar position of timing analysis by Arzoumanian et al. (1994) and and VLA measurement by Fomalont et al. (1992) were consistent with our result, when proper motion of Lyne et al. (1982) were used for propagation of position to epoch 1995.20.

PSR B0950+08 Coordinates of B0950+08 were obtained at two epochs at 1998.40 and at 1996.36.

$$\begin{cases} \alpha: & 09^h & 53^m & 9^s.30 & \pm 0.01 & \text{at 1996.36} \\ \delta: & 7^\circ & 55' & 35''.8 & \pm 0.8 & \\ \alpha: & 09^h & 53^m & 9^s.309 & \pm 0.001 & \text{at 1998.40} \\ \delta: & 7^\circ & 55' & 36''.154 & \pm 0.07 & \end{cases}$$

The reasons of larger coordinates error of VLBI observation at May 1996 than that of May 1998 are insufficient observation time, larger ionospheric effect, and wider beam size at L-band than S-band. These disadvantages were improved in the VLBI experiment in 1998. However, the large correlation between α and δ is inevitable because of single baseline observation.

The proper motions of this pulsar measured by Lyne et al., and Gwinn et al., are fairly difference from recent VLBA measurement by Brisken et al. True proper motion is uncertain, however, our absolute coordinates of pulsar supports that Brisken's proper motion if Fomalont et al.'s VLA results is used as fiducial point. Further absolute coordinates measurements should determine the true proper motion and absolute coordinates of this pulsar on the ICRF.

PSR B1933+16 Coordinates of B1933+16 were obtained at epoch 1995.2 as:

$$\begin{cases} \alpha: & 19^h & 35^m & 47^s.824 & \pm 0.006 \\ \delta: & 16^\circ & 16' & 40''.07 & \pm 0.27 \end{cases}$$

The cause of large coordinates error are mainly owing to insufficient observation time. The coordinate precision should be improved by extended observation time or by using more wider VLBI network. We are planning to do long time VLBI observation in fourth quarter of 2001.

PSR B2021+51 Coordinates of B2021+51 were obtained at epoch 1995.2 as

$$\begin{cases} \alpha: & 20^h & 22^m & 49^s.866 & \pm 0.005 \\ \delta: & 51^\circ & 54' & 50''.302 & \pm 0.01 \end{cases}$$

The pulsar coordinates of Campbell et al. (1996: VLBI), Arzoumanian et al. (1994: timing) and our results were almost consistent within their two sigmas error at epoch 1995.20. However, two different proper motions are reported by Campbell et al. (1996) with phase referenced VLBI measurements and by Lyne et al.(1982) with phase referenced radio linked interferometer. The coordinates and proper motion measured by Campbell et al. have quite small error, so they are thought to be most accurate at present. Definite and reliable answer to the question of pulsar coordinates and proper motion should be given by following absolute astrometry by VLBI, and we are planning to do that very near future.

The pulsars' coordinates measured here are based on the ICRF. Finally, the authors wish to emphasise the importance of an absolute astrometric observation on a stable reference frame. An absolute coordinates measurement on a basic reference frame is not only useful for a frame tie, but also gives a chance to produce even more improved measurements of astrometric parameters by follow-up absolute astrometry observation. It might enables the acceleration of pulsar motion by the breaking due to Interstellar medium and so on.

8.1.6 Frame Tie

Reference frame tie was performed by using pulsar's coordinates. The rotation matrix between DE200 and the ICRF were computed as follows by using 5 pulsars coordinates.

$$\mathbf{\Theta} = \begin{pmatrix} -7.4 & \pm 3 \\ -11.9 & \pm 5 \\ -9.1 & \pm 3 \end{pmatrix} (\mathrm{mas})$$

In spite of the quite limited number of pulsars, it was successful and fairly consistent with result of Folkner et al., which is used as a base of current frame tie between the ICRF and planetary ephemerides. The rotation angle component θ_y was almost the same, θ_z coincide within one sigma, and θ_x agreed within 2 sigma. The frame tie by using pulsar is more direct and simply performed by Celestial-to-Celestial coordinates comparison in contrast with the joint analysis of LLR and VLBI, which Folkner et al. used. Author demonstrated that frame tie is possible by using pulsars, even under the condition that quite limited number of pulsar is available. In our rotation vector estimation, almost only two pulsars' (PSR B1257+12 and PSR B1937+21) coordinates were main decisive factor. Although pulsar's coordinates needed to be determined high precision by both VLBI and timing, not so many pulsars satisfy this condition at present. Increasing the number of pulsars, whose coordinates are precisely measured by both VLBI and timing, is the essential to improve the accuracy of this technique. Number of pulsars, which satisfy the above mentioned condition, is expected to increase since collaboration network is expanding in the world to construct pulsar time scale.

We did not derive rotation vector between latest planetary ephemeris DE405/DE406 and the ICRF, because pulsar timing analysis has been still mostly done on the base of DE200. Consequently, most pulsar's coordinates are expressed on DE200. Recently, coordinates of PSR B1937+21 on DE405 were derived by Hanado et al. (2001), and other pulsar's coordinates on DE405/DE406 will be derived near future.

8.2 Problems and Future Prospects

Five pulsar's absolute coordinates on the ICRF have been determined in this study. We used absolute astrometry with group delay and phase delay rates in the same way with determination of ICRF sources' coordinates. We have demonstrated that only one baseline VLBI could measure the pulsar coordinates with milli arc second precision. Although precision of some pulsars' coordinates measurements were rather low. Main reasons of that were insufficient observation time and constraint of single baseline observation. Three pulsars (B0355+54, B1933+16 and B2021+51) were observed only at the first experiment at March 1995, since the main purpose that experiment was check of detectability of pulsars and not optimised for astrometric observation. The delay of completion of the K4 correlator gating function caused the loss of opportunities of repeating observation for these pulsars.

We had seen some examples of inconsistent proper motion reports based on phase delay measurements. Main reasons of them might be caused to ambiguity problem of phase measurement.

Now we have re-recognised the importance of absolute astrometry, and we are sure to be able to determine absolute coordinates of those pulsars by our VLBI observation.

Expanding the observation network should improve the precision of pulsar coordinates measurements. We started to expand the collaboration network including Canadian VLBI group. Japan (Kashima 34m) - Russia (Kalyazin) - Canada (Algonquin) VLBI observation was conducted in 2000 May with S2 VLBI system. Improvement of observation precision are expected by this triangle baseline observation.

References

Akabane K, Kaifu T., and Tabara H., Radio Astronomy (in Japanese), Kyoritsu Pub. Co Ltd. Tokyo, 1988.

Anderson B., Lyne A. G. and Peckham R. J., Proper Motions of Six Pulsars, *Nature* , Vol. 258, pp. 215-217, 1975.

Aoki S., Sôma M., Kinoshita H., and Inoue K., Convention Matrix of Epoch B 1950,0 FK 4-based Positions of Stars to Epoch J 2000.0 Positions in Accordance with the New IAU Resolutions, *Astron. Astrophys.*, Vol. 128, pp. 263-267, 1983.

Argus D. F. and Gordon R. G., No-rotation Model of Current Plate Velocities Incorporating Plate Motion Model Nuvel-1, *Geophys. Res. Lett.*, Vol. 18, pp. 2039-2042, 1991.

Arzoumanian Z., Nice D. J., and Taylor J. H., Timing Behaviour of 96 Radio Pulsars, *Astrophys. J.*, Vol. 422, pp. 671-680, 1994.

Backer D. C. and Sramek R. A., Proper Motion of Pulsars by Radio Interferometry, *Astron. J.*, Vol. 81., pp. 430-432., 1976.

Backer D. C. and Sramek R. A., Pulsar Astronomy, *Pulsars (eds. Sieber W., and Wielebinski)* pp. 205-206, 1981.

Backer D. C., Fomalont E. B., Goss W. M., Taylor J. H., and Weisberg J. M., Accurate Timing and Interferometer Positions for the Millisecond Pulsar 1937+21 and The Binary Pulsar 1913+16, *Astron. J.*, Vol. 90, pp. 2275-2280, 1985.

Bartel N., Ratner M. I., Shapiro I. I., Cappallo R. J., Rogers A. E. E., and Whitney A. R., Pulsar Astrometry via VLBI, *Astron. J.*, Vol. 90, pp. 318 - 325, 1985a.

Bartel N., Ratner M. I., Shapiro I. I., Cappallo R. J., Rogers A. E. E., and Whitney A. R., Investigation of Radiation from Pulsar PSR 0329+54 Using Mark III VLBI Observations, *Astron. J.*, Vol. 90, pp. 2535 - 2539, 1985b.

Bartel N., Chandler J. F., Ratner M. I., Shapiro I. I., Pan R., and Cappallo R. J., Towards a Frame-tie via Millisecond Pulsar VLBI, *Astron. J.*, Vol. 112, pp. 1690-1696, 1996.

Beutler, G., Executive Summary, *IGS Analysis Center Workshop,* 9-18, 1998.

Blandford R. and Teukolsky S. A., *Astrophys. J.*, Vol. 205, pg. 580, 1976.

Brisken W. F., Benson J. M., Beasley A. J., Fomalont E. B., Goss W. M., and Thorsett S. E., Measurement of the Parallax of PSR B0950+08 Using the VLBA, *Astrophys. J.*, Vol. 541, pp. 959-962, 2000.

Campbell R. M., Bartel N., Shapiro, I. I., Ratner M. I., Cappallo R. J., Whitney A. R., and Putnam N., VLBI-derived Trigonometric Parallax and Proper Motion of PSR B2021+51, *Astrophys. J. Lett.*, Vol. 461, pp. L95-L98, 1996.

Campbell R. M., Pulsar Position, Proper Motion, and Parallax via VLBI, *IAU Colloquium 177: Pulsar Astronomy - 2000 and Beyond* ASP Conf. Ser. Vol. 202, (M. Kramer, N. Wex, and R. Wielebinski eds.), pp. 135-138., 2000.

Camilo F., Foster R. S., and Wolszczan A., High-precision Timing of PSR 1713+0747: Shapiro Delay, *Astrophys. J.*, Vol. 437, pp. L39-L42, 1994.

Chao C. C., A Preliminary Estimation of Tropospheric Influence on the Range and Range Rate Data During the Closest Approach of the MM71 Mars Mission, *JPL Tech Memo,* pp. 391, 1970.

Charlot P., Radio-Source Structure in Astrometric and Geodetic Very Long Baseline Interferometry, *Astron. J.*, Vol. 99, pp. 1309-1326.

Chatterjee S., and Codes J. M., VLBI Neutron Star Astrometry: Techniques and Initial Results, *IAU Colloquium 177: Pulsar Astronomy - 2000 and Beyond* ASP Conf. Ser. Vol. 202, (M. Kramer, N. Wex, and R. Wielebinski eds.), pp. 139-140., 2000.

Clark T., Corey B. E., Davis J. L., Elgered G., Herring T. A., Hinteregger H. F., Knight C. A., Levine J. I., Lundqvist G., Ma C., Nesman E. F., Phillips R. B., Rogers A. E. E., Ronnang B. O., Ryan J. W., Schupler B. R., Shaffer D. B., Shapiro I. I., Vandenberg N. R., Webber J. C., and Whitney A. R., Precision Geodesy Using the Mark-III Very-Long Baseline Interferometer System, *IEEE Trans. Geosci. Remote Sensing,* Vol. GE-23, pp. 438-449, 1985.

Coco D. S., Coker C., and Dahlke S. R., Variability of GPS Satellite Differential Group Delay Biases, *IEEE Trans. Aero. Electr. Sys.,* Vol. 27, pp. 931-938, 1991.

Cognard I. Bourgois G., Lestrade J.-F, Biraud F., Aubry D., Darchy B., and Drouhin J.-P., High-precision Timing Observations of the Millisecond Pulsar PSR1937+21 at Nançay, *Astron. Astrophys.*, Vol. 296, pp. 169-179, 1995a,

Cognard I., Bourgois G., Lestrade J.-F, and Biraud F., Red Noise in the Timing Residuals of the Millisecond Pulsar PSR B1821-24, *Millisecond Pulsars: A Decade of Surprise*, ASP Conf. Ser. Vol. 72, (A. S. Fruchter, M. Tavani, and D. C. Backer eds.), pp. 369-371, 1995b.

Cordes J. M., Weisberg J. M., and Boriakoff V., Small-scale Electron Density Turbulence in the Interstellar Medium, *Astrophys. J.*, Vol. 288, pp. 221-247, 1985.

Cordes J. M., Space Velocities of Radio Pulsars from Interstellar Scintillation, *Astrophys. J.*, Vol. 311, pp. 183-196, 1986.

CRL, System Development of K-3 Very Long Baseline Interferometry (in Japanese), *Review of Radio Res. Lab.*, Vol. 30, 1984.

Damour T. and Deruelle N., *Ann. Inst. H. Poincare,* Vol. 44, pp. 263, 1986.

Davis J.L., Herring T. A., Shapiro I. I., Rogers A. E. E., and Elgered G., Geodesy by Radio Interferometry: Effects of Atmospheric Modeling Errors on Estimation of Baseline Length, *Radio Sci.*, Vol. 20, pp. 1593-1607, 1985.

Dewey R. J., Ojeda M. J., Gwinn C. R., Jones D. L., and Davis M. M., VLBI Astrometry of the Millisecond Pulsar B1937+21, *Astron. J.*, Vol. 111 pp. 315-319, 1996.

Doroshenko O. V. and Kopeikin S. M., High Precision Pulse Timing for Single Pulsars, *Sov. Astron-AJ.,* Vol. 34, pg. 496, 1990.

Doroshenko O. V. and Kopeikin S. M., Relativistic Effect of Gravitational Deflection of Light in Binary Pulsars, *Mon. Not. R. Astron. Soc.*, Vol. 274, pp/ 1029-1038, 1995.

Downs G. S., and Reichley P. E., JPL Pulsar Timing Observations. II. Geocentric Arrival Times, *Astrophys. J. Supp.*, Vol. 53, pp. 169-240, 1983.

Fairhead L. and Bretagnon P., An Analytical Formula for the Timing Transformation TB-TT, *Astron. Astrophys.*, Vol. 229, pp. 240-247, 1990.

Feltens J. and Schaer S., IGS Products for the Ionosphere, *IGS Analysis Center Workshop,* pp. 225-232, 1998.

Fey A. L., Clegg A. W., and Fomalont E. B., VLBA Observations of Radio Reference Frame Sources. I, *Astrophys. J. Supp.*, Vol. 105, pp. 299-330, 1996.

Fey A. L. and Charlot P., VLBA Observations of Radio Reference Frame Sources. II. Astrometric Stability Based on Observed Structure, *Astrophys. J. Supp.*, Vol. 111, p.95. 1997.

Folkner W. M., Charlot P., Finger M. H., Williams J. G., Sovers O. J., Newhall X. X., and Standish Jr. E. M., Determination of the Extragalactic-planetary Frame Tie from Joint Analysis of Radio Interferometric and Lunar Laser Ranging Measurement, *Astron. Astrophys.*, Vol. 287, pp. 279-289, 1994.

Fomalont E. B., Goss M. W., Lyne A. G., and Manchester R. N., Astrometry of 59 Pulsars: A Comparison of Interferometric and Timing Positions, *Mon. Not. R. Astron. Soc.*, Vol. 210, pp. 113-130, 1984.

Fomalont E. B., Goss W. M., Lyne A. G., Manchester R. N., and Justtanout K., Positions and Proper Motions of Pulsars, *Mon. Not. R. Astron. Soc.*, Vol. 258, pp. 497-510., 1992.

Fomalont E. B., Goss W. M., Manchester R. N., and Lyne A. G., Improved Proper Motions for Pulsars from VLA Observations, *Mon. Not. R. Astron. Soc.*, Vol. 286, pp. 81-84, 1997.

Fomalont E. B., Goss W. M., Beasley A. J., and Chatterjee S., Sub-milliarcsecond Precision of Pulsar Motions: Using In-beam Calibrators with the VLBA, *Astron. J.*, Vol. 117, pp. 3025-3030, 1999.

Frail D. A. and Weisberg J. M., A Critical Evaluation of Pulsar Distance Measurements, *Astron. J.*, Vol. 100, pp. 743-757, 1990.

Galama T. J., Paradijs J. V., Heuvel P. J., de Bruyn A. G., Campbell R. M., Vermeulen R. C., Lestrade J. -F., Verbunt F., and Schilizzi R. T., Determining Motions and Birthplaces of Pulsars through VLBI Astrometry, *IAU Colloquium 164: Emission from Galactic and Extragalactic Compact Sources*, ASP Conf. Ser. Vol. 144, (eds. J. A. Zensus, G. B. Taylor, and J. M. Wrobel), pp. 391-392, 1998.

Galt J. A. and Lyne A. G., The Interstellar Scintillation Pattern of PSR 0329+54, *Mon. Not. R. Astron. Soc.*, Vol. 158, pp. 281-290, 1972.

Guinot B. and Petit G., Atomic Time and the Rotation of Pulsars, *Astron. Astrophys.*, Vol. 248, pp. 292-296, 1991.

Gupta Y., Rickett B. J., and Lyne A. G., Refractive Interstellar Scintillation in Pulsar Dynamic Spectra, *Mon. Not. R. Astron. Soc.*, Vol. 269, pp. 1035-1068, 1994.

Gupta Y., On the Correlation between Proper-motion Velocities and Scintillation Velocities of Radio Pulsars, *Astrophys. J.*, Vol. 451, pp. 717-732, 1995.

Gwinn C. R., Taylor J. H., Weisberg J. M., and Rawley L. A., Measurement of Pulsar Parallaxes by VLBI, *Astron. J.*, Vol. 91, pp. 338-342, 1986.

Gwinn C. R., Bartel N., and Cordes J. M., Angular Broadening of Pulsars and the Distribution of Interstellar Plasma Fluctuations, *Astrophys. J.*, Vol. 410, pp. 673-685, 1993.

Gwinn C. R., Ojeda M. J., Britton M. C., Reynolds J. E., Jauncey D. L., King E. A., McCulloch P. M., Lovell J. E. J., Flanagan C. S., Smits D. P., Preston R. A., and Jones D. L., Size of the Vela Pulsar's Radio Emission Region: 500 Kilometers, *Astrophys. J.*, Vol. 483., pp. L53-L56, 1997.

Gwinn C. R., Britton M. C., Reynolds J. E., Jauncey D. L., Kind E. A., McCulloch P. M., Lovell J. E. J., and Preston R. A., Interstellar Optics, *Astrophys. J.*, Vol. 505, pp. 928-940, 1998.

Gwinn C. R., Britton M. C., Reynolds J. E., Jauncey D. L., Kind E. A., McCulloch P. M., Lovell J. E. J., and Preston R. A., Size of the Vela Pulsar's Emission Region at 13 Centimeter Wavelength, *Astrophys. J.*, Vol. 531, pp. 902-916, 2000a.

Gwinn C. R., Reynolds J. E., Jauncey D. L., Tzioumis A. K., Carlson B., Dougherty S., Rizzo D. D., Hirabayashi H., Kobayashi H., Murata Y., Edwards P. G., Quick J. F. H., Flanagan C. S., and McCulloch P. M., Observations of the Vela Pulsar Using VSOP", *Astrophysical Phenomena Revealed by Space VLBI (H. Hirabayashi, P. G. Edwards, D. W. Murphy eds.)*, published by ISAS, PP. 117-120, 2000b.

Gwinn C. R., Reynolds J. E., Jauncey D. L., Hirabayashi H., Kobayashi H., Murata Y., Edwards P. G., Carlson B., Dougherty S., Rizzo D. D., Britton M. C., McCulloch P. M., and Lovell J. E. J., Measuring the Size of the Vela Pulsar's Radio Emission Region, *IAU Colloquium 177: Pulsar Astronomy - 2000 and Beyond* ASP Conf. Ser. Vol. 202, (M. Kramer, N. Wex, and R. Wielebinski eds.), pp. 211-214., 2000c.

Hama S. and Kiuchi H, III.3 K-3 and K-4 VLBI Data Recorders, *J. Comm. Res. Lab.*, Vol. 38, Special issue No. 3, pp. 459-470., 1991.

Hama S., Sekido M., Kiuchi H., Takahashi Y., Imae M., Fujisawa K., and Hirabayashi H., First Pulsar VLBI Experiment in Japan between Kashima and Usuda, *Publ. A. S. J.*, Vol. 46, 511-514, 1994.

Hanado Y., Shibuya Y., Hosokawa M., Sekido M., Goto T., and Imae M., Timing Observation of Millisecond Pulsar PSR1937+21 using the Kashima 34m-antenna, submitted to *Publ. A. S. J.*, 2001.

Harrison P.A., Lyne A.G., and Anderson B., New Determination of the Proper Motions of 44 Pulsars, *Mon. Not. R. Astron. Soc.*, Vol. 261, pp. 113-124, 1993.

Haugan M. P., Post-newtonial Arrival-time Analysis for a Pulsar in A Binary System, *Astrophys. J.*, Vol. 296, pg. 1, 1985.

Heki K., Matsumoto K., and Folberghagen R., Three-dimensional Tracking of a Lunar Satellite with Differential Very-Long-Baseline-Interferometry, *Advances in Space Research* Vol. 23, No. 11, pp. 1821-1824. 1999.

Helfand D. J., Taylor J. H., Backus P. R., and Cordes J. M., Pulsar Timing. I Observations from 1970 to 1978, *Astrophys. J.*, Vol. 237, p.206, 1980.

Herring T. A., Modelling Atmospheric Delays in the Analysis of Space Geodetic Data, *Symposium on Refraction of Transatomospheric Signals in Geodesy, Netherlands Geodetic Commission Series,* Vol. 36, The Hague, Netherlands, pp. 157-164, 1992.

Ho C. M., Wilson B. D., Mannucci A. J., Lindqwister U. J., and Yuan D. N., A Comparative Study of Ionospheric Total Electron Content Measurements Using Global Ionospheric Map of GPS, TOPEX Radar, and the Bent Model, *Radio Sci.*, Vol. 32, pp. 1499-1512, 1997.

Imae M., Kondo T., Amagai J., Kaneko A., and Miki C., An Application of GPS Dual Frequency Codeless Receiver for Ionospheric Delay to Single Frequency Band VLBI Observation, *IEEE Trans. Instrum. Meas.,*, Vol. 40, pp. 208-211, 1991.

Imae M., Kurihara N., Kawaguchi N., Sugimoto Y., Yoshino T., Takahashi F., Hama S., Kiuchi H., Takahashi Y., Takaba H., Iwata T., Koyama Y., Hanado Y., Sekido M., Nakajima J., Kondo T., Kuroiwa H., Amagai J., Kaneko A., Uchida K., and Teshirogi T., The Main VLBI Station at Kashima, *J. Comm. Res. Lab.*, Vol. 42, pp. 5-14, 1995.

ITRF, http://lareg.ensg.ign.fr/ITRF/, 2001.

IVS: International VLBI Service products available at http: //ivscc.gsfc.nasa.gov /service/products.html, 2000.

Kaspi V. M., Taylor J. H., and Ryba M. F., High-precision Timing of Millisecond Pulsars. III. Long-Term Monitoring of PSRs B1885+09 and B1937+21, *Astrophys. J.*, Vol. 428, pp. 713-728, 1994.

Kiuchi H., Hama S., Amagai J., Abe Y., Sugimoto Y., and Kawaguchi N., III.2 K-3 and K-4 VLBI Data Acquisition Terminals, *J. Comm. Res. Lab.*, Vol. 38, Special issue No. 3, pp. 435-458., 1991.

Kiuchi H., Hama S., Amagai J., Hanado Y., Kaneko A., and Imae M., Contribution of the K-4 Systems for Future VLBI Observation, *Proc. of the International Workshop for Reference Frame Establishment and Technical Development in Space Geodesy, held in 18-21 Jan. 1993 at CRL Tokyo*, pp. 69-76, 1993.

Kiuchi H., Amagai J., Hama S., and Imae M., K-4 VLBI Data Acquisition System, *Publ. A. S. J.*, Vol. 49, No. 6 pp. 699- 708, 1997.

Kiuchi H., Kondo T., and Sekido M., Correlation Processing System, *J. Comm. Res. Lab.*, Vol. 46, pp. 47-54, 1999.

Konacki M., Lewandowski W., Wolszczan A., Doroshenko O., and Kramer M., Are There Planets around the Pulsar PSR B0329+54?, *Astrophys. J. Lett.*, Vol. 519, pp. L81-L84, 1999.

Kondo T. and Kunimori H., Bandwidth Synthesis Software KOMB (in Japanese), *Rev. Comm. Res. Lab.*, Vol. 30, pp. 199-216., 1984.

Kondo T., Amagai J., Kiuchi H, and Tokumaru M., III.6 Cross-Correlation Processing in a Computer for VLBI Fringe Tests, *J. Comm. Res. Lab.*, Vol. 38, pp. 503-512, 1991.

Kondo T., and Imae M., Precise Ionospheric Correction by Using GPS Signals for VLBI Geodetic Measurements, *Geographical Monograph 73, IUGG* Vol. 13, pp. 53-60, 1993.

Kopeikin S. M., Millisecond and Binary Pulsars as Nature's Frequency Standards -II. The Effects of Low-Frequency Timing Noise on Residuals and Measured Parameters, *Mon. Not. R. Astron. Soc.*, Vol. 305, pp. 563-590, 1999.

Koyama Y., Takaba H., Kurihara N., and Kawaguchi N, Kashima 34 m Antenna System (in Japanese), *Rev. Comm. Res. Lab.*, Vol. 36, pp. 39-50, 1990.

Koyama Y., Geodetic Results from Domestic VLBI Experiments (2) Minami-Torishima (Marcus) Experiments, *J. Comm. Res. Lab.*, Vol. 38, pp. 543-552, 1991.

KSP, VLBI Observation data, http://ksp.crl.go.jp/index.html, 2000.

Lanyi G. E. and Roth T., A Comparison of Mapped and Measured Total Ionospheric Electron Content Using Global Positioning System and Beacon Satellite Observations, *Radio Sci.*, Vol. 23, pp. 483-492. 1988.

Legge D., Astrometry of Southern Pulsars, *IAU Colloquium 177: Pulsar Astronomy - 2000 and Beyond* ASP Conf. Ser. Vol. 202, (M. Kramer, N. Wex, and R. Wielebinski eds.), pp. 141-142., 2000.

Lestrade J. -F., Preston R. A., Jones D. L., Phillips R. B., Rogers A. E. E., Titus M. A., Rioja M. J., and Gabuzda D. C., High-precision VLBI Astrometry of Radio-emitting Stars, *Astron. Astrophys.*, Vol. 344, pp. 1014-1026, 1999.

Lieske J. H., Lederle T., Fricke W., and Morado B., Expression for the Precession Quantities Based upon the IAU/1976/ System of Astronomical Constants, *Astron. Astrophys.*, Vol. 58, pp. 1-16, 1977.

Lindegren L., and Kovalevsky J., Linking the Hipparcos Catalogue to the Extragalactic Reference System, *Astron. Astrophys.*, Vol. 304, pp. 189-201, 1995.

Lyne A.G., Anderson B., and Salter M.J., The Proper Motions of 26 Pulsars, *Mon. Not. R. Astron. Soc.*, Vol. 201, pp. 503-520, 1982.

Lyne A. G. and Smith F. G., Interstellar Scintillation and Pulsar Velocities, *Nature* , Vol. 298, pp. 825-827, 1982.

Lyne A. G., Orbital Inclination and Mass of the Binary Pulsar PSR0655+64, *Nature* , Vol. 310, pp. 300-302, 1984.

Lyne A. G. and Lolimer D. R., High Birth Velocities of Radio Pulsars, *Nature* , Vol. 369, pp. 127-129, 1994.

Lyne A.G. and Graham-Smith F., Pulsar Astronomy second edition, Cambridge Astrophysics Series 31, Cambridge University Press, UK, 1998.

Ma C., Arias E. F., Eubanks T. M., Fey A. L., Gontier A.-M., Jacobs C. S., Sovers O. J., Archinal B. A., and Charlot P., The International Celestial Reference Frame as Realized by Very Long Baseline Interferometry, *Astron. J.*, Vol. 116, pp. 516-546, 1998.

Maeda K . and Kimura I., Modern theory of electro magnetic wave (in Japanese), p. 95, Ohmsha, Tokyo, 1984.

Matsumoto K., Heki K., and Rowlands D.D., Impact of Far-side Satellite Tracking on Gravity Estimation in the Selene Project, *Advances in Space Research,* Vol. 23, No. 11, pp. 1809-1822. 1999.

Manchester R. N., Newton L. M., Cooke D. J., Backus P. R., Damashek M., Taylor J. H., and Condon J. J., Further Observations of the Long-period Binary Pulsar PSR 0820+02, *Astrophys. J.*, Vol. 268, pp. 823-836, 1983.

McCarthy D. D., IERS Conventions (1996), *IERS Technical Note No. 21.,* 1996.

Minter A., VSOP Observations of PSR B0329+54, *Astrophysical Phenomena Revealed by Space VLBI (H. Hirabayashi, P. G. Edwards, D. W. Murphy eds.)*, published by ISAS, 2000.

Miyazaki S., Saito T., Sasaki M., Hatanaka Y., and Iimura Y., Expansion of GSI's Nationwide GPS Array, *Bull. Geogr. Surv. Inst.,* Vol. 43, pp. 23-34, 1997.

Moran J. E. and Rosen B. R., Estimation of the Propagation Delay through the Troposphere from Microwave Radiometer Data, *Radio Sci.*, 16., pp. 235, 1981.

Nakajima J., Koyama Y., Sekido M., Kurihara N., Kondo T., Kimura M., and Kawaguchi N., 1-Gbps VLBI, the First Detection of Fringes, *Experimental Astronomy*, Vol. 11, pp. 57-69, 2001.

Nice D. J. and Taylor J. H., PSR J2019+2425 and PSR J2322+2057 and the Proper Motions of Millisecond Pulsars, *Astrophys. J.*, Vol. 41, pp. 429-435., 1995.

Niell A. E., Global Mapping Function for the Atmosphere Delay at Radio Wavelength, *J. Geophys. Res.*, Vol. 101, pp. 3227-3246, 1996.

Nunes N. V., and Bartel N., Astrometry of the Planetary-system Millisecond Pulsar B1257+12. *IAU Colloquium 164: Emission from Galactic and Extragalactic Compact Sources*, ASP Conf. Ser. Vol. 144, (J. A. Zensus, G. B. Taylor, and J. M. Wrobel eds.), pp. 331-332, 1998

Petit G., Observations VLBI Des Pulsars Millisecondes Pour le Raccordement des Systèmes de Rèfèrence Cèlestes et la Stabilitè des Èchelles de Temps", PhD. Thesis, 1994.

Pérez-Torres M. A., Marcaide J. M., Guirado J. C., Ros E., Shapiro I. I., Ratner M. I., and Sardón, Toward Global Phase-delay VLBI Astrometry: Observations of QSO 1150+812 and BL 1803+784, *Astron. Astrophys.*, Vol. 360, pp. 161-170, 2000.

Rasmussen O., Kerridge D., Araki T., Iemori T., and Lakhina G. S., *World Data Center for Geomagnetism, KYOTO*, http://swdcdb.kugi.kyoto-u.ac.jp/.

Rickett B. J., Frequency Structure of Pulsar Intensity Variations, *Nature* , Vol. 221, pp. 158-159, 1969.

Rickett B. J., Interstellar scattering and Scintillation of Radio Waves, *Ann. Rev. Astron. Astrophys.*, Vol. 15, pp. 479-504, 1977.

Rickett B. J., Radio Propagation through the Turbulent Interstellar Plasma, *Ann. Rev. Astron. Astrophys.*, Vol. 28, pp. 561-605, 1990.

Rodin A. E., Ilyasov Yu. P., and Oreshko V. V., Timing Noise as A Source of Discrepancy Between Timing and VLBI Pulsar Positions, *IAU Colloquium 177: Pulsar Astronomy - 2000 and Beyond* ASP Conf. Ser. Vol. 202, (M. Kramer, N. Wex, and R. Wielebinski eds.), pp. 145-146, 2000.

Rodin A. E., and Sekido M., Link of Reference Frames by Pulsar Timing and VLBI, VLBI Symposium 2000 in Mizusawa, in printing 2001.

Rogers A. E. E., Very Long Baseline Interferometry with Large Effective Bandwidth for Phase-delay Measurements, *Radio Sci.*, Vol. 5, pp. 1239-1247, 1970.

Ros E., Marcaide J. M., Gurado J. C., Sardón E., and Shapiro I. I., A GPS-based Method to Model the Plasma Effects in VLBI Observations, *Astron. Astrophys.*, Vol. 356, pp. 357-362, 2000.

Saito A., Fukao S., and Miyazaki S., High Resolution Mapping of TEC Perturbations with the GSI GPS Network over Japan, *Geophys. Res. Lett.*, Vol. 25, pp. 3079-3082, 1998.

Salter M. J., Lyne A. G., and Anderson B., Measurements of the Trigonometric Parallax of Pulsars, *Nature* , Vol. 280, pp. 477-478, 1979.

Sardón E., Rius A., and Zarraoa N., Estimation of the Transmitter and Receiver Differential Biases and the Ionospheric Total Electron Content from Global Positioning System Observations, *Radio Sci.*, Vol. 29, pp. 577-586, 1994.

Schaer S., Beutler G., and Rothacher M., Mapping and Predicting the Ionosphere, *Proc. IGS Analysis Center Workshop 1998, ESA/ESOC Darmstadt in Germany, February 9-11 1998,* pp. 307-318, 1998a.

Schaer S., Gurtner W., and Feltens J. , IONEX: The ionosphere Map EXchange Format Version 1, *Proc. of IGS Analysis Center Workshop, ESA/ESOC Darmstadt in Germany, February 9-11 1998,* pp. 233-247, 1998b.

Schaer S., Mapping and Predicting the Earth's Ionosphere Using the Global Positioning System, Ph.D.Thesis, Bern University, 1999.

Scheuer P. A. G., Amplitude Variations in Pulsed Radio Sources, *Nature* , Vol. 218, pp. 920-922, 1968.

Seidelmann P. K., 1980 IAU Nutation: The Final Report of the IAU Working Group on Nutation, *Celest. Mech.*, 27, pp. 79-106, 1982.

Seiradakis, J. H., Gil, J. A., Graham, D. A., Jessner, A., Kramer, M., Malofeev, V. M., Sieber, W. and Wielebinski, R., Pulsar Profiles at Hight Frequencies. I. The Data., *Astron. Astrophys. Suppl.*, Vol. 111, pp. 205-227, 1995.

Sekido M., Hama S., Kiuchi H., Imae M. Hanado Y., Takahashi Y., Rodin A. E., and Ilyasov Y. P., Development of K4 Correlator for Pulsar VLBI Japan-Russia Baseline, *in Proc. of IAU colloquium 164, (J. A. Zensus, G. B. Taylor, J. M. Worobel eds.)*, A.S.P. Conf. Ser. Vol. 105, (BookVrafter, San Francisco) pp. 403-404, 1998.

Sekido M., Imae M., Hanado Y., Ilyasov Y. P., Oreshko V. V., Rodin A. E., Hama S., Nakajima J., Kawai E., Koyama Y., Kondo T., Kurihara N., and Hosokawa M., Astrometric VLBI Observation of PSR 0329+54, *Publ. A. S. J.*, Vol. 51, pp. 595-601, 1999a.

Sekido M., Imae M., Hanado Y., Hama S., Koyama Y., Kondo T., Nakajima J., Kawai E., Kurihara N., Ilyasov Y. P., Oreshko V. V., Rodin A. E., and Poperechenko B. A., Pulsar VLBI Experiment with the Kashima (Japan)-Kalyazin (Russia) Baseline, *New Astron. Rev.,* Vol. 43, pp. 599-602, 1999b.

Shabanova T., Evidence for A Planet around the Pulsar PSR B0329+54, *Astrophys. J.*, Vol. 453, pp. 779-782, 1995.

Shibazaki N., Neutron Star and Pulsar (in Japanese), New Cosmos Series, Baifukan Pub. Co. Ltd., Tokyo, 1993.

Sugimoto Y. and Hama S., III-2 Correlation Processor (in Japanese), *Review of Radio Res. Lab.*, Vol. 30, pp. 163-176. 1998.

Takahashi Y., Hama S., and Kondo T., K-3 Software System for VLBI and New Correlation Processing Software for K-4 Recording System, *J. Comm. Res. Lab.*, Vol. 38, pp. 481-501, 1991.

Takahashi F., Kondo T., Takahashi Y., and Koyama Y., Very Long Baseline Interferometer, Ohmsha Ltd. p. 91, 2000.

Taylor J. H. and Weisberg J. M, Further Experimental Tests of Relativistic Gravity Using the Binary Pulsar 1913+16, *Astrophys. J.*, Vol. 345, pp. 434-450, 1989.

Taylor J. H., Manchester R. N., and Lyne A. G., Catalog of 558 Pulsars, *Astrophys. J. Supp.*, Vol. 88 pp. 529-568, 1993.

Taylor J. H., and Codes J. M., Pulsar Distances and the Galactic Distribution of Free Electrons, *Astrophys. J.*, Vol. 411, pp. 674-684, 1993.

Taylor J. H., Millisecond Pulsars: Nature's of Most Stable Clocks, *Proc. of IEEE,* Vol. 79. pp. 1054-1062, 1997.

Thompson A. R., Moran J. M., and Swenson Jr. G. W., Interferometry and Synthesis in Radio Astronomy, Krieger Pub. Com., Florida, 1994.

Wahr J. M., The Forced Nutations of an Elliptical, Rotating, Elastic, and Oceanless Earth, *Geophys. J. R. Astron. Soc.*, Vol. 64, pp. 705-727, 1981.

Whitney A. R. , Precision Geodesy and Astrometry via Very-Long-Baseline Interferometry, PhD Thesis, Massachusetts Institute of Technology, 1974.

Whitney A. R., Rogers A. E. E., Hinteregger H. F., Knight C. A., Levine J. I., and Lippincott S., A Very-Long-Baseline Interferometer System for Geodetic Applications., *Radio Sci.*, Vol., 11, pp. 421-432, 1976.

Wilson B. D., Mannucci A. J, and Edwards C. D., Subdaily Northern Hemisphere Ionospheric Maps Using an Extensive Network of GPS Receivers, *Radio Sci.*, Vol. 30, pp. 639-648, 1995.

Wolszczan A., Confirmation of Earth-Mass Planets Orbiting the Millisecond Pulsar PSR B1257+12, *Science* , Vol. 264, pp. 538-542, 1994.

Yoshino T., Overview of the Key Stone Project, *J. Comm. Res. Lab.*, Vol. 46, pp. 3-6, 1999.

Zensus J. A., Diamond P. J., and Naiper P. J., Very Long Baseline Interferometry and the VLBA, Astron Soc. of Pacific Conf. Ser. Vol. 82, 1995.

Glossary

BOPP Time epoch at beginning of PP

BWS Band Width Synthesis

CEP Celestial Ephemeris Pole

CODE Center for Orbit Determination in Europe

CRL Communications Research Laboratory

DLR The Deutsches Zentrum für Luft- unt Raumfahrt

DRF Dynamical Reference Frame

EOP Earth Orientation Parameter

GPS Global Positioning System

ICRF International Celestial Reference Frame

IERS International Earth Rotation Service

IF Intermediate frequency

ISP Ionospheric point

ISS Interstellar Scintillation

ISM Interstellar Medium

ITRF International Terrestrial Reference Frame

JPL The NASA Jet Propulsion Laboratory/ California Institute of Technology

GGR Geodetic GPS receiver

GIM Global Ionosphere Map

GGR Geodetic GPS Receiver

GSFC Goddard Space Flight Center

LLR Lunar Laser Ranging

LSQ Least Square

LHCP Left Hand Circular Polarization

MIT The Massachusetts Institute for Technology

P-cal Phase calibration signal

PP Parameter Period: minimum time unit of correlator output.

PRAO Pushchino Radio Astronomy Observatory of the Astro Space Center of the Lebedev Physical Institute (Russia)

PRT Processing Reference Time

RHCP Right-Hand-Circular Polarization

SNR Signal-to-Noise Ratio

SRBMPEI Special Research Bureau of Moscow Power Engineering Institute

TAI International Atomic Time

TB Time of Solar System Barycenter

TEC Total Electron Content

TOA Time of Arrival

TT Terrestrial Time

UT1 Universal Time

UTC Coordinated Universal Time

VLBI Very-Long-Baseline Interferometry

VTEC Vertical TEC

Appendix

A Basis of Correlation Processing in VLBI and Fringe Rotation

A.1 Correlation of Received Signals

Mathematical formulation of one-baseline correlation processing in VLBI is described in this section. The XF[1] type correlation processing is in mind in this description and one will see that the necessity of fringe rotation comes from frequency conversion of an observed radio signal.

Let the observed signal voltage at two VLBI stations (X and Y) be

$$\begin{cases} x(t) &= g_x s_0 \sin\omega t + n_x \\ y(t) &= g_y s_0 \sin\omega(t-\tau_g) + n_y, \end{cases} \tag{A1}$$

where s_0 is radio flux from a radio source; g_x and g_y are gains of the X and Y stations antennas; τ_g is group delay of the signal at Y station in reference to to X station; n_x and n_y are the noises at each stations; and ω is the angular frequency of the observed radio signal. For the purpose of easy handling of the data for sampling and recording, observed signals are converted to lower frequency with local oscillators signals, whose phases are locked with hydrogen atomic frequency standards at each station. Usually not only once but also several such frequency conversions are performed to down convert to video frequency in an actual observation. Let the angular frequency of the local oscillators at the X and Y stations be ω_x and ω_y. If the upper side band (USB) is used for the observation, $\omega_x, \omega_y < \omega$. The direction of inequality is opposite if the lower side band (LSB) is used for the observation. After mixing the local signal and low-pass filtering, the observation signals are given by

$$\begin{aligned} x(t) &= g_x s_0 \sin\{(\omega-\omega_x)t + \phi_x\} + n_x \\ y(t) &= g_y s_0 \sin\{(\omega-\omega_y)t - \omega\tau_g + \phi_y\} + n_y, \end{aligned} \tag{A2}$$

where ϕ_x and ϕ_y are initial phases of local oscillators at station X and Y, respectively. Correlation coefficient is defined by

$$\rho(\tau) = \frac{\frac{1}{T}\int_0^T x(t)y(t+\tau)dt}{\sqrt{\frac{1}{T}\int_0^T x(t)^2 dt}\sqrt{\frac{1}{T}\int_0^T y(t)^2 dt}}. \tag{A3}$$

The function in the integral of the numerator is expressed by using equation (A2) as

$$x(t)y(t+\tau) = [g_x s_0 \sin\{(\omega-\omega_x)t + \phi_x\} + n_x][g_y s_0 \sin\{(\omega-\omega_y)(t+\tau) - \omega\tau_g + \phi_y\} + n_y]. \tag{A4}$$

Since the signal from the radio source is normally much smaller than the system noise temperature, then $n_x, n_y >> g_x s_0, g_y s_0$ can be assumed. Cross terms between noises n_x and n_y and radio source signal

[1] XF type correlator multiples the two signals in time domain. Another type of correlator is the FX-type VLBI correlator, which multiples the two signals in frequency domain. The FX correlator was proposed by Chikada [*Chikada,*, 1981; *Chikada et al.*, 1987; *Chikada,*1991] and realized as a correlator for VLBI Space Observatory program (VSOP)

$g_x s_0$ and $g_y s_0$ are also noise but much smaller than the term $n_x n_y$. Hence, by neglecting the cross terms, equation (A4) is approximated as

$$\begin{aligned} x(t)y(t+\tau) &\approx g_x g_y s_0^2 \sin\{(\omega-\omega_x)t+\phi_x\}\sin\{(\omega-\omega_y)(t+\tau)-\omega\tau_g+\phi_y\}+n_x\ n_y & \text{(A5)}\\ &= \frac{1}{2}g_x g_y s_0^2[\cos\{(\omega_x-\omega_y)t+(\omega-\omega_y)\tau+\phi_y-\phi_x-\omega\tau_g\} & \text{(A6)}\\ &- \cos\{(2\omega-\omega_x-\omega_y)t+(\omega-\omega_y)\tau+\phi_x+\phi_y-\omega\tau_g\}]+n_x n_y. \end{aligned}$$

Since $|(2\omega-\omega_x-\omega_y)t| \approx 2|(\omega-\omega_x)t|$, the second cosine term fade out very quickly during integration time. Consequently, the signal part of equation (A4) is expressed as

$$x(t)y(t+\tau) \approx \frac{1}{2}g_x g_y s_0^2 \cos\{(\omega_x-\omega_y)t+(\omega-\omega_y)\tau+\phi_y-\phi_x-\omega\tau_g\}. \quad \text{(A7)}$$

Let $\omega_{\rm LO}$ be true local frequency and let r_x and r_y be clock rate of hydrogen atomic standards at station X and Y, respectively. Then actual local frequency $\omega_x = \omega_{\rm LO}(1+r_x)$ and $\omega_y = \omega_{\rm LO}(1+r_y)$. The argument of cosine function of equation (A7) is thus

$$ARG = \phi_y - \phi_x + (\omega-\omega_y)(\tau-\tau_g) - \omega_y\tau_g + \omega_{\rm LO}(r_x-r_y)t. \quad \text{(A8)}$$

Even if the correlator delay model (τ) traces the actual group delay (τ_g), that is, $\tau = \tau_g$, the term $\omega\tau_g$ rotates the phase and reduces the correlation coefficient. This is called fringe rotation. Hence, compensation of the fringe rotation (fringe stopping) is necessary to obtain a correlation result. If $\omega_y = 0$, that is, if frequency conversion is not used, fringe rotation is not necessary in correlation processing. In an actual correlation process, τ does not trace τ_g smoothly but traces it in discrete steps by sampling period Δt. Hereafter, the delay-tracking correlator model is expressed by τ_k in order to express the discrete delay tracking explicitly.

A.2 Baseband Fringe Rotation

Actual fringe stopping is performed by multiplexing $\sin\phi(t)$ and $\cos\phi(t)$, where $\phi(t)$ is fringe rotation phase. When fringe stopping is performed in reference to local frequency (baseband) ω_y, the rotation phase including compensation of clock rate difference between two hydrogen atomic standards is

$$\phi(t) = \omega_{\rm LO}\tau_c - \omega_{\rm LO}(r_x-r_y)t, \quad \text{(A9)}$$

where τ_c is continuously variable delay of correlator model. Multiplexing $\cos\phi(t)$ with equation (A7) gives

$$\begin{aligned} x(t)y(t+\tau_c)\cos\phi(t) &= \frac{1}{2}g_x g_y s_0^2[\cos\{\Delta\phi+(\omega-\omega_y)(\tau_k-\tau_g)+\omega_{\rm LO}\tau_c-\omega_y\tau_g\}\\ &+\cos\{\Delta\phi+(\omega-\omega_y)(\tau_k-\tau_g)+2\omega_{\rm LO}(r_x-r_y)t-\omega_y\tau_g-\omega_{\rm LO}\tau_c\}] & \text{(A10)}\\ &+n_x n_y', & \text{(A11)} \end{aligned}$$

where $\Delta\phi = \phi_y - \phi_x$ and $n_y' = n_y\cos\phi(t)$. Since $\tau_g \approx \tau_c$ and $\omega_{\rm LO} \approx \omega_y$, the second term of equation (A11) will fade out in time scale $\pi/\omega_{\rm LO}\tau_g'$. Usually geometrical delay rate $\tau_g' \le 10^{-8}$ s/s, the time scale is thus about 70 msec for 1.4 GHz observation and it becomes shorter as observation frequency either baseline length increases The difference between correlator delay model and true group delay is expressed by Taylor series as

$$\Delta\tau_c = \tau_c - \tau_g = \Delta\tau_c^{(0)} + \Delta\tau_c^{(1)}t + \frac{1}{2}\Delta\tau_c^{(2)} + \cdots \quad \text{(A12)}$$

When terms of higher than third order in the Taylor series are neglected, the fringe-rotation-compensated products of observed signal in real (cos) and imaginary (sin) components are

$$\begin{aligned} x(\omega,t)y(\omega,t+\tau_k)\cos\phi(t) &= A\cos\{\Delta\phi+(\omega-\omega_y)\Delta\tau_k+\omega_y\Delta\tau_c\}+n_x n_y'\\ x(\omega,t)y(\omega,t+\tau_c)\sin\phi(t) &= A\sin\{\Delta\phi+(\omega-\omega_y)\Delta\tau_k+\omega_y\Delta\tau_c\}+n_x' n_y, \end{aligned} \quad \text{(A13)}$$

where $\Delta\phi = \phi_y - \phi_x$, $\Delta\tau_c = \tau_c - \tau_g$, $\Delta\tau_k = \tau_k - \tau_g$, and $A = \frac{1}{2}g_x g_y s_0^2$. Thus, temporal fringe phase consists of difference of instrumental phase offset ($\Delta\phi$), residual phase of correlator model error ($\omega_{\rm LO}\Delta\tau_c$),

and group delay residual ($(\omega - \omega_y)\Delta\tau_k$). The phase of term $(\omega - \omega_y)\Delta\tau_k$ is related to delay tracking. Since data is sampled by time interval $\Delta t = 1/2B$, where B is video bandwidth, discrete delay tracking is inevitable in digital correlation processing with XF type correlator. The K3 and K4 correlators are XF type correlators, which multiple the observed data in time domain, then saw shape phase vibration in the range from $-\omega_{\rm Video}\Delta t/2$ to $\omega_{\rm Video}\Delta t/2$ is caused by discrete delay tracking in correlation processing. An efficiency factor of loss due to this effect is given by as

$$\begin{aligned} \eta_{\rm FrBB}(f) &= \frac{1}{\Delta t}\int_{-\Delta t/2}^{\Delta t/2} \exp\{j2\pi ft\}dt \\ &= \mathrm{sinc}(\frac{\pi f}{2B}), \end{aligned} \tag{A14}$$

where f is video frequency and $\mathrm{sinc}(t) = \frac{\sin(t)}{t}$. The efficiency decreases from 1 at baseband to $2/\pi = 0.63$ at band edge.

A.3 Fringe Rotation at Band Center and 90-Degree Phase Jump

To minimise the loss of the phase vibration caused from discrete delay tracking, phase rotation at the band center is used for ordinary VLBI correlation processing in the XF-type correlator. In case of band-center-fringe-rotation, the argument of cosine function of equation (A7) is expressed as

$$ARG = \Delta\phi + (\omega - \omega_y - \pi B)(\tau_k - \tau_g) - \pi B\tau_k - (\omega_y + \pi B)\tau_g + \omega_{\rm LO}(r_x - r_y)t. \tag{A15}$$

Since delay tracking is performed by one sample of time width $\Delta t = 1/2B$, the third term of equation (A15), $\pi B\tau_k = \frac{\pi}{2}k$, causes 90-degree phase jump at every bit shift. To compensate for the third, fourth, and fifth term of this argument, fringe rotation phase

$$\phi(t) = (\omega_y + \pi B)\tau_c + \pi B\tau_k - \omega_{\rm LO}(r_x - r_y)t \tag{A16}$$

is used instead of equation (A9). Here B is positive for the USB and negative for the LSB; thus, the direction of 90-degree phase jump is changed by sideband. After fringe stopping, the argument becomes

$$ARG = \Delta\phi + (\omega - \omega_y - \pi B)(\tau_k - \tau_g) - (\omega_y + \pi B)(\tau_c - \tau_g). \tag{A17}$$

Thus, real (cos) and imaginary (sin) components of cross correlation are

$$\begin{aligned} x(\omega,t)y(\omega,t+\tau_c)\cos\phi(t) &= A\cos\{\Delta\phi + (\omega - \omega_y - \pi B)\Delta\tau_k + (\omega_y + \pi B)\Delta\tau_c\} \\ &+ n_x n'_y \\ x(\omega,t)y(\omega,t+\tau_c)\sin\phi(t) &= A\sin\{\Delta\phi + (\omega - \omega_y - \pi B)\Delta\tau_k + (\omega_y + \pi B)\Delta\tau_c\} \\ &+ n_x n'_y. \end{aligned} \tag{A18}$$

The second term of the phase is due to delay tracking. Since Delay tracking is performed in discrete steps as $\tau_k = k\Delta t$. Then, the remaining fringe phase consists of difference of instrumental phase offset ($\Delta\phi$), group delay residual ($(\omega - \omega_y - \pi B)\Delta\tau$), and residual phase of correlator model error ($(\omega_y + \pi B\Delta)\tau_c$). In this case, the variation range of the fringe phase is from $-\omega_{\rm Video}\Delta t/4$ to $\omega_{\rm Video}\Delta t/4$. The maximum phase error is $\pm\pi/4$ at the base band and band edge. An efficiency factor of loss due to this effect is given by as

$$\begin{aligned} \eta_{\rm FrBC}(f) &= \frac{1}{\Delta t}\int_{-\Delta t/2}^{\Delta t/2} \exp\{j2\pi(f - B/2)t\}dt \\ &= \mathrm{sinc}\{\pi(f - B/2)\Delta t\}, \end{aligned} \tag{A19}$$

where f is video frequency in the range of ($0 \le f \le B$). The maximum correlation loss is about 10% at the band edge (f=0 and B). When the radio source has a continuum radio spectrum and the flux is constant in the video band, mean efficiency factor due to band-center fringe rotation is

$$\bar{\eta}_{\rm FrBC} = \frac{1}{B}\int_0^B \eta_{\rm FrBC}(f)df$$

$$
\begin{aligned}
&= \frac{2}{\pi}\int_{-\pi/4}^{\pi/4}\frac{\sin u}{u}du \\
&= \frac{2}{\pi}\int_{-\pi/4}^{\pi/4}\sum_{n=i}^{\infty}(-1)^{n+1}\frac{t^{2n-2}}{(2n-1)!}dt \\
&= 1\frac{1}{3\cdot 3!}(\frac{\pi}{4})^2+\frac{1}{5\cdot 5!}(\frac{\pi}{4})^4\cdots \\
&= 1-\frac{\pi^2}{288}+\frac{\pi^4}{153600}-\cdots
\end{aligned}
\tag{A20}
$$

More information concerned with astronomical source imaging can be found in "Interferometry and Synthesis in Radio Astronomy" [*Thompson et al,*, 1994] and "Very Long Baseline Interferometry and the VLBA" [*Zensus et al.*, 1995]. VLBI application for geodesy is described by Whitney [*Whitney,* 1974]. Description of the Japanese K3 VLBI system can be found in "System Development of K-3 Very Long Baseline Interferometry" [*CRL,* 1984] (in Japanese).

B Equivalence of Bandwidth Synthesis and Least Square Estimation of Group Delay

Bandwidth synthesis (BWS) is a technique to integrate coherently separated multiple frequency channels of correlation output data and to find out a group delay parameter which maximize the delay resolution function (DRF). The phase delay rate search is eliminated in this description because determination of phase delay rate is basically done at each channel and BWS is not essential for it.

The function to be maximized is equation (3.5):

$$D(\tau_{\rm res}) = Be^{j\frac{B}{2}(\tau_{\rm res})}{\rm sinc}(\frac{B}{2}\tau_{\rm res})\sum_{i=1}^{n} g_{x,i}g_{y,i}s_{0,i}^2 \exp j\{\Delta\phi_i + \omega_{y,i}\tau_{\rm res}\}, \tag{B1}$$

where $\tau_{\rm res} = \tau - \tau_{g\rm PRT}$. The factor in front of the summation on the right hand side of the equation does not affect to result of BWS since they have a broad shape with a time span of 2/B, about 1μsec, so let's consider only the term of the summation. Multiplexing the complex conjugate of that term gives

$$\begin{aligned} |Df(\tau_{\rm res})|^2 &= |\sum_{i=1}^{n} A_i \exp j\{\Delta\phi_i + \omega_{y,i}\tau_{\rm res}\}|^2 \\ &= \sum_{i=1}^{n} A_i^2 + 2\sum_{i>j}^{n} A_iA_j \cos\{\Delta\phi_i - \Delta\phi_j + (\omega_{y,i} - \omega_{y,j})\tau_{\rm res}\}. \end{aligned} \tag{B2}$$

The DRF is maximized by the maximum of the second term of equation (B2), and its real-part gives a maximum when the argument of the cosine function is close to zero:

$$(\omega_{y,i} - \omega_{y,j})\tau_{\rm res} \sim \Delta\phi_i - \Delta\phi_j.$$

Under this condition, up to the second order of the Taylor expansion of the cosine function is,

$$Q_1 = \sum_{i>j}^{n} A_iA_j + 2\sum_{i>j}^{n} A_iA_j[1 - \frac{1}{2}\{\Delta'_{i,j} + (\omega_{y,i} - \omega_{y,j})\tau_{\rm res}\}^2], \tag{B3}$$

where $\Delta'_{i,j} = \Delta\phi_i - \Delta\phi_j$. The maximum of Q_1 is given at $\partial Q_1/\partial\tau_{\rm res} = 0$. Then,

$$\tau_{\rm res} = \frac{\sum_{i>j}^{n} A_iA_j(\omega_i - \omega_j)\Delta_{i,j}}{\sum_{i>j}^{n} A_iA_j(\omega_i - \omega_j)^2}. \tag{B4}$$

By the way, let's consider a problem : "When a set of data $\Delta\phi_i$, ω_i, and its weight A_i (i=1 – n) are given, solve coefficients of first order polynomial to best fit to the data by weighted least square ". Least square (LSQ) requires a square sum

$$Q_2 = \sum_{i=1}^{n} A_i^2(\Delta\phi_i - \omega_i\tau - \theta)^2 \tag{B5}$$

to be minimized. From the condition $\partial Q_2/\partial\tau = 0$, τ is derived as

$$\tau = \frac{(\sum_{i=1}^{n} A_i\Delta\phi_i)(\sum_{i=1}^{n} \omega_iA_i) - (\sum_{i=1}^{n} A_i\Delta\phi_i\omega_i)(\sum_{i=1}^{n} A_i)}{(\sum_{i=1}^{n} \omega_iA_i)^2 - (\sum_{i=1}^{n} \omega_i^2A_i)(\sum_{i=1}^{n} A_i)} \tag{B6}$$

$$= \frac{\sum_{i>j}^{n} A_iA_j(\Delta\phi_i - \Delta\phi_j)(\omega_i - \omega_j)}{\sum_{i>j}^{n} A_iA_j(\omega_i - \omega_j)^2} \tag{B7}$$

$$= \frac{\sum_{i>j}^{n} A_i A_j (\omega_i - \omega_j) \Delta_{i,j}}{\sum_{i>j}^{n} A_i A_j (\omega_i - \omega_j)^2}. \tag{B8}$$

Since the delay determined by two method, BWS (equation (B4)) and weighted LSQ (equation (B8)), are identical, the equivalence of BWS and LSQ was proved. It is obvious that the amplitude of the correlation coefficient of each channels corresponds to the weight of phase observable at each channel in the LSQ.

C Evaluation of TEC Map Error from RMS Difference between VLBI-measured TEC and GPS-based TEC Map

The relation between TEC map error and RMS difference of two TEC measurements is discussed for accuracy evaluation of the TEC maps. TEC observed by VLBI is expressed by

$$dTEC_{\rm VLBI} = dTEC + \epsilon_{\rm VLBI}, \tag{C1}$$

where $dTEC$ is the true difference of TEC along ray paths between two VLBI stations, and $\epsilon_{\rm VLBI}$ is the error of VLBI measurement. Vertical TEC value of GPS-based TEC map is expressed by

$$VTEC_{\rm GPS} = VTEC + \epsilon_{\rm GPS}, \tag{C2}$$

where $VTEC$ is true vertical TEC and $\epsilon_{\rm GPS}$ is error of GPS-based TEC map. TEC difference corresponding to VLBI observation (C1) is expressed by using mapping function $Fm(El)$ as

$$\begin{aligned} dTEC_{\rm GPS} &= \{VTEC_y + \epsilon_{\rm GPS,y}\}Fm(El_y) \\ &\quad -\{VTEC_x + \epsilon_{\rm GPS,x}\}Fm(El_x). \end{aligned} \tag{C3}$$

Since the effect of ray-path bending and electron density height profile are eliminated in the TEC map model, TEC difference observed by VLBI is expressed by $dTEC = VTEC_y Fm(El_y) - VTEC_x Fm(El_x)$. Then error related terms remaining in the difference between VLBI and GPS are

$$\begin{aligned} \Delta TEC &= dTEC_{\rm GPS} - dTEC_{\rm VLBI} \\ &= \epsilon_{{\rm GPS},y} Fm(El_y) - \epsilon_{{\rm GPS},x} Fm(El_x) - \epsilon_{\rm VLBI} \end{aligned} \tag{C4}$$

(i) Short baseline

Error of GPS-based TEC map, $\epsilon_{\rm GPS}$, consists of two components $\epsilon_{\rm GPS,u}$ and $\epsilon_{\rm GPS,c}$. $\epsilon_{\rm GPS,u}$ is uncorrelated error and $\epsilon_{\rm GPS,c}$ is correlated error of TEC on that baseline. When the baseline is short and the elevation angles at both stations are almost the same, $Fm(El_x) \approx Fm(El_x)$; thus, common error components are cancelled. Then, the ensemble average of ΔTEC^2 at an elevation angle El ($= El_x \approx El_y$) is expressed by error of TEC map and error of VLBI observation as follows:

$$< \Delta TEC^2 > = (\sigma^2_{u,x} + \sigma^2_{u,x}) Fm^2(El) + \sigma^2_{\rm VLBI} \tag{C5}$$

$$\approx 2\sigma^2_{u,x} Fm^2(El) + \sigma^2_{\rm VLBI}. \tag{C6}$$

Here <> means ensemble average, $\sigma^2_{u,x}$, and $\sigma^2_{u,y}$, are uncorrelated error of the TEC map for station x, y, and $\sigma^2_{\rm VLBI}$ is error of VLBI observation. And $\sigma^2_{u,x} =< \epsilon^2_{{\rm GPS},x} > \approx \sigma^2_{u,y} =< \epsilon^2_{{\rm GPS},x} >$ were used to derive equation (C5) and (C6).

(ii) Long baseline

When the baseline is long and the elevation angles at the two stations are different, common error is not cancelled out, the ensemble average of the square of equation (C4) at an elevation angle pair El_x, El_y is

$$\begin{aligned} < \Delta TEC^2 > &= \sigma^2_x Fm^2(El_x) + \sigma^2_y Fm^2(El_y) \\ &+ \sigma^2_{\rm VLBI} - 2 < \epsilon_x \epsilon_y > Fm(El_x) Fm(El_y). \end{aligned} \tag{C7}$$

$$\approx \sigma^2_x \{Fm^2(El_x) + Fm^2(El_y)\} + \sigma^2_{\rm VLBI} \tag{C8}$$

where σ_x is the error variance of the GPS-based TEC map. An approximation of $\sigma_x \approx \sigma_y$ and an assumption of no correlation between ϵ_x and ϵ_y (i.e., $< \epsilon_x \epsilon_y >= 0$) are used in approximation from equation (C7) to (C8).

D K4 Correlator Output File Format

The output format of the K4 correlator is divided into two parts: a header record (Table D.1), which contains correlation parameters about that baseline, and a data record (Table D.2), which contains correlation data. The data record corresponds to an output from one correlator board for one PP. After the a header recored is put at the beginning of the data file, set of 16 data records, correspond to 16 correlator boards, are repeated every PP.

Table D.1: K4 correlator output format (header record: 512 bytes) (Ver. 1.12).

Type	Name	Number of bytes	Address	Comment
char	excode[10]	10	0	Experimental code
short	nobs	2	10	Number of observations
char	lfile[6]	6	12	Name of Kross file
char	lbase[2]	2	18	Baseline ID
short	npp	2	20	Number of parameter period
short	pp	2	22	Period of PP
short	nkomb	2	24	Frequency of KOMB process
short	krdate[4]	8	26	Correlation processing date
char	kbfile[6]	6	34	File name of KOMB
char	srcnam[8]	8	40	Source name
short	srcra.h	2	48	Source right ascension hour
short	srcra.m	2	50	Source right ascension minute
double	srcra.s	8	52	Source right ascension second
short	srcdec.d	2	60	Source declination degree
short	srcdec.m	2	62	Source declination arc minute
double	srcdec.s	8	64	Source declination arc second
short	iprt[5]	10	72	Parameter reference time y, d, h, m, s
char	statx[8]	8	82	X Station name
char	staty[8]	8	90	Y Station name
double	x-xyz[3]	24	98	X Station coordinates
double	y-xyz[3]	24	122	Y Station coordinates
short	ostart[5]	10	146	OBS. Start time y, d, h, m, s
short	ostop[5]	10	156	OBS. Stop time y, d, h, m, s
short	srcgha.h	2	166	Greenwich Hour Angle (GHA) at PRT: hour
short	srcgha.m	2	168	GHA at PRT: minute
short	srcgha.s	8	170	GHA at PRT: second
float	tsampl	4	178	Sampling period (sec)
float	vbw	4	182	Video bandwidth (Hz)
short	nch	2	186	Number of channel
float	aclko	4	188	Clock offset
float	aclkr	4	192	Clock rate
float	dlyinx	4	196	Instrumental delay in X band
float	dlyins	4	200	Instrumental delay in S band
float	axclke	4	204	Clock diff. between X St. and UTC
double	dpi	8	208	The circular constant
double	dc	8	216	The velocity of Light
double	frqtab[16]	128	224	Radio frequency table
float	pcalf[16]	64	352	P-CAL frequency table
double	aptau[4]	32	416	A priori value of τ, $\frac{d\tau}{dt}$, $\frac{d^2\tau}{d^2t}$, and $\frac{d^3\tau}{d^3t}$

Table D.1: Continued

Type	Name	Number of bytes	Address	Comment
short	srch	2	448	Channel number for fringe search
char	cmode[2]	2	450	Correlator mode "NO" or "SE"
short	unit	2	452	Search mode lag distance between units
short	cunit	2	454	Central unit at search mode
double	crldbl	8	456	Double variable (unused)
float	plsdm	4	464	Pulsar DM
short	pndiv	2	468	Division number
char	frgmod[2]	2	470	Fringe mode "CO"nt. or "EV"ery
double	plsprd	8	472	Pulsar period (msec)
float	pofst	4	480	Division offset
bit	mode.nouse	2	484	16 - 6 bit not used
	mode.crsmode			5: Correlation mode (Auto/Cross)
	mode.dmode			4: Common data distribution or parallel
	mode.lmode			3: Lag connection in series or parallel
	mode.psrch			2: Gate mode on or off
	mode.gmode			1: Pulsar search mode of or off
char	ver[8]	8	486	Kross software version
char	dummy[14]	14	494	Not used
char	fmtflag[4]	4	508	Format flag ("KSP" or "K4")

Table D.2: K4 correlator output format (Data record: 256 Byte) per unit per PP.

Type	Name	Byte	Address	Comment
unsigned char	ksel	1	0	KSEL
unsigned char	rmks	1	1	Remarks
bit	chn			4-8: Channel number
bit	del-flag			3: del flag by KOMB
bit	dummy			1-2: not used
unsigned char	coflag	1	2	correlator flag
bit	frg-sgn			7-8: Fringe rotation sign
bit	frg-mod			6: Fringe rotator mode hard or soft
bit	frg-frq			5: Fr position, baseband or band center
bit	bit-comp			4: Fractional bit correction hard/soft
bit	update			3: Update flag
bit	dummy			1-2: not used
unsigned char	twe	1	3	Time word error flag
bit	avl			8: Data availability
bit	dummy			7: Not used
bit	crcxerr			6: X CRC error
bit	crcyerr			5: Y CRC error
bit	ymissyn			4: Y bit slip error
bit	twey			3: Y time word error
bit	xmissyn			2: X bit slip error
bit	twex			1: X time word error
unsigned long	crosp[2][18]	144	4	Cross corr. data
char	dummy1[44]	44	148	Not used
unsigned long	countp[2]	8	192	Total count
unsigned long	pcal[2][2]	16	200	pcal count X,Y
unsigned char	tim[2][7]	14	216	X,Y St. AUX, time data
long	tmdiff	4	230	Time difference in Cor.
long	fradd	4	234	Fringe rotator address
short	fbit	2	238	Fractional bit
unsigned char	comod	1	240	
bit	dummy			3-8: Not used
bit	cormode			2: Corr. bit mode (1/2)
bit	bitmode			1: 2bit weight mode
unsigned short	ipp	2	241	PP Number
short	hchan	2	243	2bit corr. high bit channel
short	lchan	2	245	2bit corr. low bit channel
char	dummy[9]	9	247	Not used

List of Publications

1. Sekido M., Hama S., Kiuchi H., Hanado Y., Takahashi Y., Imae M, Fujisawa K., and Hirabayashi H., "Pulsar VLBI Experiment Using Kashima-Usuda Baseline", Proceedings of International Symposium VLBI TECHNOLOGY: Progress and Future Observational Possibilities, (Edited by T. Sasao, S. Manabe, O. Kameya, and M. Inoue), Terrra Scientific Pub. Com. (Tokyo) Japan, pp. 306-312., 1994.

2. Sekido M, Imae M, Hanado Y., Takahashi Y., and Koyama Y., "Pulsar VLBI Experiment with Kashima (Japan)-Kalyazin (Russia) Baseline", Proceedings of IAU Colloquium 160 Pulsars: Problem and Progress, (Edited by S. Johnston, M. A. Walker, and M. Bailes), A.S.P. Conf. Ser. Vol. 105, pp. 117-118., 1996.

3. Sekido M., Hama S., Kiuchi H., Imae I., Hanado Y., Takahashi Y., Rodin A. E., Oreshko V. V., and Ilyasov Yu. P., "Development of K4 Correlator for Japan-Russia Pulsar VLBI", Proceedings of the Technical Workshop for APT and APSG 1996, pp. 183-187., 1997.

4. Sekido M., Hama S., Kiuchi H., Imae M., Hanado Y., and Takahashi Y., "Development of K4 Correlator for Pulsar VLBI:Japan-Russia Baseline", Proceedings of IAU Colloquium 164 Radio Emission from Galactic and Extragalactic compact sources (Edited by J. Anton Zensus, G. B. Taylor, and J. M. Wrobel), A.S.P. Conf. Ser. Vol. 144, pp. 403-404., 1998.

5. Sekido M., Imae M., Hanado Y., Hama S., Nakajima J., Kawai E., Koyama Y., Kondo T., Kurihara N., Hosokawa M., Ilyasov Yu. P., Oreshko V. V., and Rodin A. E., "Astrometric VLBI Observation of PSR0329+54", *Publ. A. S. J.*, Vol. 51, pp. 595-601, 1999.

6. Sekido M., Imae M., Hanado Y., Hama S., Koyama Y., Kondo T., Nakajima J., Kawai E., Kurihara N., Ilyasov Yu. P., Oreshko V. V., and Rodin A. E., "Pulsar VLBI experiment with Kashima (Japan) - Kalyazin (Russia) baseline", *New Astronomy Review*, Vol. 43, pp. 599-602, 1999.

7. Sekido M., Hama S., Imae M., Hanado Y., Takahashi Y., Ilyasov Yu. P., "Pulsar VLBI Experiment -for precise astrometry and reference frame tie-", Review of the Communications Research Lab., Vol. 45, pp. 137-149, 1999.

8. Sekido M., Kondo T., Kawai E., and Imae M., "Evaluation of GPS-based Ionospheric TEC measurements" (in Japanese), Technical Report of IEICE, A.P2000-161, SANE-2000-142 (20001-01), pp. 61-68, 2001.

9. Sekido M., Kondo T., Kawai E., Hanado Y., and Imae M., "Evaluation of GPS-based Ionospheric TEC Estimation and Application to Pulsar VLBI Observation" (in Japanese), Review of Communications Research Lab., Vol. 47, pp. 155-162, 2001.